University of Trento
Department of Mathematics

Doctoral Programme in Mathematics
in agreement with the University of Verona

38th cycle

PhD thesis

On quantum vortex reconnections

Candidate
Martina Luise

Supervisor
Prof. Nicola Sansonetto
Co-Supervisor
Prof. Renzo L. Ricca

Contents

Introduction

State of the art

This thesis analyzes the phenomenon of quantum reconnections [1, 2, 3, 4] in superfluids, in particular in Bose–Einstein condensates [5], which is a state of matter that arises when a system of bosons is cooled to extremely low temperatures, close to absolute zero [6, 7]. Under these conditions, a macroscopic fraction of the particles occupies the same quantum ground state, behaving collectively as a single coherent quantum entity described by a wavefunction that is coherent on a macroscopic scale. Since the present study focuses on temperatures much lower than the critical temperature for Bose–Einstein condensation ($T \ll T_c$), thermal excitations can be neglected, making the zero-temperature approximation appropriate and allowing the condensate dynamics to be accurately described by the Gross–Pitaevskii equation.

The Gross–Pitaevskii Equation (GPE) is a model that describes the dynamics of quantum fluids and their reconnections, independently derived by Gross and Pitaevskii in 1961 [8, 9]. The GPE is particularly suitable because it allows one to describe the structure of the vortex core, where the condensate density vanishes, providing a complete representation of the vortex geometry, and reconnections emerge spontaneously from the dynamics without the need to impose them artificially.

Despite the time-reversibility character of the GPE, irreversible behaviour of quantum reconnections emerges. The irreversibility is evident through a clear temporal asymmetry, reflected in the coefficients of the scaling law [4, 10, 11, 12, 13, 14]:

$$\delta(t) = A^{\pm}|t - t_0|^{1/2}\,,$$

where $\delta(t)$ denotes the minimum distance between vortex lines as a function of time t, and t_0 is the reconnection time. The parameters A^+ and A^-, which describe the post- and pre-reconnection regimes, respectively, satisfy the universal inequality $A^+ > A^-$, indicating that vortex lines separate more rapidly after reconnection than they approach before the event. The increase in the separation speed is explained by the fact that, as vortices approach and reconnect, their local curvature increases significantly, leading to a corresponding increase in vortex velocity. The phenomenon is described by the Localized Induction Approximation (LIA) [15, 16, 17, 18], according to which the velocity of a vortex filament is directly proportional to its local curvature.

The irreversible character of the quantum reconnection phenomenon is also observed in the loss of the length of the vortex filaments during the process: the total length tends to increase when the vortices get closer, reaching a maximum—often used as an indicator of the reconnection time—and then decreases during the separation stage. The loss

of length of vortex filaments is associated with an irreversible conversion of part of the vortex kinetic energy into sound energy [12, 19, 20, 2]. During the reconnection, a rarefaction pulse—namely a localized region of reduced density that propagates away from the interaction region—is generated and subsequently transforms into acoustic waves. In addition, so-called Kelvin waves [21, 5] propagate along the vortex lines, transferring energy toward smaller scales (higher wavenumbers), where partial dissipation occurs through sound emission [22, 23, 24, 25, 26]. As a result, an irreversible transfer occurs from the incompressible component of the kinetic energy, associated with vortex filaments, to the compressible component, related to the density waves, while the total energy of the system remains conserved.

Unlike classical fluids, where energy is dissipated, in quantum fluids the total energy is conserved during time evolution [5] and consists of kinetic, interaction, quantum, and potential contributions. Through the Helmholtz decomposition [27, 28] of the velocity field, the kinetic energy can be written as a sum of an incompressible component, responsible for the generation of Kelvin waves, and a compressible component, responsible for acoustic emission. This decomposition also allows for a numerical evaluation of the energy transfer between the two contributions of the kinetic energy during reconnection events.

Contribution of the thesis

In recent years, several vortex reconnection configurations have been investigated [29, 1, 2, 30, 31, 32, 33, 34, 35], including interactions between straight vortex lines, vortex rings, and a vortex line with a vortex ring.

In this thesis, we investigate the reconnection dynamics between a straight vortex line and a vortex ring, a configuration that extends previous studies by fixing the offset parameter to zero and introducing a non-zero inclination angle between the vortex ring and the horizontal plane, which is varied to evaluate its effect on the reconnection process. A setup close to ours is examined in [35], where both offset and inclination angle are varied; nevertheless, the dynamics can differ, as this work relies on the GPE model, which inherently captures reconnection, whereas the vortex filament approach in [35] depends on an ad hoc reconnection procedure. We analyze the evolution of the geometric properties of the vortex filaments for different values of the inclination angle, specifically their total length, curvature, and the redistribution of total energy in its components during the dynamics. By applying Helmholtz decomposition of the kinetic energy, we further characterize how the inclination angle affects the partition between incompressible and compressible components, highlighting the respective roles of Kelvin wave generation and sound emission. The results of the energy analysis are then compared with the evolution of the vortex line length and the curvature, in order to identify possible correlations between the inclination angle, geometric features, and energy redistribution during reconnection.

This work contributes to several open questions in quantum-fluid dynamics. First, vortex reconnections are regarded as a key mechanism for energy dissipation in superfluids at very low temperatures, where viscosity is absent and energy must be transferred from vortex motion to sound excitations. By tracking the evolution of the different energy components throughout the reconnection process, this thesis provides insight into how the

total energy is redistributed during the interaction. In particular, the Helmholtz decomposition of the kinetic energy allows us to quantify the partition between incompressible and compressible contributions, which are associated with vortex dynamics and Kelvin-wave excitations on the one hand, and sound emission on the other. These results contribute to understanding the mechanisms through which reconnections transfer energy in quantum fluids and support dissipation at very low temperatures. Second, the dependence of reconnection dynamics on the vortex configuration remains an active area of investigation. By varying the inclination angle, this thesis assesses the extent to which the reconnection and post-reconnection dynamics, as well as the resulting Kelvin-wave excitation and sound emission, are influenced by the initial vortex geometry. Finally, since reconnections constitute elementary processes underlying quantum turbulence, understanding how geometric factors affect energy transfer at the level of individual reconnection events may contribute to the development of more accurate descriptions of turbulent energy cascades in superfluid systems.

We also studied vortex dynamics in two-component Bose–Einstein condensates [36], which consist of two coupled condensate components corresponding to different hyperfine states of the same atomic species, different isotopes, or distinct atomic species. Depending on the inter-component interaction, the system can be in either the miscible or immiscible regime. A central goal in the study of vortex dynamics is the detection and characterization of three-dimensional vortex structures, including vortex tangles. In this context, immiscible two-component Bose–Einstein condensates provide a particularly suitable platform for vortex tracking, since vortices in the majority component can be filled by the minority component, enabling their visualization without destructive imaging of the main condensate. A key open question is whether the filling component can be regarded as a passive tracer or whether it instead modifies the underlying vortex dynamics. Addressing this issue is essential to determine the regimes in which the tracer approximation is valid and those in which the second component actively affects vortex evolution.

In this thesis, we investigate vortex reconnections between two perpendicular straight vortex lines in immiscible two-component Bose–Einstein condensates. The vortices are located in the majority component, while their cores are filled by the minority component. By varying the number of atoms in the second component, we quantify its effect on the reconnection dynamics and on the parameters of the scaling law, determining whether the reconnection process is unchanged or significantly modified.

More generally, this work clarifies how vortex dynamics in multicomponent condensates depart from the single-component case. The presence of a filling component introduces additional mass and density redistribution within the vortex cores, which can alter the local reconnection dynamics. These results are relevant for the interpretation of vortex-tracking experiments and for developing a more complete description of vortex reconnection in multicomponent quantum fluids.

Structure of the thesis

The thesis is structured as follows. In Chapter 1, the derivation of the Gross–Pitaevskii Equation is presented, both in its time-dependent and time-independent forms. The total energy of the system is also derived, and its conservation is proven. Subsequently,

the hydrodynamic interpretation of the equation is introduced, leading to the formulation of the governing equations of the system. Finally, some stationary solutions for uniform condensates and infinitely homogeneous systems are discussed. In conclusion, the phenomenon of acoustic waves (sound waves) in homogeneous and trapped potentials is analyzed. In Chapter 2, quantum vortices are introduced and their main properties analyzed. After discussing the fundamental characteristics of quantum fluids, some of the main vortex configurations are defined, including vortex lines and vortex rings, together with their dynamics according to the Localized Induction Approximation (LIA). Finally, the structure of the vortex core is studied in both homogeneous and trapped condensates. In Chapter 3, the irreversibility of quantum vortex reconnections is investigated. The scaling law of the vortex separation during the approach and separation stages is analyzed, highlighting a clear time asymmetry despite the time-reversible Gross–Pitaevskii dynamics. The role of acoustic emission and vortex line length variation is discussed as mechanisms responsible for an effective redistribution of kinetic energy into sound radiation. Kelvin waves generated during reconnections are also examined, together with their role in transferring energy toward smaller scales. Finally, a decomposition of the kinetic energy into incompressible and compressible contributions, based on the Helmholtz decomposition of the velocity field, is introduced to quantify the energy exchange between vortices and density waves. Chapters 4 and 5 present the original results of this thesis. In Chapter 4, the vortex reconnection between a straight vortex line and a vortex ring is studied. In particular, the inclination angle of the vortex ring with respect to the rectilinear vortex is varied to investigate potential relationships between angle variation, the total length and curvature of the nodal lines of the vortex cores, and the redistribution of energy among the different energy components throughout the reconnection process. In Chapter 5, the reconnection between two orthogonal straight vortex lines in an immiscible two-component Bose–Einstein condensate is studied, focusing on how the presence of a second component affects the reconnection dynamics. In particular, the number of atoms in the second component is varied, in order to investigate how this parameter influences the coefficients appearing in the scaling law.

Chapter 1

The Gross-Pitaevskii Equation

The Gross-Pitaevskii equation (GPE) is a mathematical model that describes the dynamics of the vortex reconnection in a Bose–Einstein condensate. We take into account a gas close to the zero temperature, and consider N interacting quantum particles and parametrize the system with N-body wavefunction $\mathbf{\Psi}(\mathbf{r}_1, \mathbf{r}_2, \cdots, \mathbf{r}_N, t)$, that satisfies the many-body Schrödinger equation (see [5]). By assuming a large number of particles ($N \gg 1$), the many-body wavefunction can be approximated by a macroscopic single-particle one, denoted by $\Psi(\mathbf{r}, t) \in \mathbb{C}$, with $(\mathbf{r}, t) \in \mathbb{R}^3 \times \mathbb{R}$. The single-particle wavefunction, that is a complex field, can be written via the Madelung transform (see [37, 5, 38]), as

$$\Psi(\mathbf{r}, t) = \sqrt{n(\mathbf{r}, t)} e^{\mathrm{i}\theta(\mathbf{r}, t)}\,, \tag{1.1}$$

where n is the density of the condensate, θ is the phase distribution, and we normalize it to N atoms:

$$\int |\Psi|^2 d^3\mathbf{r} = N\,. \tag{1.2}$$

The Bose–Einstein condensate is a dilute gas in such a way that the interactions can be modelled as an elastic two-body interactions similar to the van der Waals forces. This interaction is described by the contact interaction

$$U(|\mathbf{r}_1 - \mathbf{r}_2|) = g\,\delta(|\mathbf{r}_1 - \mathbf{r}_2|)\,, \tag{1.3}$$

between two atoms at positions $\mathbf{r}_1$ and $\mathbf{r}_2$, where δ is the Dirac delta function and $g = \frac{4\pi\hbar^2 a_s}{m}$ is a constant, with $\hbar$ the Planck constant, m the particle mass, and a_s the s-wave scattering length that characterizes the interactions of atoms in the low energy limit. If we take into account these interactions, the mean-field wavefunction $\Psi(\mathbf{r}, t)$ satisfies the Gross-Pitaevskii Equation [8, 9, 6, 7] (see also 1.1)

$$\mathrm{i}\hbar \frac{\partial \Psi(\mathbf{r}, t)}{\partial t} = -\frac{\hbar^2}{2m}\Delta\Psi(\mathbf{r}, t) + V(\mathbf{r}, t)\Psi(\mathbf{r}, t) + g|\Psi(\mathbf{r}, t)|^2\Psi(\mathbf{r}, t)\,, \tag{1.4}$$

where $V(\mathbf{r}, t)$ is an external potential that defines the confinement and geometry of the condensate. The first term on the right side accounts for the kinetic energy, the second one accounts for the potential energy, and the third one comes from the atomic interactions. More precisely, the nonlinear third term has the physical interpretation that at any given point in space it represents an energy contribution originating from the mean-field

interactions among all atoms in the surrounding region. The constant g is determined by the atomic species involved and could be:

- negative: if the interactions are attractive;
- equal to zero: if there are no interactions (so the equation (1.4) reduces to the Schrödinger equation);
- positive: if the interactions are repulsive.

From now on we will consider the case $g > 0$.

1.1 Derivation of the time-dependent GPE

The derivation of the time-dependent GPE relies on the minimization of the action functional (see [39, 6]) in the case of many particles,

$$S[\mathbf{\Psi}] = \int_{t_1}^{t_2} dt \int_{\mathbb{R}^{3N}} \mathcal{L}(\mathbf{\Psi}, \bar{\mathbf{\Psi}}, \dot{\mathbf{\Psi}}, \dot{\bar{\mathbf{\Psi}}}, \nabla\mathbf{\Psi}, \nabla\bar{\mathbf{\Psi}})\, d^3\mathbf{r}_1 \dots d^3\mathbf{r}_N \,,$$

where the integration is performed over the time interval $[t_1, t_2]$ and over the full $3N$-dimensional configuration space of the system,

$$\mathcal{L} = \bar{\mathbf{\Psi}}(\mathbf{r}_1, \dots, \mathbf{r}_N, t) \left(\mathrm{i}\hbar \frac{\partial}{\partial t} - \hat{H} \right) \mathbf{\Psi}(\mathbf{r}_1, \dots, \mathbf{r}_N, t)$$

is the Lagrangian, $\mathbf{\Psi} = \mathbf{\Psi}(\mathbf{r}_1, \dots, \mathbf{r}_N, t)$ the time-dependent N-body wavefunction, $\mathbf{r}_1, \dots, \mathbf{r}_N$ the positions of the N atoms and t is time. The Hamiltonian operator of the many-body system has the form

$$\hat{H} = \sum_{i=1}^{N} \left(-\frac{\hbar^2}{2m} \Delta_i + V(\mathbf{r}_i, t) \right) + \frac{1}{2} \sum_{i=1}^{N} \sum_{j \neq i}^{N} U(|\mathbf{r}_i - \mathbf{r}_j|) \tag{1.5}$$

with external potential $V(\mathbf{r}, t)$ and inter-atomic potential $U(|\mathbf{r} - \mathbf{r}'|)$. The action S is then

$$\begin{aligned} S[\mathbf{\Psi}] = \int_{t_1}^{t_2} dt \int_{\mathbb{R}^{3N}} \bar{\mathbf{\Psi}}(\mathbf{r}_1, \dots, \mathbf{r}_N, t) \Bigg(& \mathrm{i}\hbar \frac{\partial}{\partial t} + \sum_{\substack{i,j=1 \\ i \neq j}}^{N} \frac{\hbar^2}{2m} \Delta_i - V(\mathbf{r}_i, t) \\ & - \frac{1}{2} \sum_{i=1}^{N} \sum_{j \neq i}^{N} U(|\mathbf{r}_i - \mathbf{r}_j|) \Bigg) \mathbf{\Psi}(\mathbf{r}_1, \dots, \mathbf{r}_N, t)\, d^3\mathbf{r}_1 \dots d^3\mathbf{r}_N \\ = \int_{t_1}^{t_2} dt \int_{\mathbb{R}^{3N}} \Bigg(& \bar{\mathbf{\Psi}}\, \mathrm{i}\hbar\, \frac{\partial \mathbf{\Psi}}{\partial t} + \sum_{i=1}^{N} \frac{\hbar^2}{2m} \bar{\mathbf{\Psi}} \Delta_i \mathbf{\Psi} - V(\mathbf{r}_i, t) |\mathbf{\Psi}|^2 \\ & - \frac{1}{2} \sum_{i=1}^{N} \sum_{j \neq i}^{N} U(|\mathbf{r}_i - \mathbf{r}_j|) |\Psi|^2 \Bigg) d^3\mathbf{r}_1 \dots d^3\mathbf{r}_N \,. \end{aligned}$$

Now we consider a Bose–Einstein condensate in which all bosons are in the same time-dependent single-particle orbital (the so-called Hartree approximation)

$$\mathbf{\Psi}(\mathbf{r}_1,\dots,\mathbf{r}_N,t)=\prod_{i=1}^{N}\phi(\mathbf{r}_i,t)\,, \tag{1.6}$$

where ϕ satisfies vanishing boundary conditions at spatial infinity and fixed-endpoint conditions in time. We insert the ansatz into the many-body action functional to get

$$\begin{aligned}
S[\phi] &= N\int_{t_1}^{t_2}dt\int_{\mathbb{R}^3}d^3\mathbf{r}\,\bar\phi(\mathbf{r},t)\left(\mathrm{i}\hbar\frac{\partial}{\partial t}+\frac{\hbar^2}{2m}\Delta-V(\mathbf{r},t)\right)\phi(\mathbf{r},t)+\\
&+N\left(-\frac{N-1}{2}\right)\int_{t_1}^{t_2}dt\int_{\mathbb{R}^3}d^3\mathbf{r}\int_{\mathbb{R}^3}d^3\mathbf{r}'\,|\phi(\mathbf{r}',t)|^2\,U(|\mathbf{r}-\mathbf{r}'|)\,|\phi(\mathbf{r},t)|^2\\
&=N\int_{t_1}^{t_2}dt\int_{\mathbb{R}^3}d^3\mathbf{r}\,\bar\phi(\mathbf{r},t)\left(\mathrm{i}\hbar\frac{\partial}{\partial t}+\frac{\hbar^2}{2m}\Delta-V(\mathbf{r},t)-\frac{N-1}{2}\int_{\mathbb{R}^3}d^3\mathbf{r}'\,U(|\mathbf{r}-\mathbf{r}'|)\,|\phi(\mathbf{r}',t)|^2\right)\phi(\mathbf{r},t)\\
&=N\int_{t_1}^{t_2}dt\int_{\mathbb{R}^3}d^3\mathbf{r}\,\bar\phi(\mathbf{r},t)\,\mathrm{i}\hbar\frac{\partial}{\partial t}\phi(\mathbf{r},t)+N\int_{t_1}^{t_2}dt\int_{\mathbb{R}^3}d^3\mathbf{r}\,\bar\phi(\mathbf{r},t)\frac{\hbar^2}{2m}\Delta\phi(\mathbf{r},t)\\
&-N\int_{t_1}^{t_2}dt\int_{\mathbb{R}^3}d^3\mathbf{r}\,V(\mathbf{r},t)|\phi(\mathbf{r},t)|^2-\frac{N(N-1)}{2}\int_{t_1}^{t_2}dt\int_{\mathbb{R}^3}d^3\mathbf{r}\int_{\mathbb{R}^3}d^3\mathbf{r}'\,|\phi(\mathbf{r},t)|^2U(|\mathbf{r}-\mathbf{r}'|)|\phi(\mathbf{r}',t)|^2\,.
\end{aligned}$$

Now, we integrate by parts the first integral $I:=\mathrm{i}\hbar\int_{t_1}^{t_2}\bar\phi(\mathbf{r},t)\frac{\partial\phi(\mathbf{r},t)}{\partial t}\,dt$

$$\mathrm{i}\hbar\int_{t_1}^{t_2}\bar\phi(\mathbf{r},t)\frac{\partial\phi(\mathbf{r},t)}{\partial t}\,dt=\mathrm{i}\hbar[\bar\phi(\mathbf{r},t)\phi(\mathbf{r},t)]-\int_{t_1}^{t_2}\mathrm{i}\hbar\frac{\partial\bar\phi(\mathbf{r},t)}{\partial t}\phi(\mathbf{r},t)\,dt\,.$$

By using the fact that $I=\frac{I+I}{2}$, we have

$$\begin{aligned}
I&=\frac{1}{2}\left(\mathrm{i}\hbar\int_{t_1}^{t_2}\bar\phi(\mathbf{r},t)\frac{\partial\phi(\mathbf{r},t)}{\partial t}\,dt+\mathrm{i}\hbar[\bar\phi(\mathbf{r},t)\phi(\mathbf{r},t)]-\int_{t_1}^{t_2}\mathrm{i}\hbar\frac{\partial\bar\phi(\mathbf{r},t)}{\partial t}\phi(\mathbf{r},t)\,dt\right)\\
&=\frac{\mathrm{i}\hbar}{2}\int_{t_1}^{t_2}\left(\bar\phi(\mathbf{r},t)\frac{\partial\phi(\mathbf{r},t)}{\partial t}-\frac{\partial\bar\phi(\mathbf{r},t)}{\partial t}\phi(\mathbf{r},t)\right)dt\,.
\end{aligned}$$

Then we integrate by parts the second integral

$$\begin{aligned}
\int_{\mathbb{R}^3}\bar\phi(\mathbf{r},t)\frac{\hbar^2}{2m}\Delta\phi(\mathbf{r},t)\,d^3\mathbf{r}&=\lim_{|\mathbf{r}|\to\infty}\left[\bar\phi(\mathbf{r},t)\frac{\hbar^2}{2m}\nabla\phi(\mathbf{r},t)\right]-\int_{\mathbb{R}^3}\frac{\hbar^2}{2m}\nabla\bar\phi(\mathbf{r},t)\nabla\phi(\mathbf{r},t)\,d^3\mathbf{r}\\
&=-\int_{\mathbb{R}^3}\frac{\hbar^2}{2m}\nabla\bar\phi(\mathbf{r},t)\nabla\phi(\mathbf{r},t)\,d^3\mathbf{r}\,.
\end{aligned}$$

We then obtain

$$\begin{aligned}
S[\phi]=N\int_{t_1}^{t_2}dt\int_{\mathbb{R}^3}d^3\mathbf{r}\,\Bigg(&\frac{\mathrm{i}\hbar}{2}\left(\bar\phi(\mathbf{r},t)\frac{\partial\phi(\mathbf{r},t)}{\partial t}-\frac{\partial\bar\phi(\mathbf{r},t)}{\partial t}\phi(\mathbf{r},t)\right)-\frac{\hbar^2}{2m}\nabla\bar\phi(\mathbf{r},t)\nabla\phi(\mathbf{r},t)\\
&-\bar\phi(\mathbf{r},t)V(\mathbf{r},t)\phi(\mathbf{r},t)-\frac{N-1}{2}\int_{\mathbb{R}^3}|\phi(\mathbf{r}',t)|^2U(|\mathbf{r}-\mathbf{r}'|)|\phi(\mathbf{r},t)|^2\,d^3\mathbf{r}'\Bigg).
\end{aligned}$$

Hence the Lagrangian is

$$\begin{aligned}\mathcal{L} &= \mathcal{L}(\phi, \bar{\phi}, \dot{\phi}, \dot{\bar{\phi}}, \nabla\phi, \nabla\bar{\phi}) \\ &= N\Big(\frac{i\hbar}{2}(\bar{\phi}\partial_t\phi - \partial_t\bar{\phi}\,\phi) - \frac{\hbar^2}{2m}\nabla\bar{\phi}\cdot\nabla\phi - \bar{\phi}V(\mathbf{r},t)\phi \\ &\quad - \frac{N-1}{2}\int_{\mathbb{R}^3}|\phi(\mathbf{r},t)|^2 U(|\mathbf{r}-\mathbf{r}'|)|\phi(\mathbf{r}',t)|^2\,d^3\mathbf{r}'\Big).\end{aligned}$$

with $\phi := \phi(\mathbf{r},t)$. The Euler-Lagrangian equations for $\mathcal{L}$ are then

$$-\frac{\partial}{\partial t}\frac{\partial\mathcal{L}}{\partial\dot{\bar{\phi}}} + \frac{\partial\mathcal{L}}{\partial\bar{\phi}} - \nabla\cdot\left(\frac{\partial\mathcal{L}}{\partial\nabla\bar{\phi}}\right) = 0\,, \tag{1.7}$$

where

$$-\frac{\partial}{\partial t}\frac{\partial\mathcal{L}}{\partial\dot{\bar{\phi}}} = -\frac{\partial}{\partial t}\left(\frac{-N\mathrm{i}\hbar}{2}\phi\right) = \frac{N\mathrm{i}\hbar}{2}\frac{\partial\phi}{\partial t} \tag{1.8}$$

$$\begin{aligned}\frac{\partial\mathcal{L}}{\partial\bar{\phi}} &= \frac{N\mathrm{i}\hbar}{2}\frac{\partial\phi}{\partial t} - NV(\mathbf{r},t)\phi - \frac{N(N-1)}{2}\int_{\mathbb{R}^3}\phi\,U(|\mathbf{r}-\mathbf{r}'|)|\phi(\mathbf{r}')|^2\,d^3\mathbf{r}' \\ &\quad - \frac{N(N-1)}{2}\int_{\mathbb{R}^3}|\phi|^2U(|\mathbf{r}-\mathbf{r}'|)\phi(\mathbf{r}',t)\delta(\mathbf{r}-\mathbf{r}')d^3\mathbf{r}' \\ &= \frac{N\mathrm{i}\hbar}{2}\frac{\partial\phi}{\partial t} - NV(\mathbf{r},t)\phi - \frac{2N(N-1)}{2}\int_{\mathbb{R}^3}\phi U(|\mathbf{r}-\mathbf{r}'|)|\phi(\mathbf{r}',t)|^2\,d^3\mathbf{r}'\end{aligned} \tag{1.9}$$

$$-\nabla\cdot\left(\frac{\partial\mathcal{L}}{\partial\nabla\bar{\phi}}\right) = -\nabla\cdot\left(-\frac{N\hbar^2}{2m}\nabla\phi\right) = \frac{N\hbar^2}{2m}\Delta\phi\,. \tag{1.10}$$

If we substitute Eqs. (1.8),(1.9) and (1.10) into (1.7) we obtain

$$\begin{aligned}&\frac{N\mathrm{i}\hbar}{2}\frac{\partial\phi}{\partial t} + \frac{N\mathrm{i}\hbar}{2}\frac{\partial\phi}{\partial t} - NV(\mathbf{r},t)\phi - N(N-1)\int_{\mathbb{R}^3}\phi U(|\mathbf{r}-\mathbf{r}'|)|\phi(\mathbf{r}',t)|^2\,d^3\mathbf{r}' + \frac{N\hbar^2}{2m}\Delta\phi = 0 \\ &N\mathrm{i}\hbar\frac{\partial\phi}{\partial t} - NV(\mathbf{r},t)\phi - N(N-1)\int_{\mathbb{R}^3}\phi U(|\mathbf{r}-\mathbf{r}'|)|\phi(\mathbf{r}',t)|^2\,d^3\mathbf{r}' + \frac{N\hbar^2}{2m}\Delta\phi = 0 \\ &\mathrm{i}\hbar\frac{\partial\phi}{\partial t} = -\frac{\hbar^2}{2m}\Delta\phi + V(\mathbf{r},t)\phi + (N-1)\int_{\mathbb{R}^3}\phi U(|\mathbf{r}-\mathbf{r}'|)|\phi(\mathbf{r}',t)|^2\,d^3\mathbf{r}'\,.\end{aligned} \tag{1.11}$$

In the case of dilute gases we can assume (see (1.3)) that

$$U(|\mathbf{r}-\mathbf{r}'|) \simeq g\,\delta(\mathbf{r}-\mathbf{r}')\,,$$

so, by integration with respect to $\mathbf{r}'$, we obtain

$$\int_{\mathbb{R}^3}U(|\mathbf{r}-\mathbf{r}'|)\,d^3\mathbf{r}' = \int_{\mathbb{R}^3}g\,\delta(\mathbf{r}-\mathbf{r}')\,d^3\mathbf{r}' = g\,. \tag{1.12}$$

Hence we substitute the expression (1.12) into (1.11) to have

$$\mathrm{i}\hbar\frac{\partial\phi(\mathbf{r},t)}{\partial t} = -\frac{\hbar^2}{2m}\Delta\phi(\mathbf{r},t) + V(\mathbf{r},t) + (N-1)g|\phi(\mathbf{r},t)|^2\phi(\mathbf{r},t)\,. \tag{1.13}$$

Now we define the macroscopic wavefunction

$$\Psi(\mathbf{r},t) := \sqrt{N}\phi(\mathbf{r},t)\,,$$

thus

$$\phi(\mathbf{r},t) = \frac{\Psi(\mathbf{r},t)}{\sqrt{N}} \qquad |\phi(\mathbf{r},t)|^2 = \frac{|\Psi(\mathbf{r},t)|^2}{N} \qquad \int_{\mathbb{R}^3} |\Psi(\mathbf{r},t)|^2\, d^3\mathbf{r} = N\,. \tag{1.14}$$

If we substitute these expressions (1.14) in (1.13) we get

$$\begin{aligned}\frac{\mathrm{i}\hbar}{\sqrt{N}}\frac{\partial\Psi(\mathbf{r},t)}{\partial t} &= -\frac{\hbar^2}{2m}\frac{1}{\sqrt{N}}\Delta\Psi(\mathbf{r},t) + \frac{V(\mathbf{r},t)}{\sqrt{N}}\Psi(\mathbf{r},t) + (N-1)g\frac{|\Psi(\mathbf{r},t)|^2}{N}\frac{\Psi(\mathbf{r},t)}{\sqrt{N}}\\ \mathrm{i}\hbar\frac{\partial\Psi(\mathbf{r},t)}{\partial t} &= -\frac{\hbar^2}{2m}\Delta\Psi(\mathbf{r},t) + V(\mathbf{r},t)\Psi(\mathbf{r},t) + \frac{N-1}{N}g|\Psi(\mathbf{r},t)|^2\Psi(\mathbf{r},t)\,.\end{aligned} \tag{1.15}$$

We assume a large number of particles ($N \gg 1$), so in (1.15) the term $\frac{N-1}{N} \to 1$ and finally we have the desired time-dependent Gross Pitaevskii equation

$$\mathrm{i}\hbar\frac{\partial\Psi(\mathbf{r},t)}{\partial t} = -\frac{\hbar^2}{2m}\Delta\Psi(\mathbf{r},t) + V(\mathbf{r},t)\Psi(\mathbf{r},t) + g|\Psi(\mathbf{r},t)|^2\Psi(\mathbf{r},t)\,. \tag{1.16}$$

1.1.1 Energy and energy conservation

We derive the expression for the total energy functional of the Bose–Einstein condensate governed by (1.16) and discuss energy conservation, a fundamental property of the condensate [1]. For simplicity we omit the explicit dependence on $\mathbf{r}$ and t, i.e. $\Psi \equiv \Psi(\mathbf{r},t)$ and $V \equiv V(\mathbf{r},t)$.

Proposition 1.1.1. *Consider a Bose–Einstein condensate described by 1.16. The following properties hold.*

1. *The total energy functional for a wavefunction Ψ on a spatial domain $D \subset \mathbb{R}^3$ is*

$$E[\Psi] := \int_D \left[\frac{\hbar^2}{2m}|\nabla\Psi|^2 + V|\Psi|^2 + \frac{g}{2}|\Psi|^4\right] d^3\mathbf{r}\,. \tag{1.18}$$

2. *If the external potential V is time-independent, then the energy is conserved during the time evolution of the condensate.*

[1] For completeness, we recall the definitions of total mass and momentum for the condensate [5], although they will not be used in the present work. These quantities provide a connection between the microscopic field dynamics and the collective behavior of the system.

Definition 1.1.1. *Consider a Bose–Einstein condensate.*

- *The* **total mass** *is*

$$M := mN\,,$$

  where N is the number of atoms.

- *The* **momentum** *is*

$$\mathcal{P} := \frac{\mathrm{i}\hbar}{2}\int \left(\Psi\nabla\overline{\Psi} - \overline{\Psi}\nabla\Psi\right) d^3\mathbf{r}\,. \tag{1.17}$$

Proof. First we prove statement (*1*). We take the GPE

$$\mathrm{i}\hbar\frac{\partial\Psi}{\partial t} = \left[-\frac{\hbar^2}{2m}\Delta + V + g|\Psi^2|\right]\Psi\,,$$

we multiply by $\overline{\Psi}$ and apply $\Psi\overline{\Psi} = |\Psi|^2$ to get

$$\begin{aligned}\mathrm{i}\hbar\frac{\partial\Psi}{\partial t}\overline{\Psi} &= \left[-\frac{\hbar^2}{2m}\Delta + V + g|\Psi^2|\right]\Psi\overline{\Psi}\\ \mathrm{i}\hbar\frac{\partial\Psi}{\partial t}\overline{\Psi} &= -\frac{\hbar^2}{2m}\overline{\Psi}\Delta\Psi + V|\Psi|^2 + g|\Psi|^4\,.\end{aligned}$$

We integrate the previous equation all over the volume D

$$\int_D \mathrm{i}\hbar\overline{\Psi}\frac{\partial\Psi}{\partial t}\,d^3\mathbf{r} = \int_D -\frac{\hbar^2}{2m}\overline{\Psi}\Delta\Psi + V|\Psi|^2 + g|\Psi|^4\,d^3\mathbf{r} \tag{1.19}$$

and integrate by part the first term on the right side assuming that $\Psi = 0$ on the boundary

$$-\frac{\hbar^2}{2m}\int_D \overline{\Psi}\Delta\Psi\,d^3\mathbf{r} = -\frac{\hbar^2}{2m}\left(-\int_D \nabla\overline{\Psi}\nabla\Psi\,d^3\mathbf{r}\right) = \frac{\hbar^2}{2m}\int_D |\nabla\Psi|^2\,d^3\mathbf{r}\,. \tag{1.20}$$

Then we substitute the expression (1.20) found in the previous equation (1.19)

$$\int_D \mathrm{i}\hbar\overline{\Psi}\frac{\partial\Psi}{\partial t}d^3\mathbf{r} = \int_D \frac{\hbar^2}{2m}|\nabla\Psi|^2 + V|\Psi|^2 + g|\Psi|^4 d^3\mathbf{r}\,. \tag{1.21}$$

So

$$E[\Psi] = \int_D \frac{\hbar^2}{2m}|\nabla\Psi|^2 + V|\Psi|^2 + \frac{g}{2}|\Psi|^4 d^3\mathbf{r}\,.$$

Then we prove statement (*2*). We set for simplicity $a = \frac{\hbar^2}{2m}$ in (1.18), then we have

$$\begin{aligned}E'(t) &= a\int_D (\nabla\Psi_t\overline{\nabla\Psi} + \nabla\Psi\overline{\nabla\Psi}_t)\,d^3\mathbf{r} + \int_D V(\mathbf{r})(\Psi_t\overline{\Psi} + \Psi\overline{\Psi}_t)\,d^3\mathbf{r}\\ &+ \frac{g}{2}\int_D (\Psi_t\overline{\Psi} + \Psi\overline{\Psi}_t)(\Psi\overline{\Psi}) + (\Psi\overline{\Psi})(\Psi_t\overline{\Psi} + \Psi\overline{\Psi}_t)\,d^3\mathbf{r}\\ &= a\int_D \nabla\Psi_t\overline{\nabla\Psi}\,d^3\mathbf{r} + a\int_D \nabla\Psi\,\overline{\nabla\Psi}_t\,d^3\mathbf{r} + \int_D V(\mathbf{r})(\Psi_t\overline{\Psi} + \Psi\overline{\Psi}_t)\,d^3\mathbf{r}\\ &\quad + g\int_D |\Psi|^2(\Psi_t\overline{\Psi} + \Psi\overline{\Psi}_t)\,d^3\mathbf{r}\\ &= 2\mathrm{Re}\left[a\int_D \nabla\overline{\Psi}_t\cdot\nabla\Psi\,d^3\mathbf{r} + \int_D V(\mathbf{r})\overline{\Psi}\,\Psi_t\,d^3\mathbf{r} + g\int_D |\Psi|^2\overline{\Psi}\,\Psi_t\,d^3\mathbf{r}\right].\end{aligned} \tag{1.22}$$

where Re indicates the real part. Now, we take

$$\mathrm{i}\Psi_t = -a\Delta\Psi + V(\mathbf{r})\Psi + g|\Psi|^2\Psi\,, \tag{1.23}$$

multiply by $\overline{\Psi}_t$ and integrate:

$$\int_D \mathrm{i}|\Psi_t|^2\,d^3\mathbf{r} = \int_D -a\Delta\Psi\overline{\Psi}_t + (V(\mathbf{r}) + g|\Psi|^2)\Psi\overline{\Psi}_t\,d^3\mathbf{r}\,. \tag{1.24}$$

Applying the first Green's identity [2] to $\int_D -a\Delta\Psi\overline{\Psi}_t$ in (1.24), we obtain

$$\int_D \mathrm{i}|\Psi_t|^2\, d^3\mathbf{r} = -a \oint_{\partial D} \overline{\Psi}_t(\nabla\Psi\cdot\mathbf{n})\, dS + a\int_D \nabla\overline{\Psi}_t\cdot\nabla\Psi\, d^3\,\mathbf{r} + \int_D (V(\mathbf{r})+g|\Psi|^2)\Psi\overline{\Psi}_t\, d^3\mathbf{r}\,.$$

Then we add and subtract the boundary term $a\oint_{\partial D}(\nabla\Psi\cdot\mathbf{n})\overline{\Psi}_t\, dS$ in (1.22) to match the previous identity.

$$\begin{aligned} E'(t) =& 2\mathrm{Re}\Big[-a\oint_{\partial D}\overline{\Psi}_t(\nabla\Psi\cdot\mathbf{n})\, dS + a\int_D \nabla\overline{\Psi}_t\cdot\nabla\Psi\, d^3\mathbf{r} + \int_D (V(\mathbf{r})+g|\Psi|^2)\Psi\overline{\Psi}_t\, d^3\mathbf{r} + a\oint_{\partial D}\overline{\Psi}_t(\nabla\Psi\cdot\mathbf{n})dS\Big] \\ &= 2\mathrm{Re}\left[\mathrm{i}\int_D |\Psi_t|^2 + a\oint_{\partial D}\overline{\Psi}_t(\nabla\Psi\ \cdot\mathbf{n})\, dS\right] \\ &= \mathrm{Re}\left[2a\oint_{\partial D}\overline{\Psi}_t(\nabla\Psi\ \cdot\mathbf{n})\, dS\right]. \end{aligned} \tag{1.25}$$

From (1.23) have

$$\overline{\Psi}_t = -a\mathrm{i}\Delta\overline{\Psi} + \mathrm{i}(V(\mathbf{r})+g|\Psi|^2)\overline{\Psi}\,. \tag{1.26}$$

Hence substituting (1.26) in (1.25) we have,

$$\begin{aligned} E'(t) &= \mathrm{Re}\left[2a\oint_{\partial D}(-a\mathrm{i}\Delta\overline{\Psi} + \mathrm{i}(V(\mathbf{r})+g|\Psi|^2)\overline{\Psi})\,(\nabla\Psi\cdot\mathbf{n})\right] dS \\ &= \mathrm{Re}\left[-\mathrm{i}\left(2a^2\oint_{\partial D}\Delta\overline{\Psi}(\nabla\Psi\cdot\mathbf{n})\, dS - 2a\oint_{\partial D}\left(\left(V(\mathbf{r})+g|\Psi|^2\right)\overline{\Psi}\right)(\nabla\Psi\cdot\mathbf{n})\, dS\right)\right] \\ &= \mathrm{Im}\left[2a^2\oint_{\partial D}\Delta\overline{\Psi}(\nabla\Psi\cdot\mathbf{n})\, dS - 2a\oint_{\partial D}(V(\mathbf{r})+g|\Psi|^2)\overline{\Psi}(\nabla\Psi\cdot\mathbf{n})\, dS\right] \\ &= \mathrm{Im}\left[\oint_{\partial D}\left(2a^2\Delta\overline{\Psi} - 2a(V(\mathbf{r})+g|\Psi|^2)\overline{\Psi}\right)(\nabla\Psi\cdot\mathbf{n})\, dS\right]. \end{aligned}$$

where Im indicates the imaginary part and we applied $\mathrm{Re}(-\mathrm{i}z) = \mathrm{Im}(z)$, with $z\in\mathbb{C}$. Therefore, we have the following cases:

- if $\nabla\Psi$ is orthogonal to $\mathbf{n}$ or vanishing, i.e. $\nabla\Psi\cdot\mathbf{n}|_{\partial D} = 0$. then the energy is conserved;
- if D is a computational box $\mathbf{r}$ and Ψ is periodic at opposite boundaries, then the right hand side is zero, hence the energy is conserved;
- if Ψ is constant in time on ∂D, then $\overline{\Psi}_t = -a\mathrm{i}\Delta\overline{\Psi} + \mathrm{i}(V(\mathbf{r})+g|\Psi|^2)\overline{\Psi} = 0$, so the energy is conserved.

□

[2] $\int_D(\Psi\Delta\eta + \nabla\Psi\cdot\nabla\eta)\, d^3\mathbf{r} = \oint_{\partial D}\Psi(\nabla\eta\cdot\mathbf{n})\, dS$

1.2 Derivation of time-independent GPE

Proposition 1.2.1 (Time-independent Gross–Pitaevskii equation)**.** *Let us consider a Bose–Einstein condensate with $N \gg 1$ interacting bosons described by the Hamiltonian* (1.5) *(see [38]), where the external potential is assumed to be time-independent, i.e. $V(\mathbf{r}, t) \equiv V(\mathbf{r})$.*

We parametrize the system with a N-body wavefunction $\mathbf{\Psi}(\mathbf{r}_1, \dots, \mathbf{r}_N)$ and assume the Hartree approximation (see (1.6)*) in its stationary form, namely*

$$|\mathbf{\Psi}(\mathbf{r}_1, \dots, \mathbf{r}_N)\rangle = |\phi(\mathbf{r}_1)\rangle \otimes \cdots \otimes |\phi(\mathbf{r}_N)\rangle \,, \tag{1.27}$$

with a normalized one-body wavefunction $\phi \in L^2(\mathbb{R}^3)$.

Assuming a contact interaction of the form (1.3)*, $U(|\mathbf{r} - \mathbf{r}'|) = g\,\delta(\mathbf{r} - \mathbf{r}')$, the macroscopic wavefunction $\Psi(\mathbf{r}) = \sqrt{N}\phi(\mathbf{r})$ satisfies the time-independent Gross–Pitaevskii equation*

$$-\frac{\hbar^2}{2m}\Delta\Psi(\mathbf{r}) + V(\mathbf{r})\Psi(\mathbf{r}) + g|\Psi(\mathbf{r})|^2\Psi(\mathbf{r}) = \mu\Psi(\mathbf{r}) \,, \tag{1.28}$$

where μ is the chemical potential.

Proof. We use a variational approach and consider the energy functional

$$\mathcal{E}[\mathbf{\Psi}] = \frac{\langle \mathbf{\Psi}|\hat{H}|\mathbf{\Psi}\rangle}{\langle \mathbf{\Psi}|\mathbf{\Psi}\rangle} \,, \tag{1.29}$$

which is minimized by the ground-state wavefunction. Under an infinitesimal variation $\mathbf{\Psi} \to \mathbf{\Psi} + \delta\mathbf{\Psi}$, the normalization of $|\mathbf{\Psi}\rangle$ is in general not preserved. To enforce the normalization constraint, we introduce a Lagrange multiplier μ and consider the constrained functional

$$F[\mathbf{\Psi}] = \langle \mathbf{\Psi}|\hat{H}|\mathbf{\Psi}\rangle - \mu\langle \mathbf{\Psi}|\mathbf{\Psi}\rangle \,. \tag{1.30}$$

We choose $\phi_0(\mathbf{r}) \equiv \phi(\mathbf{r})$ to be normalized, i.e. $\int_{\mathbb{R}^3} |\phi(\mathbf{r})|^2\, d^3\mathbf{r} = 1$, and assume that it vanishes at the boundary of the integration domain. The idea is to determine ϕ that minimizes the functional (1.30) under the normalization constraint. Substituting the expression of the Hamiltonian

$$\hat{H} = \sum_{i=1}^{N} \frac{-\hbar^2\Delta_i}{2m} + \sum_{i=1}^{N} V(\mathbf{r}_i) + \frac{1}{2}\sum_{i=1}^{N}\sum_{j\neq i}^{N} U(|\mathbf{r}_i - \mathbf{r}_j|) \,, \tag{1.31}$$

in (1.30), we obtain

$$F[\mathbf{\Psi}] = \left\langle \mathbf{\Psi} \middle| \sum_{i=1}^{N} \frac{-\hbar^2\Delta_i}{2m} + \sum_{i=1}^{N} V(\mathbf{r}_i) + \frac{1}{2}\sum_{i=1}^{N}\sum_{j\neq i}^{N} U(|\mathbf{r}_i - \mathbf{r}_j|) \middle| \mathbf{\Psi} \right\rangle - \mu \left\langle \mathbf{\Psi}|\mathbf{\Psi} \right\rangle \,.$$

The kinetic terms reads

$$
\begin{aligned}
F_{\mathrm{kin}}[\mathbf{\Psi}] &= \left\langle \mathbf{\Psi} \middle| \sum_{i=1}^{N} \frac{-\hbar^2 \Delta_i}{2m} \middle| \mathbf{\Psi} \right\rangle \\
&= \int_{\mathbb{R}^{3N}} \bar{\mathbf{\Psi}}(\mathbf{r}_1, \dots \mathbf{r}_N) \left(\sum_{i=1}^{N} \frac{-\hbar^2 \Delta_i}{2m} \right) \mathbf{\Psi}(\mathbf{r}_1, \dots \mathbf{r}_N)\, d^3\mathbf{r}_1 \dots\, d^3\mathbf{r}_N \\
&= \sum_{i=1}^{N} \int_{\mathbb{R}^{3N}} \bar{\mathbf{\Psi}}(\mathbf{r}_1, \dots \mathbf{r}_N) \left(\frac{-\hbar^2 \Delta_i}{2m} \right) \mathbf{\Psi}(\mathbf{r}_1, \dots \mathbf{r}_N)\, d^3\mathbf{r}_1 \dots\, d^3\mathbf{r}_N \\
&= \sum_{i=1}^{N} \int_{\mathbb{R}^{3N}} \bar{\mathbf{\Psi}}(\mathbf{r}_1, \dots \mathbf{r}_N) \left(\frac{-\hbar^2}{2m} \right) \Delta_i \mathbf{\Psi}(\mathbf{r}_1, \dots \mathbf{r}_N)\, d^3\mathbf{r}_1 \dots\, d^3\mathbf{r}_N \\
&= \sum_{i=1}^{N} \int_{\mathbb{R}^{3N}} \big(\bar{\phi}(\mathbf{r}_1) \cdots \bar{\phi}(\mathbf{r}_i) \cdots \bar{\phi}(\mathbf{r}_N)\big) \left(\frac{-\hbar^2}{2m} \right) \big(\phi(\mathbf{r}_1) \cdots \Delta_i \phi(\mathbf{r}_i) \cdots \phi(\mathbf{r}_N)\big) d^3\mathbf{r}_1 \cdots d^3\mathbf{r}_N \\
&= \sum_{i=1}^{N} \int_{\mathbb{R}^{3N}} \left(\prod_{k \neq i} \bar{\phi}(\mathbf{r}_k) \phi(\mathbf{r}_k) \right) \bar{\phi}(\mathbf{r}_i) \left(-\frac{\hbar^2}{2m} \Delta_i \phi(\mathbf{r}_i) \right) d^3\mathbf{r}_1 \dots\, d^3\mathbf{r}_N \\
&= \sum_{i=1}^{N} \left(\prod_{k \neq i} \int_{\mathbb{R}^3} |\phi(\mathbf{r}_k)|^2 d^3\mathbf{r}_k \right) \left(\frac{-\hbar^2}{2m} \int_{\mathbb{R}^3} \bar{\phi}(\mathbf{r}_i) \Delta_i \phi(\mathbf{r}_i) d^3\mathbf{r}_i \right) \\
&= \sum_{i=1}^{N} \int_{\mathbb{R}^3} -\frac{\hbar^2}{2m} \bar{\phi}(\mathbf{r}_i) \Delta_i \phi(\mathbf{r}_i)\, d^3\mathbf{r}_i = -N \frac{\hbar^2}{2m} \int_{\mathbb{R}^{3N}} \bar{\phi}(\mathbf{r}) \Delta \phi(\mathbf{r})\, d^3\mathbf{r}\,. \qquad (1.32)
\end{aligned}
$$

The potential term is

$$
\begin{aligned}
F_{\mathrm{p}}[\mathbf{\Psi}] &= \left\langle \mathbf{\Psi} \middle| \sum_{i=1}^{N} V(\mathbf{r}_i) \middle| \mathbf{\Psi} \right\rangle \\
&= \int_{\mathbb{R}^{3N}} \bar{\mathbf{\Psi}}(\mathbf{r}_1, \dots \mathbf{r}_N) \left(\sum_{i=1}^{N} V(\mathbf{r}_i) \right) \mathbf{\Psi}(\mathbf{r}_1, \dots \mathbf{r}_N)\, d^3\mathbf{r}_1 \dots\, d^3\mathbf{r}_N \\
&= \int_{\mathbb{R}^{3N}} \bar{\phi}(\mathbf{r}_1) \cdots \bar{\phi}(\mathbf{r}_i) \cdots \bar{\phi}(\mathbf{r}_N) \left(\sum_{i=1}^{N} V(\mathbf{r}_i) \right) \phi(\mathbf{r}_1) \cdots \bar{\phi}(\mathbf{r}_i) \cdots \bar{\phi}(\mathbf{r}_N)\, d^3\mathbf{r}_1 \dots d^3\mathbf{r}_N \\
&= \sum_{i=1}^{N} \int_{\mathbb{R}^3} \left(\prod_{k \neq i} |\phi(\mathbf{r}_k)|^2 \right) \bar{\phi}(\mathbf{r}_i) V(\mathbf{r}_i) \phi(\mathbf{r}_N) \left(\prod_{k \neq i} d^3\mathbf{r}_k \right) d^3\mathbf{r}_i \\
&= \sum_{i=1}^{N} \left(\prod_{k \neq i} \int_{\mathbb{R}^3} |\phi(\mathbf{r}_k)|^2\, d^3\mathbf{r}_k \right) \left(\int_{\mathbb{R}^3} \bar{\phi}(\mathbf{r}_i) V(\mathbf{r}_i) \phi(\mathbf{r}_i)\, d^3\mathbf{r}_i \right) \\
&= \sum_{i=1}^{N} \int_{\mathbb{R}^3} \bar{\phi}(\mathbf{r}_i) V(\mathbf{r}_i) \phi(\mathbf{r}_i)\, d^3\mathbf{r}_i = N \int_{\mathbb{R}^3} \bar{\phi}(\mathbf{r}) V(\mathbf{r}) \phi(\mathbf{r})\, d^3\mathbf{r}\,. \qquad (1.33)
\end{aligned}
$$

The interaction term takes the form

$$
\begin{aligned}
F_{\text{int}}[\mathbf{\Psi}] &= \left\langle \mathbf{\Psi} \middle| \frac{1}{2}\sum_{i=1}^{N}\sum_{j\neq i}^{N} U(|\mathbf{r}_i-\mathbf{r}_j|) \middle| \mathbf{\Psi} \right\rangle \\
&= \frac{1}{2}\int_{\mathbb{R}^{3N}} \bar{\mathbf{\Psi}}(\mathbf{r}_1,\ldots,\mathbf{r}_N)\sum_{i=1}^{N}\sum_{j\neq i}^{N} U(|\mathbf{r}_i-\mathbf{r}_j|)\mathbf{\Psi}(\mathbf{r}_1,\ldots,\mathbf{r}_N) d^3\mathbf{r}_1\ldots d^3\mathbf{r}_N \\
&= \frac{1}{2}\sum_{i=1}^{N}\sum_{j\neq i}^{N}\int_{\mathbb{R}^{3N}} \left(\prod_{k=1}^{N}\bar{\phi}(\mathbf{r}_k)\right) U(|\mathbf{r}_i-\mathbf{r}_j|) \left(\prod_{k=1}^{N}\phi(\mathbf{r}_k)\right) d^3\mathbf{r}_1\ldots\mathbf{r}_N \\
&= \frac{1}{2}\sum_{i=1}^{N}\sum_{j\neq i}^{N}\int_{\mathbb{R}^3}\int_{\mathbb{R}^3}\int_{\mathbb{R}^3}\left(\prod_{k\neq i,j}\bar{\phi}(\mathbf{r}_k)\phi(\mathbf{r}_k)\right)|\phi(\mathbf{r}_i)|^2|\phi(\mathbf{r}_j)|^2 U(|\mathbf{r}_i-\mathbf{r}_j|)\left(\prod_{k\neq i,j} d^3\mathbf{r}_k\right) d^3\mathbf{r}_i d^3\mathbf{r}_j \\
&= \frac{1}{2}\sum_{i=1}^{N}\sum_{j\neq i}^{N}\left(\prod_{k\neq i,j}\int_{\mathbb{R}^3}|\phi(\mathbf{r}_k)|^2 d^3\mathbf{r}_k\right)\int_{\mathbb{R}^3}\int_{\mathbb{R}^3}|\phi(\mathbf{r}_i)|^2|\phi(\mathbf{r}_j)|^2 U(|\mathbf{r}_i-\mathbf{r}_j|)\, d^3\mathbf{r}_i d^3\mathbf{r}_j \\
&= \frac{1}{2}\sum_{i=1}^{N}\sum_{j\neq i}^{N}\int_{\mathbb{R}^3}\int_{\mathbb{R}^3}|\phi(\mathbf{r}_i)|^2|\phi(\mathbf{r}_j)|^2 U(|\mathbf{r}_i-\mathbf{r}_j|)\, d^3\mathbf{r}_i d^3\mathbf{r}_j \\
&= \frac{N(N-1)}{2}\int_{\mathbb{R}^3}\int_{\mathbb{R}^3}|\phi(\mathbf{r})|^2\, U(|\mathbf{r}-\mathbf{r}'|)|\phi(\mathbf{r}')|^2\, d^3\mathbf{r} d^3\mathbf{r}'\,. \qquad (1.34)
\end{aligned}
$$

Finally the Lagrangian multiplier term becomes

$$
\begin{aligned}
F_\mu[\mathbf{\Psi}] &= \mu\langle\mathbf{\Psi}|\mathbf{\Psi}\rangle \\
&= \mu\int_{\mathbb{R}^{3N}}\bar{\mathbf{\Psi}}(\mathbf{r}_1,\ldots,\mathbf{r}_N)\mathbf{\Psi}(\mathbf{r}_1,\ldots,\mathbf{r}_N)\, d^3\mathbf{r}_1\ldots d^3\mathbf{r}_N \\
&= \mu\int_{\mathbb{R}^{3N}}\bar{\phi}(\mathbf{r}_1)\cdots\bar{\phi}(\mathbf{r}_i)\cdots\bar{\phi}(\mathbf{r}_N)\phi(\mathbf{r}_1)\cdots\phi(\mathbf{r}_i)\cdots\phi(\mathbf{r}_N)\, d^3\mathbf{r}_1\ldots d^3\mathbf{r}_N \\
&= \mu\int_{\mathbb{R}^{3N}}\prod_{i=1}^{N}|\phi(\mathbf{r}_k)|^2\, d^3\mathbf{r}_1\ldots d^3\mathbf{r}_N \\
&= \mu\prod_{i=1}^{N}\int_{\mathbb{R}^3}|\phi(\mathbf{r}_i)|^2\, d^3\mathbf{r}_i \\
&= \mu\left(\int_{\mathbb{R}^3}\bar{\phi}(\mathbf{r})\phi(\mathbf{r})\, d^3\mathbf{r}\right)^N. \qquad (1.35)
\end{aligned}
$$

Now, we perform a small variation of the wave-function by letting $\phi(\mathbf{r}) \to \phi(\mathbf{r}) + \delta\phi(\mathbf{r})$. ϕ is a complex function, so instead of varying the real and imaginary parts, we consider ϕ and $\bar{\phi}$ as independent variables. Thus, we compute the functional derivatives for all the

terms (1.32), (1.33), (1.34) and (1.35). For the kinetic term (1.32) we have

$$\begin{aligned} F_{\mathrm{kin}}[\phi, \bar{\phi} + \delta\bar{\phi}] &= -N\frac{\hbar^2}{2m}\int_{\mathbb{R}^3} (\bar{\phi}(\mathbf{r}) + \delta\bar{\phi}(\mathbf{r}))\Delta\phi(\mathbf{r})\, d^3\mathbf{r} \\ &= -N\frac{\hbar^2}{2m}\int_{\mathbb{R}^3} \bar{\phi}(\mathbf{r})\Delta\phi(\mathbf{r}) + \delta\bar{\phi}(\mathbf{r})\Delta\phi(\mathbf{r})\, d^3\mathbf{r}\,, \\ \delta F_{\mathrm{kin}}[\phi, \bar{\phi}] &= F_{\mathrm{kin}}[\phi, \bar{\phi} + \delta\bar{\phi}] - F_{\mathrm{kin}}[\phi, \bar{\phi}] \\ &= -N\frac{\hbar^2}{2m}\int_{\mathbb{R}^3} \bar{\phi}(\mathbf{r})\Delta\phi(\mathbf{r}) + \delta\bar{\phi}(\mathbf{r})\Delta\phi(\mathbf{r})\, d^3\mathbf{r} + N\frac{\hbar^2}{2m}\int_{\mathbb{R}^3} \bar{\phi}(\mathbf{r})\nabla^2\phi(\mathbf{r})\, d^3\mathbf{r} \\ &= -N\frac{\hbar^2}{2m}\int_{\mathbb{R}^3} \delta\bar{\phi}(\mathbf{r})\Delta\phi(\mathbf{r})\, d^3\mathbf{r}\,, \\ \frac{\delta F_{\mathrm{kin}}[\phi, \bar{\phi}]}{\delta\bar{\phi}} &= -N\frac{\hbar^2}{2m}\Delta\phi(\mathbf{r})\,. \end{aligned}$$

For the potential term (1.33) we get

$$\begin{aligned} F_{\mathrm{p}}[\phi, \bar{\phi} + \delta\bar{\phi}] &= N\int_{\mathbb{R}^3} (\bar{\phi}(\mathbf{r}) + \delta\bar{\phi}(\mathbf{r}))V(\mathbf{r})\phi(\mathbf{r})\, d^3\mathbf{r} \\ &= N\int_{\mathbb{R}^3} \bar{\phi}(\mathbf{r})V(\mathbf{r})\phi(\mathbf{r}) + \delta\bar{\phi}(\mathbf{r})V(\mathbf{r})\phi(\mathbf{r})\, d^3\mathbf{r}\,, \\ \delta F_{\mathrm{p}}[\phi, \bar{\phi}] &= F_{\mathrm{p}}[\phi, \bar{\phi} + \delta\bar{\phi}] - F_{\mathrm{p}}[\phi, \bar{\phi}] \\ &= N\int_{\mathbb{R}^3} \bar{\phi}(\mathbf{r})V(\mathbf{r})\phi(\mathbf{r}) + \delta\bar{\phi}(\mathbf{r})V(\mathbf{r})\phi(\mathbf{r})\, d^3\mathbf{r} - N\int_{\mathbb{R}^3} \bar{\phi}(\mathbf{r})V(\mathbf{r})\phi(\mathbf{r})\, d^3\mathbf{r} \\ &= N\int_{\mathbb{R}^3} \delta\bar{\phi}(\mathbf{r})V(\mathbf{r})\phi(\mathbf{r})\, d^3\mathbf{r}\,, \\ \frac{\delta F_{\mathrm{p}}[\phi, \bar{\phi}]}{\delta\bar{\phi}} &= NV(\mathbf{r})\phi(\mathbf{r})\,. \end{aligned}$$

For the interaction term (1.34) we have

$$
\begin{aligned}
&F_{\text{int}}[\phi,\bar{\phi}+\delta\bar{\phi}] = \tfrac{N(N-1)}{2}\int_{\mathbb{R}^3}\int_{\mathbb{R}^3}\phi(\mathbf{r})(\bar{\phi}(\mathbf{r})+\delta\bar{\phi}(\mathbf{r}))U(|\mathbf{r}-\mathbf{r}'|)\phi(\mathbf{r}')(\bar{\phi}(\mathbf{r}')+\delta\bar{\phi}(\mathbf{r}'))\,d^3\mathbf{r}d^3\mathbf{r}' \\
&= \tfrac{N(N-1)}{2}\int_{\mathbb{R}^3}\int_{\mathbb{R}^3}(\bar{\phi}(\mathbf{r})+\delta\bar{\phi}(\mathbf{r}))(\bar{\phi}(\mathbf{r}')+\delta\bar{\phi}(\mathbf{r}'))U(|\mathbf{r}-\mathbf{r}'|)\phi(\mathbf{r})\phi(\mathbf{r}')\,d^3\mathbf{r}d^3\mathbf{r}' \\
&= \tfrac{N(N-1)}{2}\int_{\mathbb{R}^3}\int_{\mathbb{R}^3}\Big(\bar{\phi}(\mathbf{r})\bar{\phi}(\mathbf{r}')+\bar{\phi}(\mathbf{r})\delta\bar{\phi}(\mathbf{r}')+\delta\bar{\phi}(\mathbf{r})\bar{\phi}(\mathbf{r}')+\mathcal{O}(\delta^2)\Big)U(|\mathbf{r}-\mathbf{r}'|)\phi(\mathbf{r})\phi(\mathbf{r}')d^3\mathbf{r}d^3\mathbf{r}' \\
&= \tfrac{N(N-1)}{2}\int_{\mathbb{R}^3}\int_{\mathbb{R}^3}\Big(|\phi(\mathbf{r})|^2|\phi(\mathbf{r}')|^2+|\phi(\mathbf{r})|^2\phi(\mathbf{r}')\delta\bar{\phi}(\mathbf{r}')+|\phi(\mathbf{r}')|^2\phi(\mathbf{r})\delta\bar{\phi}(\mathbf{r})\Big)U(|\mathbf{r}-\mathbf{r}'|)d^3\mathbf{r}d^3\mathbf{r}'
\end{aligned}
$$

$$
\begin{aligned}
&\delta F_{\text{int}}[\phi,\bar{\phi}] = F_{\text{int}}[\phi,\bar{\phi}+\delta\bar{\phi}] - F_{\text{int}}[\phi,\bar{\phi}] \\
&= \frac{N(N-1)}{2}\int_{\mathbb{R}^3}\int_{\mathbb{R}^3}\Big(|\phi(\mathbf{r})|^2\phi(\mathbf{r}')\delta\bar{\phi}(\mathbf{r}')+|\phi(\mathbf{r}')|^2\phi(\mathbf{r})\delta\bar{\phi}(\mathbf{r})\Big)U(|\mathbf{r}-\mathbf{r}'|)\,d^3\mathbf{r}d^3\mathbf{r}' \\
&= \frac{N(N-1)}{2}\Bigg(\int_{\mathbb{R}^3}\int_{\mathbb{R}^3}|\phi(\mathbf{r})|^2\phi(\mathbf{r}')U(|\mathbf{r}-\mathbf{r}'|)\delta\bar{\phi}(\mathbf{r}')\,d^3\mathbf{r}d^3\mathbf{r}' \\
&\quad+\int_{\mathbb{R}^3}\int_{\mathbb{R}^3}|\phi(\mathbf{r}')|^2\phi(\mathbf{r})U(|\mathbf{r}-\mathbf{r}'|)\delta\bar{\phi}(\mathbf{r})\,d^3\mathbf{r}d^3\mathbf{r}'\Bigg) \\
&= N(N-1)\int_{\mathbb{R}^3}\int_{\mathbb{R}^3}|\phi(\mathbf{r}')|^2\phi(\mathbf{r})U(|\mathbf{r}-\mathbf{r}'|)\delta\bar{\phi}(\mathbf{r})\,d^3\mathbf{r}d^3\mathbf{r}'
\end{aligned}
$$

where terms of order $\mathcal{O}(\delta^2)$ have been neglected and dummy variables have been exchanged to combine the two contributions. Furthermore, we obtain

$$
\frac{\delta F_{\text{int}}[\phi,\bar{\phi}]}{\delta\bar{\phi}} = N(N-1)\left(\int_{\mathbb{R}^3}|\phi(\mathbf{r}')|^2U(|\mathbf{r}-\mathbf{r}'|)\,d^3\mathbf{r}'\right)\phi(\mathbf{r})\,.
$$

For the Lagrangian multiplier term (1.35) we compute

$$
\begin{aligned}
&F_\mu[\phi,\bar\phi+\delta\bar\phi] = \mu\bigg(\int_{\mathbb{R}^3}\phi(\mathbf{r})\Big(\bar\phi(\mathbf{r})+\delta\bar\phi(\mathbf{r})\Big)d^3\mathbf{r}\bigg)^N\\
&=\mu\bigg(\int_{\mathbb{R}^3}\phi(\mathbf{r})\bar\phi(\mathbf{r})\,d^3\mathbf{r}+\int_{\mathbb{R}^3}\phi(\mathbf{r})\delta\bar\phi(\mathbf{r})\,d^3\mathbf{r}\bigg)^N,\\
&\delta F_\mu[\phi,\bar\phi]=F_\mu[\phi,\bar\phi+\delta\bar\phi]-F_\mu[\phi,\bar\phi]\\
&=\mu\bigg(\int_{\mathbb{R}^3}\phi(\mathbf{r})\bar\phi(\mathbf{r})\,d^3\mathbf{r}+\int_{\mathbb{R}^3}\phi(\mathbf{r})\delta\bar\phi(\mathbf{r})\,d^3\mathbf{r}\bigg)^N-\mu\left(\int_{\mathbb{R}^3}\bar\phi(\mathbf{r})\phi(\mathbf{r})\,d^3\mathbf{r}\right)^N\\
&=\mu\bigg(\int_{\mathbb{R}^3}\phi(\mathbf{r})\bar\phi(\mathbf{r})d^3\mathbf{r}\bigg)^N+\mu N\bigg(\int_{\mathbb{R}^3}\phi(\mathbf{r})\bar\phi(\mathbf{r})d^3\mathbf{r}d^3\mathbf{r}\bigg)^{N-1}\int_{\mathbb{R}^3}\phi(\mathbf{r})\delta\bar\phi(\mathbf{r})\,d^3\mathbf{r}\\
&-mu\bigg(\int_{\mathbb{R}^3}\phi(\mathbf{r})\bar\phi(\mathbf{r})d^3\mathbf{r}\bigg)^N\\
&=\mu N\bigg(\int_{\mathbb{R}^3}\phi(\mathbf{r})\bar\phi(\mathbf{r})d^3\mathbf{r}d^3\mathbf{r}\bigg)^{N-1}\int_{\mathbb{R}^3}\phi(\mathbf{r})\delta\bar\phi(\mathbf{r})\,d^3\mathbf{r}\\
&=\mu N\int_{\mathbb{R}^3}\phi(\mathbf{r})\delta\bar\phi(\mathbf{r})d^3\mathbf{r}\,,\\
&\frac{\delta F_\mu[\phi,\bar\phi]}{\delta\bar\phi}=\mu N\phi(\mathbf{r})\,.
\end{aligned}
$$

Now, we collect all the terms to find the variation

$$
\begin{aligned}
&\frac{\delta F[\phi,\bar\phi]}{\delta\bar\phi}=\frac{\delta F_{\rm kin}[\phi,\bar\phi]}{\delta\bar\phi}+\frac{\delta F_{\rm p}[\phi,\bar\phi]}{\delta\bar\phi}+\frac{\delta F_{\rm int}[\phi,\bar\phi]}{\delta\bar\phi}+\frac{\delta F_\mu[\phi,\bar\phi]}{\delta\bar\phi}\\
&=-N\frac{\hbar^2}{2m}\Delta\phi(\mathbf{r})+NV(\mathbf{r})\phi(\mathbf{r})+N(N-1)\bigg(\int_{\mathbb{R}^3}|\phi(\mathbf{r}')|^2U(|\mathbf{r}-\mathbf{r}'|)d^3\mathbf{r}'\bigg)\phi(\mathbf{r})+\mu N\phi(\mathbf{r})\\
&=N\bigg(-\frac{\hbar^2}{2m}\Delta\phi(\mathbf{r})+V(\mathbf{r})\phi(\mathbf{r})+(N-1)\bigg(\int_{\mathbb{R}^3}|\phi(\mathbf{r}')|^2U(|\mathbf{r}-\mathbf{r}'|)d^3\mathbf{r}'\bigg)\phi(\mathbf{r})+\mu\phi(\mathbf{r})\bigg)\\
&=0\,.
\end{aligned}
$$

Therefore, the quantity in brackets must be zero

$$
\begin{aligned}
&-\frac{\hbar^2}{2m}\Delta\phi(\mathbf{r})+V(\mathbf{r})\phi(\mathbf{r})+(N-1)\bigg(\int_{\mathbb{R}^3}|\phi(\mathbf{r}')|^2U(|\mathbf{r}-\mathbf{r}'|)d^3\mathbf{r}'\bigg)\phi(\mathbf{r})+\mu\phi(\mathbf{r})=0\\
&-\frac{\hbar^2}{2m}\Delta\phi(\mathbf{r})+V(\mathbf{r})\phi(\mathbf{r})+(N-1)\bigg(\int_{\mathbb{R}^3}|\phi(\mathbf{r}')|^2U(|\mathbf{r}-\mathbf{r}'|)d^3\mathbf{r}'\bigg)\phi(\mathbf{r})=\mu\phi(\mathbf{r})\,. \qquad (1.36)
\end{aligned}
$$

Recalling that in the case of dilute gases we can assume (see (1.3)) that

$$U(|\mathbf{r}-\mathbf{r}'|)\simeq g\,\delta(\mathbf{r}-\mathbf{r}')\,,$$

so, by integration with respect to $\mathbf{r}'$, we obtain

$$\int_{\mathbb{R}^3} U(|\mathbf{r}-\mathbf{r}'|)\, d^3\mathbf{r}' = \int_{\mathbb{R}^3} g\,\delta(\mathbf{r}-\mathbf{r}')\, d^3\mathbf{r}' = g\,. \tag{1.37}$$

Hence by substituting the expression (1.37) into (1.36) we have

$$-\frac{\hbar^2}{2m}\Delta\phi(\mathbf{r}) + V(\mathbf{r})\phi(\mathbf{r}) + (N-1)g|\phi(\mathbf{r})|^2\phi(\mathbf{r}) = \mu\phi(\mathbf{r})\,. \tag{1.38}$$

Now we define the macroscopic wavefunction

$$\Psi(\mathbf{r},t) := \sqrt{N}\phi(\mathbf{r})\,,$$

thus

$$\phi(\mathbf{r}) = \frac{\Psi(\mathbf{r})}{\sqrt{N}} \qquad |\phi(\mathbf{r})|^2 = \frac{|\Psi(\mathbf{r})|^2}{N} \qquad \int_{\mathbb{R}^3} |\Psi(\mathbf{r})|^2\, d^3\mathbf{r} = N\,. \tag{1.39}$$

By substituting these expressions (1.39) into (1.38) we get

$$\begin{aligned} -\frac{\hbar^2}{2m}\frac{1}{\sqrt{N}}\Delta\Psi(\mathbf{r}) + \frac{V(\mathbf{r})}{\sqrt{N}}\Psi(\mathbf{r}) + (N-1)g\frac{|\Psi(\mathbf{r})|^2}{N}\frac{\Psi(\mathbf{r})}{\sqrt{N}} &= \mu\frac{\Psi(\mathbf{r})}{\sqrt{N}} \\ -\frac{\hbar^2}{2m}\Delta\Psi(\mathbf{r}) + V(\mathbf{r})\Psi(\mathbf{r}) + \frac{(N-1)}{N}g|\Psi(\mathbf{r})|^2\Psi(\mathbf{r}) &= \mu\Psi(\mathbf{r})\,. \end{aligned} \tag{1.40}$$

By assuming a large number of particles ($N \gg 1$) the term $\frac{N-1}{N} \to 1$ and the time-independent Gross Pitaevskii equation

$$-\frac{\hbar^2}{2m}\Delta\Psi(\mathbf{r}) + V(\mathbf{r})\Psi(\mathbf{r}) + g|\Psi(\mathbf{r})|^2\Psi(\mathbf{r}) = \mu\Psi(\mathbf{r})\,, \tag{1.41}$$

where μ is called the chemical potential,is obtained. □

We now discuss some fundamental properties of the chemical potential.

Proposition 1.2.2. *The chemical potential satisfies [5]*

(i) $\mu = \frac{1}{N}(E_{\text{kin}} + E_{\text{p}} + 2E_{\text{int}})\,.$

(ii) $\mu \simeq \frac{\delta E}{\delta N}$.

Proof. (i) We multiply the time-independent GPE (1.41) by $\bar{\Psi}(\mathbf{r})$ and we integrate over $\mathbf{r}$ obtaining

$$\int_{\mathbb{R}^3} -\frac{\hbar^2}{2m}\bar{\Psi}(\mathbf{r})\Delta\Psi(\mathbf{r}) + \bar{\Psi}(\mathbf{r})V(\mathbf{r})\Psi(\mathbf{r}) + \bar{\Psi}(\mathbf{r})g|\Psi(\mathbf{r})|^2\Psi(\mathbf{r})\, d^3\mathbf{r} = \int_{\mathbb{R}^3} \mu\Psi(\mathbf{r})\bar{\Psi}(\mathbf{r})\, d^3\mathbf{r}\,, \tag{1.42}$$

then we derive by part the first term on the left side assuming that $\Psi = 0$ at infinity

$$-\frac{\hbar^2}{2m}\int_{\mathbb{R}^3} \bar{\Psi}(\mathbf{r})\Delta\Psi(\mathbf{r})\, d\mathbf{r} = -\left(-\frac{\hbar^2}{2m}\int_{\mathbb{R}^3} \nabla\bar{\Psi}(\mathbf{r})\nabla\Psi(\mathbf{r})\, d\mathbf{r}\right) = \frac{\hbar^2}{2m}\int_{\mathbb{R}^3} |\nabla\Psi(\mathbf{r})|^2\, d^3\mathbf{r}\,. \tag{1.43}$$

Thus, we substitute expression (1.43) into (1.42) to get

$$\int_{\mathbb{R}^3}\left(\frac{\hbar^2}{2m}|\nabla\Psi(\mathbf{r})|^2+V(\mathbf{r})|\Psi(\mathbf{r})|^2+g|\Psi(\mathbf{r})|^4\right)d^3\mathbf{r}=\mu\int_{\mathbb{R}^3}|\Psi(\mathbf{r})|^2\,d^3\mathbf{r}.$$

Finally assuming the normalized condition (1.2) we have

$$\int_{\mathbb{R}^3}\left(\frac{\hbar^2}{2m}|\nabla\Psi(\mathbf{r})|^2+V(\mathbf{r})|\Psi(\mathbf{r})|^2+g|\Psi(\mathbf{r})|^4\right)d^3\mathbf{r}=\mu N\,, \tag{1.44}$$

and comparing the last equation (1.44) with (1.18) we observe that

$$E_{\rm kin}+E_{\rm p}+2E_{\rm int}=\mu N\,.$$

Hence

$$\mu=\frac{1}{N}(E_{\rm kin}+E_{\rm p}+2E_{\rm int})\,. \tag{1.45}$$

(ii) First of all we assume that $\phi(\mathbf{r})$ is the solution of (1.38), so it is the function that minimize the functional (1.30) under the normalization constraint. Hence we consider the energy functional (1.29) that has a minimum for the function $\phi(\mathbf{r})$ and using (1.32), (1.33), (1.34) and (1.37) we get

$$\begin{aligned}E[\phi,N]&=-N\frac{\hbar^2}{2m}\int\bar\phi(\mathbf{r})\Delta\phi(\mathbf{r})\,d^3\mathbf{r}+N\int_{\mathbb{R}^3}\bar\phi(\mathbf{r})V(\mathbf{r})\phi(\mathbf{r})\,d^3\mathbf{r}+\tfrac{N(N-1)}{2}g\int_{\mathbb{R}^3}|\phi(\mathbf{r})|^2\,|\phi(\mathbf{r})|^2d^3\mathbf{r}\\&=-N\frac{\hbar^2}{2m}\int_{\mathbb{R}^3}\bar\phi(\mathbf{r})\Delta\phi(\mathbf{r})\,d^3\mathbf{r}+N\int_{\mathbb{R}^3}\bar\phi(\mathbf{r})V(\mathbf{r})\phi(\mathbf{r})\,d^3\mathbf{r}+\tfrac{N^2-N}{2}g\int_{\mathbb{R}^3}|\phi(\mathbf{r})|^2\,|\phi(\mathbf{r})|^2\,d^3\mathbf{r}\,.\end{aligned}$$

Then we have

$$\frac{\delta E}{\delta N}=\frac{\partial E}{\partial N}+\frac{\delta E}{\delta\phi}\frac{\partial\phi}{\partial N}=\frac{\partial E}{\partial N}\,,$$

because $\frac{\delta E}{\delta\phi}=0$ since ϕ is the variational solution.

Hence we compute

$$\begin{aligned}\frac{\partial E}{\partial N}&=-\frac{\hbar^2}{2m}\int_{\mathbb{R}^3}\bar\phi(\mathbf{r})\Delta\phi(\mathbf{r})\,d^3\mathbf{r}+\int_{\mathbb{R}^3}\bar\phi(\mathbf{r})V(\mathbf{r})\phi(\mathbf{r})\,d^3\mathbf{r}+\frac{2N-1}{2}g\int_{\mathbb{R}^3}|\phi(\mathbf{r})|^2\,|\phi(\mathbf{r})|^2\,d^3\mathbf{r}\\&=-\frac{\hbar^2}{2m}\int_{\mathbb{R}^3}\bar\phi(\mathbf{r})\Delta\phi(\mathbf{r})\,d^3\mathbf{r}+\int_{\mathbb{R}^3}\bar\phi(\mathbf{r})V(\mathbf{r})\phi(\mathbf{r})\,d^3\mathbf{r}+\left(N-\frac{1}{2}\right)g\int_{\mathbb{R}^3}|\phi(\mathbf{r})|^2\,|\phi(\mathbf{r})|^2\,d^3\mathbf{r}\,.\end{aligned}$$

On the other side, we multiply (1.38) by $\bar\phi(\mathbf{r})$ and we integrate over $\mathbf{r}$ to have

$$\begin{aligned}\int_{\mathbb{R}^3}-\frac{\hbar^2}{2m}\bar\phi\Delta\phi\,d^3\mathbf{r}+\int_{\mathbb{R}^3}\bar\phi V(\mathbf{r})\phi\,d^3\mathbf{r}+(N-1)\,g\int_{\mathbb{R}^3}\bar\phi|\phi|^2\phi\,d^3\mathbf{r}&=\int_{\mathbb{R}^3}\mu\,\bar\phi\phi\,d^3\mathbf{r}\\\int_{\mathbb{R}^3}-\frac{\hbar^2}{2m}\bar\phi\Delta\phi\,d^3\mathbf{r}+\int_{\mathbb{R}^3}\bar\phi V(\mathbf{r})\phi\,d^3\mathbf{r}+(N-1)\,g\int_{\mathbb{R}^3}|\phi|^2|\phi|^2\,d^3\mathbf{r}&=\mu\,,\end{aligned}$$

where $\phi:=\phi(\mathbf{r})$ and $\bar\phi:=\bar\phi(\mathbf{r})$. Finally, for a large number of particles $N\gg1$, $N-\frac{1}{2}\simeq N-1$ and then

$$\mu\simeq\frac{\delta E}{\delta N}\,.$$

□

1.3 Time-dependent GPE with chemical potential

In this section we introduce a reformulation of the time-dependent GPE based on a phase transformation involving the chemical potential.

First we give the definition of stationary state.

Definition 1.3.1. *A solution of the time-dependent Gross–Pitaevskii equation* (1.16) *is called* **stationary** *if the density is time-independent, i.e.*

$$|\Psi(\mathbf{r},t)|^2 = |\psi(\mathbf{r})|^2 .$$

This implies that stationary states differ in time only by a global phase factor.

Remark 1. Stationary states of the time-dependent Gross–Pitaevskii dynamics correspond to solutions of the time-independent GPE. The ground state of a Bose–Einstein condensate is given by the lowest-energy stationary solution.

This property leads to the following characterization of stationary solutions.

Proposition 1.3.1. *Stationary solutions of the time-dependent Gross–Pitaevskii equation* (1.16) *have the form*

$$\Psi(\mathbf{r},t) = \psi(\mathbf{r})e^{-\mathrm{i}\mu t/\hbar},$$

where μ is the chemical potential.

Proof. We substitute the ansatz

$$\Psi(\mathbf{r},t) = \psi(\mathbf{r})e^{-\mathrm{i}\mu t/\hbar}$$

into the time-dependent Gross–Pitaevskii equation (1.16), obtaining

$$\begin{aligned}
\mathrm{i}\hbar\frac{\partial}{\partial t}\left(\psi(\mathbf{r})e^{-\mathrm{i}\mu t/\hbar}\right) &= -\frac{\hbar^2}{2m}\Delta\left(\psi(\mathbf{r})e^{-\mathrm{i}\mu t/\hbar}\right) + V(\mathbf{r})\psi(\mathbf{r})e^{-\mathrm{i}\mu t/\hbar} + g\left|\psi(\mathbf{r})\right|^2\psi(\mathbf{r})e^{-\mathrm{i}\mu t/\hbar} \\
\mu\psi(\mathbf{r})e^{-\mathrm{i}\mu t/\hbar} &= -\frac{\hbar^2}{2m}(\Delta\psi(\mathbf{r}))e^{-\mathrm{i}\mu t/\hbar} + V(\mathbf{r})\psi(\mathbf{r})e^{-\mathrm{i}\mu t/\hbar} + g|\psi(\mathbf{r})|^2\psi(\mathbf{r})e^{-\mathrm{i}\mu t/\hbar} .
\end{aligned}$$

Dividing by the common factor $e^{-\mathrm{i}\mu t/\hbar}$ yields

$$\mu\psi(\mathbf{r}) = -\frac{\hbar^2}{2m}\Delta\psi(\mathbf{r}) + V(\mathbf{r})\psi(\mathbf{r}) + g|\psi(\mathbf{r})|^2\psi(\mathbf{r}) ,$$

which is the time-independent Gross–Pitaevskii equation (1.28). □

We now extend this phase transformation to the full time-dependent dynamics.

Proposition 1.3.2. *Let $\Psi(\mathbf{r},t)$ be a solution of the time-dependent Gross–Pitaevskii equation* (1.16) *with a static external potential $V(\mathbf{r})$. Then, under the transformation*

$$\Psi(\mathbf{r},t) = \tilde{\Psi}(\mathbf{r},t)\, e^{-\mathrm{i}\mu t/\hbar},$$

the function $\tilde{\Psi}(\mathbf{r},t)$ satisfies

$$\mathrm{i}\hbar\frac{\partial\tilde{\Psi}(\mathbf{r},t)}{\partial t} = \left(-\frac{\hbar^2}{2m}\Delta + V(\mathbf{r}) + g|\tilde{\Psi}(\mathbf{r},t)|^2 - \mu\right)\tilde{\Psi}(\mathbf{r},t). \tag{1.46}$$

Proof. We introduce the transformation

$$\Psi(\mathbf{r},t) = \tilde{\Psi}(\mathbf{r},t)\, e^{-\mathrm{i}\mu t/\hbar},$$

which separates the global phase associated with the chemical potential.

In contrast to the stationary case, $\tilde{\Psi} \equiv \tilde{\Psi}(\mathbf{r},t)$ is still allowed to depend on time. Substituting the transformation into the time-dependent GPE (1.16) and dividing by $e^{-\mathrm{i}\mu t/\hbar}$, yields

$$\begin{aligned}
\mathrm{i}\hbar\frac{\partial}{\partial t}\left(\tilde{\Psi}e^{-\mathrm{i}\mu t/\hbar}\right) &= -\frac{\hbar^2}{2m}\Delta\left(\tilde{\Psi}e^{-\mathrm{i}\mu t/\hbar}\right) + V(\mathbf{r})\,\tilde{\Psi}e^{-\mathrm{i}\mu t/\hbar} + g|\tilde{\Psi}|^2\tilde{\Psi}e^{-\mathrm{i}\mu t/\hbar} \\
\mathrm{i}\hbar\left(\frac{\partial\tilde{\Psi}}{\partial t} - \frac{\mathrm{i}\mu}{\hbar}\tilde{\Psi}\right)e^{-\mathrm{i}\mu t/\hbar} &= -\frac{\hbar^2}{2m}(\Delta\tilde{\Psi})e^{-\mathrm{i}\mu t/\hbar} + V(\mathbf{r})\tilde{\Psi}e^{-\mathrm{i}\mu t/\hbar} + g|\tilde{\Psi}|^2\tilde{\Psi}e^{-\mathrm{i}\mu t/\hbar} \\
\mathrm{i}\hbar\frac{\partial\tilde{\Psi}}{\partial t} &= \left(-\frac{\hbar^2}{2m}\Delta + V(\mathbf{r}) + g|\tilde{\Psi}|^2 - \mu\right)\tilde{\Psi}.
\end{aligned}$$

□

1.4 Hydrodynamic formulation of the GPE

Let us consider the condensate as a fluid, defined by its density and velocity distributions.

Definition 1.4.1. *Let*

$$\Psi(\mathbf{r},t) = \sqrt{n(\mathbf{r},t)}e^{\mathrm{i}\theta(\mathbf{r},t)}\,, \tag{1.47}$$

be the **Madelung transform** *[37], where n is a real valued function. We define:*

- *the* **number density**
$$n(\mathbf{r},t) := |\Psi(\mathbf{r},t)|^2\,, \tag{1.48}$$
- *the* **mass density**
$$\rho(\mathbf{r},t) := mn(\mathbf{r},t)\,, \tag{1.49}$$
- *the* **fluid velocity field**
$$\mathbf{v}(\mathbf{r},t) := \frac{\hbar}{m}\nabla\theta(\mathbf{r},t)\,, \tag{1.50}$$
with $\theta(\mathbf{r},t)$ defined on $\Omega = D \setminus \mathcal{Z}(t)$ and $\mathcal{Z}(t) := \{\mathbf{r}\in D : \Psi(\mathbf{r},t) = 0\}$.
- *the* **healing length**
$$\xi := \frac{\hbar}{\sqrt{gmn}} \tag{1.51}$$

In the following of this section, for the sake of simplicity, we denote $n(\mathbf{r},t)$, $\theta(\mathbf{r},t)$, $\rho(\mathbf{r},t)$, $\mathbf{v}(\mathbf{r},t)$ and the potential $V(\mathbf{r},t)$ by n, θ, ρ, $\mathbf{v}$ and V.

The following theorem shows that, under the Madelung transformation, the GPE can be rewritten in the form of hydrodynamic equations for the condensate density and velocity field.

Theorem 1.4.1. *The superfluid hydrodynamic equations are*

(i) the continuity equation

$$\frac{\partial n}{\partial t} + \nabla \cdot (n\mathbf{v}) = 0\,. \tag{1.52}$$

(ii) the momentum equation

$$mn\left(\frac{\partial \mathbf{v}}{\partial t} + (\mathbf{v}\cdot\nabla)\mathbf{v}\right) = -\nabla(P + P') - n\nabla V \tag{1.53}$$

where

- $P := \frac{gn^2}{2}$ *is the pressure*
- $P' := -\frac{\hbar^2}{4m} n\Delta(\ln n)$ *is the quantum pressure*.

Proof. We want to derive the governing equations of the dynamics. We insert the expression (1.47) of the Madelung transform into the time-dependent GPE (1.4). We have

$$\mathrm{i}\hbar\frac{\partial}{\partial t}\left(\sqrt{n}e^{\mathrm{i}\theta}\right) = -\frac{\hbar^2}{2m}\Delta\left(\sqrt{n}e^{\mathrm{i}\theta}\right) + V\sqrt{n}e^{\mathrm{i}\theta} + gn(\sqrt{n}e^{\mathrm{i}\theta})\,. \tag{1.54}$$

Then, we make the following computations

$$\frac{\partial}{\partial t}\left(\sqrt{n}e^{\mathrm{i}\theta}\right) = \frac{1}{2\sqrt{n}}\frac{\partial n}{\partial t}e^{\mathrm{i}\theta} + \sqrt{n}\mathrm{i}\frac{\partial\theta}{\partial t}e^{\mathrm{i}\theta} = e^{\mathrm{i}\theta}\left(\frac{1}{2\sqrt{n}}\frac{\partial n}{\partial t} + \sqrt{n}\mathrm{i}\frac{\partial\theta}{\partial t}\right)\,, \tag{1.55}$$

and

$$\begin{aligned}\Delta\left(\sqrt{n}e^{\mathrm{i}\theta}\right) &= \Delta\left(\sqrt{n}\right)e^{\mathrm{i}\theta} + \sqrt{n}\Delta\left(e^{\mathrm{i}\theta}\right) + 2\nabla\left(\sqrt{n}\right)\nabla\left(e^{\mathrm{i}\theta}\right)\\ &= \Delta\left(\sqrt{n}\right)e^{\mathrm{i}\theta} + \sqrt{n}e^{\mathrm{i}\theta}\left(\mathrm{i}\Delta\theta - (\nabla\theta)^2\right) + 2\frac{1}{2\sqrt{n}}\nabla n\mathrm{i}\nabla\theta e^{\mathrm{i}\theta}\,;\end{aligned} \tag{1.56}$$

where we have used

$$\begin{aligned}\nabla\left(e^{\mathrm{i}\theta}\right) &= \mathrm{i}\nabla\theta e^{\mathrm{i}\theta}\,,\\ \Delta\left(e^{\mathrm{i}\theta}\right) &= \nabla\left(\mathrm{i}\nabla\theta e^{\mathrm{i}\theta}\right) = \mathrm{i}\Delta\theta e^{\mathrm{i}\theta} + \mathrm{i}\nabla\theta\mathrm{i}\nabla\theta e^{\mathrm{i}\theta} = \mathrm{i}\Delta\theta e^{\mathrm{i}\theta} - (\nabla\theta)^2 e^{\mathrm{i}\theta}\\ &= e^{\mathrm{i}\theta}\left(\mathrm{i}\Delta\theta - (\nabla\theta)^2\right)\,,\\ \nabla\left(\sqrt{n}\right) &= \frac{1}{2\sqrt{n}}\nabla n\,.\end{aligned}$$

After that, we substitute the previously derived expressions (1.55) and (1.56) in (1.54) to get

$$\begin{aligned}\mathrm{i}\hbar e^{\mathrm{i}\theta}\left(\frac{1}{2\sqrt{n}}\frac{\partial n}{\partial t} + \sqrt{n}\mathrm{i}\frac{\partial\theta}{\partial t}\right) = -\frac{\hbar^2}{2m}\Bigg(&\Delta\left(\sqrt{n}\right)e^{\mathrm{i}\theta} + \sqrt{n}e^{\mathrm{i}\theta}\left(\mathrm{i}\Delta\theta - (\nabla\theta)^2\right) +\\ &+ \frac{1}{\sqrt{n}}\nabla n\mathrm{i}\nabla\theta e^{\mathrm{i}\theta}\Bigg) + V\sqrt{n}e^{\mathrm{i}\theta} + gn\sqrt{n}e^{\mathrm{i}\theta}\,.\end{aligned} \tag{1.57}$$

Hence, we simplify and do computation, we have the following

$$\begin{aligned}\frac{\mathrm{i}\hbar}{2\sqrt{n}}\frac{\partial n}{\partial t}-\sqrt{n}\hbar\frac{\partial\theta}{\partial t}=&-\frac{\hbar^2}{2m}\Delta\left(\sqrt{n}\right)-\frac{\hbar^2}{2m}\sqrt{n}\mathrm{i}\Delta\theta+\frac{\hbar^2}{2m}\sqrt{n}\left(\nabla\theta\right)^2+\\&-\frac{\hbar^2}{2m}\frac{\nabla(n)}{\sqrt{n}}\mathrm{i}\nabla\theta+V\sqrt{n}+g\sqrt{n^3}\,.\end{aligned}\tag{1.58}$$

Finally, we separate the real and imaginary terms.

(i) If we take the imaginary parts of (1.58) and do calculations, we obtain

$$\begin{aligned}\frac{\hbar}{2\sqrt{n}}\frac{\partial n}{\partial t}&=-\frac{\hbar^2}{2m}\sqrt{n}\Delta\theta-\frac{\hbar^2}{2m}\frac{\nabla(n)}{\sqrt{n}}\nabla\theta\\\frac{\partial n}{\partial t}&=\frac{-\hbar n}{m}\Delta\theta-\frac{\hbar}{m}\nabla(n)\nabla\theta\\\frac{\partial n}{\partial t}&+\frac{\hbar n}{m}\Delta\theta+\frac{\hbar}{m}\nabla(n)\nabla\theta=0\\\frac{\partial n}{\partial t}&+\nabla\left(n\frac{\hbar}{m}\nabla\theta\right)=0\,,\end{aligned}$$

and so, remembering expression (1.50), the resulting equation is

$$\frac{\partial n}{\partial t}+\nabla\cdot(n\mathbf{v})=0\,.\tag{1.59}$$

The last (1.59) is the classical continuity equation and describes the conservation of the number of atoms.

(ii) On the other hand, we take the real part in (1.58), do calculations and use expression (1.50), we have

$$\begin{aligned}-\sqrt{n}\hbar\frac{\partial\theta}{\partial t}&=-\frac{\hbar^2}{2m}\Delta\left(\sqrt{n}\right)+\frac{\hbar^2}{2m}\sqrt{n}\left(\nabla\theta\right)^2+V\sqrt{n}+g\sqrt{n^3}\\-\hbar\frac{\partial\theta}{\partial t}&=-\frac{\hbar^2}{2m\sqrt{n}}\Delta\left(\sqrt{n}\right)+\frac{\hbar^2}{2m}\left(\nabla\theta\right)^2+V+gn\\-m\frac{\partial}{\partial t}\left(\frac{\hbar\theta}{m}\right)-\frac{\hbar^2}{2m}\left(\nabla\theta\right)^2&=-\frac{\hbar^2}{2m}\frac{\Delta\left(\sqrt{n}\right)}{\sqrt{n}}+V+gn\\-m\frac{\partial}{\partial t}\left(\frac{\hbar\theta}{m}\right)-\frac{m\mathbf{v}^2}{2}&=-\frac{\hbar^2}{2m}\frac{\Delta\left(\sqrt{n}\right)}{\sqrt{n}}+V+gn\\\nabla\left(-m\frac{\partial}{\partial t}\left(\frac{\hbar\theta}{m}\right)-\frac{m\mathbf{v}^2}{2}\right)&=\nabla\left(-\frac{\hbar^2}{2m}\frac{\Delta\left(\sqrt{n}\right)}{\sqrt{n}}+V+gn\right)\\-m\frac{\partial}{\partial t}\mathbf{v}&=\nabla\left(\frac{1}{2}m\mathbf{v}^2-\frac{\hbar^2}{2m}\frac{\Delta\left(\sqrt{n}\right)}{\sqrt{n}}+V+gn\right)\,.\end{aligned}$$

So we gain the following equation

$$m\frac{\partial}{\partial t}\mathbf{v}=-\nabla\left(\frac{1}{2}m\mathbf{v}^2+V+gn-\frac{\hbar^2}{2m}\frac{\Delta\left(\sqrt{n}\right)}{\sqrt{n}}\right)\,,\tag{1.60}$$

that is the momentum equation and the term $\frac{\Delta(\sqrt{n})}{\sqrt{n}}$ is called the quantum pressure term. We can write it in another form. We multiply (1.60) by n and do some calculation, we have

$$\begin{aligned}
mn\frac{\partial \mathbf{v}}{\partial t} &= -n\nabla\left(\frac{1}{2}m\mathbf{v}^2 + V + gn - \frac{\hbar^2}{2m}\frac{\Delta\sqrt{n}}{\sqrt{n}}\right)\\
mn\frac{\partial \mathbf{v}}{\partial t} &= -n\nabla\left(\frac{1}{2}m\mathbf{v}^2\right) - n\nabla V - n\nabla\left(gn\right) - n\nabla\left(-\frac{\hbar^2}{2m}\frac{\Delta\sqrt{n}}{\sqrt{n}}\right)\\
mn\frac{\partial \mathbf{v}}{\partial t} &= -n\frac{1}{2}m2\left(\mathbf{v}\cdot\nabla\right)\mathbf{v} - n\nabla V - \nabla\left(\frac{gn^2}{2}\right) - n\nabla\left(-\frac{\hbar^2}{2m}\frac{\Delta\sqrt{n}}{\sqrt{n}}\right)\\
mn\left(\frac{\partial \mathbf{v}}{\partial t} + \left(\mathbf{v}\cdot\nabla\right)\mathbf{v}\right) &= -n\nabla V - \nabla\left(\frac{gn^2}{2}\right) - n\nabla\left(-\frac{\hbar^2}{2m}\frac{\Delta\sqrt{n}}{\sqrt{n}}\right). \qquad (1.61)
\end{aligned}$$

Then, we expand the last term on the right side of (1.61),

$$\begin{aligned}
-n\nabla\left(-\frac{\hbar^2}{2m}\frac{\Delta\left(\sqrt{n}\right)}{\sqrt{n}}\right) &= n\frac{\hbar^2}{2m}\nabla\left(\frac{\Delta\left(\sqrt{n}\right)}{\sqrt{n}}\right)\\
&= n\frac{\hbar^2}{2m}\left(\frac{\nabla\Delta\left(\sqrt{n}\right)\sqrt{n} - \Delta\left(\sqrt{n}\right)\nabla\left(\sqrt{n}\right)}{n}\right)\\
&= \frac{\hbar^2}{2m}\left(\nabla\Delta\left(\sqrt{n}\right)\sqrt{n} - \Delta\left(\sqrt{n}\right)\nabla\left(\sqrt{n}\right)\right) \qquad (1.62)
\end{aligned}$$

Now, we derive the following

$$\begin{aligned}
\nabla\left(\sqrt{n}\right) &= \frac{\nabla n}{2\sqrt{n}}\\
\Delta\left(\sqrt{n}\right) &= \left(\Delta n2\sqrt{n} - \nabla n\frac{\nabla n}{\sqrt{n}}\right)\frac{1}{4n} = \left(\Delta n2\sqrt{n} - \frac{\left(\nabla n\right)^2}{\sqrt{n}}\right)\frac{1}{4n} = \frac{\Delta n}{2\sqrt{n}} - \frac{\left(\nabla n\right)^2}{4\sqrt{n^3}} \qquad (1.63)\\
\nabla\left(\Delta\left(\sqrt{n}\right)\right) &= \frac{\nabla\left(\Delta n\right)2\sqrt{n} - \Delta n\frac{\nabla n}{\sqrt{n}}}{4n} - \frac{2\nabla n\Delta n4\sqrt{n^3} - \left(\nabla n\right)^2 6\sqrt{n}\nabla n}{16n^3} \qquad (1.64)\\
\nabla\left(\Delta\left(\sqrt{n}\right)\right)\sqrt{n} &= \frac{\nabla\left(\Delta n\right)2n - \Delta n\nabla n}{4n} - \frac{8\nabla n\Delta nn^2 - \left(\nabla n\right)^3 6n}{16n^3}. \qquad (1.65)
\end{aligned}$$

We substitute expressions (1.63), (1.64) and (1.65) in expression (1.62) and we obtain

$$\begin{aligned}
&\frac{\hbar^2}{2m}\left(\frac{\nabla(\Delta n)\,2n-\Delta n\nabla n}{4n}-\frac{8\nabla n\Delta n n^2-(\nabla n)^3 6n}{16n^3}-\left(\frac{\Delta n}{2\sqrt{n}}-\frac{(\nabla n)}{4\sqrt{n^3}}\right)\frac{\nabla n}{2\sqrt{n}}\right)=\\
&=\frac{\hbar^2}{2m}\left(\frac{\nabla(\Delta n)\,8n^3-\Delta n\nabla n 4n^2-8\nabla n\Delta n n^2+6n(\nabla n)^3-4n^2\Delta n\nabla n+2n(\nabla n)^3}{16n^3}\right)\\
&=\frac{\hbar^2}{2m}\left(\frac{\nabla(\Delta n)\,8n^3-16n^2\Delta n\nabla n+8n(\nabla n)^3}{16n^3}\right)\\
&=\frac{\hbar^2}{2m}\left(\frac{\nabla(\Delta n)\,8n^2-16n\Delta n\nabla n+8(\nabla n)^3}{16n^2}\right)\\
&=\frac{\hbar^2}{2m}\left(\frac{n^2\nabla(\Delta n)-2n\nabla n\Delta n+(\nabla n)^3}{2n^2}\right)\\
&=-\nabla\left(-\frac{\hbar^2}{4m}n\Delta(\ln n)\right). \qquad (1.66)
\end{aligned}$$

The last expression (1.66) is obtained because,

$$\begin{aligned}
-\nabla\left(-\frac{\hbar^2}{4m}n\Delta(\ln n)\right)&=\frac{\hbar^2}{4m}\nabla(n\Delta(\ln n))=\frac{\hbar^2}{4m}\nabla\left(n\frac{\Delta n n-(\nabla n)^2}{n^2}\right)\\
&=\frac{\hbar^2}{4m}\nabla\left(\frac{\Delta n n-(\nabla n)^2}{n}\right)\\
&=\frac{\hbar^2}{2m}\left(\nabla(\Delta n)-\nabla\left(\frac{(\nabla n)^2}{n}\right)\right)\\
&=\frac{\hbar^2}{4m}\left(\nabla(\Delta n)-\frac{2\nabla n\Delta n n-(\nabla n)^2\nabla n}{n^2}\right)\\
&=\frac{\hbar^2}{4m}\left(\frac{n^2\nabla(\Delta n)-2\nabla n\Delta n n+(\nabla n)^3}{n^2}\right).
\end{aligned}$$

Finally (1.61) becomes

$$\begin{aligned}
mn\left(\frac{\partial\mathbf{v}}{\partial t}+(\mathbf{v}\cdot\nabla)\,\mathbf{v}\right)&=-n\nabla V-\nabla\left(\frac{gn^2}{2}\right)-\nabla\left(-\frac{\hbar^2}{4m}n\Delta(\ln n)\right)\\
mn\left(\frac{\partial\mathbf{v}}{\partial t}+(\mathbf{v}\cdot\nabla)\mathbf{v}\right)&=-\nabla(P+P')-n\nabla V \qquad (1.67)
\end{aligned}$$

where

- $P=\frac{gn^2}{2}$ is the pressure
- $P'=-\frac{\hbar^2}{4m}n\Delta(\ln n)$ is called the quantum pressure.

□

Remark 2. We notice that the pressure depends only on the number density n, so the condensate is a barotropic fluid. Furthermore, the quantum pressure is a pure quantum effect, in fact it disappears when the Planck's constant $\hbar$ is equal to zero. In particular, it is zero in a uniform condensate, because n is constant.

Remark 3. The order of magnitude of P and P' are $P \sim gn^2$ and $P' \sim \frac{\hbar^2 n}{m\xi^2}$, where ξ is the length scale of the variations of n. Then $P'/P \sim \frac{\hbar^2}{mng\xi^2}$, so P' becomes negligible ($P' \ll P$) in the limit of length scales larger than ξ. This length scale is given by the healing length defined as

$$\xi := \frac{\hbar}{\sqrt{gmn}} \tag{1.68}$$

Under the Madelung transformation, the energy functional (1.18) of the Gross–Pitaevskii equation can be expressed in terms of the density n and velocity field $\mathbf{v}$, leading to a hydrodynamic decomposition of the energy.

Theorem 1.4.2. *Let us consider the Madelung transform* (1.47)*, the energy integral* (1.18) *can be written as*

$$E = \int_D \left[\frac{\hbar^2}{2m} \left(\nabla\sqrt{n}\right)^2 + \frac{mn\mathbf{v}^2}{2} + Vn + \frac{gn^2}{2} \right] d^3\mathbf{r}\,, \tag{1.69}$$

where the first term on the right side represents the quantum energy that originates from the localized motion of confined particles and disappears in a spatially uniform system. The second term is the kinetic energy associated to the motion of the fluid. The third term is the potential energy and the fourth term is the internal (or interaction) energy.

Proof. We consider the Madelung transform (1.47) and we compute

$$\nabla\Psi = \nabla\sqrt{n}e^{\mathrm{i}\theta} + \sqrt{n}\mathrm{i}e^{\mathrm{i}\theta}\nabla\theta = \left(\nabla\sqrt{n} + \sqrt{n}\mathrm{i}\nabla\theta\right)e^{\mathrm{i}\theta}$$

$$\nabla\bar{\Psi} = \nabla\sqrt{n}e^{-\mathrm{i}\theta} + \sqrt{n}(-\mathrm{i})e^{-\mathrm{i}\theta}\nabla\theta = \left(\nabla\sqrt{n} - \sqrt{n}\mathrm{i}\nabla\theta\right)e^{-\mathrm{i}\theta}$$

$$|\nabla\Psi|^2 = \nabla\Psi\nabla\bar{\Psi} = \left(\nabla(\sqrt{n}) + \sqrt{n}\mathrm{i}\nabla\theta\right)e^{\mathrm{i}\theta}\left(\nabla(\sqrt{n}) - \sqrt{n}\mathrm{i}\nabla\theta\right)e^{-\mathrm{i}\theta} = (\nabla\sqrt{n})^2 + n(\nabla\theta)^2\,.$$

Thus, the expression of the energy (1.18) becomes

$$\begin{aligned}
E &= \int_D \left[\frac{\hbar^2}{2m}|\nabla\Psi|^2 + V(\mathbf{r},t)|\Psi|^2 + \frac{g}{2}|\Psi|^4 \right] d^3\mathbf{r} \\
&= \int_D \left[\frac{\hbar^2}{2m}\left((\nabla\sqrt{n})^2 + n(\nabla\theta)^2\right) + Vn + \frac{g}{2}n^2 \right] d^3\mathbf{r} \\
&= \int_D \left[\frac{\hbar^2}{2m}(\nabla\sqrt{n})^2 + \frac{\hbar^2}{2m}n\left(\frac{m}{\hbar}\mathbf{v}\right)^2 + Vn + \frac{g}{2}n^2 \right] d^3\mathbf{r} \\
&= \int_D \left[\frac{\hbar^2}{2m}\left(\nabla\sqrt{n}\right)^2 + \frac{mn\mathbf{v}^2}{2} + Vn + \frac{gn^2}{2} \right] d^3\mathbf{r}\,.
\end{aligned}$$

□

1.5 Stationaty solutions in infinite or semi-infinite homogeneous systems

Many general properties of atomic condensates can be understood considering homogeneous condensate in an infinitely-sized or semi infinitely-side system. We assume $\Psi(\mathbf{r})$ real for the simple solutions that we discuss in this Section.

1.5.1 Uniform condensate

Definition 1.5.1. *A* **uniform condensate** *is defined as a state in which the wavefunction* $\Psi(\mathbf{r})$ *is spatially constant, i.e.*

$$\Psi(\mathbf{r}) = \sqrt{n_0}e^{i\theta},$$

where n_0 *is the density of the condensate and* θ *is a constant phase.*

In a homogeneous system, i.e. in the absence of an external potential $V(\mathbf{r}) = 0$, the system is translationally invariant and the Gross–Pitaevskii Equation admits a uniform condensate as its ground-state solution. This corresponds to the simplest nontrivial stationary state of the GPE, characterized by a constant density, which serves as the reference background for studying excitations and perturbations.

Proposition 1.5.1. *Let* $V = 0$. *Then the stationary uniform solution of the time-independent GPE* (1.41) *is*

$$\Psi(\mathbf{r}) = \Psi_0 = \sqrt{\frac{\mu}{g}}\,. \tag{1.70}$$

Proof. For $V = 0$ the time-independent GPE (1.41) becomes

$$-\frac{\hbar^2}{2m}\Delta\Psi(\mathbf{r}) + g|\Psi(\mathbf{r})|^2\Psi(\mathbf{r}) = \mu\Psi(\mathbf{r})\,.$$

We want to find the uniform solution so we have that $\Delta\Psi(\mathbf{r}) = 0$, hence

$$g|\Psi(\mathbf{r})|^2\Psi(\mathbf{r}) = \mu\Psi(\mathbf{r})\,,$$

and assuming that $\Psi(\mathbf{r}) \neq 0$ we have

$$|\Psi(\mathbf{r})|^2 = \frac{\mu}{g}\,.$$

So the solution is

$$\Psi(\mathbf{r}) = \Psi_0 = \sqrt{\frac{\mu}{g}}\,.$$

□

Remark 4. The corresponding number density and mass densities are, respectively

$$n = n_0 = |\Psi_0|^2 = \frac{\mu}{g}\,, \qquad \rho = \rho_0 = m\frac{\mu}{g}\,.$$

1.5.2 Condensate near a wall

We now study the effect of a hard-wall boundary on the condensate. In particular we consider a semi-infinite one-dimensional domain, where the presence of the boundary at $x = 0$ forces the condensate wave function to vanish at the wall. In this setting the Gross–Pitaevskii Equation admits a stationary solution describing how the condensate density recovers from zero at the boundary to its constant asymptotic value at infinity.

Theorem 1.5.2. *Let us consider a one-dimensional hard wall defined by*

$$V(x) = \begin{cases} \infty & \text{for } x < 0\,, \\ 0 & \text{for } x \geq 0\,. \end{cases} \tag{1.71}$$

In the semi-infinite region $x \geq 0$, the solution of the the 1-dim time-independent GPE

$$\mu\Psi(x) = -\frac{\hbar}{2m}\frac{\partial^2\Psi(x)}{\partial x^2} + g|\Psi(x)|^2\Psi(x)\,, \tag{1.72}$$

satisfying the boundary conditions $\Psi(0) = 0$ and $\Psi(x \to \infty) = \Psi_0$, is given by

$$\Psi(x) = \Psi_0 \tanh\left(\frac{x}{\xi}\right)\,. \tag{1.73}$$

Proof. Let us consider the potential (1.71). We notice that no atoms exist in the region $x < 0$ (since this would require infinite energy), and so the boundary condition in $x = 0$ is $\Psi(0) = 0$. On the other hand, far from the wall (in the positive x direction), the condensate must recover its bulk form, giving the second boundary condition that is $\Psi(x) \to \Psi_0 = \sqrt{\frac{\mu}{g}}$ for $x \to \infty$. We take the 1-*dim* time-independent GPE (1.72). For simplicity of notation we set $\Psi(x) = \Psi$ and denote $\Psi'' = \frac{\partial^2\Psi}{\partial x^2}$. Multiplying the equation by Ψ' and assuming that Ψ' does not vanish identically, we obtain

$$\begin{aligned} \mu\Psi\Psi' &= -\frac{\hbar^2}{2m}\Psi''\Psi' + g\Psi^3\Psi' \\ \frac{\hbar^2}{2m}\Psi''\Psi' &= g\Psi^3\Psi' - \mu\Psi\Psi' \\ \frac{\hbar^2}{2m}\frac{1}{2}\frac{d}{dx}(\Psi'^2) &= \frac{d}{dx}\left(\frac{g}{4}\Psi^4 - \frac{\mu}{2}\Psi^2\right)\,. \end{aligned}$$

Now we integrate with respect to x, thus

$$\begin{aligned} \int_0^\infty \frac{\hbar^2}{2m}\frac{1}{2}\frac{d}{dx}(\Psi'^2) &= \int_0^\infty \frac{d}{dx}\left(\frac{g}{4}\Psi^4 - \frac{\mu}{2}\Psi^2\right) \\ \frac{\hbar^2}{4m}\Psi'^2 &= \frac{g}{4}\Psi^4 - \frac{\mu}{2}\Psi^2 + C\,. \end{aligned} \tag{1.74}$$

Then we apply the boundary conditions to determine the constant C. So for $x = 0$, $\Psi(0) = 0$ and $\Psi'(0) = 0$, while for $x \to \infty$, $\Psi(x) \to \Psi_0$ and $\Psi'(x) \to 0$, leading to

$$0 = \frac{g}{4}\Psi_0^4 - \frac{\mu}{2}\Psi_0^2 + C \Leftrightarrow C = \frac{\mu}{2}\frac{\mu}{g} - \frac{g}{4}\frac{\mu^2}{g^2} \Leftrightarrow C = \frac{\mu^2}{4g}\,.$$

We substitute the value of C into (1.74), obtaining

$$\begin{aligned}
\frac{\hbar^2}{4m}\Psi'^2 = \frac{g}{4}\Psi^4 - \frac{\mu}{2}\Psi^2 + \frac{\mu^2}{4g} \quad &\Leftrightarrow \quad \frac{\hbar^2}{4m}\Psi'^2 = \frac{g}{4}\Psi^4 - \frac{g}{4}\frac{4}{g}\frac{\mu}{2}\Psi^2 + \frac{g}{g}\frac{\mu^2}{4g} \\
\frac{\hbar^2}{4m}\Psi'^2 = \frac{g}{4}\Psi^4 - \frac{g}{4}\frac{2\mu}{g}\Psi^2 + \frac{g}{4}\left(\frac{\mu^2}{g^2}\right) \quad &\Leftrightarrow \quad \frac{\hbar^2}{4m}\Psi'^2 = \frac{g}{4}\left(\Psi^4 - \frac{2\mu}{g}\Psi^2 + \frac{\mu^2}{g^2}\right) \\
\frac{\hbar^2}{4m}\Psi'^2 = \frac{g}{4}\left(\Psi^4 - 2\Psi_0^2\Psi^2 + \Psi_0^4\right) \quad &\Leftrightarrow \quad \frac{\hbar^2}{4m}\Psi'^2 = \frac{g}{4}\left(\Psi^2 - \Psi_0^2\right)^2 \\
\Psi'^2 = \frac{4m}{\hbar^2}\frac{g}{4}\left(\Psi^2 - \Psi_0^2\right)^2 \quad &\Rightarrow \quad \Psi' = \pm\sqrt{\frac{gm}{\hbar^2}\left(\Psi^2 - \Psi_0^2\right)^2}\,.
\end{aligned}$$

We know that Ψ increases with x and that $\Psi^2 - \Psi_0^2 < 0$ for $0 < \Psi < \Psi_0$, so we take the negative sign

$$\Psi' = -\frac{\sqrt{gm}}{\hbar}(\Psi^2 - \Psi_0^2)\,.$$

Then, we separate the variables and we integrate

$$\begin{aligned}
\frac{d\Psi}{dx} = -\frac{\sqrt{gm}}{\hbar}(\Psi^2 - \Psi_0^2) \quad &\Leftrightarrow \quad \int \frac{d\Psi}{\Psi^2 - \Psi_0^2} = -\int \frac{\sqrt{gm}}{\hbar}dx \\
-\int \frac{d\Psi}{\Psi_0^2 - \Psi^2} = -\frac{\sqrt{gm}}{\hbar}x \quad &\Leftrightarrow \quad \int \frac{d\Psi}{\Psi_0^2\left(1 - \frac{\Psi^2}{\Psi_0^2}\right)} = \frac{\sqrt{gm}}{\hbar}x \\
\int \frac{\frac{\Psi_0}{\Psi_0}d\Psi}{\Psi_0^2\left(1 - \left(\frac{\Psi}{\Psi_0}\right)^2\right)} = \frac{\sqrt{gm}}{\hbar}x \quad &\Leftrightarrow \quad \frac{\Psi_0}{\Psi_0^2}\int \frac{\frac{1}{\Psi_0}}{1 - \left(\frac{\Psi}{\Psi_0}\right)^2}d\Psi = \frac{\sqrt{gm}}{\hbar}x \\
\operatorname{atanh}\left(\frac{\Psi}{\Psi_0}\right) = \Psi_0\frac{\sqrt{gm}}{\hbar}x \quad &\Leftrightarrow \quad \operatorname{atanh}\left(\frac{\Psi}{\Psi_0}\right) = \frac{\sqrt{gm\Psi_0^2}}{\hbar}x \\
\operatorname{atanh}\left(\frac{\Psi}{\Psi_0}\right) = \frac{\sqrt{gmn}}{\hbar}x \quad &\Rightarrow \quad \frac{\Psi}{\Psi_0} = \tanh\left(\frac{\sqrt{gmn}}{\hbar}x\right) \\
&\Rightarrow \quad \Psi = \Psi_0\tanh\left(\frac{x}{\xi}\right).
\end{aligned}$$

□

We notice that the healing length ξ is then the characteristic minimal distance over which Ψ changes spatially.

1.6 Dimensionless variables

In general[3], it is more convenient to work with numbers that were of order unity, since some parameters which appear in the GPE equation are not independent. Hence, it is useful to introduce dimensionless variables and rewrite the GPE in dimensionless form.

Theorem 1.6.1. *The time-dependent GPE with a constant potential* V_0

$$i\hbar\frac{\partial\Psi}{\partial t} = -\frac{\hbar^2}{2m}\Delta\Psi + V_0\Psi + g|\Psi|^2\Psi\,, \tag{1.75}$$

can be rewritten in dimensionless form as

$$\mathrm{i}\frac{\partial\Psi'}{\partial t'} = -\frac{1}{2}\Delta'\Psi' + V_0'\Psi' + g'|\Psi'|^2\Psi'\,, \tag{1.76}$$

where $\Psi' = \Psi\frac{\sqrt{\xi^3}}{\sqrt{N}}$, $t' = \frac{t}{\tau}$ *with* $\tau = \frac{m\xi^2}{\hbar}$, $V_0' = \frac{V_0}{E_0}$, $g' = \frac{gN}{\xi^3 E_0}$, *with* $E_0 = \frac{\hbar^2}{m\xi^2}$.

Proof. We have seen that the healing length $\xi = \frac{\hbar}{\sqrt{mng}}$ is the characteristic minimal distance over which Ψ changes spatially. So, it could be a useful unit of length. Then we define $\tau = \frac{m\xi^2}{\hbar}$ as unit of time. Now, we introduce the following dimensionless variables,

$$x' = \frac{x}{\xi} \qquad y' = \frac{y}{\xi} \qquad z' = \frac{z}{\xi} \qquad t' = \frac{t}{\tau} \tag{1.77}$$

and

$$\Psi' = \Psi\frac{\sqrt{\xi^3}}{\sqrt{N}} \tag{1.78}$$

so the new wavefunction is normalized,

$$\int |\Psi'|^2 d^3\mathbf{r} = 1\,. \tag{1.79}$$

We have to substitute these new variables into the GPE, so first we need to determine the corresponding derivative relations. Using the chain rule, we obtain,

$$\frac{d}{dx} = \frac{1}{\xi}\frac{d}{dx'} \qquad \frac{d}{dy} = \frac{1}{\xi}\frac{d}{dy'} \qquad \frac{d}{dz} = \frac{1}{\xi}\frac{d}{dz'} \qquad \frac{d}{dt} = \frac{1}{\tau}\frac{d}{dt'}\,. \tag{1.80}$$

Therefore, the gradient and the Laplacian operators acting on the primed variables are defined as,

$$\nabla = \frac{1}{\xi}\nabla', \qquad \Delta = \frac{1}{\xi^2}\Delta'\,. \tag{1.81}$$

Thus, using the expression (1.78), the temporal derivative in (1.75) can be expressed as

$$\frac{\partial\Psi}{\partial t} = \frac{\partial}{\partial t}\left(\sqrt{N}\frac{1}{\sqrt{\xi^3}}\Psi'\right) = \sqrt{N}\frac{1}{\xi^3}\frac{1}{\tau}\frac{\partial\Psi'}{\partial t'}\,, \tag{1.82}$$

[3]For numerical reasons.

the Laplacian becomes

$$\Delta\Psi = \Delta\left(\frac{\sqrt{N}}{\sqrt{\xi^3}}\Psi'\right) = \frac{\sqrt{N}}{\sqrt{\xi^3}}\Delta\Psi' = \frac{\sqrt{N}}{\sqrt{\xi^3}}\frac{1}{\xi^2}\Delta'\Psi'\,, \tag{1.83}$$

and the interaction term yields

$$|\Psi|^2\Psi = \left(\frac{N}{\sqrt{\xi^3}}\Psi'\right)^2\left(\frac{\sqrt{N}}{\sqrt{\xi^3}}\Psi'\right) = \frac{\sqrt{N^3}}{\sqrt{\xi^9}}|\Psi'|^2\Psi'\,. \tag{1.84}$$

Now, we substitute the previous results (1.82) (1.83) and (1.84) in the (1.75) of the GPE

$$\mathrm{i}\hbar\sqrt{N}\frac{1}{\xi^3}\frac{1}{\tau}\frac{\partial\Psi'}{\partial t'} = -\frac{\hbar^2}{2m}\frac{\sqrt{N}}{\sqrt{\xi^3}}\frac{1}{\xi^2}\Delta'\Psi' + V_0\frac{N}{\sqrt{\xi^3}}\Psi' + g\frac{\sqrt{N^3}}{\sqrt{\xi^9}}|\Psi'|^2\Psi'\,. \tag{1.85}$$

Subsequently, we simplify the previous equation and replace the value of τ

$$\mathrm{i}\hbar\frac{\hbar}{m\xi^2}\frac{\partial\Psi'}{\partial t'} = -\frac{\hbar^2}{2m\xi^2}\Delta'\Psi' + V_0\Psi' + g\frac{N}{\sqrt{\xi^3}}|\Psi'|^2\Psi'\,. \tag{1.86}$$

Then, we define

$$E_0 = \frac{\hbar^2}{m\xi^2} \tag{1.87}$$

and substitute it in the equation (1.86) to have

$$\mathrm{i}E_0\frac{\partial\Psi'}{\partial t'} = -\frac{1}{2}E_0\Delta'\Psi' + V_0\psi' + g\frac{N}{\xi^3}|\Psi'|^2\Psi'\,. \tag{1.88}$$

Finally, we divided the last equation by E_0 and we obtain

$$\mathrm{i}\frac{\partial\Psi'}{\partial t'} = -\frac{1}{2}\Delta'\Psi' + \frac{V_0}{E_0}\Psi' + \frac{gN}{\xi^3E_0}|\Psi'|^2\Psi'$$

$$\mathrm{i}\frac{\partial\Psi'}{\partial t'} = -\frac{1}{2}\Delta'\Psi' + V_0'\Psi' + g'|\Psi'|^2\Psi'\,,$$

where $V_0' = \frac{V_0}{E_0}$ and $g' = \frac{gN}{\xi^3E_0}$. □

1.7 Sound waves

In the Section 1.4 we have seen that the condensate described by the GPE can be seen as a special kind of fluid, similar to the idealized Euler fluid without viscosity. The dynamics of the condensate exhibits a variety of interesting time-dependent phenomena, from sound waves to vortices. Of particular relevance is the study of perturbations of the ground state, both in the homogeneous and in the presence of a trapping potential, including the analysis of sound waves.

Definition 1.7.1. *Consider a Bose–Einstein condensate.* **Sound waves** *are small-lengthscale density perturbations of the ground state which oscillate periodically.*

We now derive the behaviour of these perturbations for a homogeneous and a trapped condensate.

1.7.1 Homogeneous condensate

First of all we derive the expression of the Bogoliuv dispersion relation.

Theorem 1.7.1 (Bogoliubov dispersion relation)**.** *Consider a Bose–Einstein condensate in the absence of an external potential. Let* $\psi_0 = \sqrt{\frac{\mu}{g}}$ *be the uniform stationary state of the condensate. Small excitations around this state have the angular frequency*

$$\omega(k) = \sqrt{\left(\frac{\hbar k^2}{2m}\right)^2 + \frac{gn_0}{m}k^2}\,, \tag{1.89}$$

which is known as the dispersion relation *or the* Bogoliubov dispersion relation*. It relates the wave's angular frequency* ω *to its wavenumber* $k = |\mathbf{k}| = \sqrt{k_x^2 + k_y^2 + k_z^2}$*, where* $\mathbf{k}$ *is the wave vector, or its period* $\frac{2\pi}{\omega}$ *to its wavelength* $\frac{2\pi}{k}$*.*

Proof. First of all, the governing equation of motion is (1.46), where the chemical potential μ is introduced to fix the average particle number and to remove the trivial global phase evolution of the condensate, so that stationary states become time-independent in this frame:

$$\mathrm{i}\hbar\frac{\partial\psi}{\partial t} = -\frac{\hbar^2}{2m}\Delta\psi + g|\psi|^2\psi + V\psi - \mu\psi\,.$$

Now, we take $V = 0$, the GPE becomes,

$$\mathrm{i}\hbar\frac{\partial\psi}{\partial t} = -\frac{\hbar^2}{2m}\Delta\psi + g|\psi|^2\psi - \mu\psi\,. \tag{1.90}$$

We know that the steady solution of this equation is the uniform state $\psi_0 = \sqrt{\frac{\mu}{g}}$ with number density $n_0 = |\psi_0|^2 = \frac{\mu}{g}$. We perturb this uniform state by assuming a wavefunction with the form,

$$\psi(\mathbf{r}, t) = \psi_0 + \varepsilon\psi_1(\mathbf{r}, t) + \varepsilon^2\psi_2(\mathbf{r}, t) + \cdots\,, \tag{1.91}$$

where $\varepsilon \ll 1$ is a small parameter and the functions ψ_1, ψ_2, etc must be determined. Substituting (1.91) into terms of (1.90), noting that the temporal and spatial derivatives of the steady uniform background ψ_0 are zero, and neglecting the term which are quadratic or of higher order in ε, we have,

$$\mathrm{i}\hbar\frac{\partial\psi}{\partial t} = \mathrm{i}\hbar\frac{\partial(\psi_0+\varepsilon\psi_1)}{\partial t} = \mathrm{i}\hbar\varepsilon\frac{\partial\psi_1}{\partial t} \tag{1.92}$$

$$-\frac{\hbar^2}{2m}\Delta\psi = -\frac{\hbar^2}{2m}\Delta(\psi_0+\varepsilon\psi_1) = -\frac{\hbar^2}{2m}\varepsilon\Delta\psi_1 \tag{1.93}$$

$$\begin{aligned} g|\psi|^2\psi &= g(\psi_0+\varepsilon\psi_1)(\psi_0+\varepsilon\psi_1)^*(\psi_0+\varepsilon\psi_1) \\ &= g(\psi_0^2+\varepsilon(\psi_0\psi_1^*+\psi_0\psi_1))(\psi_0+\varepsilon\psi_1) \\ &= g(n_0+\varepsilon(\psi_0\psi_1^*+\psi_0\psi_1))(\psi_0+\varepsilon\psi_1) \\ &= gn_0\psi_0 + gn_0\varepsilon\psi_1 + g\varepsilon\psi_0^2\psi_1^* + g\varepsilon\psi_0^2\psi_1 \\ &= \mu\psi_0 + \varepsilon\mu(2\psi_1+\psi_1^*) \end{aligned} \tag{1.94}$$

$$\mu\psi = \mu(\psi_0+\varepsilon\psi_1)\,. \tag{1.95}$$

Substituting Eqs. (1.92),(1.93),(1.94),(1.95) into (1.90), we get

$$\begin{aligned} \mathrm{i}\hbar\varepsilon\frac{\partial\psi_1}{\partial t} &= -\frac{\hbar^2}{2m}\varepsilon\Delta\psi_1 + \mu\psi_0 + \varepsilon\mu(2\psi_1+\psi_1^*) - \mu(\psi_0+\varepsilon\psi_1) \\ \mathrm{i}\hbar\varepsilon\frac{\partial\psi_1}{\partial t} &= -\frac{\hbar^2}{2m}\varepsilon\Delta\psi_1 + \varepsilon\mu\psi_1 + \varepsilon\mu\psi_1^*\,. \end{aligned}$$

We divided the last equation by ε, to obtain

$$\mathrm{i}\hbar\frac{\partial\psi_1}{\partial \mathrm{t}} = -\frac{\hbar^2}{2m}\Delta\psi_1 + \mu\psi_1^* + \mu\psi_1\,. \tag{1.96}$$

This is the linearized equation of motion for the perturbations. We look for travelling wave solutions of the general form,

$$\psi_1(x,t) = Ae^{\mathrm{i}(\mathbf{k}\cdot\mathbf{r}-\omega t)} + B^*e^{-\mathrm{i}(\mathbf{k}\cdot\mathbf{r}-\omega t)}\,, \tag{1.97}$$

where A and B are complex amplitudes which depend on the initial condition, $\mathbf{k}$ is the wave vector, $k = |\mathbf{k}| = \sqrt{k_x^2+k_y^2+k_z^2}$ is the wavenumber and ω is the angular frequency of the wave. Substituting (1.97) into the terms of (1.96) we have

$$\frac{\partial\psi_1}{\partial t} = -\mathrm{i}\omega Ae^{\mathrm{i}(\mathbf{k}\cdot\mathbf{r}-\omega t)} + \mathrm{i}\omega B^*e^{-\mathrm{i}(\mathbf{k}\cdot\mathbf{r}-\omega t)} \tag{1.98}$$

$$\nabla\psi_1 = \mathrm{i}\mathbf{k}Ae^{\mathrm{i}(\mathbf{k}\cdot\mathbf{r}-\omega t)} - \mathrm{i}\mathbf{k}B^*e^{-\mathrm{i}(\mathbf{k}\cdot\mathbf{r}-\omega t)} \tag{1.99}$$

$$\Delta\psi_1 = -|\mathbf{k}|^2Ae^{\mathrm{i}(\mathbf{k}\cdot\mathbf{r}-\omega t)} - |\mathbf{k}|^2B^*e^{-\mathrm{i}(\mathbf{k}\cdot\mathbf{r}-\omega t)} \tag{1.100}$$

$$\psi_1^* = A^*e^{-\mathrm{i}(\mathbf{k}\cdot\mathbf{r}-\omega t)} + Be^{\mathrm{i}(\mathbf{k}\cdot\mathbf{r}-\omega t)}\,. \tag{1.101}$$

Then, we substitute Eqs. (1.97), (1.98),(1.99),(1.100),(1.101) into (1.96), getting

$$\begin{aligned} \mathrm{i}\hbar\left(-\mathrm{i}\omega Ae^{\mathrm{i}(\mathbf{k}\cdot\mathbf{r}-\omega t)} + \mathrm{i}\omega B^*e^{-\mathrm{i}(\mathbf{k}\cdot\mathbf{r}-\omega t)}\right) &= -\frac{\hbar^2}{2m}\left(-|\mathbf{k}|^2Ae^{\mathrm{i}(\mathbf{k}\cdot\mathbf{r}-\omega t)} - |\mathbf{k}|^2B^*e^{-\mathrm{i}(\mathbf{k}\cdot\mathbf{r}-\omega t)}\right) \\ &\quad + \mu\left(Ae^{\mathrm{i}(\mathbf{k}\cdot\mathbf{r}-\omega t)} + B^*e^{-\mathrm{i}(\mathbf{k}\cdot\mathbf{r}-\omega t)}\right) \\ &\quad + \mu\left(A^*e^{-\mathrm{i}(\mathbf{k}\cdot\mathbf{r}-\omega t)} + Be^{\mathrm{i}(\mathbf{k}\cdot\mathbf{r}-\omega t)}\right)\,. \end{aligned} \tag{1.102}$$

We equal the similar terms to have the following system,

$$\begin{cases} -\mathrm{i}^2\hbar\omega A = \frac{\hbar^2|\mathbf{k}|^2}{2m}A + \mu B + \mu A \\ \mathrm{i}^2\hbar\omega B^* = \frac{|\mathbf{k}|^2\hbar^2}{2m}B^* + \mu A^* + \mu B^* \end{cases} \Rightarrow \begin{cases} \hbar\omega A = \frac{\hbar^2|\mathbf{k}|^2}{2m}A + \mu B + \mu A \\ \hbar\omega B^* = -\frac{|\mathbf{k}|^2\hbar^2}{2m}B^* - \mu A^* - \mu B^* \,. \end{cases} \tag{1.103}$$

This is equivalent to solve,

$$\begin{pmatrix} \frac{\hbar^2|\mathbf{k}|^2}{2m} + \mu & \mu \\ -\mu & -\left(\frac{\hbar^2|\mathbf{k}|^2}{2m} + \mu\right) \end{pmatrix} \begin{pmatrix} A \\ B^* \end{pmatrix} = \hbar\omega \begin{pmatrix} A \\ B^* \end{pmatrix} . \tag{1.104}$$

The (1.104) admits solutions if and only if

$$\det \begin{pmatrix} \frac{\hbar^2|\mathbf{k}|^2}{2m} + \mu - \hbar\omega & \mu \\ -\mu & -\left(\frac{\hbar^2|\mathbf{k}|^2}{2m} + \mu + \hbar\omega\right) \end{pmatrix} = 0 \,. \tag{1.105}$$

We do computations, to have

$$\begin{aligned} &-\frac{\hbar^4|\mathbf{k}|^4}{4m^2} - \mu\frac{\hbar^2|\mathbf{k}|^2}{2m} - \frac{\hbar^3|\mathbf{k}|^2}{2m}\omega - \mu\frac{\hbar^2|\mathbf{k}|^2}{2m} - \mu^2 - \mu\hbar\omega + \frac{\hbar^3|\mathbf{k}|^2\omega}{2m}| + \mu\hbar\omega + \hbar^2\omega^2 + \mu^2 = 0 \\ &-\frac{\hbar^4|\mathbf{k}|^4}{4m^2} - \mu\frac{\hbar^2|\mathbf{k}|^2}{m} + \hbar^2\omega^2 = 0 \\ &\omega^2 = \frac{\hbar^2|\mathbf{k}|^4}{4m^2} + \frac{\mu|\mathbf{k}|^2}{m} \,. \end{aligned}$$

We substitute $\mu = n_0 g$, to find that non-trivial (non-zero) solutions of (1.96) for A and B exist only if

$$\omega = \sqrt{\left(\frac{\hbar|\mathbf{k}|^2}{2m}\right)^2 + \frac{n_0 g}{m}|\mathbf{k}|^2} \,. \tag{1.106}$$

□

Remark 5. For repulsive interactions ($g > 0$), we have that:

- in the limit of large k (i.e. short waves), the wave behaves like a free particle ($\omega \sim k^2$);
- in the limit of small k (i.e. long waves), the k^4 term in the dispersion relation (1.89) is negligible and w is linear in k. This linear behaviour is characteristic of sound waves, and the angular frequencies are real. The phase velocity of the sound waves is

$$\mathbf{v}_{ph} := \frac{\omega}{k} \approx \sqrt{\frac{n_0 g}{m}} \,,$$

  which is approximately constant for all wavelengths.

Hence, we can define the speed of sound in the case of a homogeneous condensate.

Definition 1.7.2. *The speed of sound in a homogeneous condensate ($V = 0$) is defined as*

$$C := \sqrt{\frac{n_0 g}{m}}\,, \tag{1.107}$$

and it is called **Bogoliubov velocity**.

Now we can analyze the behavior of the sound waves in the case of a homogeneous condensate.

Proposition 1.7.2. *Consider a homogeneous Bose–Einstein condensate ($V = 0$). Let $n_0 = \frac{\mu}{g}$ be the state of uniform density of the condensate. By perturbing this state, we obtain the wave equation*

$$\frac{\partial^2}{\partial t}\delta n(\mathbf{r},t) = C^2 \Delta \delta n(\mathbf{r},t) \tag{1.108}$$

where $\delta n(\mathbf{r},t) = n(\mathbf{r},t) - n_0$ s.t. $\delta n(\mathbf{r},t) \ll n_0$ are density perturbations about the background condensate and $C = \sqrt{\frac{n_0 g}{m}}$.

Proof. First of all we assume $V = 0$ and that we are in the limit of long waves, that is the wavelength is much larger than the healing length. Hence we can neglect the quantum pressure term in (1.60). The motion is described by the corresponding hydrodynamic equations which take the form

$$\begin{cases} \frac{\partial}{\partial t} + \nabla \cdot (n(\mathbf{r},t)\mathbf{v}(\mathbf{r},t)) = 0\,, \\ m\frac{\partial \mathbf{v}(\mathbf{r},t)}{\partial t} = -\nabla\left(\frac{1}{2}m\mathbf{v}(\mathbf{r},t)^2 + g n(\mathbf{r},t)\right). \end{cases} \tag{1.109}$$

Then we perturb the state of uniform density $n = n_0 = \frac{\mu}{g}$ and we apply the following linearization

$$\begin{aligned} n(\mathbf{r},t) &= n_0 + \delta n(\mathbf{r},t) \\ \mathbf{v}(\mathbf{r},t) &= 0 + \delta \mathbf{v}(\mathbf{r},t)\,, \end{aligned}$$

where $\delta n(\mathbf{r},t) \ll n_0$ are density perturbations about the background homogeneous condensate. Substituting the linearization into the hydrodynamics equations (1.109) we obtain

$$\begin{aligned} \frac{\partial (n_0 + \delta n)}{\partial t} + \nabla \cdot ((n_0 + \delta n)\delta \mathbf{v})) &= 0 \\ \frac{\partial \delta n}{\partial t} + n_0 \nabla \cdot (\delta \mathbf{v}) &= 0\,, \end{aligned} \tag{1.110}$$

and

$$\begin{aligned} m\frac{\partial \delta \mathbf{v}(\mathbf{r},t)}{\partial t} &= -\nabla\left(\frac{1}{2}m\delta\mathbf{v}(\mathbf{r},t)^2 + g(n_0 + \delta n(\mathbf{r},t))\right) \\ m\frac{\partial \delta \mathbf{v}(\mathbf{r},t)}{\partial t} &= -\nabla\Big(g n_0 + g\delta n(\mathbf{r},t)\Big) \\ \frac{\partial \delta \mathbf{v}(\mathbf{r},t)}{\partial t} &= -\frac{g}{m}\nabla \delta n(\mathbf{r},t)\,. \end{aligned} \tag{1.111}$$

If take the time derivative of (1.110) and substituting expression (1.111) we have

$$\begin{aligned}
\frac{\partial^2 \delta n(\mathbf{r},t)}{\partial t} + n_0 \nabla \cdot \left(\frac{\partial \delta \mathbf{v}(\mathbf{r},t)}{\partial t} \right) &= 0 \\
\frac{\partial^2 \delta n(\mathbf{r},t)}{\partial t} + n_0 \nabla \cdot \left(-\frac{g}{m} \nabla \delta n(\mathbf{r},t) \right) &= 0 \\
\frac{\partial^2 \delta n(\mathbf{r},t)}{\partial t} - \frac{g n_0}{m} \nabla \cdot \left(\nabla \delta n(\mathbf{r},t) \right) &= 0 \\
\frac{\partial^2 \delta n(\mathbf{r},t)}{\partial t} &= \frac{g n_0}{m} \Delta \delta n(\mathbf{r},t)\,.
\end{aligned}$$

□

Hence in the case of a homogeneous condensate the solutions of (1.108) are sound waves propagating with the Bogoliubov velocity $C = \sqrt{\frac{g n_0}{m}}$.

1.7.2 Trapped condensate

We now analyze the behaviour of sound waves in a trapped condensate. We first recall the Thomas–Fermi approximation, which is useful for studying sound waves in this context.

Definition 1.7.3. *The* **Thomas–Fermi approximation** *consists in neglecting the kinetic energy term in the time-independent GPE* (1.41) *leading to*

$$\begin{aligned}
&V(\mathbf{r})\Psi_{TF}(\mathbf{r}) + g|\Psi_{TF}(\mathbf{r})|^2 \Psi_{TF}(\mathbf{r}) = \mu \Psi_{TF}(\mathbf{r}) \\
&\iff (V(\mathbf{r}) + g|\Psi_{TF}(\mathbf{r})|^2 - \mu_{TF})\Psi_{TF}(\mathbf{r}) = 0\,,
\end{aligned}$$

where the "TF" denotes that we are considering the Thomas–Fermi approximation. Introducing the Thomas-Fermi density $n_{TF}(\mathbf{r}) = |\Psi_{TF}(\mathbf{r})|^2$, the last equation becomes

$$(V(\mathbf{r}) + g n_{TF}(\mathbf{r}) - \mu_{TF})\Psi_{TF}(\mathbf{r}) = 0\,.$$

Hence there are two cases:

- *if $\Psi_{TF}(\mathbf{r}) = 0$, then $n(\mathbf{r})_{TF} = 0$;*
- *if $\Psi(\mathbf{r})_{TF} \neq 0$, then $n(\mathbf{r})_{TF} = \frac{\mu_{TF} - V(\mathbf{r})}{g}$. Since $n_{TF}(\mathbf{r}) \geq 0$, we have*

$$n_{TF}(\mathbf{r}) = \begin{cases} \dfrac{\mu_{TF} - V(\mathbf{r})}{g} & \text{if} \quad \mu_{TF} > V(\mathbf{r})\,, \\ 0 & \text{if} \quad \mu_{TF} \leq V(\mathbf{r})\,. \end{cases} \tag{1.112}$$

In the following Theorem we analyze the phenomenon of sound waves in a trapped condensate.

Theorem 1.7.3. *Let $n(\mathbf{r})$ the equilibrium configuration of the density profile of a trapped Bose Einstein condensate (V_0 constant). If we consider $\delta n(\mathbf{r},t) = n(\mathbf{r},t) - n(\mathbf{r})$ the change of the density profile with respect to the equilibrium configuration $n(\mathbf{r})$, then $\delta n(\mathbf{r},t)$ satisfies the wave equation*

$$\frac{\partial^2 \delta n}{\partial t} = \nabla \cdot \left[c(\mathbf{r})^2 \nabla \delta n \right] , \tag{1.113}$$

with $c^2(\mathbf{r}) = \frac{gn(\mathbf{r})}{m}$.

Proof. First we neglect the quantum pressure term in (1.60) (this is known as the Thomas-Fermi approximation (see [7])), obtaining

$$m\frac{\partial \mathbf{v}(\mathbf{r},t)}{\partial t} + \nabla\left(\frac{1}{2}m\mathbf{v}(\mathbf{r},t)^2 + V_0 + gn(\mathbf{r},t)\right) = 0\,. \tag{1.114}$$

Then we apply the linearization

$$n(\mathbf{r},t) = n(\mathbf{r}) + \delta n(\mathbf{r},t) \tag{1.115}$$
$$\mathbf{v}(\mathbf{r},t) = 0 + \delta \mathbf{v}(\mathbf{r},t)\,, \tag{1.116}$$

and we substitute expression (1.115) and (1.116) into (1.114), neglecting the terms of quadratic order

$$\begin{aligned} m\frac{\partial \delta\mathbf{v}(\mathbf{r},t)}{\partial t} + \nabla\left(\frac{1}{2}m\delta\mathbf{v}(\mathbf{r},t)^2 + V_0 + g(n(\mathbf{r}) + \delta n(\mathbf{r},t))\right) &= 0 \\ m\frac{\partial \delta\mathbf{v}(\mathbf{r},t)}{\partial t} + \nabla\left(V_0 + gn(\mathbf{r}) + g\delta n(\mathbf{r},t)\right) &= 0\,. \end{aligned}$$

Then we recognize the expression (1.112) $\mu_{\mathrm{TF}} = V_0 + gn(\mathbf{r})$, so we have

$$\begin{aligned} m\frac{\partial \delta\mathbf{v}(\mathbf{r},t)}{\partial t} + \nabla\left(\mu_{TF} + g\delta n(\mathbf{r},t)\right) &= 0 \\ m\frac{\partial \delta\mathbf{v}(\mathbf{r},t)}{\partial t} + \nabla\left(g\delta n(\mathbf{r},t)\right) &= 0 \\ m\frac{\partial \delta\mathbf{v}(\mathbf{r},t)}{\partial t} + g\nabla\left(\delta n(\mathbf{r},t)\right) &= 0 \\ \frac{\partial \delta\mathbf{v}(\mathbf{r},t)}{\partial t} &= -\frac{g}{m}\nabla\left(\delta n(\mathbf{r},t)\right), \end{aligned} \tag{1.117}$$

where we know that $\nabla\mu_{\mathrm{TF}} = 0$. Now we substitute expression (1.115) and (1.116) into (1.52), neglecting again the terms of quadratic order, leading to

$$\begin{aligned} \frac{\partial(n(\mathbf{r}) + \delta n(\mathbf{r},t))}{\partial t} + \nabla\cdot((n(\mathbf{r}) + \delta n(\mathbf{r},t))\delta\mathbf{v}(\mathbf{r},t)) &= 0 \\ \frac{\partial \delta n(\mathbf{r},t)}{\partial t} + \nabla\cdot(n(\mathbf{r})\delta\mathbf{v}(\mathbf{r},t)) &= 0 \end{aligned} \tag{1.118}$$

We take the time derivative of the linearized continuity equation (1.118) and we get

$$\frac{\partial^2 \delta n(\mathbf{r},t)}{\partial t^2} + \nabla \cdot \left(n(\mathbf{r}) \frac{\partial \delta \mathbf{v}(\mathbf{r},t)}{\partial t} \right) = 0 \,.$$

Finally we substitute expression (1.117) into the last equation yielding to

$$\begin{aligned}
\frac{\partial^2 \delta n(\mathbf{r},t)}{\partial t^2} + \nabla \cdot \left(n(\mathbf{r}) \left(-\frac{g}{m} \nabla \left(\delta n(\mathbf{r},t) \right) \right) \right) &= 0 \\
\frac{\partial^2 \delta n(\mathbf{r},t)}{\partial t^2} + \nabla \cdot \left(-\frac{n(\mathbf{r}) g}{m} \nabla \left(\delta n(\mathbf{r},t) \right) \right) &= 0 \\
\frac{\partial^2 \delta n(\mathbf{r},t)}{\partial t^2} &= \nabla \cdot \left(\frac{n(\mathbf{r}) g}{m} \nabla \left(\delta n(\mathbf{r},t) \right) \right) \\
\frac{\partial^2 \delta n(\mathbf{r},t)}{\partial t^2} &= \nabla \cdot \left(c^2(\mathbf{r}) \nabla \left(\delta n(\mathbf{r},t) \right) \right) .
\end{aligned}$$

□

We observe that the validity of Eqs. (1.113) is based on the assumption that spatial variations of the density are smooth both in the ground state and during the oscillations.

Hence the sound waves are described as solutions of the linear wave equation governing small density perturbations of the condensate density and the quantity $c(\mathbf{r})$ has the clear meaning of a local sound velocity. Thus we can give the following.

Definition 1.7.4. *Consider a trapped Bose–Einstein condensate. The local* **speed of sound** $c(\mathbf{r})$ *is defined as the coefficient in the linear wave equation* (1.113) *that is*

$$c(\mathbf{r}) := \sqrt{\frac{g n(\mathbf{r})}{m}} \,.$$

We notice that in a trapped condensate the speed of sound will vary with the position due to the spatial dependence of the density and it is less near the edge of the condensate where the density tends to zero.

Chapter 2

Quantum vortices

In this chapter we describe the quantum vortices, their form and their key properties. First, we give the definition of a quantum vortex.

Definition 2.0.1. *Let $D \subset \mathbb{R}^d$, $d = 2, 3$, and let $\Psi \in L^2(D \times \mathbb{R}, \mathbb{C})$ be the wavefunction of a Bose–Einstein condensate. Let us consider the Madelung decomposition of Ψ:*

$$\Psi(\mathbf{r}, t) = \sqrt{n(\mathbf{r}, t)}\, e^{i\theta(\mathbf{r},t)}, \qquad n(\mathbf{r}, t) = |\Psi(\mathbf{r}, t)|^2,$$

where the phase $\theta(\mathbf{r}, t)$ is defined on $\Omega = D \setminus \mathcal{Z}(t)$, with

$$\mathcal{Z}(t) := \{\mathbf{r} \in D : \Psi(\mathbf{r}, t) = 0\}.$$

A **quantum vortex** *is a connected component of $\mathcal{Z}(t)$ such that, for any simple closed curve $\mathcal{C} \subset D \setminus \mathcal{Z}(t)$ enclosing exactly one component of $\mathcal{Z}(t)$, the phase $\theta(\mathbf{r}, t)$ has integer degree, namely*

$$\frac{1}{2\pi} \oint_{\mathcal{C}} \nabla\theta(\mathbf{r}, t) \cdot d\mathbf{l} = q, \qquad q \in \mathbb{Z}.$$

The integer q is called the **charge** *of the vortex.*

2.1 Properties of quantum fluids

In the following proposition we analyze some important properties of quantum fluids in order to deduce the relevant features of quantum vortices.

Proposition 2.1.1. *A quantum fluid has the following properties:*

(i) it is a viscosity-free (inviscid) fluid;

(ii) the circulation is quantized;

(iii) its flow is irrotational.

Proof. (i) The superfluid hydrodynamic equations (1.52) and (1.53) contain no viscous term. Hence a Bose–Einstein condensate is an inviscid fluid and there is no viscosity to slow down the flow and bring it to a stop.

(ii) We consider the condensate wavefunction

$$\Psi(\mathbf{r},t) = R(\mathbf{r},t)e^{\mathrm{i}\theta(\mathbf{r},t)}$$

where $R(\mathbf{r},t)$ is the amplitude and $\theta(\mathbf{r},t)$ is the phase. Let $\mathcal{C}$ be a simple closed path of arbitrary shape through a region of the condensate. The integrated change in the phase is

$$\Delta\theta = \oint_{\mathcal{C}} \nabla\theta \cdot d\boldsymbol{\ell} \tag{2.1}$$

where the vector $d\boldsymbol{\ell}$ is the line element of integration. Let Ψ_0 and Ψ_1 denote the wavefunction evaluated at the starting and final points of $\mathcal{C}$, respectively. Since the two points are the same and Ψ must be single-valued, the condition $\Psi_1 = \Psi_0$ means that,

$$Re^{i\theta_1} = Re^{i\theta_0} \quad \Longrightarrow \quad e^{i(\theta_1-\theta_0)} = 1\,,$$

which implies

$$\Delta\theta = 2\pi q \quad q = 0, \pm1, \pm2, \dots\ . \tag{2.2}$$

A non-zero value of q precludes the existence of a globally single-valued phase field on the region enclosed by $\mathcal{C}$. Therefore, consistency with the single-valuedness of Ψ requires the presence of at least one point where $R = 0$ and consequently $\Psi = 0$. Recalling that the phase distribution defines the fluid's velocity via

$$\mathbf{v} = \left(\frac{\hbar}{m}\right)\nabla\theta\,, \tag{2.3}$$

eq. (2.2) implies that the circulation Γ around the path $\mathcal{C}$ is either 0 or a multiple of the quantum of circulation $\kappa = \frac{\hbar}{m}$,

$$\Gamma = \oint_{\mathcal{C}} \mathbf{v}\cdot d\boldsymbol{\ell} = \oint_{\mathcal{C}} \left(\frac{\hbar}{m}\right)\nabla\theta\cdot d\boldsymbol{\ell} = \frac{\hbar}{m}\oint_{\mathcal{C}} \nabla\theta\cdot d\boldsymbol{\ell} = \frac{\hbar}{m}2\pi q = q\kappa\,. \tag{2.4}$$

(iii) The vorticity field $\omega = \nabla\times\mathbf{v}$ trivially vanishes by using the expression of $\mathbf{v}$ in (2.3)

$$\nabla\times\left(\frac{\hbar}{m}\nabla\theta\right) = 0\,. \tag{2.5}$$

□

In the following remark we point out some features of the quantized vortices.

Remark 6.

1. A key feature of quantized vortices is the quantization of the circulation (2.4), which distinguishes condensate flow from that of ordinary fluids where the circulation can take arbitrary values.

2. Consider the simple case of 2-dimensional flow in the xy plane. Assume that q in (2.2) does not vanish and that the path $\mathcal{C}$ is a circle of radius r centered at the singularity. Using polar coordinates (r, ϑ), the line element is $d\boldsymbol{\ell} = rd\theta\hat{e}_\vartheta$, where $\hat{e}_\vartheta$ is the unit vector in the azimuthal direction ϑ. Then the circulation becomes,

$$\Gamma = \oint_{\mathcal{C}} \mathbf{v} \cdot d\boldsymbol{\ell} = \oint_0^{2\pi} r\mathbf{v} \cdot \hat{\mathbf{e}}_\vartheta d\vartheta = 2\pi r v_\vartheta \,. \tag{2.6}$$

If we compare (2.6) with (2.4), we obtain the fluid's azimuthal speed around the singularity

$$v_\vartheta = \frac{q\kappa}{2\pi r} = \frac{q}{2\pi r}\frac{h}{m} = \frac{q}{2\pi r}\frac{2\pi\hbar}{m} = \frac{q\hbar}{rm} \,. \tag{2.7}$$

From (2.7) we can deduce that:

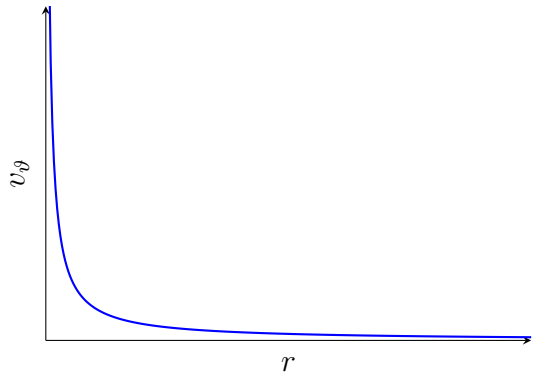

Figure 2.1: Plot of the velocity $v_\vartheta = \frac{q\hbar}{rm}$.

(a) if $q \neq 0$ the velocity around the singularity (see Figure 2.1)
- decreases to zero at infinity ($v_\vartheta \to 0$ as $r \to \infty$)
- diverges approaching the singularity ($v_\vartheta \to \infty$ as $r \to 0$) and the flow becomes faster and faster;

(b) if we increase q, the flow speed increases discontinuously, because q takes only discrete values. The sign of q determines the direction of the flow (clockwise or anticlockwise) around the singularity.

We have a clearer picture of the nature of the singularity because it is a quantized vortex line, a whirlpool in the fluid.

3. We have seen that the flow of a condensate is irrotational. Physically it means that a fluid element that circulates around the axis of a vortex line does not undergo any local rotation, (as it does in solid body rotation), but preserves its orientation. Nevertheless, the singularity itself contributes to the vorticity according to

$$\omega = \kappa\delta^2(\mathbf{r})\hat{\mathbf{e}}_z \,,$$

where $\delta^2(\mathbf{r})$ is the 2-dimensional delta function. It may seem paradoxical that a quantum vortex has zero vorticity. The crucial point is that, while the condensate

flow is irrotational, isolated vortex line singularities are allowed. In classical fluids, the vorticity ω can take arbitrary values, allowing vortices to differ in strength and spatial extent. In a condensate, by contrast, (2.4) imposes a strict quantum-mechanical constraint: the flow around a singularity is characterized by fixed form and intensity.

2.2 Vortex line and vortex ring

We now give the definitions of the main forms and structures of quantum vortices (see Figure 2.2).

Definition 2.2.1. *A* **quantum vortex line** *is a quantum vortex whose nodal set component $Z(t)$ is, for each t, a connected 1-dimensional curve in $\Omega = D \setminus \mathcal{Z}(t)$. The vortex core is the tubular neighborhood of radius a_0 around the curve:*

$$Core(t) := \{\mathbf{r} \in \Omega : \mathrm{dist}(\mathbf{r}, \mathcal{Z}(t)) \leq a_0\}\,.$$

Here, $Z(t)$ represents the axis of the vortex, while $Core(t)$ is the physical tubular region around it where the density is depleted.

Definition 2.2.2. *A* **straight quantum vortex line** *is a quantum vortex line whose axis $Z(t)$ is a straight line in $\mathbb{R}^3$ for all times t. The vortex core radius a_0 is constant.*

Definition 2.2.3. *A* **quantum vortex filament** *is the geometric representation of a quantum vortex line as an oriented 1-dimensional curve, neglecting the finite size of the core radius a_0. The filament approximation assumes that the core radius is much smaller than the local radius of curvature and the filament's length.*

Definition 2.2.4. *A* **quantum vortex ring** *is a vortex line that closes on itself to form a loop diffeomorphic to a circle.*

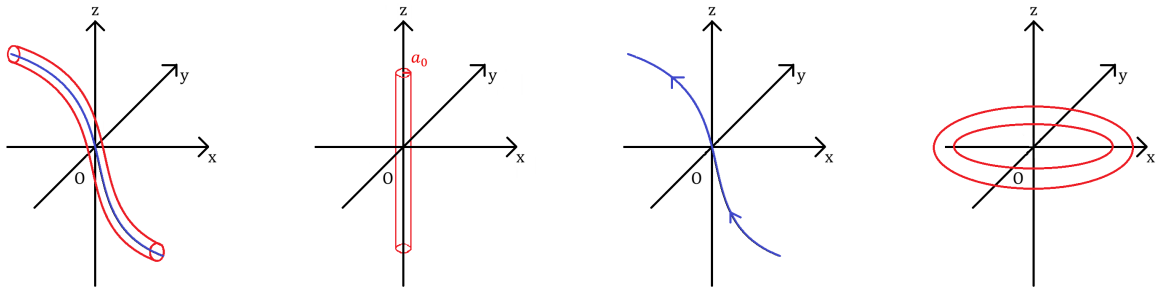

Figure 2.2: First: quantum vortex line. Second: quantum straight vortex line. Third: quantum vortex filament. Fourth: quantum vortex ring. Figure adapted from [5].

The motion of a vortex filament is governed by the velocity field induced by the vorticity through the Biot–Savart law.

Definition 2.2.5 (Biot–Savart law and vortex filament representation)**.** *Let us consider a* $3-$dim *unbounded domain where the velocity vanishes at infinity and let* $\boldsymbol{\omega}$ *be the vorticity field of an incompressible fluid at a point* $\mathbf{r}^*$*. The velocity field at a point* $\mathbf{r}$ *is given by the* **Biot–Savart law** *[16]*

$$\mathbf{v}_{BSL}(\mathbf{r}) = \frac{1}{4\pi}\int_{\mathbb{R}^3} \frac{\boldsymbol{\omega}(\mathbf{r}^*)\times(\mathbf{r}-\mathbf{r}^*)}{|\mathbf{r}-\mathbf{r}^*|^3}\, d\mathbf{r}^*\,. \tag{2.8}$$

For a vortex filament, where the vorticity is concentrated along a smooth curve $\mathcal{C}$ *carrying circulation* Γ*, the* **Biot–Savart law** *reduces to the* **filament form**

$$\mathbf{v}_{BSL}(\mathbf{r}) = \frac{\Gamma}{4\pi}\oint_{\mathcal{C}} \frac{d\boldsymbol{\ell}(\mathbf{r}^*)\times(\mathbf{r}-\mathbf{r}^*)}{|\mathbf{r}-\mathbf{r}^*|^3}\,, \tag{2.9}$$

where $d\boldsymbol{\ell}$ *is the infinitesimal vector element.*

The evaluation of (2.9) at points close to the filament axis leads to a singular velocity field; by retaining only the dominant local contribution of the Biot–Savart integral, one obtains the so-called Localized Induction Approximation (LIA), which provides a first approximation of the self-induced motion of a quantum vortex filament [15, 16, 17, 18].

Definition 2.2.6. *The self-induced velocity of a quantum vortex filament is described by the* **Localized Induction Approximation** *(***LIA***)*

$$\mathbf{v}_{LIA}(\mathbf{r}) \sim \frac{\Gamma}{2\pi\varepsilon}\hat{\mathbf{e}}_\vartheta + c\hat{\mathbf{b}} \quad as \quad \mathbf{r}\to\mathbf{r}^*\,, \tag{2.10}$$

where Γ *is the vortex circulation,* ε *is the distance of a point* $\mathbf{r}$ *from the vortex axis* $\mathcal{C}$*,* c *is the curvature of the vortex axis ,* $\mathbf{r}^*$ *is a point on the vortex axis and* $\hat{\mathbf{e}}_\vartheta = \hat{\mathbf{n}}\cos(\vartheta) + \hat{\mathbf{b}}\sin(\vartheta)$*, with* $\hat{\mathbf{n}}$ *the unit normal and* $\hat{\mathbf{b}}$ *the unit binormal and* ϑ *the angle between* $\hat{\mathbf{e}}_\vartheta$ *and* $\hat{\mathbf{n}}$ *in the plane normal to the vortex axis.*

Remark 7. We underline the fact that the motion is given by two contributions (see (2.10) and Figure 2.3):

- a rotational motion around the vortex axis;
- a translational motion along the local binormal direction, whose strength is proportional to the local curvature c.

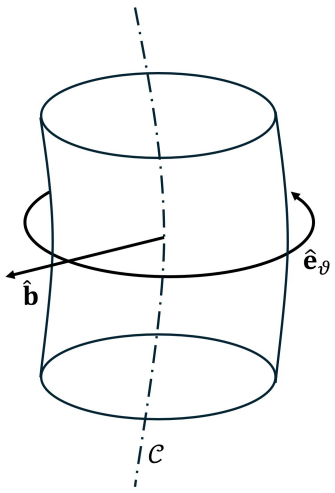

Figure 2.3: Components of the self-induced velocity of a quantum vortex filament described by the Localized Induction Approximation (LIA).

Having introduced the LIA, we can now observe that for a circular vortex ring the curvature is constant and equal to $\frac{1}{R}$. Hence all its elements move with the same binormal velocity, so that the ring travels along a straight line at a constant speed which is inversely proportional to its radius.

2.3 The structure of the vortex core

In this section we study the structure of the vortex in the neighborhood of the axis of the vortex ($r \to 0$) where the velocity becomes infinite (see (2.7)). For the sake of simplicity we consider the case of a straight vertical vortex line (see Section 5.4 of [5]):

Proposition 2.3.1. *Let $D = \{(r, \vartheta, z) \in \mathbb{R}_0^+ \times [0, 2\pi) \times \mathbb{R}\}$ and consider a straight vortex line aligned in the z direction in a Bose-Einstein condensate. Let $\Psi \in L^2(D, \mathbb{C})$ be the wavefunction of the system s.t. $\Psi(r, \vartheta, z) = A(r)e^{\mathrm{i}q\vartheta}$ with $A(r) \in \mathbb{R}$ and $q \in \mathbb{Z}$. The function $A(r)$ satisfies the following radial equation*

$$\mu A(r) = -\frac{\hbar^2}{2m}\frac{1}{r}\frac{d}{dr}\left(r\frac{dA(r)}{dr}\right) + \frac{\hbar^2 q^2}{2mr^2}A(r) + V(r)A(r) + gA^3(r)\,. \tag{2.11}$$

Proof. We work in cylindrical coordinates and consider a straight vortex line aligned along the the z-axis. We assume $\Psi(r, \vartheta, z) = A(r)e^{\mathrm{i}q\vartheta}$ and substituting this ansatz into

the time-independent GPE (1.41) we obtain

$$\mu A(r)e^{\mathrm{i}q\vartheta} = -\frac{\hbar^2}{2m}\Delta(A(r)e^{\mathrm{i}q\vartheta}) + V(r)A(r)e^{\mathrm{i}q\vartheta} + gA(r)e^{\mathrm{i}q\vartheta}A(r)e^{-\mathrm{i}q\vartheta}A(r)e^{\mathrm{i}q\vartheta}$$
$$\mu A(r)e^{\mathrm{i}q\vartheta} = -\frac{\hbar^2}{2m}\frac{1}{r}\frac{\partial}{\partial r}\left(r\frac{\partial}{\partial r}A(r)e^{\mathrm{i}q\vartheta}\right) - \frac{\hbar^2}{2m}\frac{1}{r^2}\frac{\partial^2}{\partial\vartheta^2}\left(A(r)e^{\mathrm{i}q\vartheta}\right) + V(r)A(r)e^{\mathrm{i}q\vartheta} + gA^3(r)e^{\mathrm{i}q\vartheta}$$
$$\mu A(r)e^{\mathrm{i}q\vartheta} = -\frac{\hbar^2}{2m}\frac{1}{r}\frac{d}{dr}\left(r\frac{dA(r)}{dr}e^{\mathrm{i}q\vartheta}\right) - \frac{\hbar^2}{2m}\frac{1}{r^2}(-A(r)q^2e^{\mathrm{i}q\vartheta}) + V(r)A(r)e^{\mathrm{i}q\vartheta} + gA^3(r)e^{\mathrm{i}q\vartheta}$$
$$\mu A(r)\cancel{e^{\mathrm{i}q\vartheta}} = -\frac{\hbar^2}{2m}\frac{1}{r}\frac{d}{dr}\left(r\frac{dA(r)}{dr}\right)\cancel{e^{\mathrm{i}q\vartheta}} + \frac{\hbar^2}{2m}\frac{A(r)q^2}{r^2}\cancel{e^{\mathrm{i}q\vartheta}} + V(r)A(r)\cancel{e^{\mathrm{i}q\vartheta}} + gA^3(r)\cancel{e^{\mathrm{i}q\vartheta}}$$
$$\mu A(r) = -\frac{\hbar^2}{2m}\frac{1}{r}\frac{d}{dr}\left(r\frac{dA(r)}{dr}\right) + \frac{\hbar^2q^2}{2mr^2}A(r) + V(r)A(r) + gA^3(r)\,,$$

where we used

$$\Delta = \frac{1}{r}\frac{\partial}{\partial r}\big(r\frac{\partial}{\partial r}\big) + \frac{1}{r^2}\frac{\partial^2}{\partial\vartheta^2} + \frac{\partial^2}{\partial z^2}$$

and

$$\frac{\partial}{\partial\vartheta}\big(A(r)e^{\mathrm{i}q\vartheta}\big) = A(r)\mathrm{i}qe^{\mathrm{i}q\vartheta} \Rightarrow \frac{\partial^2}{\partial\vartheta^2}\left(A(r)e^{\mathrm{i}q\vartheta}\right) = A(r)\mathrm{i}^2q^2e^{\mathrm{i}q\vartheta}\,.$$

□

The above proposition shows that the Gross–Pitaevskii Equation reduces to a one-dimensional nonlinear differential equation for the radial profile $A(r)$. The term proportional to q^2/r^2 reflects the presence of quantized circulation and is responsible for the vanishing of the condensate density at the vortex core.

We now examine the configuration of a straight vortex line in the case of a homogeneous condensate.

2.3.1 Homogeneous condensate

Consider a straight vortex line in a homogeneous condensate. Eq. (2.11) has no exact solution and it must be solved numerically for $A(r)$. We impose the following boundary conditions

- $A(r) \to 0$ for $r \to 0$,
- $A(r) \to \Psi_0$ for $r \to \infty$.

The corresponding density profile $n(r) = A^2$ is shown in Fig. 2.4 (represented by the solid blue line).

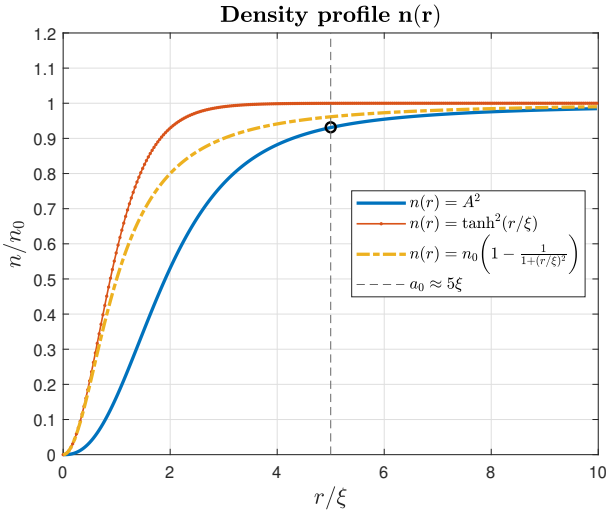

Figure 2.4: Radial density profile $n(r)$ of a $q = 1$ vortex in a homogeneous condensate (solid blue line). Density profile for a static condensate whose density is pinned to zero (orange line with markers). Approximation for a density profile of a single-charged vortex in a homogeneous condensate (dashed yellow line). Figure adapted from [5].

We notice that the axis of the vortex is surrounded by a region where the density is depleted, forming a tube of radius $a_0 \approx 5\xi$, called the ***vortex core radius*** (by convention, the vortex core radius is chosen as the radius where the condensate density reaches roughly $90 - 95\%$ of the background value). Moreover we observe that for small r, the density scales as $r^{|q|}$. Although the velocity diverges for $r \to 0$, the density vanishes, meaning that there are no atoms which move at infinite speed. We can therefore interpret a vortex as a 'hole' surrounded by (quantized) circulation.

Furthermore we recall that in Section 1.5.2 we considered a condensate subject to the external potential defined in expression (1.71). In this setting the condensate is static, since Ψ can be chosen to be real (hence $\nabla S = 0$ and $\mathbf{v} = 0$) and the system is homogeneous in the bulk, where the external potential is constant, while spatial variations of the density occur only in the vicinity of the boundary. Consequently the density relaxes towards its background value following a characteristic $\tanh^2(x/\xi)$ profile.

We then observe that the vortex density profile in the case of a homogeneous potential (solid blue line in Fig. 2.4) is slightly broader than the $\tanh^2(x/\xi)$ profile (orange line with markers in Fig. 2.4) and approaches the background density more gradually. This slower relaxation is due to the kinetic energy of the circulating flow, which generates an outward centrifugal force on the fluid.

A useful approximation for the vortex density profile for a single-charged vortex is given in the following definition [5].

Definition 2.3.1. *An* **analytic approximation for the density profile of a single-charged vortex** *in a homogeneous Bose-Einstein condensate is given by*

$$n(r) = n_0 \left(1 - \frac{1}{1 + r'^2}\right)$$

(see dashed yellow line in Fig. 2.4), where $n_0 = \frac{\mu}{g}$ *is the bulk density far from the vortex and* $r' = r/\xi$*, with* $\xi = \frac{\hbar}{\sqrt{mgn_0}}$ *the healing length.*

Remark 8. We remark that the fact that a vortex line is a 'hole' surrounded by circulating flow has an important mathematical consequence: a condensate with vortices is a multiply-connected region, hence the classical Stokes Theorem does not apply. Nevertheless, the circulation around a closed curve enclosing the vortex can be nonzero.

Remark 9. In a trapped condensate the vortex generates a similar tube surrounded by quantized circulation. The main difference with a homogeneous condensate is that the density is no longer uniform. Hence, since the healing length depends on the local density, the thickness of the vortex core varies with position within the trap.

Chapter 3

Vortex reconnections

Vortex reconnections are observed in the context of plasma physics [40] and both classical [41] and quantum fluids [42, 3]. They play an important role in the transfer of energy in superfluid turbulence, fine-scale mixing of classical fluid turbulence [43], and solar physics [44]. Individual quantum vortex reconnections were first observed in [45] by analyzing the trajectories of solid hydrogen tracers in superfluid ^{4}He. We give the definition of quantum vortex reconnection.

Definition 3.0.1. *[46] A* **quantum vortex reconnection** *is the process through which two quantum vortices cross, each of them breaking into two parts and exchanging part of itself for part of the other. This may lead to a change of topology of the quantum vortices.*

A vortex reconnection follows a scheme reported in Fig. 3.1.

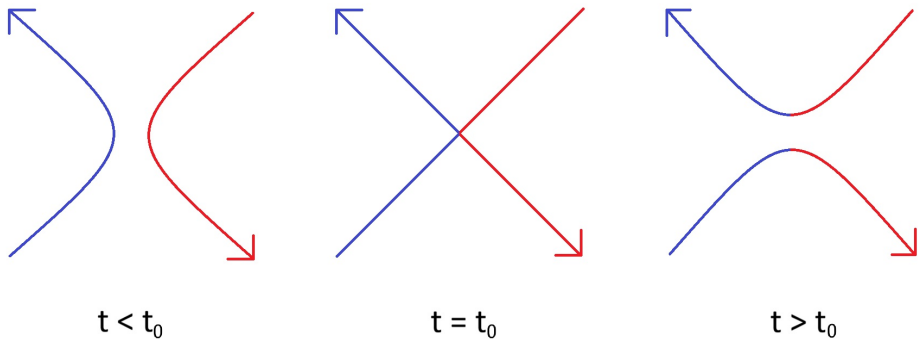

Figure 3.1: Scheme of vortex reconnection between two vortex lines. The arrows indicate the direction of the vorticity (the rotation of the fluid around the axis of the vortex). Left: before the reconnection ($t < t_0$). Middle: at the moment of reconnection ($t = t_0$). Right: after the reconnection ($t > t_0$). Figure adapted from [5].

Vortex reconnections occur in both classical and quantum fluids, although they present some differences

- in classical inviscid fluids, governed by the Euler equation, vortex reconnections are not admissible;
- in classical viscous fluids, governed by Navier-Stokes equations, reconnections are possible by involving energy dissipation;
- in quantum fluids, governed by the GPE, reconnections are possible, by the presence of the quantum pressure term in the GPE, and involve conservation of energy.

3.1 Example of reconnections

In this section we present some reconnection configurations that have been investigated in the literature.

3.1.1 A pair of quantum straight vortex lines

In the case of a pair of straight vortex lines the possible configurations are studied in several works [29, 47, 1, 2, 48]. In the following we summarize the evolution of reconnections depending on the initial relative circulation of the vortices.

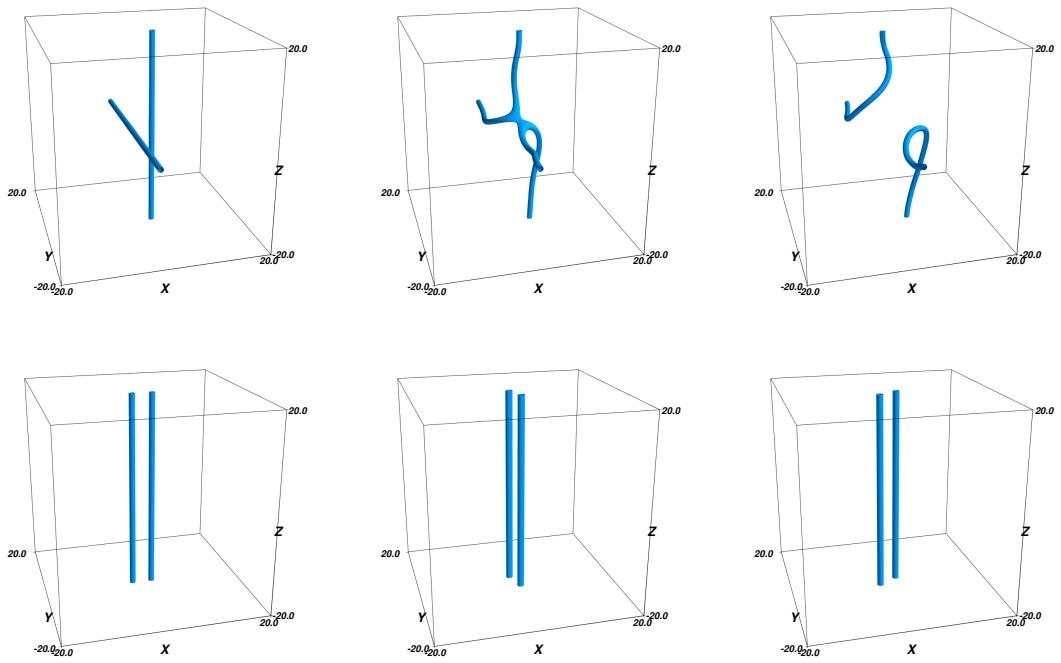

Figure 3.2: First row: reconnection between orthogonal (90°) quantum straight vortex lines. Numerical simulation reproducing the results of [48]. Second row: parallel (0°) quantum straight vortex lines, which do not reconnect but rotate relative to each other.

- Antiparallel (180°) (see Figure 3.2): the vortex lines are locally aligned with opposite circulation. They attract each other, the cores fuse locally, reconnection occurs, and then they separate into a new configuration.

- Orthogonal (90°) (see Figure 3.2): the two vortices locally twist around each other so that, at their point of closest approach, they become anti-parallel. They then approach, reconnect, and subsequently separate again.
- Parallel (0°) (see Figure 3.2): the vortex lines have the same circulation direction. In this case, the vortices do not reconnect; instead, they may rotate around or slide next to each other.
- Intermediate orientations: the reconnection occurs if the vortices are sufficiently close to the antiparallel configuration.

3.1.2 A pair of quantum vortex rings

Various studies investigated reconnections between quantum vortex rings, showing that the outcomes depend strongly on the initial geometry and relative orientation of the rings.

An important work is [20], where the authors investigate the reconnection of two quantum vortex rings with the same radius moving toward each other along the same direction with the axes of propagation offset by an initial distance (see Figure 3.3). As the rings approach, the nearest parts of the vortex rings become locally antiparallel and the vortices stretch in the collision plane. When the cores meet, the local circulation cancels and the lines reconnect, forming two deformed rings. During the reconnection, a rarefaction pulse is generated, which evolves into a sound wave, dissipating part of the vortex energy. The outgoing rings have smaller radii, reflecting the energy loss due to sound emission (see Section 3.2.2).

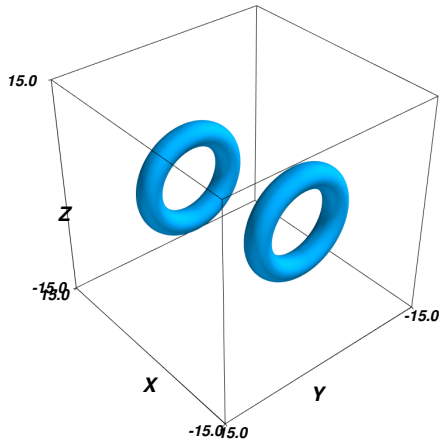

Figure 3.3: Initial configuration of two quantum vortex ring of equal radius with parallel propagation directions and finite lateral offset, a setup that leads to local antiparallel alignment and vortex reconnection accompanied by sound emission.

In [30] two planar vortex rings with the same radius are located on the x-z plane, separated by an initial distance and moving in the positive x direction. During the evolution

the rings interact, forming a pyramidal cusp that trails behind the rest of the moving vortex configuration. The authors repeat the calculation for different initial separations, finding that the resulting minimum distance between the rings follows the universal scaling law (see Section 3.2.1). Additionally the authors define the intravortex and intervortex angles of the pyramidal cusp formed as the two vortices approach the reconnection. The results show that the reconnecting angles remain approximately constant, independently of the initial distance between the vortex rings.

In [31] two separated vortex rings are positioned symmetrically and mutually inclined at an angle with respect to the horizontal plane, so that they are not coaxial but mutually tilted. The rings move toward each other and progressively bend in the region of closest approach due to their mutual interaction. The filaments become locally nearly antiparallel, and the distance between their cores decreases to the scale of the core size. At this stage reconnection occurs: the antiparallel segments locally reconnect, exchanging tails and producing a new topological configuration (see Figure 3.4).

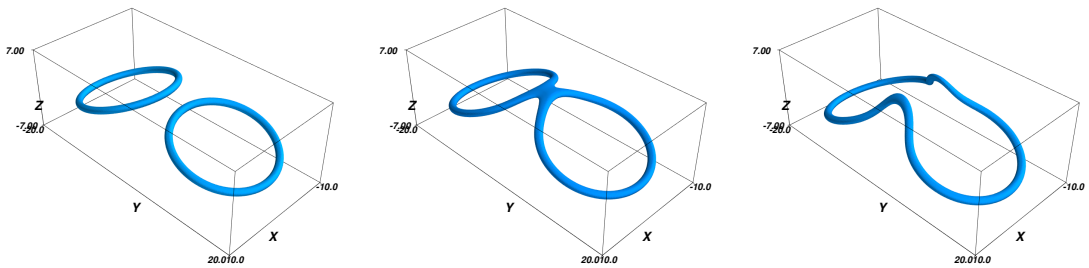

Figure 3.4: Dynamics of vortex reconnection between two symmetrically placed, mutually tilted quantum vortex rings. Numerical simulation reproducing the results of [31].

Moreover, in [32] the authors study the interaction between two circular rings of similar radii traveling in the same direction with laterally offset axes. The results reveal four possible outcomes, determined solely by the impact parameter: the rings may pass each other on the inside or outside without interacting, or they may reconnect, producing one or two deformed rings.

Furthermore, in [33] two vortex rings with same radius are placed on mutually orthogonal planes, x-y plane and the y-z plane. The system decays through a series of reconnections to produce finally three unlinked, unfolded, almost planar vortex loops (see Figure 3.5).

3.1.3 A quantum straight vortex line and a quantum vortex ring

Recent research has explored reconnections between rings and lines, highlighting the range of phenomena that can occur during such processes.

In [30] the authors study the interaction of a vortex line, aligned in the z direction, with a vortex ring located in the y-z plane, with center at $y = D$ such that $D \in \mathbb{R}^+$ and which moves in the positive x direction. The geometry of the initial configuration can be parametrized by the angle Θ between the vortex ring and the vortex line, with

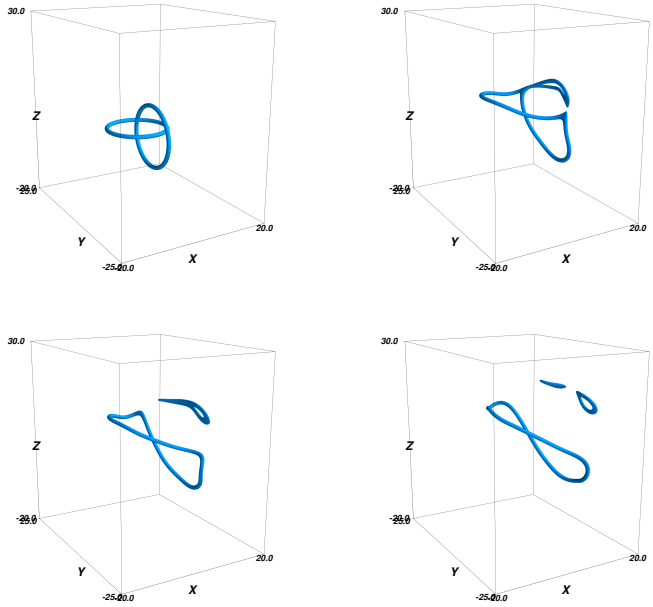

Figure 3.5: Evolution of two linked vortex rings showing a reconnection cascade leading to three unlinked loops. Numerical simulation reproducing the results of [33].

$0° \leq \Theta \leq 180°$. The authors find that the minimum distance between the vortices before reconnection follows the universal scaling law (see Section 3.2.1), with coefficients close to those observed in ring–ring reconnections. However, unlike the ring–ring case, the post-reconnection cusp is not universal: the reconnecting angles depend strongly on the initial geometric parameter Θ. For $\Theta < 50°$, reconnection does not occur, because the nearby segments become nearly parallel, rotate around each other due to having the same circulation, and the ring is deflected past the line.

The work [34] presents the scattering of a vortex ring by a straight vortex line (aligned in the z direction) varying the initial ring offset. Using a vortex tracking algorithm, they extract the positions of the ring and line to compute lengths and energies. The results indicate that compressible kinetic energy is negligible compared to incompressible kinetic energy. Although quantum energy rises sharply during the reconnection event, it remains substantially lower than the incompressible kinetic energy. Moreover, the initial offset strongly affects the outcome: for certain values, the vortex ring can pass by the line without undergoing reconnection, while intermediate offsets lead to reconnections, sometimes resulting in complete absorption of the ring by the line. Positive offsets produce smaller, faster rings, whereas negative offsets yield larger, slower rings. The scattering process also induces an asymmetric deflection and velocity change of the ring, partially balanced by energy transferred into Kelvin-wave excitations along the line.

In [35] the authors examine the interaction between a vortex ring and a straight vortex line along the z-axis. The ring is initially offset from the line and the ring's velocity forms an angle with respect to the x-y plane. The vortices can reconnect and, depending on the impact parameter and the angle with respect to the x-y plane, there are three possible outcomes. A first consequence is the absorption of the ring, with possible formation of

stable hump solitons. A second possibility is the creation of a loop soliton that propagates along the line, and a third result could be the emission of a secondary vortex ring following a self-reconnection of the loop. All processes generate Kelvin waves of various wavelengths. The main result is that after a ring–line reconnection the loop soliton is the most probable outcome, while secondary ring emission or ring absorption dominates for small angles.

3.2 Irreversibility of quantum vortex reconnections

As seen in Chapter 1, the model of the dynamics of quantum fluids at zero temperature is governed by the time-dependent Gross-Pitaevskii Equation (1.16), which is (formally) time-reversible, as stated and proved in the following

Proposition 3.2.1. *Let $\Psi(\mathbf{r},t)$ be a solution of the time-dependent Gross Pitaevskii Equation* (1.16) *with a real potential $V(\mathbf{r})$. Then the function $\tilde{\Psi}(\mathbf{r},t) := \overline{\Psi}(\mathbf{r},-t)$ is also a solution of* (1.16)*. In particular, the time-dependent Gross Pitaevskii Equation* (1.16) *is formally time-reversible.*

Proof. We substitute $t \to -t$ into (1.16), remembering that $\frac{\partial}{\partial(-t)} = \frac{\partial t}{\partial(-t)}\frac{\partial}{\partial t} = -\frac{\partial}{\partial t}$,

$$\begin{aligned}
\mathrm{i}\hbar\frac{\partial\Psi(\mathbf{r},-t)}{\partial(-t)} &= -\frac{\hbar^2}{2m}\Delta\Psi(\mathbf{r},-t) + V(\mathbf{r})\Psi(\mathbf{r},-t) + g|\Psi(\mathbf{r},-t)|^2\Psi(\mathbf{r},-t)\\
-\mathrm{i}\hbar\frac{\partial\Psi(\mathbf{r},-t)}{\partial t} &= -\frac{\hbar^2}{2m}\Delta\Psi(\mathbf{r},-t) + V(\mathbf{r})\Psi(\mathbf{r},-t) + g|\Psi(\mathbf{r},-t)|^2\Psi(\mathbf{r},-t)\,.
\end{aligned}$$

Then, we take the complex conjugate of both sides of the previous equation taking into account that $V(\mathbf{r})$ is real, to have

$$\begin{aligned}
\mathrm{i}\hbar\frac{\partial\overline{\Psi}(\mathbf{r},-t)}{\partial t} &= -\frac{\hbar^2}{2m}\overline{\Delta\Psi}(\mathbf{r},-t) + \overline{V}(\mathbf{r})\overline{\Psi}(\mathbf{r},-t) + g|\overline{\Psi}(\mathbf{r},-t)|^2\overline{\Psi}(\mathbf{r},-t)\\
\mathrm{i}\hbar\frac{\partial\overline{\Psi}(\mathbf{r},-t)}{\partial t} &= -\frac{\hbar^2}{2m}\Delta\overline{\Psi}(\mathbf{r},-t) + V(\mathbf{r})\overline{\Psi}(\mathbf{r},-t) + g|\overline{\Psi}(\mathbf{r},-t)|^2\overline{\Psi}(\mathbf{r},-t)\,.
\end{aligned}$$

Hence if $\Psi(\mathbf{r},t)$ is a solution of the time-dependent GPE, then we obtain that $\tilde{\Psi}(\mathbf{r},t) := \overline{\Psi}(\mathbf{r},-t)$ is also a solution, demonstrating that the Gross-Pitaevskii Equation is time-reversible. □

Although the time-dependent Gross–Pitaevskii equation is exactly time-reversible, vortex reconnections exhibit an effective irreversibility. During a reconnection event, part of the kinetic energy associated with the vortices is converted into sound waves. These waves propagate away from the reconnection region and are not recovered in the subsequent vortex dynamics. As a consequence, part of the energy and dynamical information associated with the vortex configuration is transferred to sound waves, even though the complete Gross–Pitaevskii dynamics remains reversible. An exact reversal of the process would require all dispersed sound waves to retrace their paths and coherently reconstruct at the reconnection site, a condition of vanishingly small probability.

In the following subsections, we discuss the main phenomena associated with this effective irreversibility, including the temporal asymmetry observed during vortex reconnections, as described by the scaling law for the minimum vortex separation, sound emission

and vortex length loss, the generation of Kelvin waves, and the consequent transfer of kinetic energy from the incompressible component, associated with vortex filaments, to the compressible component, associated with density waves.

3.2.1 The scaling law

The minimum separation between two reconnecting vortices in both classical fluids and superfluids obeys a universal scaling law with respect to time [13, 2, 10, 11, 12, 4, 14].

Proposition 3.2.2. *The minimum distance between the reconnecting vortices $\delta^{\pm}$ scales with time t, according to the form*

$$\delta^{\pm}(t) = A^{\pm}(\kappa|t - t_0|)^{\frac{1}{2}}\,, \tag{3.1}$$

where t_0 is the reconnection time, $\kappa = \frac{h}{m}$ is the quantum of circulation, and the dimensionless prefactors A^- and A^+ refer, respectively, to before $(t < t_0)$ and after $(t > t_0)$ the reconnection.

As stated in [4], in the case of a pure superfluid at temperature $T = 0\,K$, the theoretical works based on the GPE [19, 12] have shown that

$$A^+ > A^-\,, \tag{3.2}$$

evidencing that, after the reconnection, vortex lines move away from each other faster than in the initial approach, despite the fact that GPE dynamics is time-reversible and conservative. The faster separation of defects, due to the higher speed of the separated vortex lines, results from the higher curvature of the recombined strands immediately after reconnection. According to the Local Induction Approximation (LIA) (see Definition 2.2.6) a higher curvature leads to an increase in the velocity of vortex defects, and therefore to a shorter separation time compared to the approach stage. Hence peaks of total curvature are signatures of the reconnection events.

The temporal asymmetry $A^+ > A^-$ is therefore interpreted as a nontrivial manifestation of irreversibility, as it originates from an ideal hydrodynamic process independent of the small-scale regularization mechanism of the fluid.

In the following subsections, we report some studies that interpret the time asymmetry as originating from the generation of a sound pulse after the reconnection event.

3.2.2 Sound emission and length loss

It was shown theoretically in [20] that a portion of the length of the vortex line is destroyed during a reconnection process, and this loss of length is due to part of the kinetic energy of the vortices that is transformed into energy emission in the form of a rarefaction pulse (i.e. a localized depletion of density that propagates outward), generated after the reconnection. Moreover, the rarefaction pulse is subsequently dispersed into sound waves [49, 2] with a wavelength of a few healing lengths. Hence the sound emission may act as a dissipation mechanism, playing a role analogous to viscous dissipation in ordinary

fluids, where kinetic energy is converted into heat. Furthermore, it was estimated in [19, 12] that the energy of the sound pulse emitted during a reconnection event reads

$$E_{\text{pulse}} = -\frac{\Delta L}{L_0} E_{\text{tot}} \,,$$

where E_{tot} is the total superfluid energy, ΔL and L_0 are the variation of the total length and the initial length of the vortex filaments, respectively. This energy loss was shown to depend on the ratio

$$\frac{A^+}{A^-} = \cot\left(\frac{\phi^+}{2}\right) , \tag{3.3}$$

where ϕ^+ is the macroscopic reconnecting angle formed by the hyperbola asymptotes when considering filaments after the reconnection (see Figure 3.6). Ratio (3.3) in turn defines the approaching angle of collision between the vortices: indeed it was demonstrated in [19] that

$$E_{\text{pulse}} > 0, \text{ for } \phi^+ < \frac{\pi}{2} \text{ or equivalently for } A^+ \geq A^- \,,$$

implying that unless energy is externally provided to the reconnecting vortices, it is energetically impossible to have a reconnection event when $A^+ < A^-$, correspondingly to $\phi^+ > \frac{\pi}{2}$.

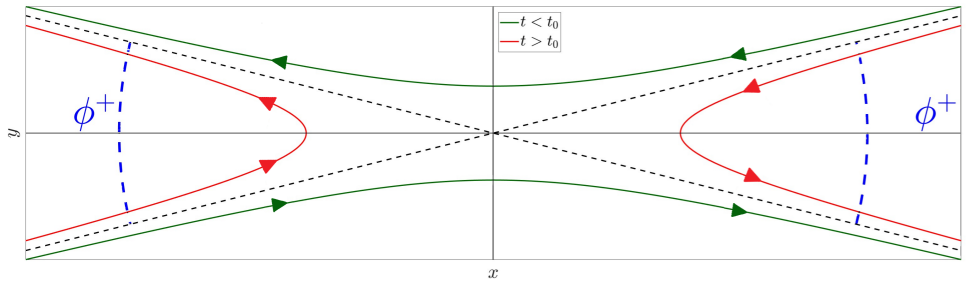

Figure 3.6: Reconnecting angle ϕ^+. Figure adapted from [19]

We recall that acoustic energy is also created when vortices accelerate [24, 50].

Additionally the temporal evolution of the total length of the defect lines is used to examine the reconnection process and to identify the reconnection time. In general the total length tends to increase as the vortex cores approach each other, and the peak of normalized total length after stretching is used as a signature to detect the reconnection time [31, 51]. In the post-reconnection stage the rate of change $|\delta L/\delta t|$ (where t indicates the time) is higher than in the pre-reconnection phase [12] due to the induction effect of the Biot-Savart law, confirming the time asymmetry of the process.

3.2.3 Kelvin waves

A reconnection event also generates the so-called Kelvin waves, defined as follows

Definition 3.2.1. *[21, 26, 5] A* **Kelvin wave** *is a sinusoidal or helical perturbation of the vortex core away from its rest position. The angular velocity of Kelvin waves with infinitesimal amplitude A and wavelength $\lambda \gg a_0$ is*

$$\omega_0 \approx \frac{\kappa k^2}{4\pi}\left(\ln\left(\frac{1}{\kappa a_0}\right) - 0.116\right), \tag{3.4}$$

where a_0 is the vortex core radius, $k = \frac{2\pi}{\lambda}$ is the wavenumber, and κ is the quantum of circulation.

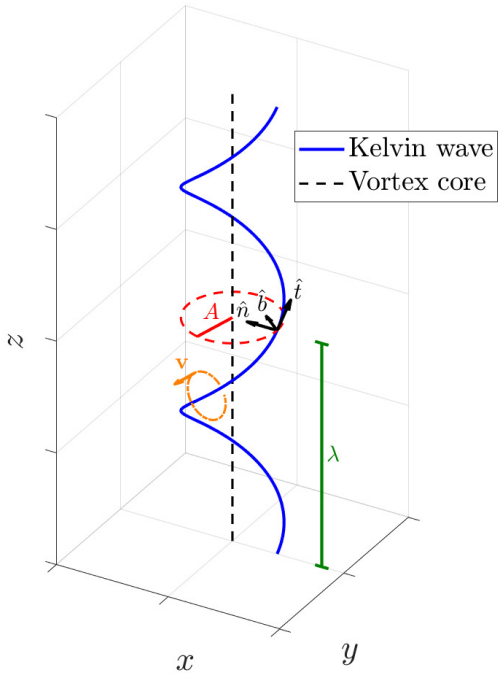

Figure 3.7: Kelvin waves. The waves rotate along the binormal direction, opposite to the direction of the flow. Figure adapted from [5].

During a reconnection event between two or a few quantum vortices, the generated Kelvin waves propagate along vortex lines (see Figure 3.8), transferring the superfluid kinetic energy to smaller scales (i.e. higher wavenumbers k) [22]. At sufficiently small scales, this energy is partially dissipated through the radiation of sound [24]. The process can be divided into three stages:

1. first, vortex reconnections generate sharp kinks on the vortex filaments;
2. second, the kinks evolve into the Kelvin waves on either side of the reconnection cusp;
3. finally, the Kelvin waves with
$$k > k_2\,,$$
where $k_2 = \left(\frac{C}{\sqrt{A}\kappa l}\right)^{1/2}$ (with l vortex separation distance) [24], are strongly damped by acoustic emission.

After the reconnection, the energy spectrum $E_{\rm k}(k)$, defined such that

$$\frac{\rho}{2}\int \mathbf{v}(\mathbf{r})^2\, d^3\mathbf{r} = \int_0^\infty E_{\rm k}(k)\, dk\,,$$

scales as k^{-1} [23, 25], a signature of energy distributed along isolated vortex lines rather than a fully developed turbulent cascade. Some energy peaks shift toward the small k region [22] and, if some dissipative mechanism operates for wavenumbers above k_2, the kinetic energy is transferred from small k to large k scales, being dissipated at $k = k_2$ by the nonlinear wave interaction, resulting in an overall decay of the total kinetic energy.

Moreover, the Kelvin wave cascade is also evident in the spectra of vortex line curvature, torsion and filament velocity [23]. In the post-reconnection regime the curvature spectrum $E_c(k)$ such that

$$\frac{1}{2}\int c^2(s)ds = \int_0^\infty E_c(k)\, dk \quad \text{(with } c \text{ local curvature and } s \text{ the arc length)}$$

becomes approximately flat, indicating that all curvature scales contribute roughly equally to the energy, while a roll-off appears at higher wavenumbers due to dissipation or numerical resolution limits. Similarly the torsion $E_T(k)$ and filament velocity spectra $E_L(k)$

$$\frac{1}{2}\int \tau^2(s)ds = \int_0^\infty E_T(k)\, dk \quad (\tau \text{ torsion}) \qquad \frac{1}{2}\int \mathbf{v}_{LIA}^2(s)ds = \int_0^\infty E_L(k)\, dk\,,$$

also become approximately constant over the range of wavenumbers corresponding to the Kelvin wave cascade, reflecting that nonlinear interactions between Kelvin waves redistribute energy locally along the filament, independently of global system parameters.

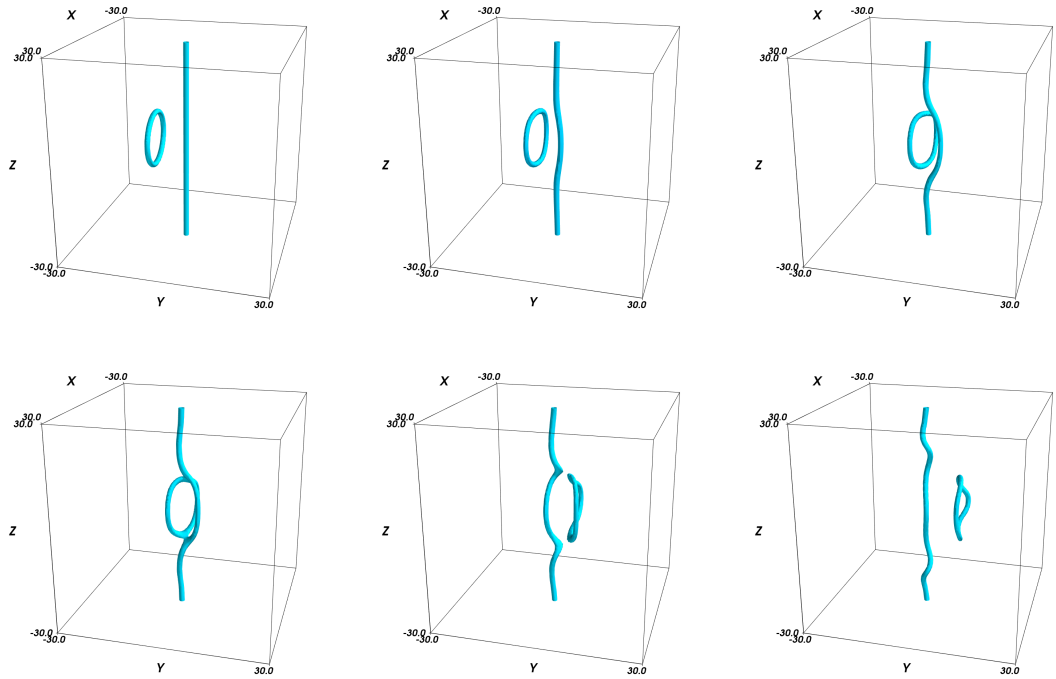

Figure 3.8: Reconnection between a vortex ring which hits a straight vortex. After the collision the straight vortex is perturbed by Kelvin waves.

3.2.4 Kinetic energy decomposition

We pointed out that when a vortex reconnection occurs in a quantum fluid a sound pulse is excited. This phenomenon results in an irreversible transfer of a portion of the kinetic energy (1.69)

$$E_{\mathrm{k}} = \frac{1}{2}\int_D \rho \mathbf{v}^2 d^3\mathbf{r}$$

from the incompressible component, associated with vortex filaments, to the compressible component, associated with density waves [5, 19], while the total energy (1.69) remains conserved. This framework allows for a quantitative determination of the energy exchanges between the vortices and the density waves in the superfluid.

To numerically evaluate this energy transfer, we decompose the kinetic energy into the incompressible and compressible contributions [27, 47, 34, 12]. This separation is obtained by applying the Helmholtz decomposition to the vector field $\sqrt{\rho}\mathbf{v}$ defined on D (see Theorem A.0.2), yielding

$$\sqrt{\rho}\mathbf{v} = (\sqrt{\rho}\mathbf{v})^{\mathrm{i}} + (\sqrt{\rho}\mathbf{v})^{\mathrm{c}}\,, \tag{3.5}$$

where the incompressible component $(\sqrt{\rho}\mathbf{v})^{\mathrm{i}}$ satisfies $\nabla\cdot(\sqrt{\rho}\mathbf{v})^{\mathrm{i}} = 0$, and the compressible component $(\sqrt{\rho}\mathbf{v})^{\mathrm{c}}$ satisfies $\nabla\times(\sqrt{\rho}\mathbf{v})^{\mathrm{c}} = 0$ (see e.g. [52] for details).

As a consequence of this decomposition, the kinetic energy can be written as

$$E_{\mathrm{k}} = E_{\mathrm{k}}^{\mathrm{i}} + E_{\mathrm{k}}^{\mathrm{c}}\,,^{1} \tag{3.6}$$

where

$$E_{\mathrm{k}}^{\mathrm{i}} := \frac{1}{2}\int_D \big((\sqrt{\rho}\mathbf{v})^{\mathrm{i}}\big)^2 d^3\mathbf{r} \qquad \text{and} \qquad E_{\mathrm{k}}^{\mathrm{c}} := \frac{1}{2}\int_D \big((\sqrt{\rho}\mathbf{v})^{\mathrm{c}}\big)^2 d^3\mathbf{r}\,.$$

A sharp increase in compressible kinetic energy $E_{\mathrm{k}}^{\mathrm{c}}$ is observed during the reconnection event, which is attributed to a corresponding loss of incompressible kinetic energy $E_{\mathrm{k}}^{\mathrm{i}}$ [12]. In particular, the energy transferred to the emitted sound pulse is computed as

$$E_{\mathrm{pulse}} = -\Delta E_{\mathrm{k}}^{\mathrm{i}} = E_{\mathrm{k}}^{\mathrm{i}}(t^+) - E_{\mathrm{k}}^{\mathrm{i}}(t^-)\,,$$

where t^- and t^+ denote two times taken immediately before and immediately after the vortex reconnection event, respectively.

[1] In (3.6), $E_{\mathrm{k}}^{\mathrm{i}}$ denotes the incompressible component, associated with Kelvin wave generation, while $E_{\mathrm{k}}^{\mathrm{c}}$ denotes the compressible component, associated with sound-wave emission.

Chapter 4

Quantum reconnection of an inclined vortex ring with a straight vortex line: energy distribution and geometric analysis

In this chapter, we investigate the evolution of the reconnection between a straight vortex line and a vortex ring, whose dynamics is governed by the Gross–Pitaevskii Equation (GPE) [8, 9]. This configuration extends the initial setup proposed in [30] and [34], by keeping the offset parameter fixed at zero and introducing a non-zero inclination angle between the vortex ring and the horizontal plane, which is varied to explore its impact on the reconnection dynamics. These different choices in the initial geometrical setting lead to distinct reconnection dynamics that emerge specifically from the geometry and go beyond those obtained by varying the offset parameter at a fixed angle.

A configuration more similar to ours is that considered in [35], where both the offset and the inclination angle are varied. However, the resulting dynamics may still differ since the present work employs the GPE model, which naturally accounts of the reconnection process, whereas the vortex filament method, used in [35], needs a reconnection strategy provided by a specific method.

For each angular value, we first compute the total length and curvature of the nodal lines, and then we analyze how the components of the total energy redistribute during the process. Subsequently, by applying the Helmholtz decomposition to the kinetic energy following the approach of [47, 34] we discover how the angle variation influences the partitioning between the incompressible and compressible components, revealing the generation of Kelvin waves and the emission of sound waves. Finally, the results of the total and kinetic energy analysis are compared with the measurements of vortex line length and curvature, aiming to identify possible correlations between the inclination angle of the vortex ring, geometric features, and energy redistribution during the reconnection. This analysis provides new insights in the role of the geometric configuration in quantum vortex reconnections and offers a framework for interpreting the energy transfer mechanism in quantum vortex dynamics.

4.1 Physical model, geometric tools and energy decompositions

4.1.1 Physical model

As introduced in Chapter 1, the dynamics of quantum vortices is successfully described by the Gross–Pitaevskii Equation (GPE). This is, indeed, an excellent model for studying the reconnection process between a quantum vortex ring and a straight quantum vortex line because reconnections occur naturally, without the need to force or model them [2]. Following [48, 51], we set $V_0' = -\frac{1}{2}$ and $g' = \frac{1}{2}$ in (1.76), so that the non-dimensional form of the GPE reads

$$\frac{\partial \Psi}{\partial t} = \frac{\mathrm{i}}{2}\nabla^2\Psi + \frac{\mathrm{i}}{2}(1 - |\Psi|^2)\Psi, \tag{4.1}$$

where we omit the prime ($'$) to simplify the notation. Here the particle mass m and the reduced Planck constant $\hbar$ have been set to 1 for simplicity in the non-dimensional form. The complex wave function $\Psi = \sqrt{\rho}e^{\mathrm{i}\theta}$ then allows a fluid-dynamics interpretation (see Section 1.4) in terms of fluid density $\rho = |\Psi|^2$ and velocity field $\mathbf{v} = \nabla\theta$ via Madelung transform (1.47). Quantum vortices are phase defects characterized by a density profile that monotonically increases from zero at the vortex centerline to a uniform background value (normalized to 1) as $|\mathbf{r}| \to \infty$ (see Section 2.3.1). As such, they evolve over time within a medium of uniform density, except in the vortex core region. The size of the vortex core is of the order of the healing length ξ, which turns out to be equal to 1 due to the normalization employed while deriving (4.1).

4.1.2 Numerical details

We investigate numerically the reconnection phenomenon using (4.1), with initial conditions given by an inclined vortex ring moving towards a steady straight vortex line. The circulation Γ of both vortices is 2π due to the normalization [5]. The initial wave function Ψ_0 at time $t = 0$ is

$$\Psi_0 = \sqrt{\rho_{0L}\rho_{0R}}\exp[\mathrm{i}(\theta_{0L} + \theta_{0R})]\,, \tag{4.2}$$

where ρ_{0L} and ρ_{0R} denote the density distribution of the straight vortex line and the vortex ring, respectively, while θ_{0L} and θ_{0R} are the corresponding phases. Both densities are computed using the 4-th order Padé approximation (see [53]), while θ_{0L} is set to change by 2π in a plane orthogonal to the vortex line; for the vortex ring, the phase θ_{0R} follows the construction described in [31].

At $t = 0$ the vortex line passes through the origin of the domain, which we call C_L (see Figure 4.1), and has direction $\vec{n}_L = (0, 0, -1)$. The vortex ring, with radius $R = 8$, is centered in $C_R = (-20, 0, 15)$ and has normal vector $\vec{n}_R = (1, 0, -\tan\alpha)$, where α is the angle in the xz plane between the axis x and the normal $\vec{n}_R$.

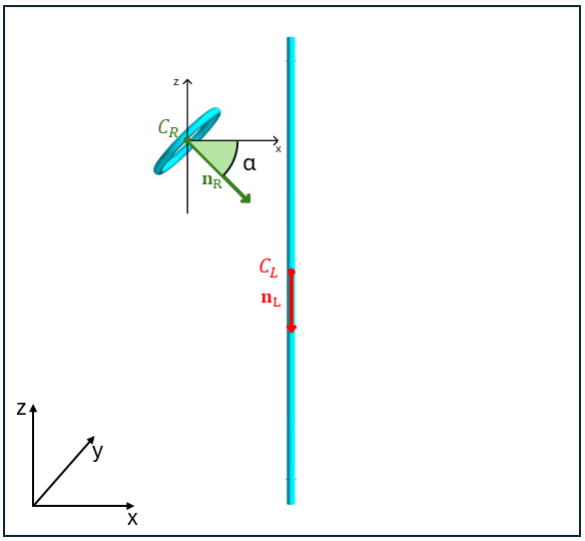

Figure 4.1: Initial configuration, at $t = 0$, of the vortex ring and vortex line. C_R and $\vec{n}_R$ denote the center and the normal vector ring's plane, respectively. $\vec{n}_L$ indicates the direction of the vortex line, and $C_L = (0, 0, 0)$ represents the origin.

The spatial domain is $\Sigma = [-40, 40] \times [-30, 30] \times [-55, 35]$ with spatial resolution $\Delta x = \Delta y = \Delta z = \xi/2$ (where ξ is the healing length), i.e. the number of points is $161 \times 121 \times 181$. The numerical integration of (4.1) is performed using second order equispaced finite difference with homogeneous Neumann boundary conditions for the spatial discretization, whereas the time integration employs second-order Strang splitting method as in [48, 54]. The time step τ is set equal to $1/10$, while the final time T is the simulation time at which the vortex ring reaches the boundary of the computational domain. We remark that for each chosen angle α the final time T is different, therefore all the plots in Section 4.2 have different final time on the t-axis depending on the value of α.

Numerical simulations (see Figure 4.2) show that the dynamics evolves through three distinct stages: initially, before reconnection, the system consists of two separate structures, the vortex ring and the straight vortex line; then the first reconnection takes place and a single continuous curve is observed. Finally, a second reconnection occurs giving rise to a (non-straight) vortex filament and a non-planar vortex ring. For a complete simulation see the Supplemental Material [55]. We note that the loop solitons, observed for a similar configuration in [35] where the vortex filament method is employed, are not present in our reconnection process possibly because of the use of different models or slightly different geometrical parameters . Moreover, we do not observe any absorption of the ring by the vortex line, since in our setting the offset parameter is zero. The energy decomposition and geometrical analysis for the cases with both nonzero offset and angular variations will be investigated in a future work. The three-steps pattern described above, which will recur through the work, suggests that the curvature and the length of the filaments would change quite considerably during the reconnection process and that Kelvin and sound waves would be generated. In what follows, we introduce the tools to track them.

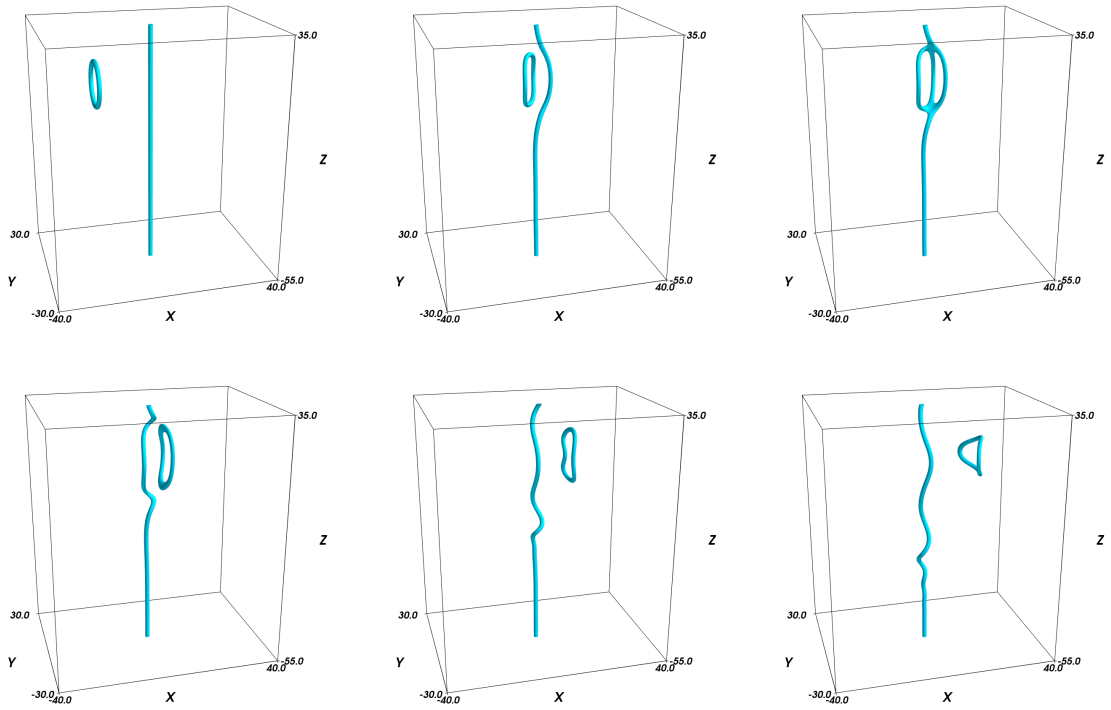

Figure 4.2: Frames of time evolution of reconnection process for initial angle $\alpha = 0°$ of the sloped vortex ring. Isosurfaces of $\rho = 0.2$.

4.1.3 Geometric tools

We analyze the evolution of the total length and curvature of the vortex-core nodal lines, numerically extrapolated as in [2, 51], during the reconnection process aiming to understand a possible relation between these geometric quantities. We recall the definitions of total length L and curvature K:

$$L := \sum_{i=1}^{N} \oint_{\mathcal{C}_i} ds, \qquad K_i := \frac{1}{L_i} \oint_{\mathcal{C}_i} c_i(s) ds\,, \tag{4.3}$$

where $i = 1, \dots, N$ is the number of nodal lines $\mathcal{C}_i$, s is the arc length, L_i is the length of the single nodal line and $c_i(s) = ||C_i''(s)||$ is the local curvature. We underline the fact that we consider the total curvature of the nodal lines and not the local one.

4.1.4 Total energy components and decomposition of kinetic energy

In the setting proposed in 4.1.1, the non-dimensional total energy of the system (1.69), which is constant under the GPE, becomes [51]

$$E_{\text{tot}} = \underbrace{\frac{1}{8}\int_\Sigma \frac{|\nabla\rho|^2}{\rho} d^3\mathbf{r}}_{E_{\text{q}}} + \underbrace{\frac{1}{2}\int_\Sigma \rho|\mathbf{v}|^2 d^3\mathbf{r}}_{E_{\text{k}}} \underbrace{-\frac{1}{2}\int_\Sigma \rho d^3\mathbf{r}}_{E_{\text{p}}} + \underbrace{\frac{1}{4}\int_\Sigma \rho^2 d^3\mathbf{r}}_{E_{\text{int}}}, \tag{4.4}$$

where E_{q} is the quantum energy, E_{k} is the kinetic energy, E_{p} is the potential energy and E_{int} is the internal energy. We stress the fact that the energy components are an average all over the fluid, and not the components of the energy of the vortex filaments.

Furthermore, in order to understand the possible generation of Kelvin and sound waves, we consider the decomposition of the kinetic energy of the system into its incompressible and compressible contributions by applying the well-known Helmholtz decomposition (see Proposition A.0.2) to the vector field $\mathbf{u} = \sqrt{\rho}\mathbf{v}$. The decomposition of $\sqrt{\rho}\mathbf{v}$ is here computed solving the Poisson equation (A.3)[1]:

$$\nabla \cdot (\sqrt{\rho}\mathbf{v}) = -\Delta\Phi\,, \tag{4.5}$$

with Φ a scalar potential function. We express the quantity $\sqrt{\rho}\mathbf{v}$ as $\mathrm{Im}(\nabla\Psi e^{-\mathrm{i}\theta})$, where Im indicates the imaginary part, since using the Madelung transformation (1.47) we have

$$\begin{aligned}
\Psi &= \sqrt{\rho}e^{\mathrm{i}\theta} \\
\nabla\Psi &= \nabla(\sqrt{\rho})e^{\mathrm{i}\theta} + \sqrt{\rho}\mathrm{i}\nabla\theta e^{\mathrm{i}\theta} \\
\nabla\Psi e^{-\mathrm{i}\theta} &= \nabla(\sqrt{\rho})e^{\mathrm{i}\theta}e^{-\mathrm{i}\theta} + \sqrt{\rho}\mathrm{i}\nabla\theta e^{\mathrm{i}\theta}e^{-\mathrm{i}\theta} = \nabla(\sqrt{\rho}) + \sqrt{\rho}\mathrm{i}\nabla\theta \\
\mathrm{Im}(\nabla\Psi e^{-\mathrm{i}\theta}) &= \sqrt{\rho}\nabla\theta = \sqrt{\rho}\mathbf{v}\,.
\end{aligned}$$

We numerically solve the Poisson equation (4.5) using the Fourier method. Thus, let consider the computation domain

$$\Sigma = [h_{L_x}, h_{R_x}] \times [h_{L_y}, h_{R_y}] \times [h_{L_y}, h_{R_y}]\,,$$

with $\mathbf{h}_L = (h_{L_x}, h_{L_y}, h_{L_z})$ and $\mathbf{h}_R = (h_{R_x}, h_{R_y}, h_{R_z})$ denoting the left and right boundaries along each direction, we have

$$\Phi(\mathbf{r}) = \sum_{\mathbf{k}} \hat{\Phi}(\mathbf{k})\, \exp\left(2\pi\mathrm{i} \sum_{\mu=x,y,z} \frac{k_\mu(r_\mu - h_{L_\mu})}{h_{R_\mu} - h_{L_\mu}}\right)$$

$$\mathbf{u}(\mathbf{r}) = \sum_{\mathbf{k}} \hat{\mathbf{u}}(\mathbf{k})\, \exp\left(2\pi\mathrm{i} \sum_{\mu=x,y,z} \frac{k_\mu(r_\mu - h_{L_\mu})}{h_{R_\mu} - h_{L_\mu}}\right)$$

$$\nabla\Phi(\mathbf{r}) = \sum_{\mathbf{k}} \begin{pmatrix} \frac{2\pi i k_x}{h_{R_x} - h_{L_x}} \hat{\Phi}(\mathbf{k}) \\ \frac{2\pi i k_y}{h_{R_y} - h_{L_y}} \hat{\Phi}(\mathbf{k}) \\ \frac{2\pi i k_z}{h_{R_z} - h_{L_z}} \hat{\Phi}(\mathbf{k}) \end{pmatrix} \exp\left(2\pi i \sum_{\mu=x,y,z} \frac{k_\mu(r_\mu - h_{L_\mu})}{h_{R_\mu} - h_{L_\mu}}\right)$$

$$-\Delta\Phi(\mathbf{r}) = -\sum_{\mathbf{k}} \hat{\Phi}(\mathbf{k}) \left(\sum_{\mu=x,y,z} \left(\frac{2\pi\mathrm{i}k_\mu}{h_{R_\mu} - h_{L_\mu}}\right)^2\right) \exp\left(2\pi\mathrm{i} \sum_{\mu=x,y,z} \frac{k_\mu(r_\mu - h_{L_\mu})}{h_{R_\mu} - h_{L_\mu}}\right)$$

$$\nabla \cdot \mathbf{u}(\mathbf{r}) = \sum_{\mathbf{k}} \left(\sum_{\mu=x,y,z} \frac{2\pi\mathrm{i}k_\mu}{h_{R_\mu} - h_{L_\mu}}\, \hat{u}_\mu(\mathbf{k})\right) \exp\left(2\pi\mathrm{i} \sum_{\mu=x,y,z} \frac{k_\mu(r_\mu - h_{L_\mu})}{h_{R_\mu} - h_{L_\mu}}\right)\,,$$

[1] In the numerical implementation the equation is written using a different sign convention but the two formulations are equivalent.

where $\mathbf{r} = (r_x, r_y, r_z) = (x, y, z) \in \Sigma$, $\mathbf{k} = (k_x, k_y, k_z)$ are the discrete Fourier modes, $\hat{\mathbf{u}}(\mathbf{k}) = (\hat{u}_1(\mathbf{k}), \hat{u}_2(\mathbf{k}), \hat{u}_3(\mathbf{k}))$ and $\hat{\Phi}(\mathbf{k})$ are the the coefficients of the discrete Fourier transform of $\mathbf{u}(\mathbf{r})$ and Φ respectively, and $\hat{u}_\mu(\mathbf{k})$ is the Fourier transform of the μ-component of $\mathbf{u}$. Equating the coefficients we obtain

$$-\left[\sum_{\mu=x,y,z}\left(\frac{2\pi \mathrm{i} k_\mu}{h_{R_\mu}-h_{L_\mu}}\right)^2\right]\hat{\Phi}(\mathbf{k}) = \sum_{\mu=x,y,z}\frac{2\pi \mathrm{i} k_\mu}{h_{R_\mu}-h_{L_\mu}}\,\hat{u}_\mu(\mathbf{k})$$

$$\hat{\Phi}(\mathbf{k}) = -\frac{\sum_{\mu=x,y,z}\frac{2\pi \mathrm{i} k_\mu}{h_{R_\mu}-h_{L_\mu}}\,\hat{u}_\mu(\mathbf{k})}{\sum_{\mu=x,y,z}\left(\frac{2\pi \mathrm{i} k_\mu}{h_{R_\mu}-h_{L_\mu}}\right)^2}\,. \tag{4.6}$$

Then we define

$$\Lambda_\mu(\mathbf{k}) = \frac{2\pi i\, k_\mu}{h_{R_\mu}-h_{L_\mu}}$$

to get $\Lambda(\mathbf{k}) = (\Lambda_x(\mathbf{k}), \Lambda_y(\mathbf{k}), \Lambda_z(\mathbf{k}))$, and the sum of squares

$$\Lambda_s^2(\mathbf{k}) = \Lambda_x^2(\mathbf{k}) + \Lambda_y^2(\mathbf{k}) + \Lambda_z^2(\mathbf{k}).$$

Using this notation (4.6) can be rewritten as

$$\hat{\Phi}(\mathbf{k}) = -\frac{\Lambda(\mathbf{k})\cdot\hat{\mathbf{u}}(\mathbf{k})}{\Lambda_s^2(\mathbf{k})}, \quad \mathbf{k}\neq 0, \tag{4.7}$$

where the discrete Fourier transform of the vector field $\mathbf{u}(\mathbf{r})$ is

$$\hat{\mathbf{u}}(\mathbf{k}) = \mathcal{F}[\mathbf{u}](\mathbf{k}) = \sum_{\mathbf{r}\in\Sigma}\mathbf{u}(\mathbf{r})e^{-2\pi \mathrm{i}\mathbf{k}\cdot(\mathbf{r}-\mathbf{h}_L)}\,.$$

The zero Fourier mode is set to

$$\hat{\Phi}(\mathbf{0}) = 0\,,$$

which corresponds to fixing the spatial average of the potential to zero, since only the gradient of Φ affects the vector field $\mathbf{u}$ and a constant shift does not contribute.

Numerically we find $\hat{\Phi}(\mathbf{k})$ using (4.7) and the compressible and incompressible components of $\mathbf{u}$ are obtained as

$$(\sqrt{\rho}\mathbf{v})^{\mathrm{c}} = -\nabla\Phi(\mathbf{r}) = -\mathcal{F}^{-1}[\Lambda(\mathbf{k})\hat{\Phi}(\mathbf{k})]$$
$$(\sqrt{\rho}\mathbf{v})^{\mathrm{i}} = \sqrt{\rho}\mathbf{v} - (\sqrt{\rho}\mathbf{v})^{\mathrm{c}}\,.$$

The Fourier transform and its inverse are implemented using the following definitions:

```
 ft = @(u) fftshift(fftn(u));
ift = @(u) real(ifftn(ifftshift(u)));
```

where we use the MATLAB function `fftn` to compute the N-dimensional discrete Fourier transform of arrays, and reconstruct the arrays with `ifftn`. Moreover, the MATLAB functions `fftshift` and `ifftshift` center the zero-frequency mode in the arrays, ensuring a symmetric representation of positive and negative Fourier modes and consistent

application of the spectral operators, while the inverse transform is restricted to the real part to remove negligible numerical imaginary components.

We obtain finally

$$E_{\mathrm{k}} = E_{\mathrm{k}}^{\mathrm{i}} + E_{\mathrm{k}}^{\mathrm{c}}\,, \tag{4.8}$$

where

$$E_{\mathrm{k}}^{\mathrm{i}} = \frac{1}{2}\int_{\Sigma} \left((\sqrt{\rho}\mathbf{v})^{\mathrm{i}} \right)^2 d^3\mathbf{r} \quad \text{and} \quad E_{\mathrm{k}}^{\mathrm{c}} = \frac{1}{2}\int_{\Sigma} \left((\sqrt{\rho}\mathbf{v})^{\mathrm{c}} \right)^2 d^3\mathbf{r}\,.$$

4.2 Numerical results and their analysis

In this section we report a detailed analysis of the numerical simulations carried out by changing the initial angle α between the normal plane to the vortex line and the normal to vortex ring (see Figure 4.1). We have considered $\alpha = 0°$, $\alpha = 15°\,, \alpha = 30°\,, \alpha = 45°\,, \alpha = 60°$ and $\alpha = 75°$, as shown in Figure 4.3. These numerical simulations are available in the Supplemental Material [55], with selected frames shown in Figure 4.4. In all cases we see that, regardless of value of the angle α, both the vortex ring and line undergo deformations before the first and after the second reconnection. Additionally, the first reconnection occurs once the deformed vortex ring touches the deformed vortex line.

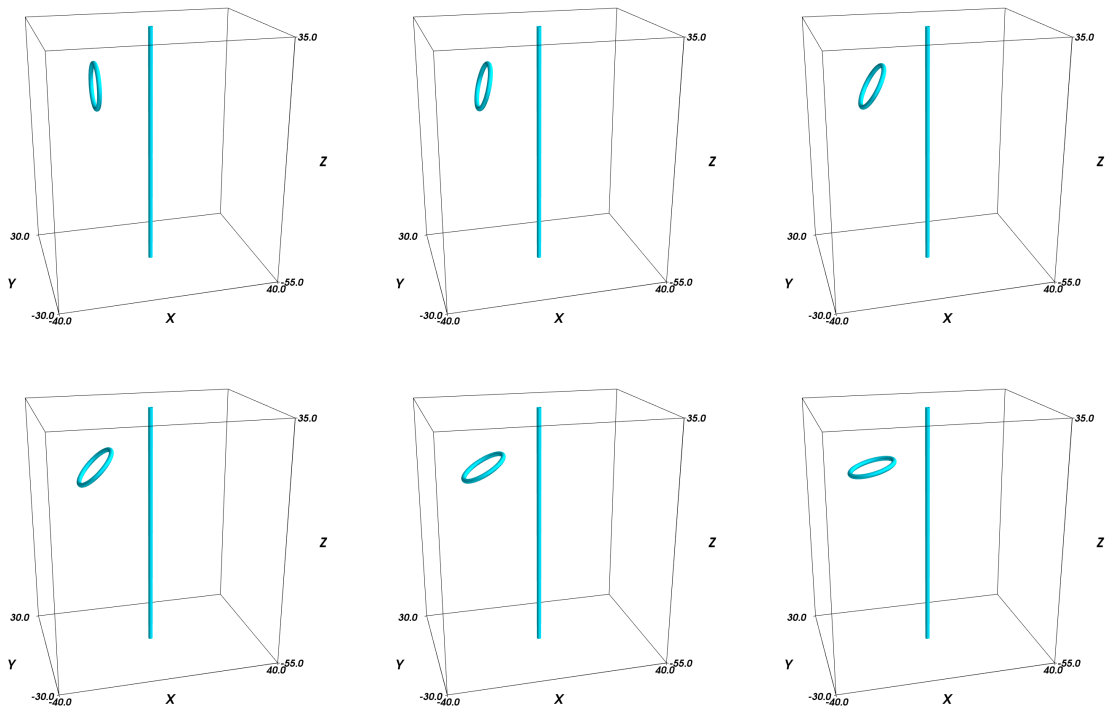

Figure 4.3: Configurations of initial conditions with different values of angle α. From top left to bottom right, $\alpha = 0°$, $\alpha = 15°$, $\alpha = 30°$, $\alpha = 45°$ $\alpha = 60°$ and $\alpha = 75°$. Center of the vortex ring: $C_R = (-20,\ 0,\ 15)$. Ring normal coordinates: $\vec{n}_R = (1,\ 0,\ -\tan\alpha)$. Center of the vortex line: $C_L = (0,\ 0,\ 0)$. Line direction coordinates: $\vec{n}_L = (0,\ 0,\ -1)$. Isosurfaces of $\rho = 0.2$ are plotted to visualize the vortices cores.

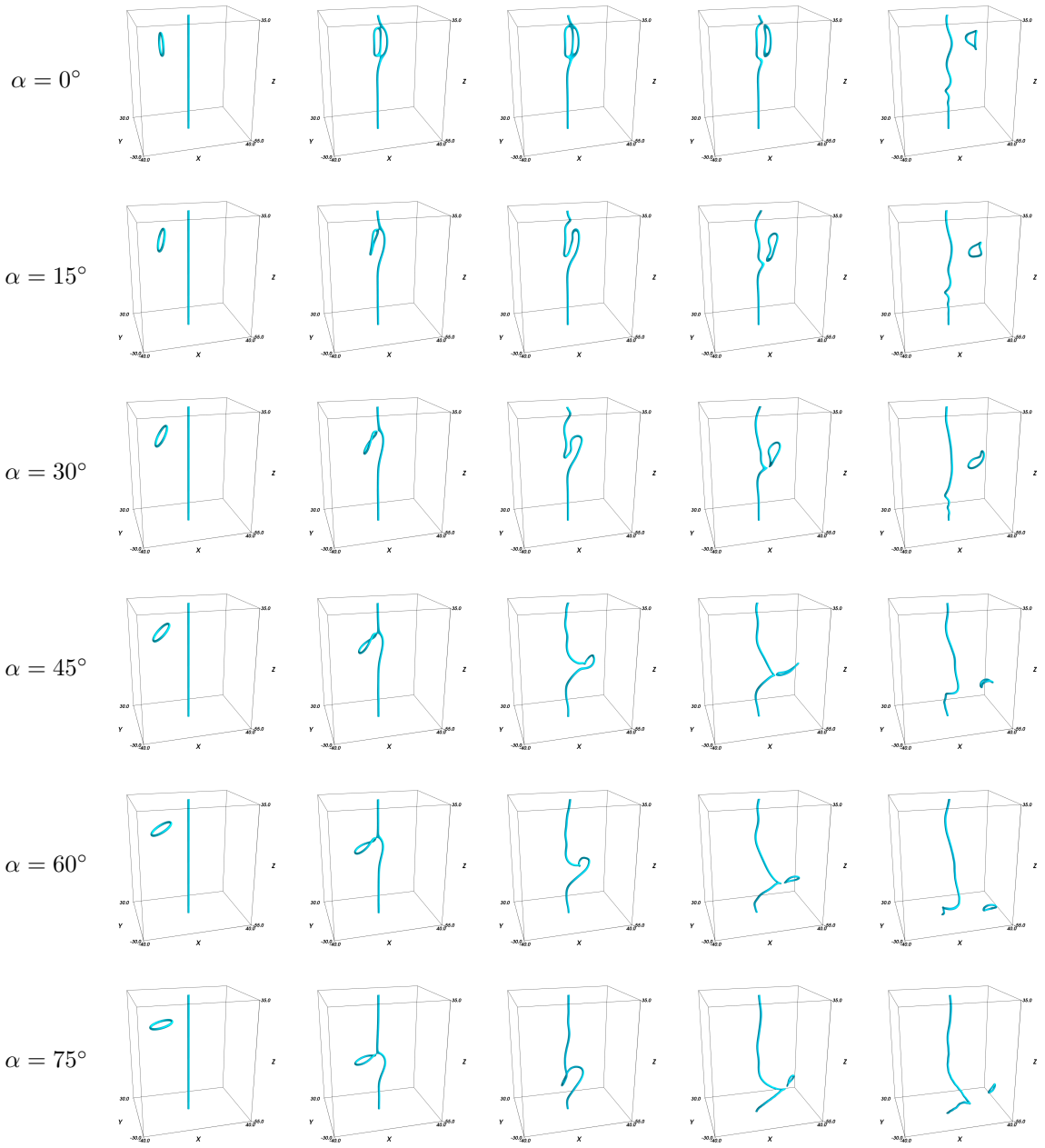

Figure 4.4: Frames of time evolution of reconnection process with different initial angle α of the sloped vortex ring. From top to the bottom: $\alpha = 0°$, $\alpha = 15°$, $\alpha = 30°$, $\alpha = 45°$, $\alpha = 60°$, $\alpha = 75°$. Isosurfaces of $\rho = 0.2$.

4.2.1 Behaviour of total length and curvature during the reconnection process

For each value of the angle α we have computed the total length (4.3) which is reported in Figure 4.5. It is clear that, regardless of the initial angle, it increases before the reconnections (indicated by vertical dashed lines) and subsequently decreases, thus generating two peaks corresponding to the two reconnections. This is consistent with the results in [2, 12, 51]. Since reconnection events generate sound waves (see Section 3.2.2), the decrease in the total length is associated to sound emission. On the other hand we observe that far away from the reconnections the total length has approximately the same value for any α, reflecting the fact that reconnection is a local phenomenon. More precisely the total length at initial and final time are approximately the same. Furthermore, we observe that the interval between the two reconnections increases with increasing α implying that the second reconnection occurs more slowly.

The time evolution of the total curvature (4.3) is presented in Figure 4.6. Before the first reconnection the straight vortex line undergoes a deformation from the outset and the signature of this phenomenon is visible in the increase of the curvature of the line (denoted by red squares) as the first reconnection approaches. The curvature of the vortex ring (denoted by green circles) remains close to its initial value $\frac{1}{R} = \frac{1}{8} = 0.125$ until the first reconnection. After this event, the total curvature of the single curve (denoted in blue stars) remains approximately constant, with a value close to the average of curvatures of the two individual curves just before the first reconnection. Finally, after the second reconnection, the total curvatures of the vortex line and ring increase compared to their respective values before the first reconnection, thus possibly reflecting the irreversible nature of vortex reconnections, as pointed out in Section 3.2.1. We observe that the total curvature of both the vortex ring and the vortex line presents oscillations after the second reconnection with particular emphasis in the cases $\alpha = 0°$, $\alpha = 15°, \alpha = 30°$ and $\alpha = 45°$. These oscillations emerge in the simulation as the vortex ring deforms into a distorted ellipse, with a higher local curvature at its ends, and the line becomes perturbed, suggesting the presence of Kelvin waves (see Section 3.2.3). We notice that, for $\alpha > 45°$, after the second reconnection the total curvature of the vortex ring increases monotonically with the angle.

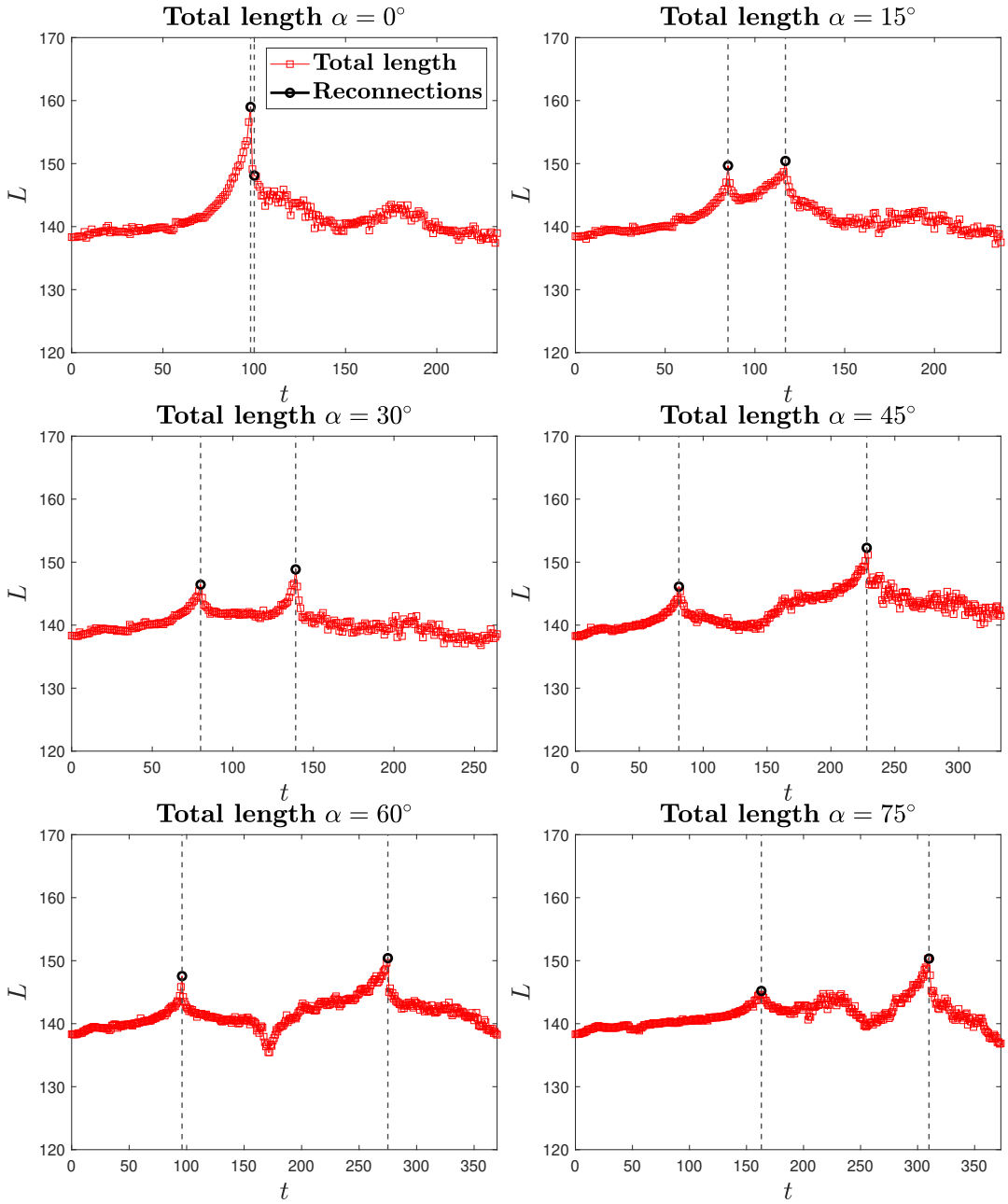

Figure 4.5: Total length L (non-dimensionalized by the healing length ξ) of nodal lines versus time t for each angle α. Vertical dashed lines indicate reconnection events. The absolute value of the difference between the final $L(T)$ and initial length L_0 for $\alpha = 0°, 15°, 30°, 45°, 60°, 75°$ is respectively $|L(T) - L_0| = 0.6321, 0.9640, 0.2299, 3.1979, 0.0753, 1.4332$.

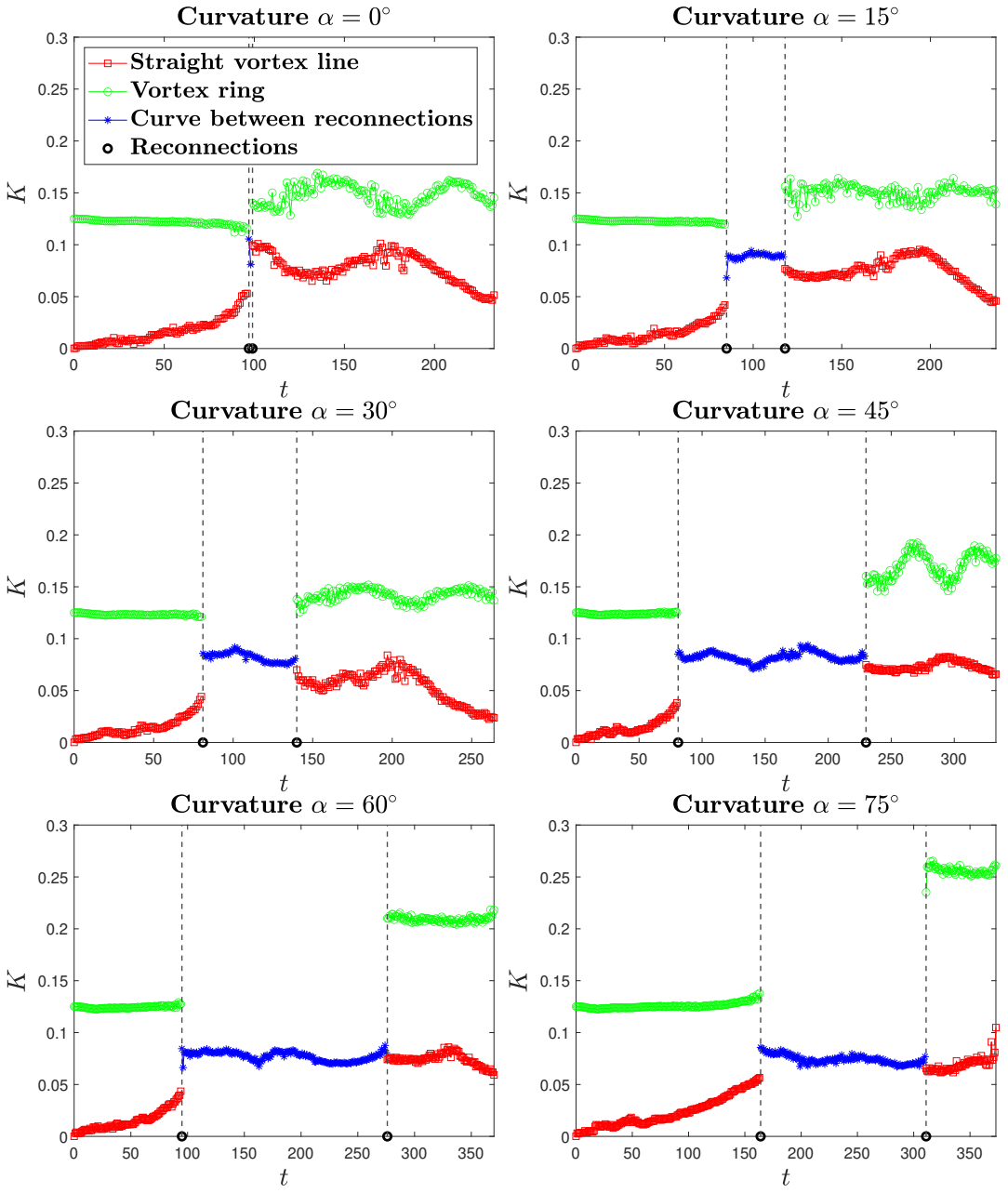

Figure 4.6: Total curvature K of nodal lines versus time t for each angle of inclination α of the vortex ring. The green circles represents the total curvature of the vortex ring, the red squares indicates the total curvature of the straight vortex line, and the blue stars indicate the total curvature of the curve between the two reconnection events. Vertical dashed lines denote reconnection events.

4.2.2 Behavior of energy components during the reconnection process

In Figures 4.8-4.12, we report the time evolution of each energy component (4.4) for different values of α. From the plot of kinetic energy, in Figure 4.8, we notice an initial depression. This happens because, as is known, the vortex ring is not a stationary solution of the GPE. Thus, it changes its radius, so the density varies and hence the energy too. Therefore, an initial time interval is necessary for the solution to stabilize itself. We analyzed that this interval of time is up to $t = 23$. Then we also see some peaks. They are related to the edge effects. In fact, starting from the beginning, the ring and the vortex line interact with each other, then the fluid around is perturbed. This perturbation collides with the edges of the box, it is bounced back, interacting with itself, and repeats this behavior during all the simulation. To be sure that it is caused by the interaction with the walls, we enlarge the domain setting Σ = [-50,50] x [-40 40] x [-65 45] with the same spatial resolution. We notice that the peaks happen at different times. This confirms the supposition because the size of the domain is different and so the bounce occurs at different moments.

Since each energy component (4.4) changes in mean linearly in time, we perform a linear least-squares fit using the MATLAB function `polyfit`, from time $t = 23$ until the final time T. Thus we obtain the slopes m_{E_q}, m_{E_k}, m_{E_p}, and m_{E_int} of the quantum, kinetic, potential, and interaction energy components, respectively. In Figure 4.13, we report the time evolution of each energy component (4.4) for different values of α, with the slopes shown in the legends. It is immediately evident that $m_{E_\mathrm{k}}+m_{E_q}+m_{E_p}+m_{E_\mathrm{int}} = m_{E_\mathrm{tot}} = 0$, thus indicating that the energy components compensate each other being the energy constant throughout the dynamics. To better analyze their behaviors, the linear fits are plotted in a single figure for different values of α (see Figure 4.13: quantum energy in blue diamonds, kinetic energy in light-blue squares, potential in green triangles and internal energy in purple dots). It is clear that

- m_{E_k} decreases with increasing angle α, $m_{E_\mathrm{k}} > 0$ for $\alpha < 45°$ and $m_{E_\mathrm{k}} < 0$ for $\alpha \geq 45°$. This suggests that the kinetic energy E_k increases for $\alpha < 45°$, with a progressively diminishing positive rate of change. For $\alpha \geq 45°$, E_k decreases and the rate of change becomes increasingly negative;

- m_{E_q} is approximately constant for all values of α and $m_{E_q} > 0$. This indicates that the quantum energy E_q increases with α, maintaining a uniform rate of change. For $\alpha = 0°$ the outcomes are the same as those obtained in [34].

- m_{E_int} increases with increasing angle α, $m_{E_\mathrm{int}} < 0$ for $\alpha < 45°$ and $m_{E_\mathrm{int}} > 0$ for $\alpha \geq 45°$. This means that the internal energy E_int decreases for $\alpha < 45°$ with a negative rate of change that progressively diminishes, and it increases for $\alpha \geq 45°$, with an increasing trend characterized by a growing positive slope;

- $m_{Ep} = 0$ for every angle α, indicating that the potential energy E_p is constant for each value of α.

Based on these facts, it follows that for each α the kinetic, quantum, and internal energy components play the main role in the redistribution of energy (see Eq (4.4)) as

the potential component remains constant. Specifically, the kinetic E_{k} and internal E_{int} energies take opposite behavior, and this happens at $\alpha \approx 45°$. Further checks revealed that this exchange occurs at $\bar{\alpha} = 43°$. It should be noticed that the sum of kinetic and internal energy is compensated by the constant increase rate of the quantum energy E_q. Indeed, $m_{E_{\mathrm{k}}} + m_{E_{\mathrm{int}}} = -m_{Eq}$ for every angle α, up to numerical accuracy.

To quantify how well the total energy is conserved in the numerical simulations, we also evaluate the relative variation of the total energy defined as

$$\frac{E_{\mathrm{tot}}(t)}{E_{\mathrm{tot}}(0)} - 1.$$

Figure 4.7 shows the temporal evolution of this quantity for all angular configurations considered. For all cases, the relative variation remains below 10^{-4} throughout the evolution, indicating that the total energy is conserved to within 10^{-4}.

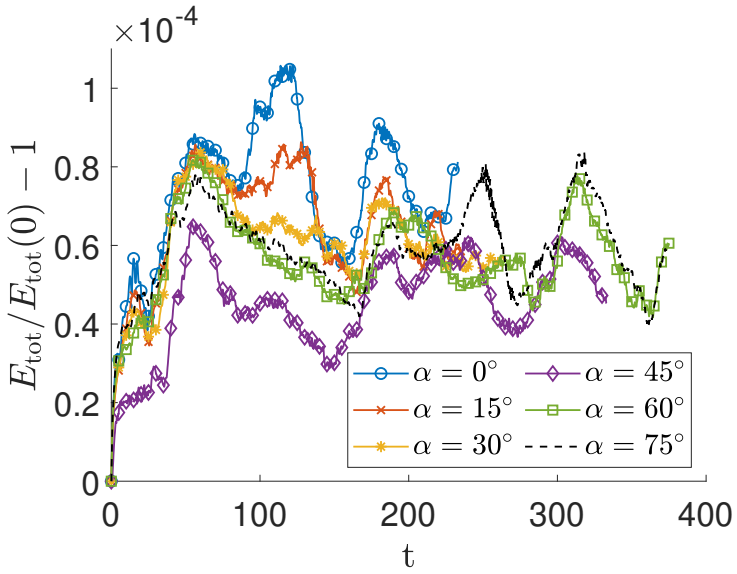

Figure 4.7: Temporal evolution of the relative total energy conservation error, $E_{\mathrm{tot}}(t)/E_{\mathrm{tot}}(0) - 1$, for all the values of angle α.

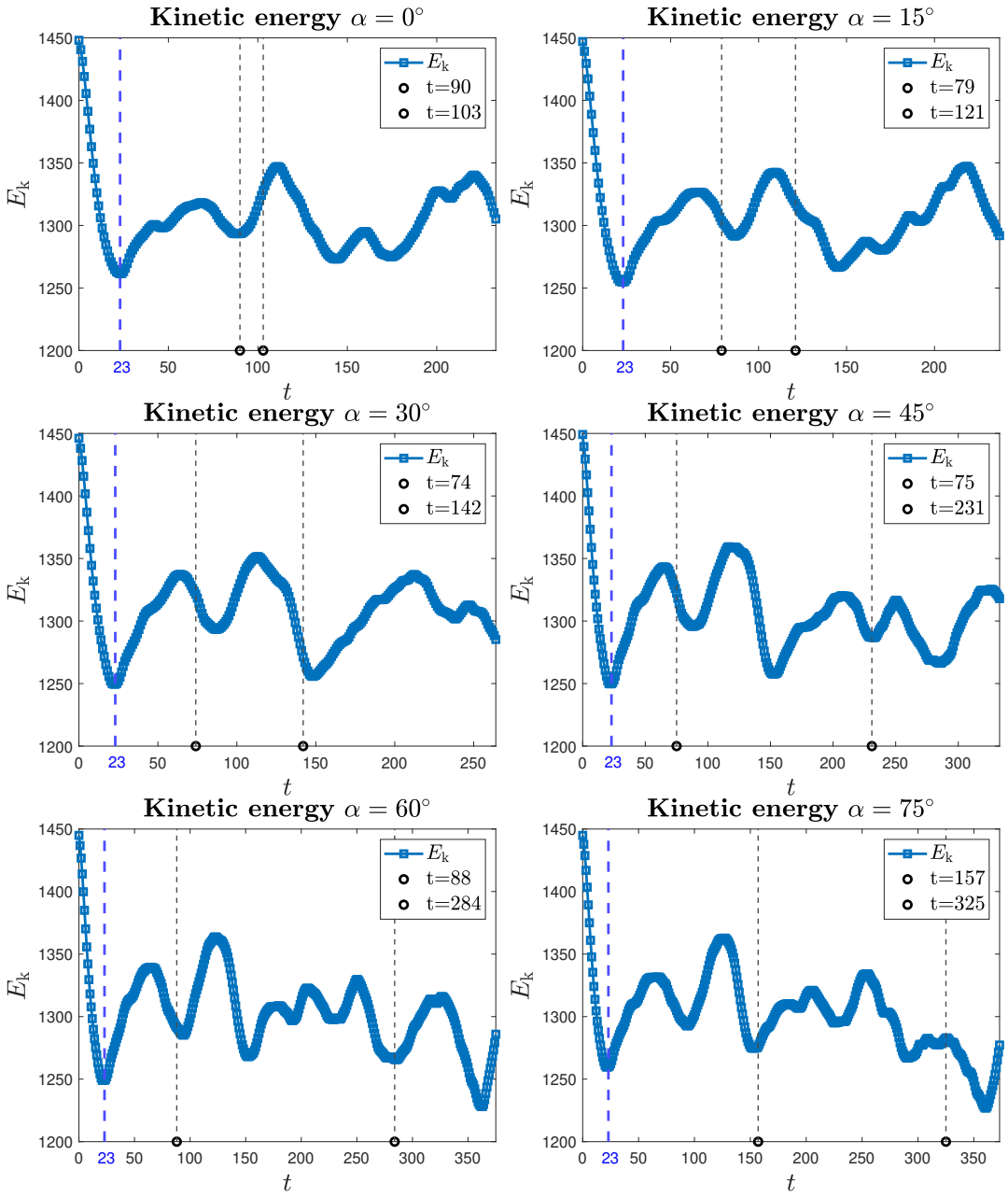

Figure 4.8: Evolution of kinetic energy for different values of angle α. Dashed line indicate reconnection events.

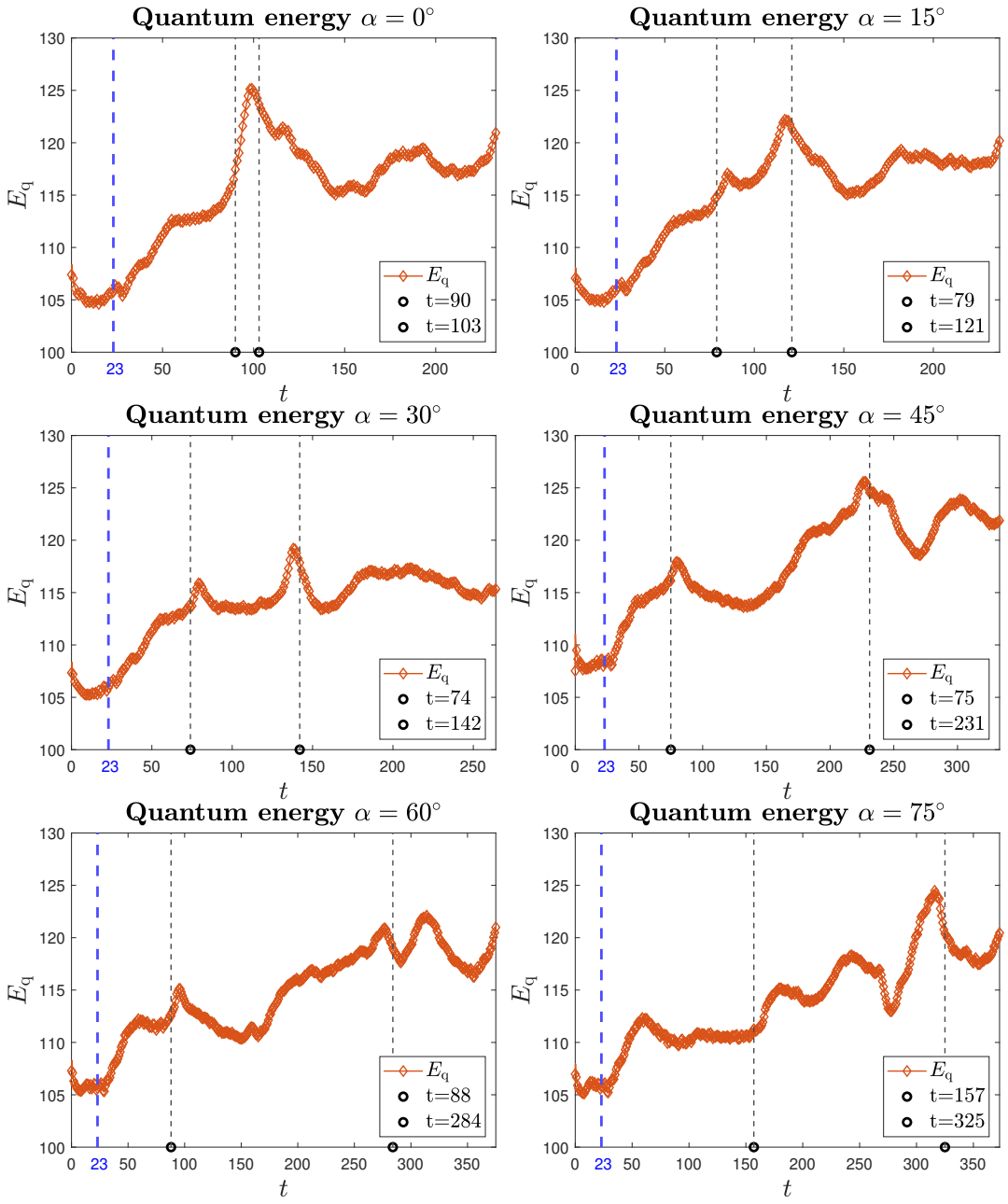

Figure 4.9: Evolution of quantum energy for different values of angle α. Dashed line indicate reconnection events.

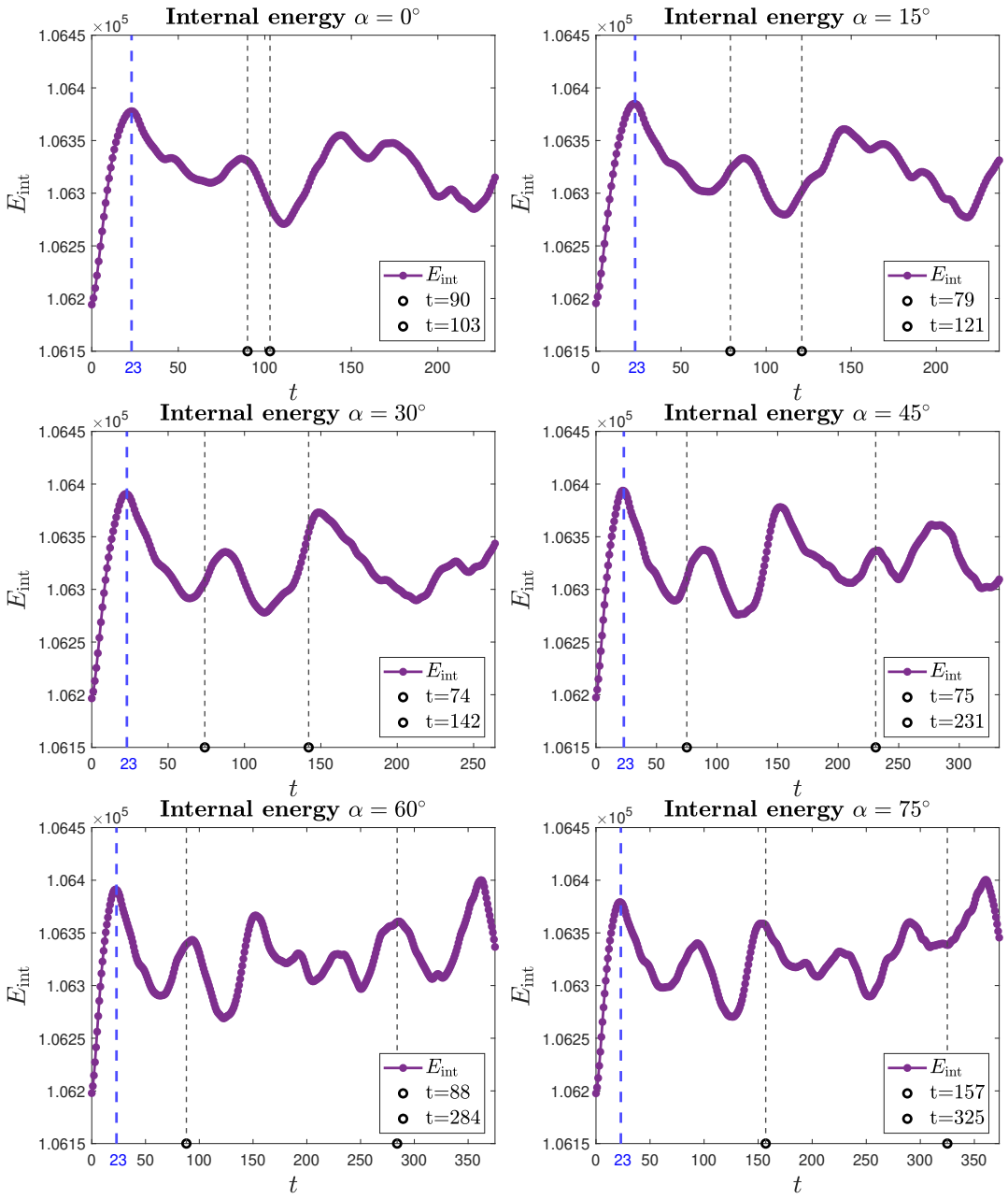

Figure 4.10: Evolution of interaction energy for different values of angle α. Dashed line indicate reconnection events.

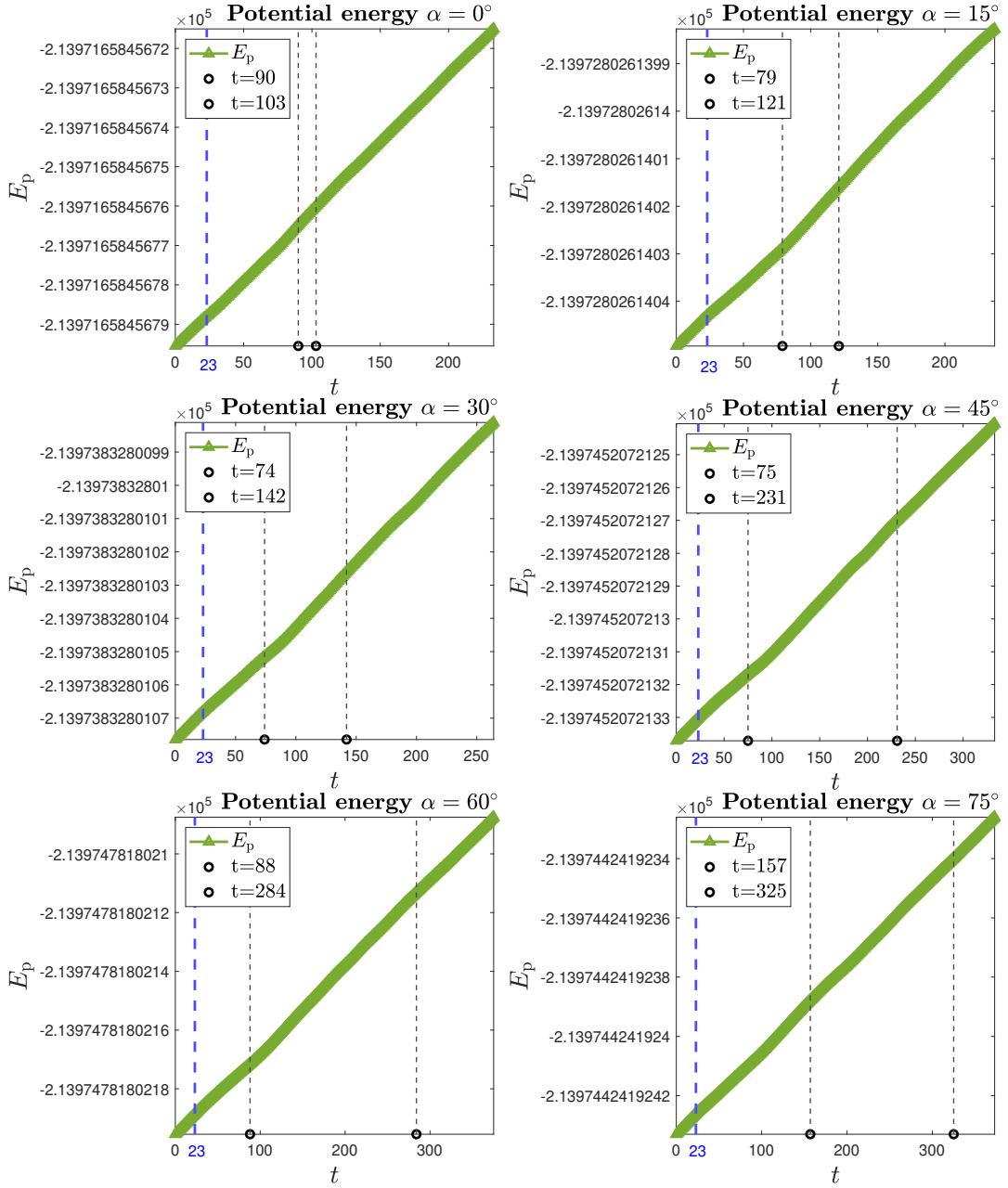

Figure 4.11: Evolution of potential energy for different values of angle α. Dashed line indicate reconnection events.

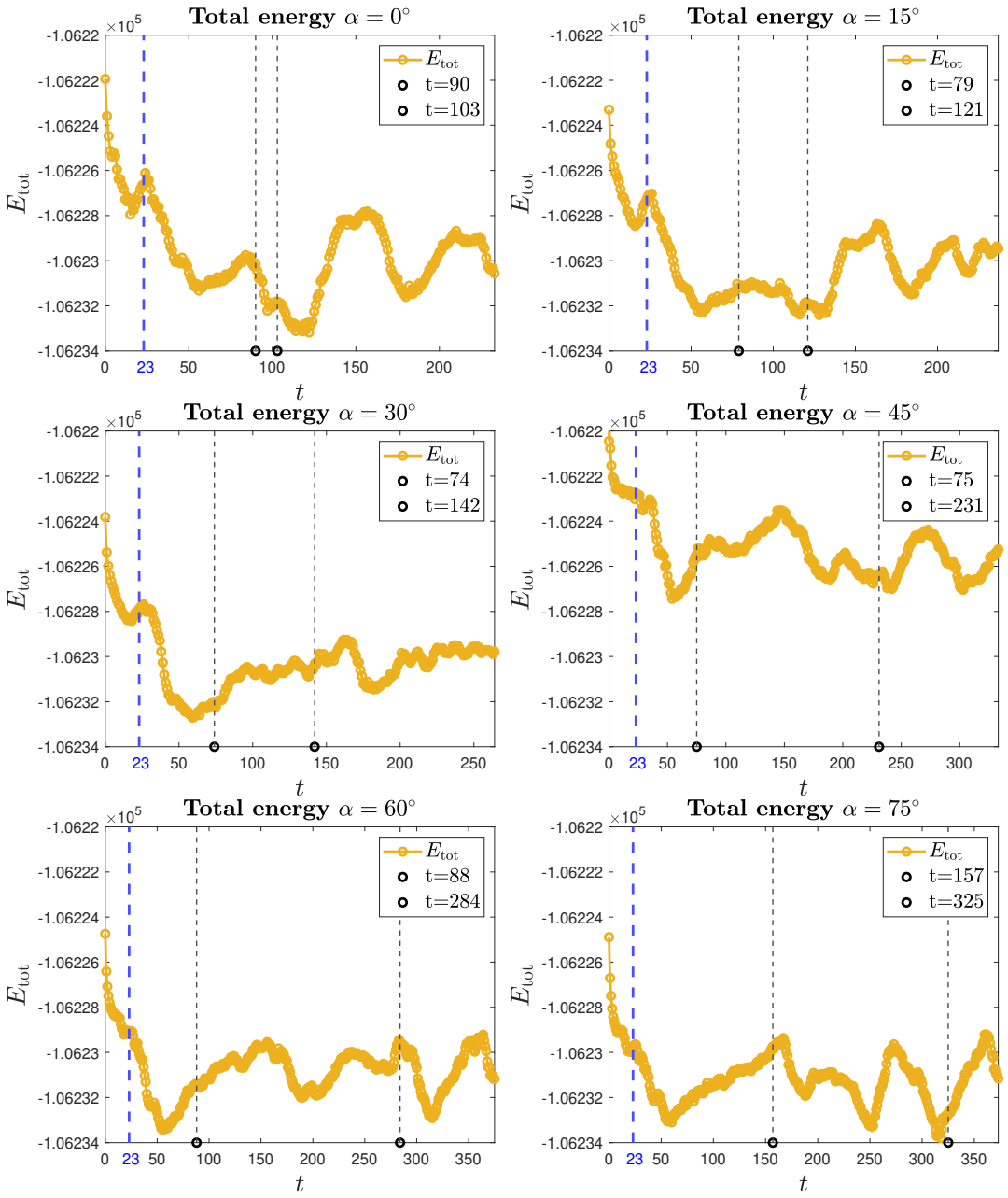

Figure 4.12: Evolution of total energy for different values of angle α. Dashed line indicate reconnection events.

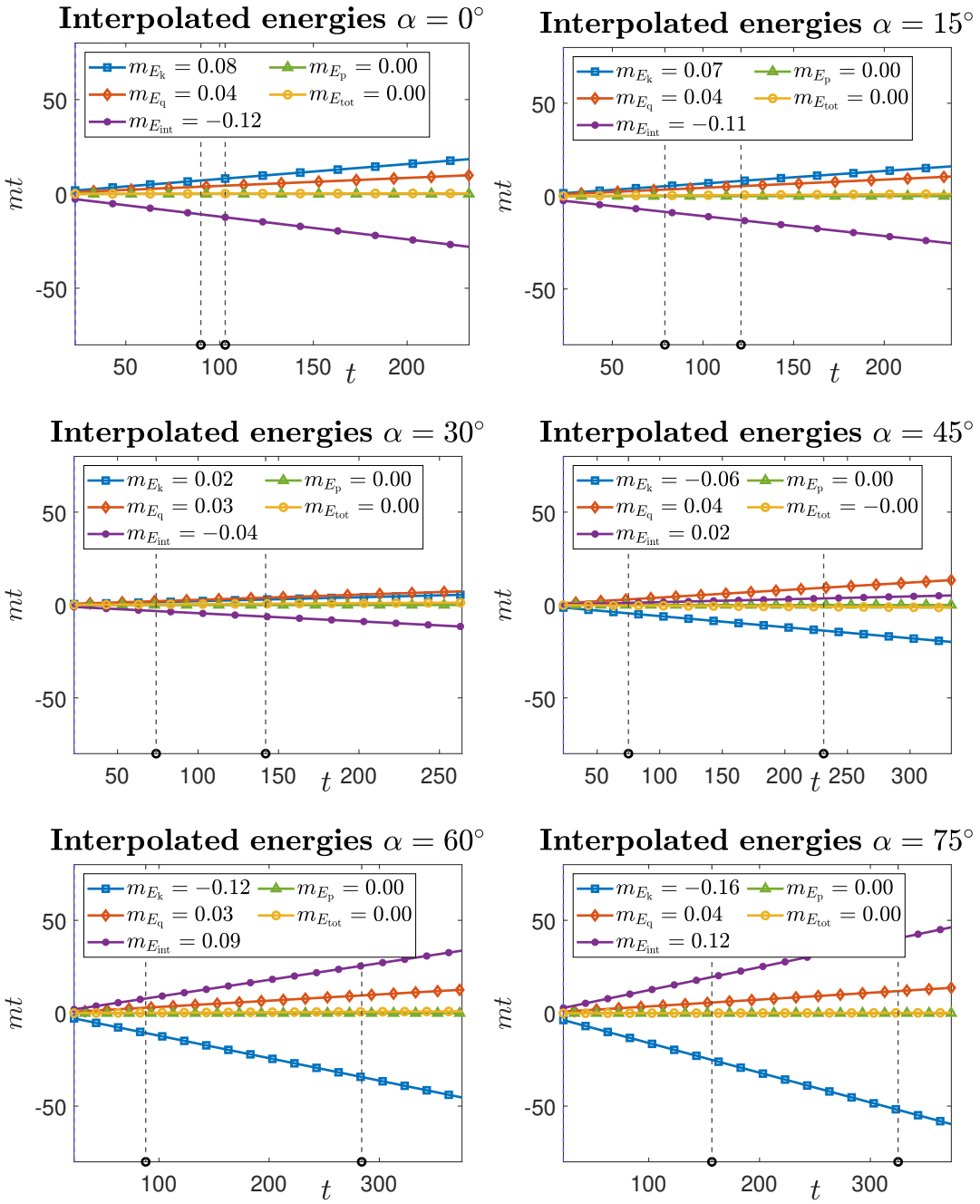

Figure 4.13: Linear least-squares fit of energy components (4.4) for different values of the angle α : kinetic energy (light blue squares), quantum energy (orange diamonds), potential energy (green triangles), internal energy (purple dots) and total energy (yellow circles). The respectively angular coefficients m of the fit lines are located in the legends. The plot starts from $t \approx 23$ (the time necessary for the solution of the (4.1) to stabilize itself) until the final time T which is different for each α. Dashed line indicate reconnection events.

4.2.3 Behavior of incompressible and compressible contributions to kinetic energy during the reconnection process

For each time step, we first compute the compressible and incompressible contributions to the kinetic energy by performing the Helmholtz decomposition outlined in Section 4.1.4. The results are shown in Figure 4.15-4.16. Then we linearly fit them using the same procedure as in Section 4.2.2. The evolution of incompressible (red triangles) and of the compressible (black crosses) components is reported in Figure 4.17, together with the slopes $m_{E_k^i}$ and $m_{E_k^c}$, respectively. It is evident that $m_{E_k^i} + m_{E_k^c} = m_{E_k}$ (up to numerical inaccuracy), so equation (4.8) is satisfied. For completeness, the fit of the total kinetic energy is also displayed. We observe that

- $m_{E_k^i} < 0$ for each α and decreases as α increases, thus E_k^i decreases for each value of α, and the decreasing rate becomes more significant as the angle increases;
- $m_{E_k^c} > 0$ for each α implying an increase in compressible kinetic energy E_k^c which is related to the emission of sound waves, as we can observe in Figure 4.14 where isosurfaces of $\rho = 0.98$ are plotted showing the pulse of sound that is emitted after the reconnection events. However, $m_{E_k^c}$ decreases as the angle increases, indicating that the increase of E_k^c becomes less pronounced as the angle α grows, therefore the production of sound waves is more intense at $\alpha = 0°$, corresponding to the first configuration shown in Figure 4.3.

We also notice in Figure 4.17 that as the angle increases, the fit of the kinetic energy seems to head from the compressible to the incompressible component, suggesting that the more the angle increases the more the kinetic energy is composed mainly by its incompressible part.

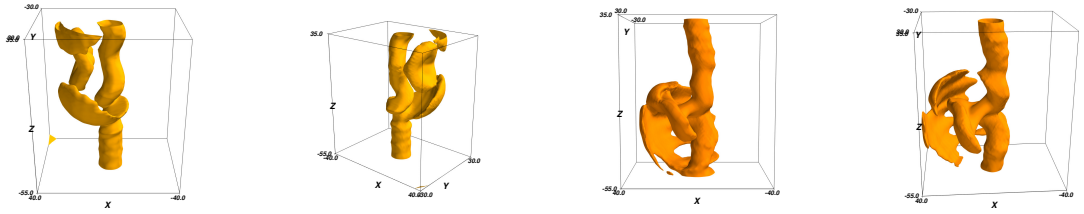

(a) $\alpha = 0°$, $t = 135$ **(b)** $\alpha = 0°$, $t = 135$ **(c)** $\alpha = 60°$, $t = 205$ **(d)** $\alpha = 60°$, $t = 215$

Figure 4.14: Emission of the sound pulse during the second reconnection is shown from different perspectives: for $\alpha = 0°$ in panels (a) and (b), and for $\alpha = 60°$ in panels (c) and (d). The isosurfaces are set at $\rho = 0.98$. For the complete simulations including all angle variations, see the Supplemental Material [55].

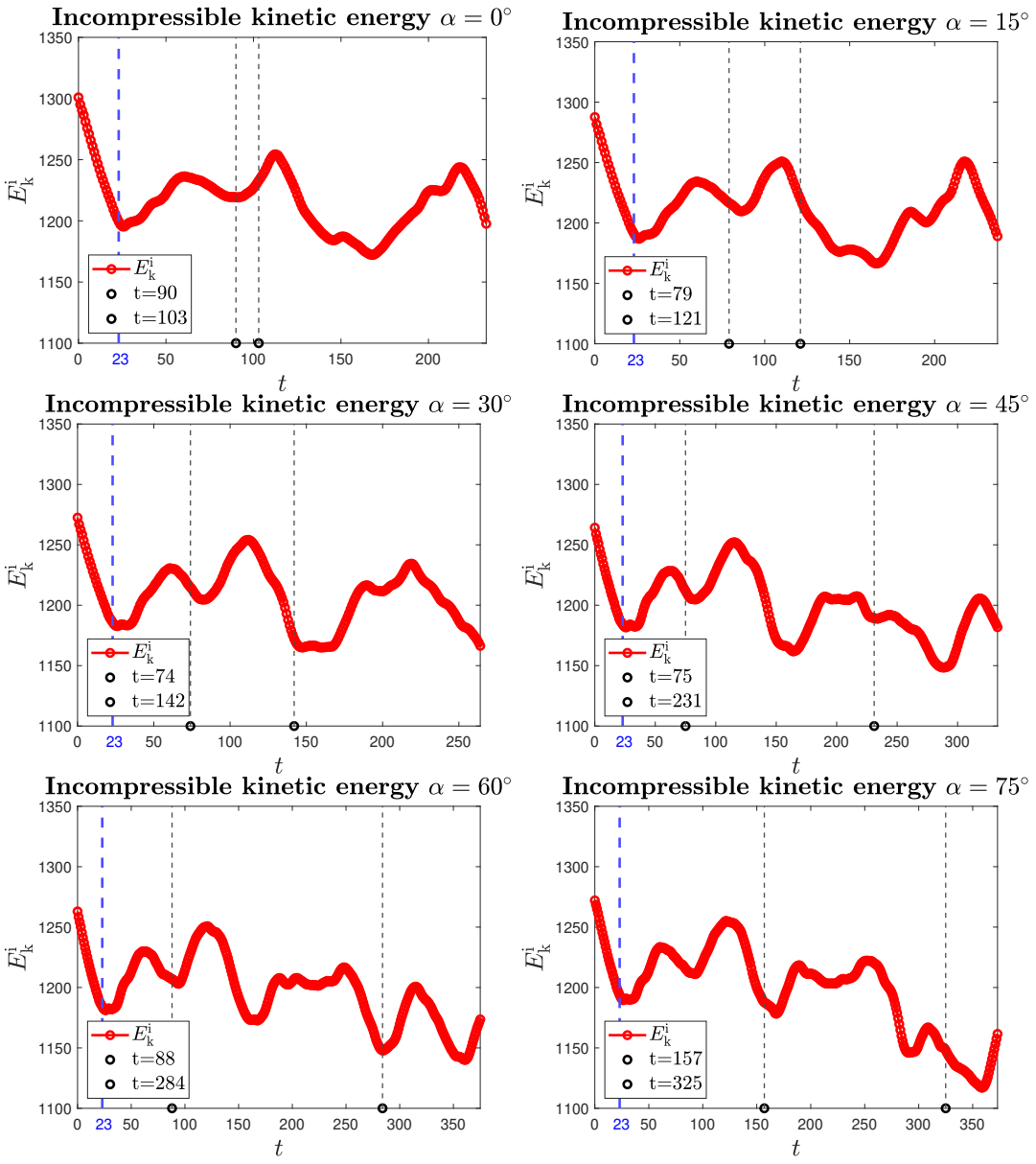

Figure 4.15: Evolution of incompressible kinetic energy for different values of angle α. Dashed line indicate reconnection events.

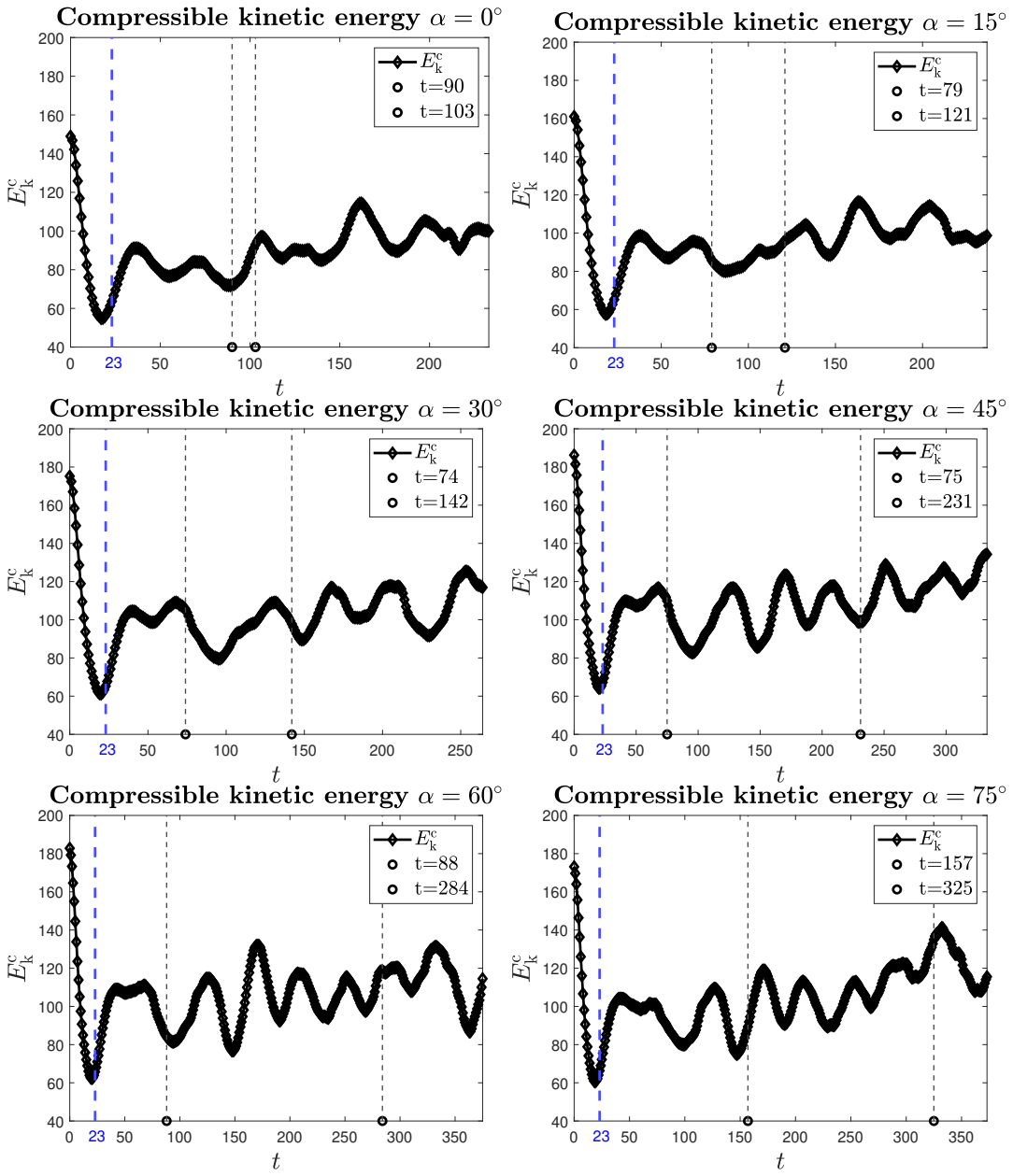

Figure 4.16: Evolution of compressible kinetic energy for different values of angle α. Dashed line indicate reconnection events.

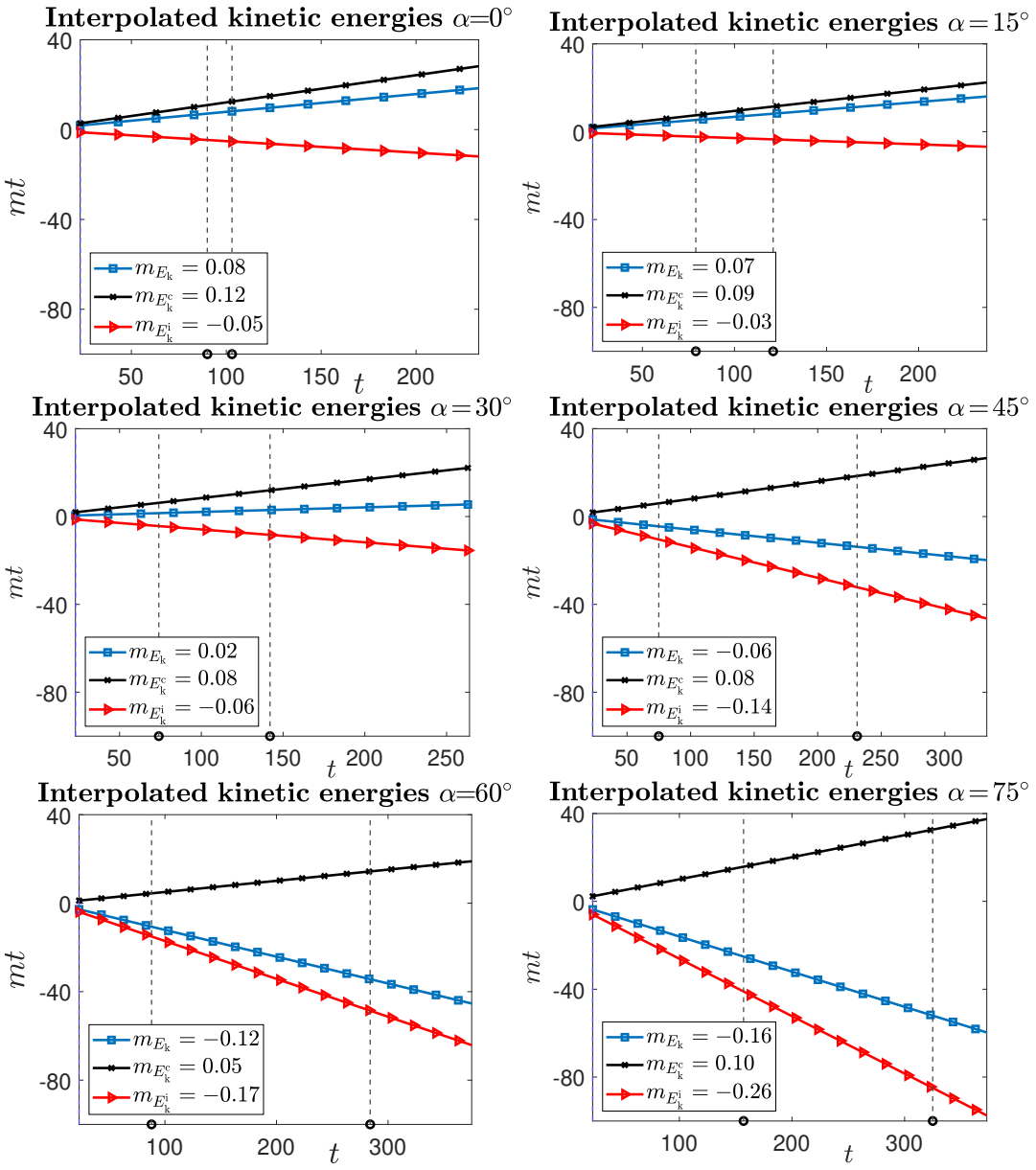

Figure 4.17: Linear least-squares fit of kinetic energy decomposition (4.8) for different values of the angle α : compressible kinetic energy (black crosses), incompressible kinetic energy (red triangles), kinetic energy (light blues squares). The respectively angular coefficients m of the fit lines are located in the legends. We recall that the plot starts from $t = 23$ (the time necessary for the solution of the (4.1) to stabilize itself) until the final time T which is different for each α. Dashed line indicate reconnection events. For $\alpha = 0°$ the kinetic energy decomposition leads to the same results as those obtained in [34].

To fully characterize the behavior of the different energy components, Figure 4.18 shows the temporal evolution of all energy contributions for each angular configuration, with all components plotted on the same graph. A logarithmic scale is adopted on the vertical axis to account for the markedly different orders of magnitude of the energy terms. The graph reveals that the energy budget is predominantly governed by the interaction and potential energy contributions, both of which remain approximately at values of the order of 10^5 throughout the evolution. These terms exceed the total kinetic energy by more than one order of magnitude, while the latter remains confined to the 10^3 range. Within the kinetic contribution, the incompressible kinetic energy ($E_{\mathrm{k}}^{\mathrm{i}}$) dominates and directly overlaps with the total kinetic energy curve (E_{k}), whereas the compressible kinetic energy ($E_{\mathrm{k}}^{\mathrm{c}}$) is positioned one order of magnitude lower, close to the 10^2 range. At this same lower energy scale, the quantum energy contribution is found to be of the order of 10^2. Although approximately three orders of magnitude smaller than the dominant interaction energy, this term exhibits the greatest sensitivity to the microscopic dynamics of the system, making it an indicator of the fine-scale physical processes associated with vortex reconnection. Finally we observe that the magnitude of the total energy ($|E_{\mathrm{tot}}|$) remains consistently stable throughout the evolution, settling just below the 10^5 threshold.

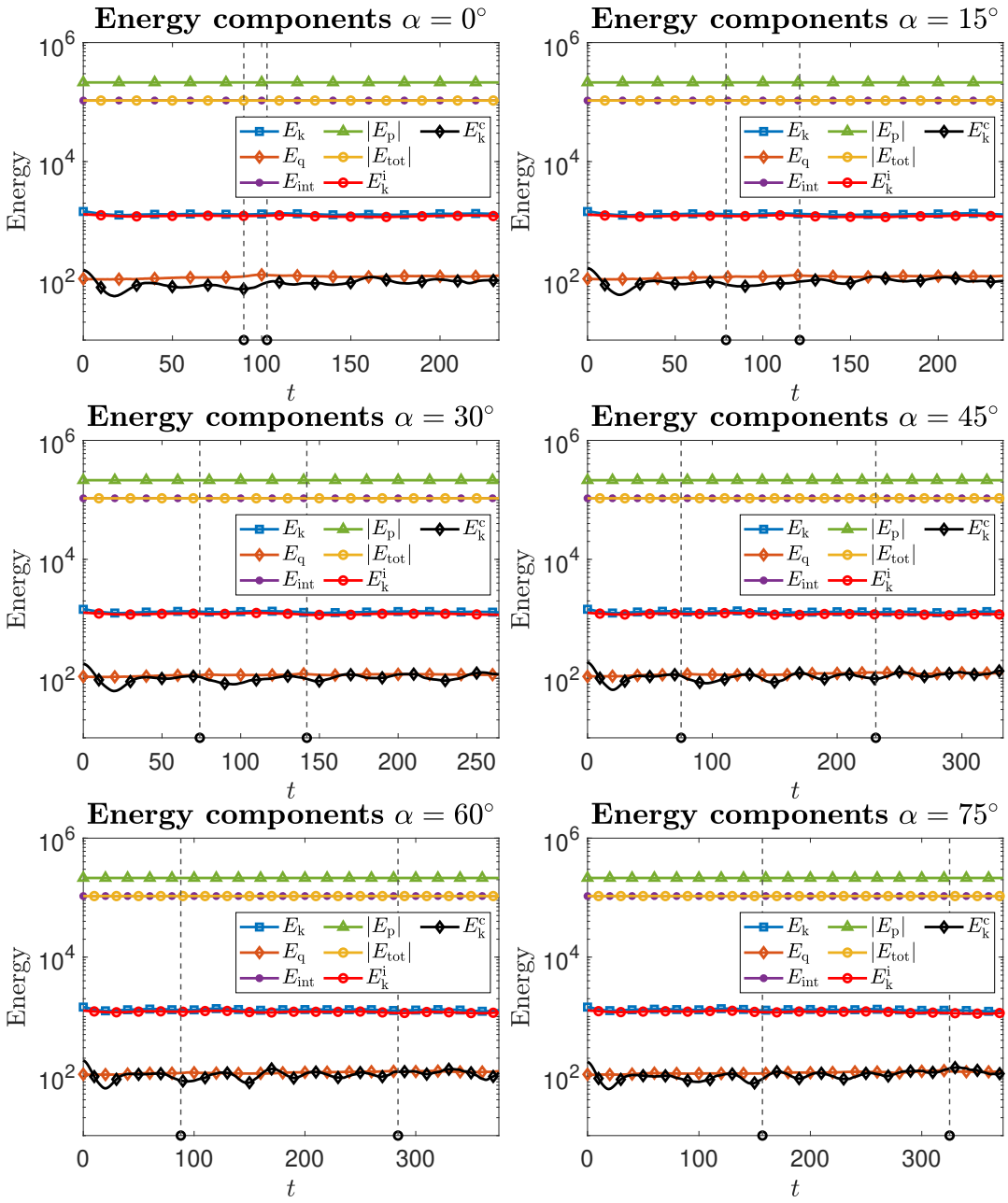

Figure 4.18: Evolution of different components of total energy on a semi-logarithmic plot for different values of angle α. Dashed line indicate reconnection events.

4.3 Analysis of negative symmetric angles

We also consider the symmetric angles $\alpha \to -\alpha$, setting the center of the ring with an opposite z-coordinate and imposing the z-dimension of the spatial domain as the interval $[-35, 55]$, in order to visualize the full dynamics of the reconnection as reported in Figure 4.19. We observed a symmetry in the evolution of the reconnection dynamics with respect to the xy-plane (for a complete simulation see the Supplemental Material [55]), as well as identical outcomes in the analysis of the total length (see Figures 4.20), total curvatures (see Figure 4.21), and in the decomposition of the total and kinetic energy (see Figures 4.22-4.23). We suggest that this symmetry is due to the conservation of the line circulation which does not "asymmetrize" the dynamics, since the angle α is varied with respect to the xy-plane. A possible direction for future study would be to initially set the ring rotating about its vertical axis while keeping the offset equal to zero; in this way an asymmetry similar to that reported in [34] might be observed. In the following section we compute the trajectory of the vortex ring center of mass and its velocity, for every positive and negative values of α, to further verify the presence of the symmetry.

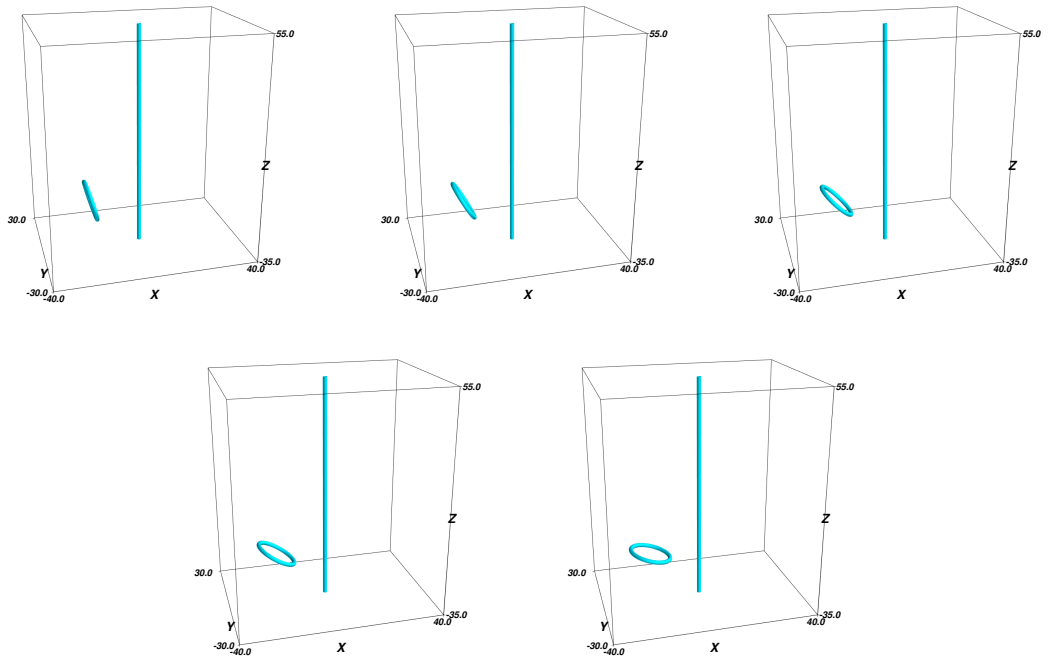

Figure 4.19: Configurations of initial conditions with different negative values of angle α. From top left to bottom right, $\alpha = -15°$, $\alpha = -30°$, $\alpha = -45°$, $\alpha = -60°$ and $\alpha = -75°$. Center of the vortex ring: $C_R = (-20,\ 0,\ -15)$. Ring normal coordinates: $\vec{n}_R = (1,\ 0,\ -\tan\alpha)$. Center of the vortex line: $C_L = (0,\ 0,\ 0)$. Line direction coordinates: $\vec{n}_L = (0,\ 0,\ -1)$. The center of the ring has the opposite z-coordinate with respect to the ring center in the case with positive α, and the z-dimension of the spatial domain is also reversed taking the interval $[-35, 55]$, in order to visualize all the dynamics of the reconnection. Isosurfaces of $\rho = 0.2$ are plotted to visualize the vortices cores.

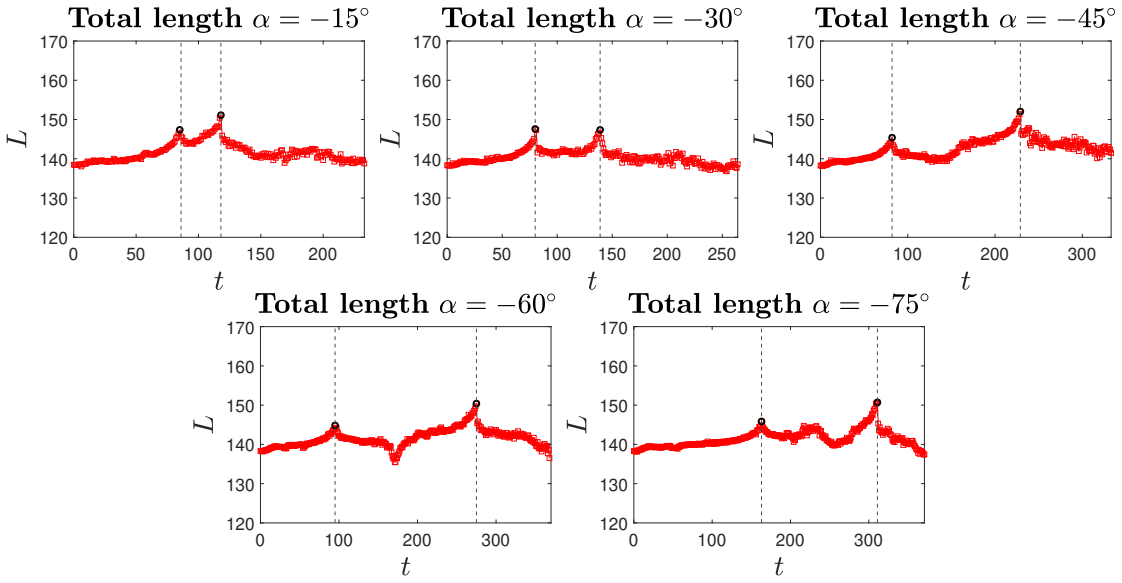

Figure 4.20: Total length L (non-dimensionalized by the healing length ξ) of nodal lines versus time t for each angle α. Vertical dashed lines indicate reconnection events.

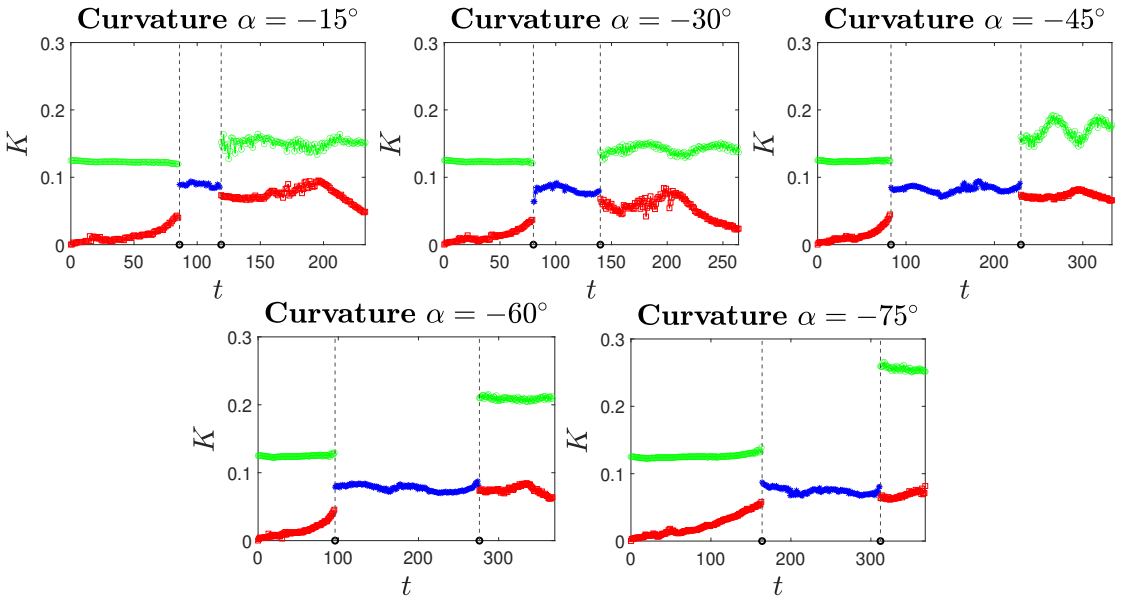

Figure 4.21: Total curvature K of nodal lines versus time t for each angle of inclination α of the vortex ring. The green circles represents the total curvature of the vortex ring, the red squares indicates the total curvature of the straight vortex line, and the blue stars indicate the total curvature of the curve between the two reconnection events. Vertical dashed lines denote reconnection events.

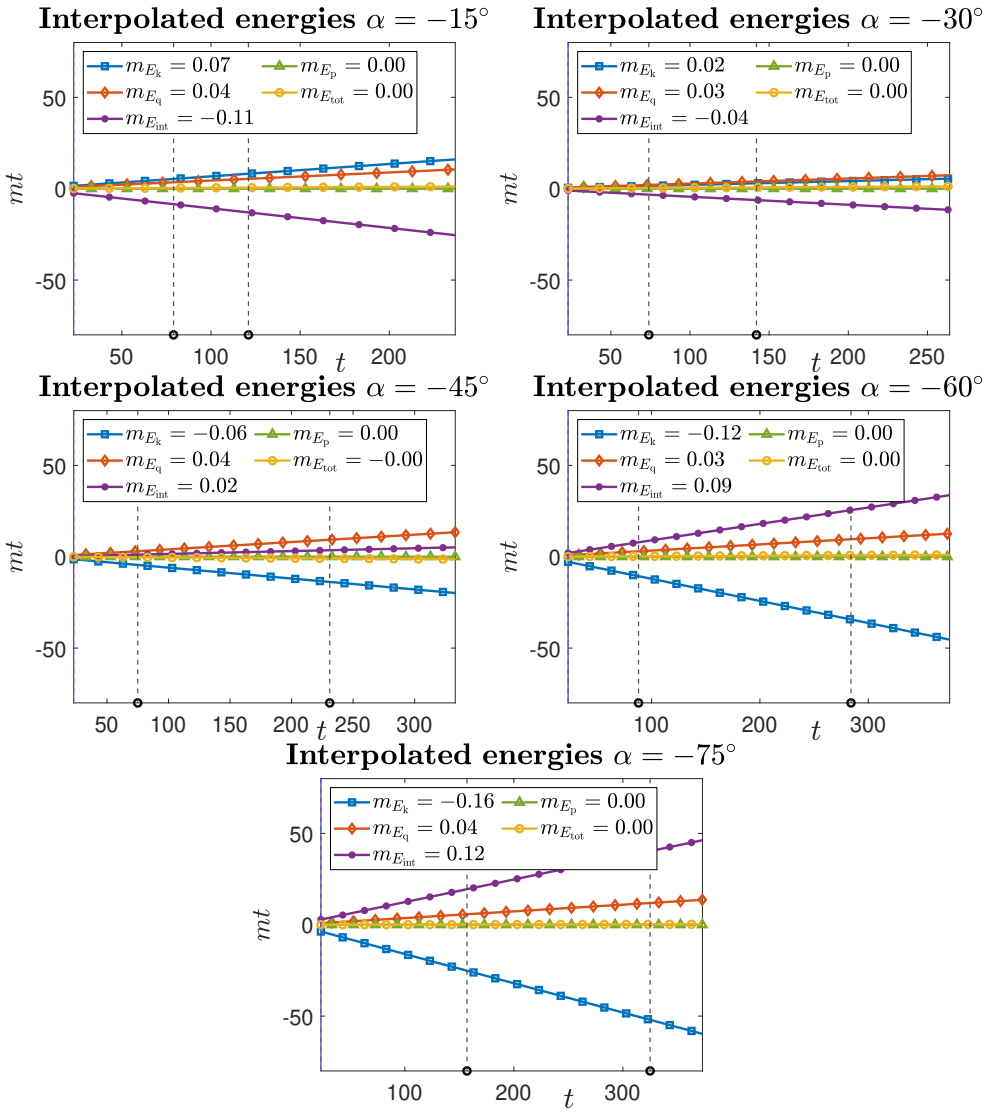

Figure 4.22: Linear least-squares fit of energy components for different values of the angle α : kinetic energy (light blue squares), quantum energy (orange diamonds), potential energy (green triangles), internal energy (purple dots) and total energy (yellow circles). The respectively angular coefficients m of the fit lines are located in the legends. Dashed line indicate reconnection events.

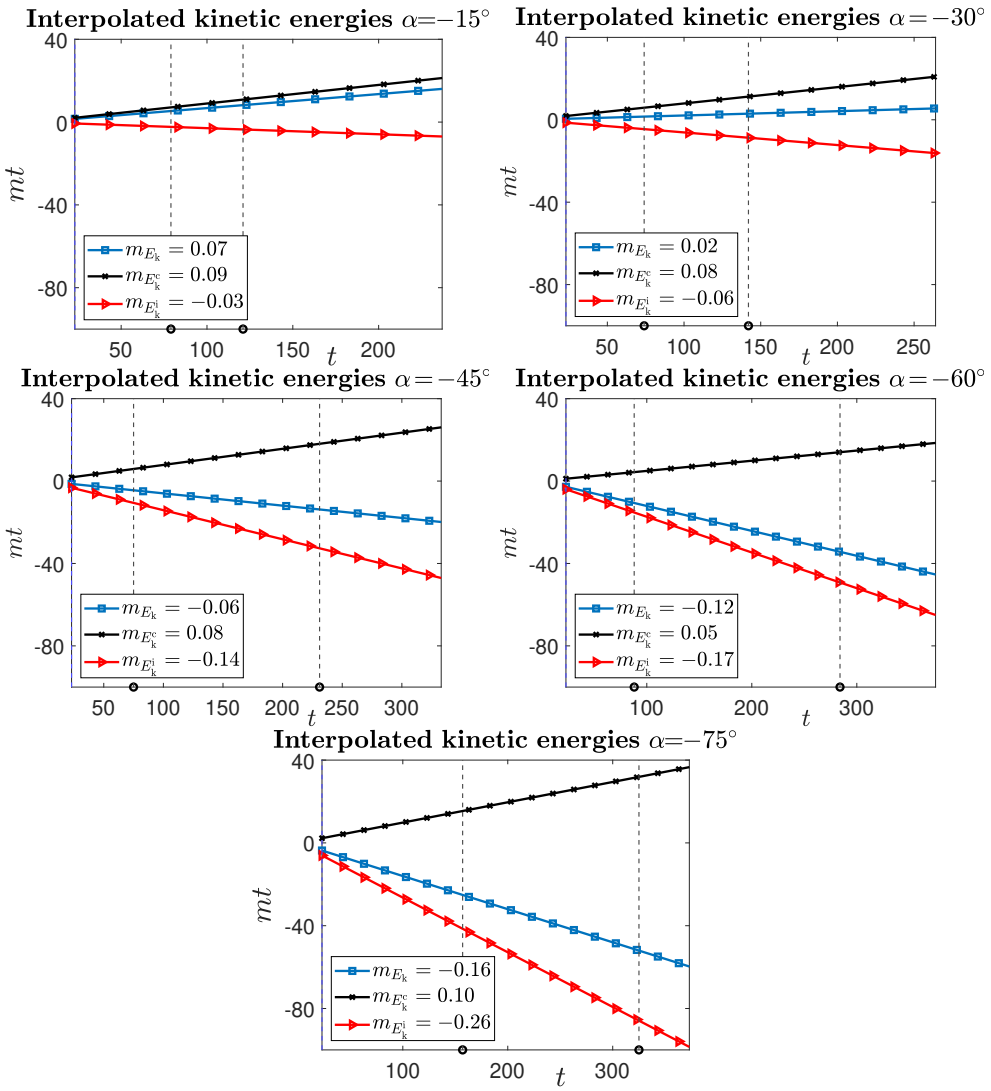

Figure 4.23: Linear least-squares fit of kinetic energy decomposition for different values of the angle α : compressible kinetic energy (black crosses), incompressible kinetic energy (red triangles), kinetic energy (light blues squares). The respectively angular coefficients m of the fit lines are located in the legends. Dashed line indicate reconnection events.

4.3.1 Trajectory and velocity of ring center of vorticity

We numerically extrapolate the nodal lines of the vortices cores as done in [2, 51] and we compute the ring's "centre of vorticity"

$$x_{CM}^{R} := \left(\frac{1}{n} \sum_{i=1}^{n} x_i, \frac{1}{n} \sum_{i=1}^{n} y_i, \frac{1}{n} \sum_{i=1}^{n} z_i \right), \tag{4.9}$$

with $n = \text{n}^\circ$ of points $P_i(x_i, y_i, z_i)$ of the ring nodal line. We plot the trajectory of (4.9) on the xy, xz, and yz planes in Figures 4.24, 4.25, and 4.26, since the ring dynamics spans all three planes.

Additionally, as done in [34], we calculate the vortex ring's velocity as

$$\mathbf{v}_{\text{ring}} := \frac{\Delta x_{CM}^{R}}{\Delta t},$$

and evaluate the ratio $\frac{\mathbf{v}_{\text{ringfin}}}{\mathbf{v}_{\text{ringin}}}$, where $\mathbf{v}_{\text{ringfin}}$ and $\mathbf{v}_{\text{ringin}}$ are the mean value of the velocity calculated respectively after and before the reconnection (since, as stated in [34], the motion of the ring can be considered uniform due to the slight interaction with the vortex line).

To complete the analysis, we determine the deflection angles

$$\begin{aligned} \theta &= \theta_{\text{in}} - \theta_{\text{fin}} \\ \beta &= \beta_{\text{in}} - \beta_{\text{fin}} \\ \gamma &= \gamma_{\text{in}} + \gamma_{\text{fin}} \end{aligned}$$

on the xy-plane, xz-plane and yz-plane respectively, for each value of α (see Figures 4.24-4.26). The result of this study is reported in Figures 4.27-4.28 and the conclusion is that there is an evidence of a symmetry, w.r.t the positive/negative values of α, in the computed values of the deflection angles θ, β, γ and in the velocity values (see Figure 4.28), up to some numerical inaccuracy.

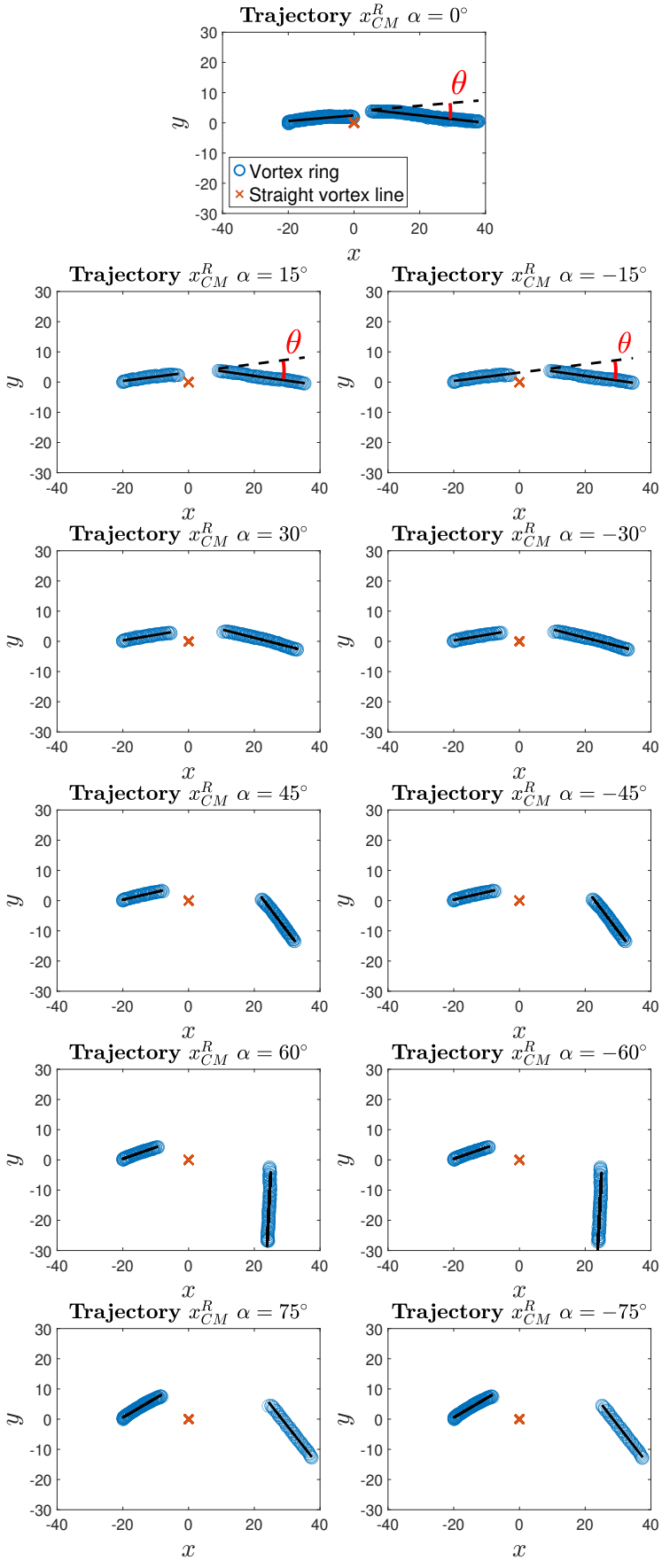

Figure 4.24: Trajectory of the ring centre of vorticity x^R_{CM} on the xy-plane for each angle α.

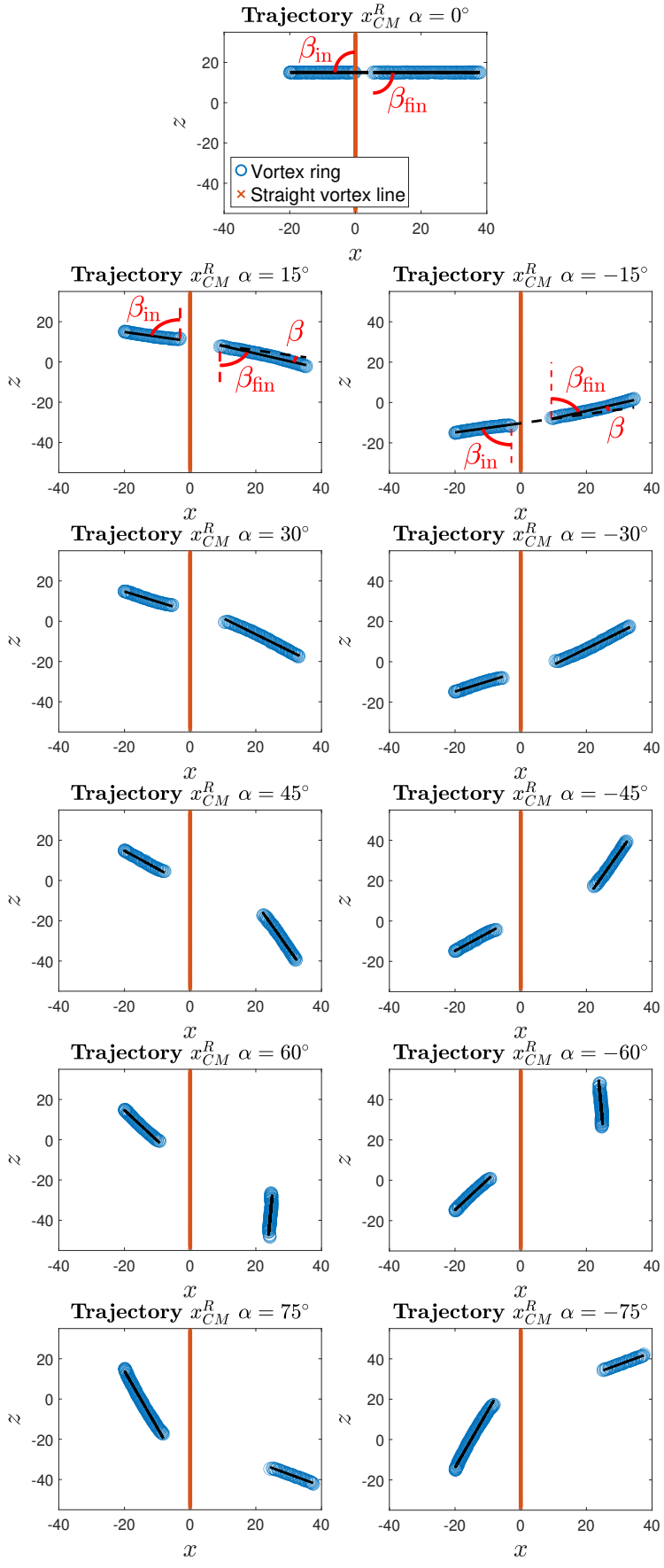

Figure 4.25: Trajectory of the ring centre of vorticity x^R_{CM} on the xz-plane for each angle α.

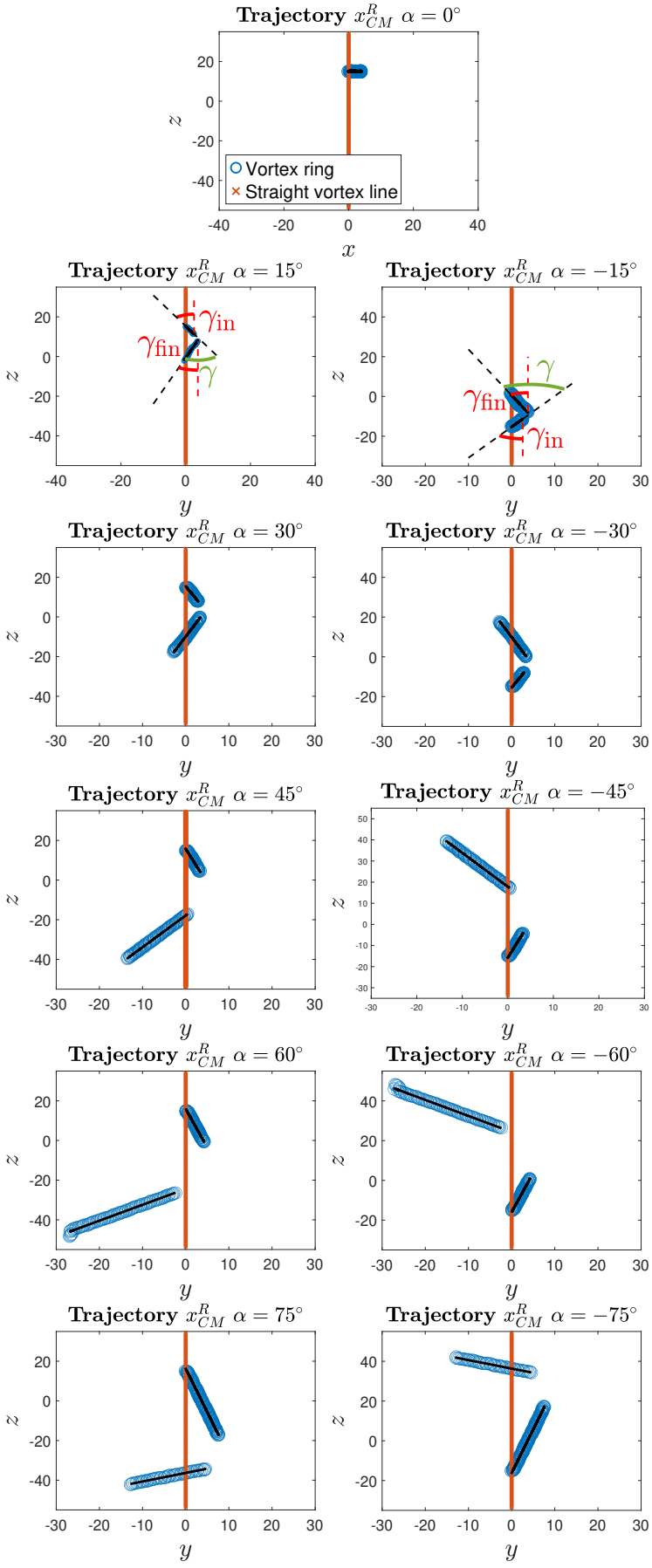

Figure 4.26: Trajectory of the ring centre of vorticity x^R_{CM} on the yz-plane for each angle α.

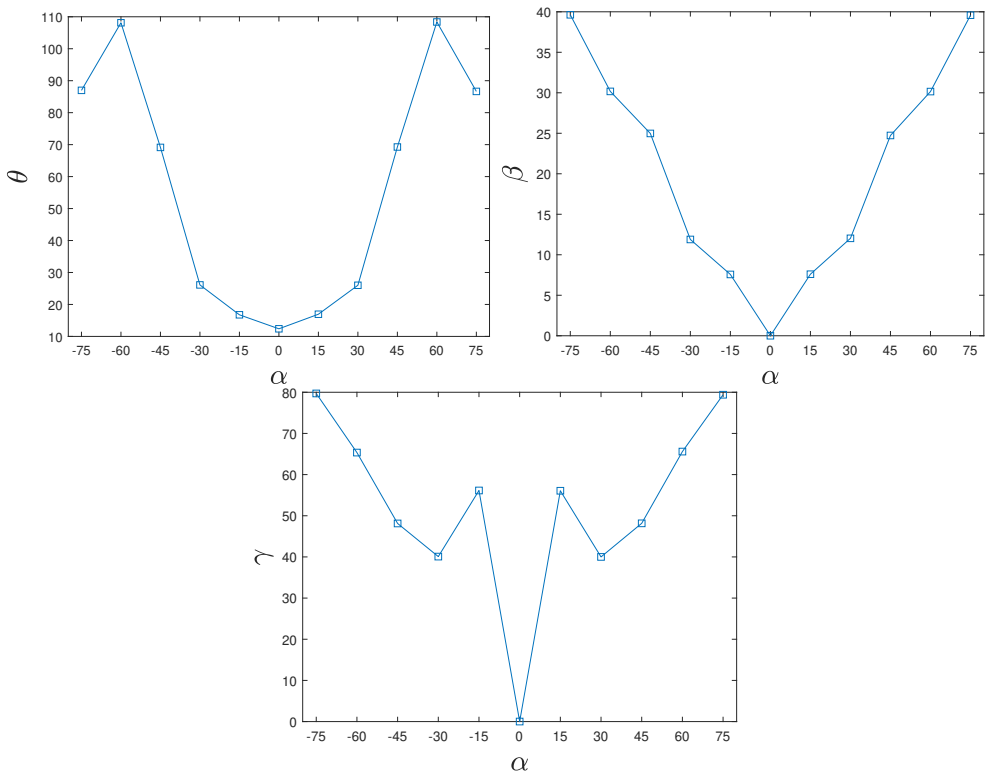

Figure 4.27: Deflection angles of the trajectory of the vortex ring center of mass for each angle α. From top to the bottom: on the xy-plane, on the xz-plane and on the yz-plane.

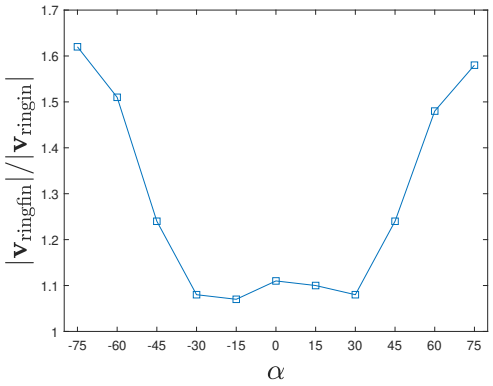

Figure 4.28: Variation of the final ring velocity magnitude as a function of α. There is an evidence of symmetry up to numerical inaccuracy.

4.4 Concluding remarks

We have studied the reconnection between an inclined vortex ring and a straight vortex line within the framework of superfluids, whose dynamics is driven by the Gross-Pitaevskii Equation (GPE). They first reconnect in a single curve, and then reconnect again giving rise to a 'curved' vortex line and a perturbed vortex ring.

We have analyzed the behavior of the total length and curvature of the vortex centerlines and the re-distribution of energy among its components as the angle α between the plane of the vortex ring and the vortex line varies. The total length exhibits two peaks corresponding to the reconnections, while the curvatures of the ring and the line increase after the second reconnection with respect to their values before the first reconnection. These phenomena occur for every angle analyzed.

By linearly fitting the time evolution of the different components of energy we have found the existence of a *critical* angle $\bar{\alpha}$ at which the coefficient m_{E_k} and m_{E_int} (kinetic and internal components, respectively) change signs. In particular, the coefficient m_{E_k} is positive for $\alpha < \bar{\alpha}$ and negative otherwise, whereas the opposite occurs for m_{E_int}. The slope m_{E_q} of the quantum contribution to the total energy remains consistently positive independently of the angle α, therefore the quantum energy grows at a constant rate regardless of the angle and, due to the conservation of total energy, the internal energy must compensate for the trend of the kinetic energy by showing an opposite behavior. The further decomposition of the kinetic energy into its incompressible and compressible components shows that the coefficient $m_{E_\mathrm{k}^\mathrm{i}}$ of the linear fit of the former is negative and decreases with increasing α, whereas the coefficient $m_{E_\mathrm{k}^\mathrm{c}}$ of the latter is positive and decreases with α, a clear sign of the generation of sound waves.

The fact that the curvature is associated, via the Localized Induction Approximation (LIA) [17], with the velocity of the nodal lines and thus with their kinetic energy, and that for each angle the total curvature of both the line and the vortex ring after the second reconnection increases with respect to their initial values, allows us to deduce that the loss of incompressible kinetic energy in the fluid is compensated by a corresponding increase in the kinetic energy of the lines themselves.

The decomposition of kinetic energy also reveals that the generation of sound waves is maximal at $\alpha = 0°$. As the angle increases, the growth rate of the compressible kinetic energy progressively decreases. This behavior is further confirmed by the analysis of the iso-surfaces of density (see Figure 4.14), which reveals that the acoustic impulse is weaker as the angle α grows.

On the contrary, for larger values of α, the kinetic energy is predominantly composed of the incompressible component, which exhibits a more pronounced decrease as α increases. This leads to a progressive decline in the value of m_{E_k}, a trend further driven by the attenuation of the growth rate of the compressible component. For $\alpha > \bar{\alpha}$, m_{E_k} becomes negative, indicating a gradual decrease in kinetic energy beyond these angular values. Correspondingly, for $\alpha > \bar{\alpha}$, we have observed an increase in the curvature of the ring after the second reconnection. We deduce once again that, since curvature is associated with the velocity of the nodal lines, the progressive loss of the fluid's incompressible kinetic energy with increasing angle is offset by a progressive increase in the kinetic energy of the nodal lines.

Chapter 5

Vortex reconnections in a binary immiscible Bose-Einstein condensate

Vortex dynamics is also studied in two-component Bose–Einstein condensates (BECs), which consist of two condensate components formed by distinct hyperfine states of states of the same atomic species, different isotopes of the same element, or entirely different atomic species. The components can be either in the miscible or immiscible regime.

One of the main goals in the studies of vortex dynamics, both experimentally and theoretically, is the detection of three - dimensional vortex structures, including systems with tangled vortices. In this context a two-component BEC in the immiscible regime is a suitable setting for tracking vortices, since the vortices in the majority component - which contains the majority of the total atoms - are infilled by the second component acting as a passive tracer without destructively imaging the majority component. Nevertheless the presence of the minority component may affect vortex dynamics, depending on the number of atoms filling the vortices. Hence it is crucial to identify regimes in which the filling component does not significantly influence vortex dynamics. Conversely, in more extreme cases, the filling component may give rise to novel vortex dynamics behaviors that have no counterpart in conventional single-component superfluids.

In this work we investigate a vortex reconnection between two perpendicular straight vortex lines in immiscible two-component BECs [36] where the vortices reside in the majority component, whereas their cores are filled by the minority component. We vary the number of atoms in the second condensate and analyze the coefficients in the scaling law (3.1) to study how the minority component affects the reconnection dynamics, and whether the process remains unchanged or becomes faster or slower.

5.1 The model

Let us consider species 1 to be the majority component and refer to species 2 as the infilling component. Our aim is to simulate a reconnection between two perpendicular vortex lines in condensate 1, infilled by condensate 2. We now introduce the equations that govern this dynamics.

Definition 5.1.1. *The system of two BECs which are dilute and weakly interacting in*

the zero-temperature limit, is governed by **coupled Gross-Pitaevskii Equations** *:*

$$\begin{cases} \mathrm{i}\hbar\frac{\partial\Psi_1}{\partial t} &= -\frac{\hbar^2}{2m_1}\Delta\Psi_1 + V_1(\mathbf{r})\Psi_1 + g_{11}|\Psi_1|^2\Psi_1 - \mu_1\Psi_1 + g_{12}|\Psi_2|^2\Psi_1\,, \\ \mathrm{i}\hbar\frac{\partial\Psi_2}{\partial t} &= -\frac{\hbar^2}{2m_2}\Delta\Psi_2 + V_2(\mathbf{r})\Psi_2 + g_{22}|\Psi_2|^2\Psi_2 - \mu_2\Psi_2 + g_{12}|\Psi_1|^2\Psi_2\,, \end{cases} \tag{5.1}$$

where $\Psi_k = \Psi_k(\mathbf{r},t)$ is the mean-field wave function of the k-th component, $k = 1, 2$, m_k is the mass of the atomic species in the k-th component and the intra- and inter- species interactions are given by

$$g_{11} = \frac{4\pi\hbar^2 a_{11}}{m_1}\,, \qquad g_{22} = \frac{4\pi\hbar^2 a_{22}}{m_2}\,, \qquad g_{12} = \frac{2\pi\hbar^2 a_{12}(m_1+m_2)}{m_1 m_2}\,.$$

The density profiles of the components are $n_1(\mathbf{r},t) = |\Psi_1(\mathbf{r},t)|^2$ and $n_2(\mathbf{r},t)| = |\Psi_2(\mathbf{r},t)|^2$, and the components are normalized to N_1 and N_2 atoms.

In our setting we impose that the two condensates are in the same external potential, thus $V_1(\mathbf{r}) = V_2(\mathbf{r}) = V(\mathbf{r})$, and we will work in natural units of the majority component.

We then introduce dimensionless variables :

- density in terms of the uniform density $n_{01} = \frac{\mu_1}{g_{11}}$,
- energy in terms of the chemical potential $\mu_1 = n_{01}g_{11}$,
- lengths in terms of the healing length $\xi_1 = \frac{\hbar}{\sqrt{n_{01}m_1 g_{11}}} = \frac{\hbar}{\sqrt{\mu_1 m_1}}$,
- time in terms of $\tau_1 = \frac{\hbar}{\mu_1}$.

In these units (5.1) takes the following dimensionless form.

Proposition 5.1.1. *The system of two BEC's which are dilute and weakly interacting in the zero-temperature limit, is governed by the following coupled dimensionless Gross-Pitaevskii Equations (CGPE):*

$$\begin{cases} \mathrm{i}\frac{\partial\Psi_1'}{\partial t'} = & \Big(-\frac{1}{2}\Delta' + |\Psi_1'|^2 + V' - 1 + g_{12}'|\Psi_2'|^2\Big)\Psi_1'\,, \\ \mathrm{i}\frac{\partial\Psi_2'}{\partial t'} = & \Big(-\frac{1}{2}m'\Delta' + g_{22}'|\Psi_2'|^2 + V' - \mu_{22}' + g_{12}'|\Psi_1'|^2\Big)\Psi_2'\,, \end{cases} \tag{5.2}$$

where $\Psi_k = \sqrt{n_{01}}\Psi_k'$, $t' = t/\tau_1$, $\Delta' = \frac{1}{\xi_1^2}\Delta$, $V' = V/\mu_1$, $m' = m_1/m_2$ is the ratio of atomic masses m_k, $g_{12}' = g_{12}/g_{11}$ is the ratio of the inter- and intraspecies interaction parameters, $g_{22}' = g_{22}/g_{11}$ is the ratio of the intraspecies interaction parameters and $\mu_{22}' = g_{22}'\frac{n_2}{n_1}$ is the ratio of the chemical potentials. The (5.2) *still preserves the normalization conditions*

$$N_k = \xi_1^3 n_{01}\int |\Psi_k'|^2\, d^3\mathbf{r}'\,,$$

up to a factor $\xi_1^3 n_{01}$, which must be included to recover the physical number of particles.

Proof. Let us introduce the following dimensionless variables

$$x' = \frac{x}{\xi_1}, \quad y' = \frac{y}{\xi_1}, \quad z' = \frac{z}{\xi_1}, \quad t' = \frac{t}{\tau_1} \tag{5.3}$$

and

$$\Psi_1 = \varphi\,\Psi_1', \quad \Psi_2 = \varphi\,\Psi_2' \quad \text{with} \quad \varphi = \sqrt{n_{01}}\,. \tag{5.4}$$

The relations for spatial and time derivatives, using the chain rule, are

$$\frac{d}{dx} = \frac{1}{\xi_1}\frac{d}{dx'} \quad \frac{d}{dy} = \frac{1}{\xi_1}\frac{d}{dy'} \quad \frac{d}{dz} = \frac{1}{\xi_1}\frac{d}{dz'} \quad \frac{d}{dt} = \frac{1}{\tau_1}\frac{d}{dt'}\,. \tag{5.5}$$

Hence the Laplacian operator acting on the primed variables is

$$\Delta = \frac{1}{\xi^2}\Delta'\,. \tag{5.6}$$

Now we substitute the expressions (5.5), (5.4) and (5.6) into (5.1), obtaining

$$\begin{cases} \mathrm{i}\hbar\frac{1}{\tau}\frac{\partial(\varphi\Psi_1')}{\partial t'} = -\frac{\hbar^2}{2m_1}\frac{1}{\xi^2}\Delta'(\varphi\Psi_1') + V\varphi\Psi_1' + g_{11}|\varphi\Psi_1'|^2\varphi\Psi_1' - \mu_1\varphi\Psi_1' + g_{12}|\varphi\Psi_2'|^2\varphi\Psi_1'\,, \\ \mathrm{i}\hbar\frac{1}{\tau}\frac{\partial(\varphi\Psi_2')}{\partial t'} = -\frac{\hbar^2}{2m_2}\frac{1}{\xi^2}\Delta'(\varphi\Psi_2') + V\varphi\Psi_2' + g_{22}|\varphi\Psi_2'|^2\varphi\Psi_2' - \mu_2\varphi\Psi_2' + g_{12}|\varphi\Psi_1'|^2\varphi\Psi_2'\,. \end{cases}$$

Additionally we divided by φ

$$\begin{cases} \mathrm{i}\hbar\frac{1}{\tau}\frac{\partial\Psi_1'}{\partial t'} = -\frac{\hbar^2}{2m_1\xi^2}\Delta'\Psi_1' + V\Psi_1' + g_{11}\varphi^2|\Psi_1'|^2\Psi_1' - \mu_1\Psi_1' + g_{12}\varphi^2|\Psi_2'|^2\Psi_1'\,, \\ \mathrm{i}\hbar\frac{1}{\tau}\frac{\partial\Psi_2'}{\partial t'} = -\frac{\hbar^2}{2m_2\xi^2}\Delta'\Psi_2' + V\Psi_2' + g_{22}\varphi^2|\Psi_2'|^2\Psi_2' - \mu_2\Psi_2' + g_{12}\varphi^2|\Psi_1'|^2\Psi_2'\,, \end{cases}$$

and replace the value of $\tau_1 = \frac{\hbar}{\mu_1}$, getting

$$\begin{cases} \mathrm{i}\cancel{\hbar}\frac{\mu_1}{\cancel{\hbar}}\frac{\partial\Psi_1'}{\partial t'} = -\frac{\cancel{\hbar^2}\mu_1\cancel{m_1}}{2\cancel{m_1}\cancel{\hbar^2}}\Delta'\Psi_1' + V\Psi_1' + \cancel{g_{11}}\frac{\mu_1}{\cancel{g_{11}}}|\Psi_1'|^2\Psi_1' - \mu_1\Psi_1' + g_{12}\frac{\mu_1}{g_{11}}|\Psi_2'|^2\Psi_1'\,, \\ \mathrm{i}\cancel{\hbar}\frac{\mu_1}{\cancel{\hbar}}\frac{\partial\Psi_2'}{\partial t'} = -\frac{\cancel{\hbar^2}\mu_1 m_1}{2m_2\cancel{\hbar^2}}\Delta'\Psi_2' + V\Psi_2' + g_{22}\frac{\mu_1}{g_{11}}|\Psi_2'|^2\Psi_2' - \mu_2\Psi_2' + g_{12}\frac{\mu_1}{g_{11}}|\Psi_1'|^2\Psi_2'\,. \end{cases}$$

Then we divide by μ_1 to have

$$\begin{cases} \mathrm{i}\frac{\partial\Psi_1'}{\partial t'} = -\frac{1}{2}\Delta'\Psi_1' + \frac{V}{\mu_1}\Psi_1' + |\Psi_1'|^2\Psi_1' - \Psi_1' + \frac{g_{12}}{g_{11}}|\Psi_2'|^2\Psi_1'\,, \\ \mathrm{i}\frac{\partial\Psi_2'}{\partial t'} = -\frac{m_1}{2m_2}\Delta'\Psi_2' + \frac{V}{\mu_1}\Psi_2' + \frac{g_{22}}{g_{11}}|\Psi_2'|^2\Psi_2' - \frac{\mu_2}{\mu_1}\Psi_2' + \frac{g_{12}}{g_{11}}|\Psi_1'|^2\Psi_2'\,. \end{cases}$$

Finally we define

$$V' = \frac{V}{\mu_1}\,, \quad g_{12}' = \frac{g_{12}}{g_{11}}\,, \quad m' = \frac{m_2}{m_1}\,, \quad g_{22}' = \frac{g_{22}}{g_{11}}\,, \quad \mu_{22}' = \frac{\mu_2}{\mu_1} = \frac{n_2 g_{22}}{n_1 g_{11}} = g_{22}'\frac{n2}{n1}\,,$$

and we have

$$\begin{cases} \mathrm{i}\frac{\partial\Psi_1'}{\partial t'} = -\frac{1}{2}\Delta'\Psi_1' + V'\Psi_1' + |\Psi_1'|^2\Psi_1' - \Psi_1' + g_{12}'|\Psi_2'|^2\Psi_1'\,, \\ \mathrm{i}\frac{\partial\Psi_2'}{\partial t'} = -\frac{1}{2}m'\Delta'\Psi_2' + V'\Psi_2' + g_{22}'|\Psi_2'|^2\Psi_2' - \mu_{22}'\Psi_2' + g_{12}'|\Psi_1'|^2\Psi_2'\,. \end{cases}$$

Furthermore, the total number of particles for component k is

$$N_k = \int |\Psi_k|^2 \, d^3\mathbf{r} = \int n_{01}|\Psi_k'|^2 \xi_1^3 \, d^3\mathbf{r}' = n_{01}\xi_1^3 \int |\Psi_k'|^2 \, d^3\mathbf{r}'$$

since

$$\mathbf{r} = \xi_1 \mathbf{r}' \quad \text{hence} \quad d^3\mathbf{r} = \xi_1^3 d^3\mathbf{r}' \,,$$

and

$$\Psi_k = \sqrt{n_{01}}\Psi_k' \quad \text{hence} \quad |\Psi_k|^2 = n_{01}|\Psi_k'|^2 \,.$$

□

We consider the two-component system (5.2) in the immiscible regime, i.e.

$$g_{12}^2 > g_{11}g_{22} \,, \tag{5.7}$$

corresponding to

$$(g_{11}g_{12}')^2 > g_{11}g_{11}g_{22}' \quad \Rightarrow \quad \cancel{g_{11}^2}(g_{12}')^2 > \cancel{g_{11}^2}g_{22}' \quad \Rightarrow \quad (g_{12}')^2 > g_{22}' \tag{5.8}$$

in dimensionless variables. For notational convenience, the primes will be omitted throughout the remainder of this chapter.

The total energy of the system is given in the following proposition.

Proposition 5.1.2. *The total energy corresponding of the system* (5.2) *is*

$$\begin{aligned} E = \int \Bigg[& \frac{1}{2}|\nabla\Psi_1|^2 + \frac{1}{2}m|\nabla\Psi_2|^2 + \frac{1}{2}|\Psi_1|^4 + \frac{1}{2}g_{22}|\Psi_2|^4 + g_{12}|\Psi_1|^2|\Psi_2|^2 \\ & + (V-1)|\Psi_1|^2 + (V-\mu_{22})|\Psi_2|^2 \Bigg] \, d^3\mathbf{r} \,. \end{aligned} \tag{5.9}$$

Proof. Let us consider (5.2), we multiply the first equation by $\overline{\Psi_1}$ and the second by $\overline{\Psi_2}$, and integrate over the volume:

$$\int \overline{\Psi_1}\, \mathrm{i}\frac{\partial\Psi_1}{\partial t} \, d^3\mathbf{r} = \int \Big[-\frac{1}{2}\Delta\Psi_1 + |\Psi_1|^2\Psi_1 + g_{12}|\Psi_2|^2\Psi_1 + (V-1)\Psi_1 \Big] \overline{\Psi_1} \, d^3\mathbf{r} \tag{5.10}$$

$$\int \overline{\Psi_2}\, \mathrm{i}\frac{\partial\Psi_2}{\partial t} d^3\mathbf{r} = \int \Big[-\frac{1}{2}m\Delta\Psi_2 + g_{22}|\Psi_2|^2\Psi_2 + g_{12}|\Psi_1|^2\Psi_2 + (V-\mu_{22})\Psi_2 \Big] \overline{\Psi_2} \, d^3\mathbf{r} \,. \tag{5.11}$$

Using integration by parts on the Laplacian terms and assuming boundary conditions that vanish at the boundary we have:

$$-\int \overline{\Psi_1}(\Delta\Psi_1) \, d^3\mathbf{r} = \int |\nabla\Psi_1|^2 d^3\mathbf{r} \,, \quad -\int \overline{\Psi_2}(\Delta\Psi_2) \, d^3\mathbf{r} = \int |\nabla\Psi_2|^2 d^3\mathbf{r} \,.$$

Thus Eqs. (5.10)(5.11) become

$$\int \overline{\Psi_1}\, \mathrm{i}\frac{\partial\Psi_1}{\partial t} \, d^3\mathbf{r} = \int \Big[\frac{1}{2}|\nabla\Psi_1|^2 + |\Psi_1|^4 + g_{12}|\Psi_2|^2|\Psi_1|^2 + (V-1)|\Psi_1|^2 \Big] \, d^3\mathbf{r}$$

$$\int \overline{\Psi_2}\, \mathrm{i}\frac{\partial\Psi_2}{\partial t} d^3\mathbf{r} = \int \Big[\frac{1}{2}m|\nabla\Psi_2|^2 + g_{22}|\Psi_2|^4 + g_{12}|\Psi_1|^2|\Psi_2|^2 + (V-\mu_{22})|\Psi_2|^2 \Big] \, d^3\mathbf{r} \,.$$

Since $\mathrm{i}\frac{\partial \Psi_k}{\partial t} = \frac{\delta E}{\delta \overline{\Psi}_k}$, with $k = 1, 2$, the total energy functional reads:

$$E = \int \left[\frac{1}{2}|\nabla\Psi_1|^2 + \frac{1}{2}m|\nabla\Psi_2|^2 + \frac{1}{2}|\Psi_1|^4 + \frac{1}{2}g_{22}|\Psi_2|^4 + g_{12}|\Psi_1|^2|\Psi_2|^2 \right.$$
$$\left. + (V-1)|\Psi_1|^2 + (V-\mu_{22})|\Psi_2|^2 \right] d^3\mathbf{r}\,.$$

□

5.2 Numerical details

We set $g_{22} = 1.0$, $g_{12} = 1.1$ in (5.2), in order to satisfy the immiscible regime (5.8), and take $m = 1$. With the aim of varying the number of atoms in the second component, we change the parameter $\frac{n_2}{n_1}$ that appears in the expression of $\mu_{22} = g_{22}\frac{n_2}{n_1}$. The selected values are $\frac{n_2}{n_1} = 0, 0.25, 0.5$ and 0.75.

Then we impose a circular hard-wall potential with radius $R = 15$, sufficiently large to ensure that the boundary conditions do not affect the infilled vortex solutions. In our framework the hard-wall trapping potential is defined as

$$V(x,y,z) = \begin{cases} 10 & \text{if } \sqrt{x^2+y^2} \geq R \ \vee \ z \geq 15 \ \vee \ z \leq -15\,, \\ 0 & \text{otherwise}\,. \end{cases}$$

For the numerical solution of (5.2) we employ a second-order equispaced finite-difference scheme for the spatial discretization, while the discretization of the action of the three-dimensional Laplacian Δ is computed using the `mump` function [56]. The spatial domain is $[-20, 20]^3$, with spatial resolution $\Delta x = \Delta y = \Delta z = 1/2$ (i.e. a grid of 81^3 points). Time integration is performed using the second-order Adams-Bashforth method:

$$\begin{cases} \Psi_1^{n+2} &= \Psi_1^{n+1} + \frac{\tau}{2}(3\,F_1(\Psi_1^{n+1}, \Psi_2^{n+1}) - F_1(\Psi_1^n, \Psi_2^n))\,, \\ \Psi_2^{n+2} &= \Psi_2^{n+1} + \frac{\tau}{2}(3\,F_2(\Psi_1^{n+1}, \Psi_2^{n+1}) - F_2(\Psi_1^n, \Psi_2^n))\,, \end{cases}$$

where τ is the time step set to $1/200$, and

$$F_1(\Psi_1, \Psi_2) = -\mathrm{i}\left(-\frac{1}{2}\Delta + |\Psi_1|^2 + V - 1 + g_{12}\,|\Psi_2|^2 \right)\Psi_1$$
$$F_2(\Psi_1, \Psi_2) = -\mathrm{i}\left(-\frac{1}{2}m\Delta + g_{22}|\Psi_2|^2 + V - \mu_{22} + g_{12}\,|\Psi_1|^2 \right)\Psi_2\,.$$

Since the Adams-Bashforth method is a two-step scheme, the first time step is computed using an explicit Euler method to initialize the procedure.

In the following Sections we describe the approach used to perform the numerical simulations of the vortex reconnections.

5.2.1 Tests for numerical convergence

In this subsection we numerically verify the accuracy of the time discretization, keeping the spatial grid fixed. The test is carried out using the post-imprinting initial conditions $\Psi_{1\,\mathrm{vgs}}$, $\Psi_{2\,\mathrm{vgs}}$, for $N_2/L = 2.9115$ (see Section 5.2.3) which serve as the starting point for the real-time vortex dynamics simulations. The error is measured in the infinity norm with respect to the reference solution (computed using 12800 time steps) for both the wave functions Ψ_1 and Ψ_2. The tested time steps are $100, 200, 400, 800$ and 1600. The final time is set to $T = 1$. The results, reported in Figure 5.1, show a clear decay of the error consistent with the expected second-order convergence rate of the employed Adams–Bashforth scheme.

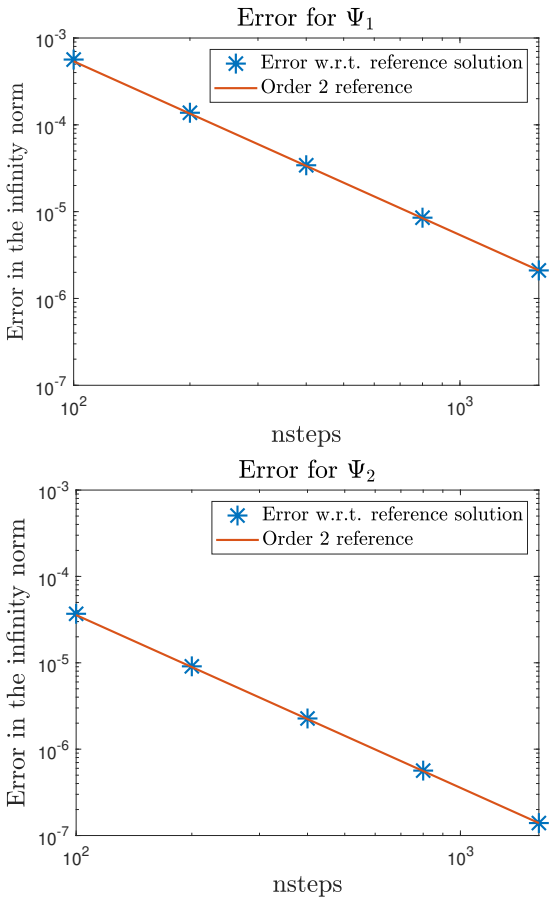

Figure 5.1: Time-step convergence test for the numerical scheme. The spatial discretization is kept fixed, while the time steps are varied. The final time is $T = 1$. The solid line represents a second-order reference slope.

We also compute the total energy (5.9) of the system and the number of atoms of both components for all tested values of the time steps, to assess the robustness of the numerical scheme. As shown in Figure 5.2, the total energy remains essentially constant for all considered time steps. Similarly, the number of atoms of both components remains stable across all considered time steps. These results match with the theoretical expectations.

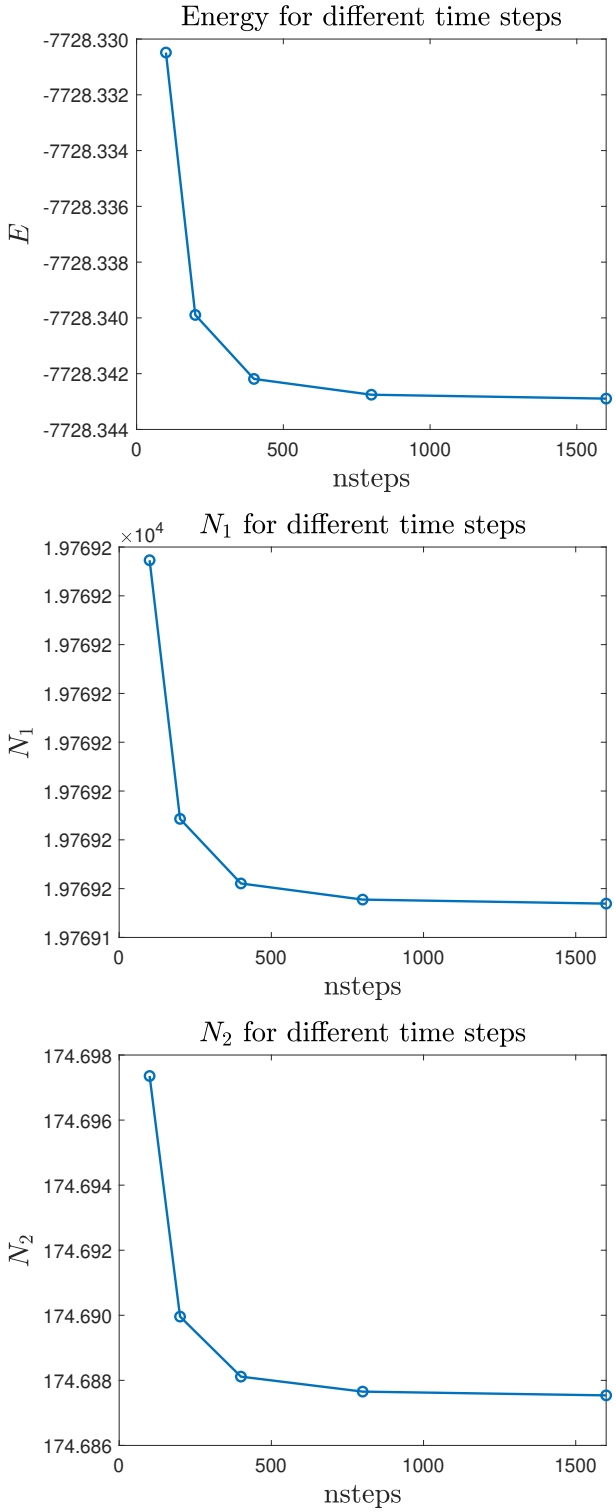

Figure 5.2: Energy and the number of atoms of both components for different nsteps. All quantities remain conserved up to numerical precision, confirming the stability and robustness of the numerical scheme.

5.2.2 Preparation of the first condensate

First we have to "prepare" the first condensate in the absence of the second component. The initial condition for the condensate 1 is constructed using the Thomas-Fermi approximation 1.7.3:

$$|\Psi_{01\,\mathrm{gs}}|^2\Psi_{01\,\mathrm{gs}} + V\Psi_{01\,\mathrm{gs}} - \Psi_{01\,\mathrm{gs}} = 0 \quad \Rightarrow \quad \Psi_{01\,\mathrm{gs}}\left(|\Psi_{01\,\mathrm{gs}}|^2 + V - 1\right) = 0\,.$$

Therefore

$$|\Psi_{01\,\mathrm{gs}}|^2 = \begin{cases} 1-V & \text{if} \quad 1 \geq V \\ 0 & \text{if} \quad 1 < V \end{cases} \quad = \quad \begin{cases} 1 & \text{if} \quad r \in C, \\ 0 & \text{if} \quad r \notin C, \end{cases}$$

where

$$C = \left\{(x,y,z) \in [-20,20]\times[-20,20]\times[-20,20] \;\middle|\; \sqrt{x^2+y^2} < R,\ z \in (-15,15)\right\}$$

is the cylindrical region where the potential V is zero, thus containing condensate 1. Hence we impose

$$\Psi_{01\,\mathrm{gs}} = \begin{cases} 1 & \text{if} \quad 1 \geq V \\ 0 & \text{if} \quad 1 < V \end{cases} = \begin{cases} 1 & r \in C\,, \\ 0 & r \notin C\,. \end{cases} \tag{5.12}$$

We set the second component $\Psi_{02\,\mathrm{gs}} = 0$ throughout the entire domain.

We numerically solve (5.2) for $n_2/n_1 = 0$, with initial conditions (5.12), by using *imaginary-time propagation*[1] [5, 36] until a final time $T = 10$, in order to evolve the solution toward the lowest-energy state of the system (see Figure 5.4). Following this method, the time step is taken as $-\mathrm{i}\tau$, and at each step the solution Ψ_1 is rescaled to conserve the number of atoms:

$$\Psi_1 = \Psi_1\sqrt{\frac{N_{01\,\mathrm{gs}}}{N_1}}, \tag{5.13}$$

where

$$N_{01\,\mathrm{gs}} = \int |\Psi_{01\,\mathrm{gs}}|^2\, d^3\mathbf{r}, \quad N_1 = \int |\Psi_1|^2\, d^3\mathbf{r}. \tag{5.14}$$

At the end of this procedure, we obtain the ground-state wave functions $\Psi_{1\,\mathrm{gs}}$ and $\Psi_{2\,\mathrm{gs}}$, with the latter being zero throughout the domain (see Figure 5.3).

[1] Imaginary-time propagation transforms the time-dependent equation into a diffusion-like equation, allowing the system to relax toward its lowest-energy (ground) state by exponentially suppressing excited states [57].

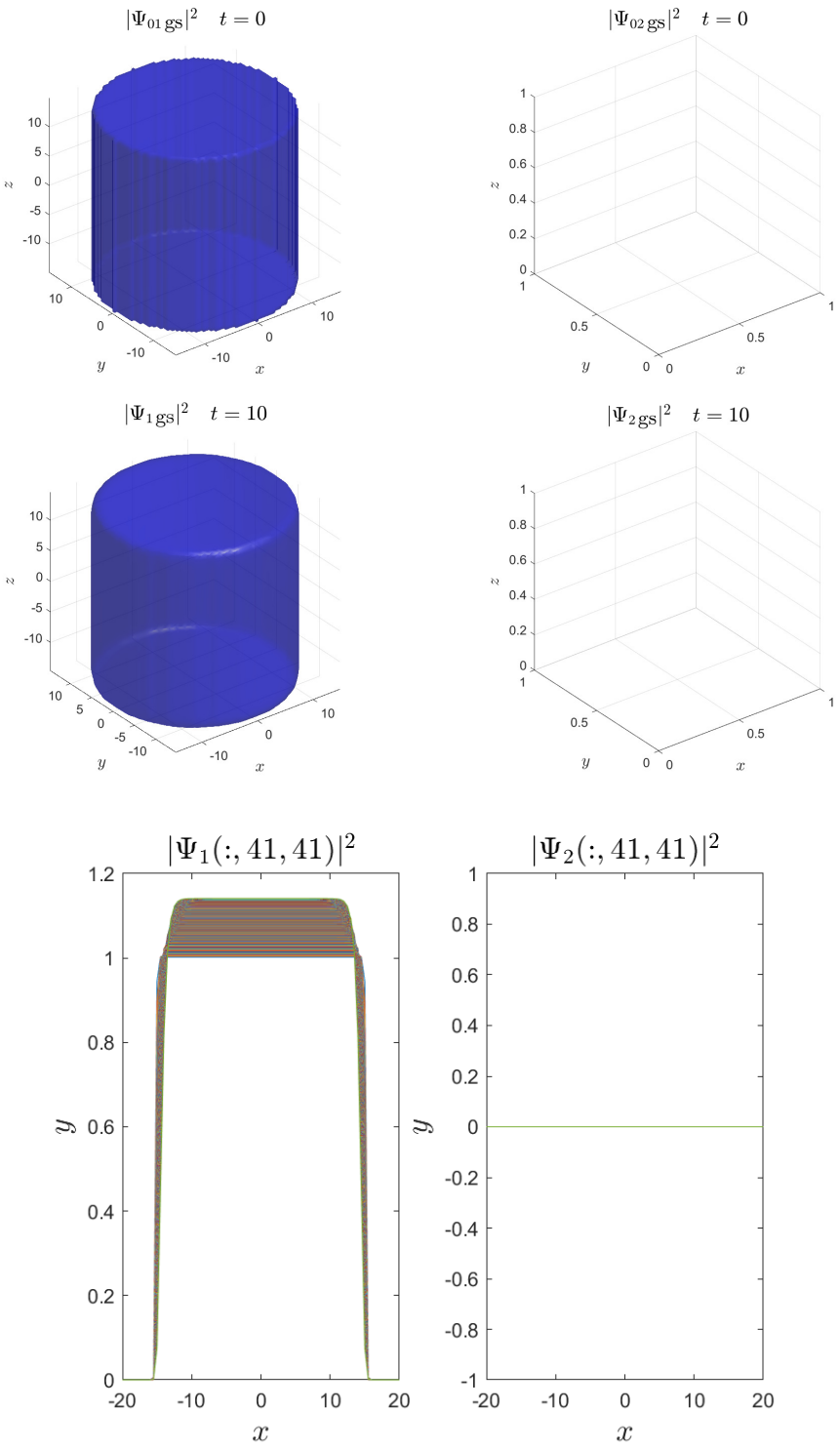

Figure 5.3: First row: density of condensate 1 (left) and condensate 2 (right) before vortex imprinting and imaginary-time propagation. Second row: density of condensate 1 (left) and condensate 2 (right) before vortex imprinting and after imaginary-time propagation. Isosurfaces of $\rho = 0.3$. Third row: slice of density of condensate 1 (left) and condensate 2 (right) during imaginary time propagation.

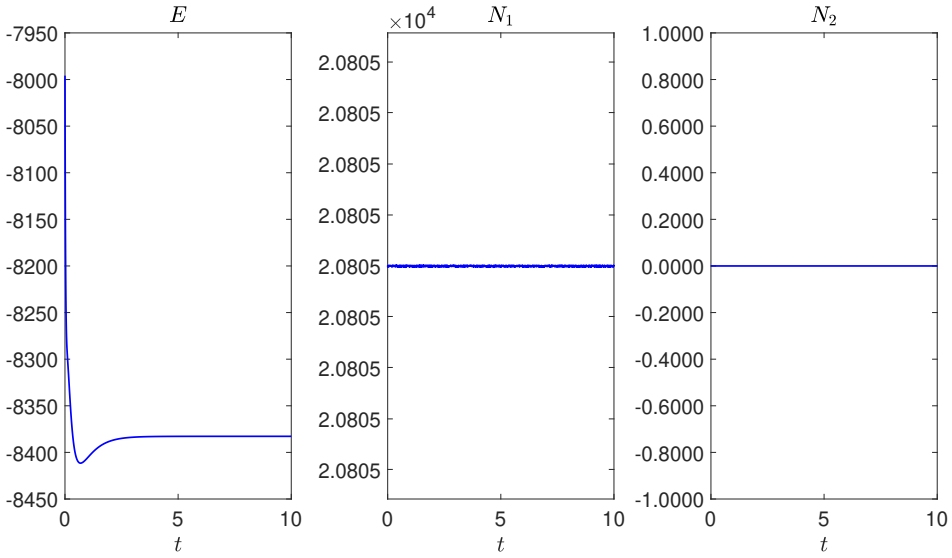

Figure 5.4: Evolution during imaginary time propagation and before vortex imprinting of total energy (5.9)) (left), N_1 (middle) and N_2 (right), where N_1 and N_2 represent the number of atoms of the two components. We observe that the system relaxes toward the lowest-energy state while conserving the number of atoms in the first condensate; the number of atoms in the second condensate remains constantly zero.

5.2.3 Vortex imprinting

Subsequently, vortices are imprinted in the first component condensate. To this end we introduce two perpendicular vortex lines in the majority component, i.e. in the cylinder C, with vortex core radius $a_0 = 2$, centered at $C_1 = [0, 0, -4]$ and $C_2 = [0, 0, 4]$, and with orientation vectors $\mathbf{n}_1 = [0, -1, 0]$ and $\mathbf{n}_2 = [1, 0, 0]$, respectively. We define the tubular region $\mathcal{T} \subseteq C$ corresponding to the vortex cores as

$$\mathcal{T} = \begin{cases} \left\{(x,y,z) \in [-20,20]^3 \;\middle|\; \sqrt{y^2+z^2} < a_0,\ \sqrt{x^2+y^2} < R\right\} & \text{vortex along } x\,, \\ \left\{(x,y,z) \in [-20,20]^3 \;\middle|\; \sqrt{x^2+z^2} < a_0,\ \sqrt{x^2+y^2} < R\right\} & \text{vortex along } y\,. \end{cases}$$

Moreover, the vortex cores are filled with the second component for every value of $\frac{n_2}{n_1}$. This procedure defines new initial conditions $\Psi_{01\,\mathrm{vgs}}$ and $\Psi_{02\,\mathrm{vgs}}$. The initial condition for the condensate 2 is constructed again via the Thomas-Fermi approximation (1.7.3):

$$V\Psi_{02} + g_{22}|\Psi_{02}|^2\Psi_{02} - \mu_{22}\Psi_{02} = 0 \quad \Rightarrow \quad \Psi_{02}(V + g_{22}|\Psi_{02}|^2 - \mu_{22}) = 0\,,$$

which yields

$$|\Psi_{02}|^2 = \begin{cases} \frac{\mu_{22}-V}{g_{22}} & \text{if} \quad \mu_{22} \geq V\,, \\ 0 & \text{if} \quad \mu_{22} < V\,. \end{cases}$$

The external potential V is equal to zero inside the cylinder C and takes the value 10 outside it. Moreover, μ_{22} assumes the values $0, 0.25, 0.5$ and 0.75. Therefore the density

of the second component is nonzero only inside $\mathcal{T}$. Thus we have

$$|\Psi_{02}|^2 = \begin{cases} \frac{\mu_{22}}{g_{22}} = \frac{n_2}{n_1} & \text{if} \quad r \in \mathcal{T}\,, \\ 0 & \text{if} \quad r \notin \mathcal{T}\,, \end{cases}$$

where we replaced the expression of $\mu_{22} = g_{22}\frac{n_2}{n_1}$. Therefore we obtain

$$\Psi_{02} = \begin{cases} \sqrt{\frac{n_2}{n_1}} & \text{if} \quad r \in \mathcal{T}\,, \\ 0 & \text{if} \quad r \notin \mathcal{T}\,. \end{cases}$$

Hence, numerically, first we imprint the vortex along the axes y setting the new initial conditions, which we call $\Psi_{01\,\mathrm{vgs1}}$ and $\Psi_{02\,\mathrm{vgs1}}$, as

$$\Psi_{01\,\mathrm{vgs1}} = \Psi_{1\,\mathrm{gs}} \cdot \frac{\delta x - \mathrm{i}\delta z}{\sqrt{(\delta x)^2 + (\delta z)^2}} \cdot \frac{\sqrt{(\delta x)^2 + (\delta z)^2}}{\sqrt{1 + (\delta x)^2 + (\delta z)^2}} \tag{5.15}$$

$$\Psi_{02\,\mathrm{vgs1}} = \Psi_{2\,\mathrm{gs}} + \sqrt{\frac{n_2}{n_1}} \quad \text{if} \quad \sqrt{(\delta x)^2 + (\delta z)^2} < a_0 \quad \text{and} \quad \sqrt{(\delta x)^2 + (\delta y)^2} < R\,, \tag{5.16}$$

with $\delta x = x_i - 0$ $\delta y = y_j - 0$, $\delta z = z_k + 4$, for every point (x_i, y_j, z_k) in the numerical domain, $a_0 = 2$ and $R = 15$. In expression (5.15) we multiplied the previously obtained ground state wavefunction $\Psi_{1\,\mathrm{gs}}$ by two factors. One is a phase factor, which introduces the correct circulation around the vortex line. The second is a smooth radial modulation, which enforces the vanishing of the condensate 1 density in the vortex core while leaving it unchanged outside. For the second component (see expression (5.16)) we applied the Thomas-Fermi approximation: we add to the ground state wavefunction $\Psi_{2\,\mathrm{gs}}$ (equal to 0 in all the numerical domain) the constant quantity $\sqrt{\frac{n_2}{n_1}}$ inside the vortex cores, while $\Psi_{02\,\mathrm{vgs1}} = \Psi_{2\,\mathrm{gs}}$ elsewhere. Subsequently we imprint the vortex along the axes x defining

$$\Psi_{01\,\mathrm{vgs}} = \Psi_{01\,\mathrm{vgs1}} \cdot \frac{\delta y + \mathrm{i}\delta z}{\sqrt{(\delta y)^2 + (\delta z)^2}} \cdot \frac{\sqrt{(\delta y)^2 + (\delta z)^2}}{\sqrt{1 + (\delta y)^2 + (\delta z)^2}}$$

$$\Psi_{02\,\mathrm{vgs}} = \Psi_{02\,\mathrm{vgs1}} + \sqrt{\frac{n_2}{n_1}} \quad \text{if} \quad \sqrt{(\delta y)^2 + (\delta z)^2} < a_0 \quad \text{and} \quad \sqrt{(\delta x)^2 + (\delta y)^2} < R\,,$$

with $\delta x = x_i - 0$ $\delta y = y_j - 0$, $\delta z = z_k - 4$, for every point (x_i, y_j, z_k) in the numerical domain, $a_0 = 2$ and $R = 15$.

We compute the initial conditions $\Psi_{01\,\mathrm{vgs}}$ and $\Psi_{02\,\mathrm{vgs}}$ for each value of $\frac{n_2}{n_1}$. To better understand the influence of the number of atoms in the second component on the scaling law, we consider the ratios $\frac{n_2}{n_1} = 0,\ 0.25,\ 0.5,\ 0.75$ and express them in terms of $N_2/L = 0,\ 2.9115,\ 5.8229,\ 8.7344$ (see Table 5.1), where N_2/L denotes the number of atoms in the second component per total vortex length $L = 60$.

We then impose $\Psi_{01\,\mathrm{vgs}}$ and $\Psi_{02\,\mathrm{vgs}}$ as new initial conditions and we again numerically integrate (5.2) up to the final time $T = 10$ using imaginary-time propagation, in order to reach the lowest-energy state of the system (see Figures 5.5-5.8). The following operations are performed at each time step.

- The wave functions are rescaled as

$$\Psi_1 = \Psi_1 \sqrt{\frac{N_{01\,\mathrm{vgs}}}{N_1}}, \quad \Psi_2 = \Psi_2 \sqrt{\frac{N_{02\,\mathrm{vgs}}}{N_2}},$$

  where

$$N_{01\,\mathrm{vgs}} = \int |\Psi_{01\,\mathrm{vgs}}|^2 \, d^3\mathbf{r}, \qquad N_1 = \int |\Psi_1|^2 \, d^3\mathbf{r},$$
$$N_{02\,\mathrm{vgs}} = \int |\Psi_{02\,\mathrm{vgs}}|^2 \, d^3\mathbf{r}, \qquad N_2 = \int |\Psi_2|^2 \, d^3\mathbf{r}.$$

  For $N_2/L = 0$ no rescaling is applied to Ψ_2 since it remains identically zero throughout the domain. These re normalizations ensure the conservation of the number of atoms in both condensates (see Figure 5.5-5.8).

- The wave function Ψ_1 is decomposed into modulus and phase,

$$\Psi_1 = |\Psi_1| e^{\mathrm{i}\theta_1},$$

  with

$$|\Psi_1| = \sqrt{(\mathrm{Re}(\Psi_1))^2 + (\mathrm{Im}(\Psi_1))^2} \quad \text{and} \quad \theta_1 = \arg(\Psi_1) = \tan^{-1}\left(\frac{\mathrm{Im}(\Psi_1)}{\mathrm{Re}(\Psi_1)}\right).$$

  Then the phase θ_1 is reset according to

$$\Psi_1 = |\Psi_1| e^{\mathrm{i}\theta_{01\,\mathrm{vgs}}},$$

  where

$$\theta_{01\,\mathrm{vgs}} = \arg(\Psi_{01\,\mathrm{vgs}}) = \tan^{-1}\left(\frac{\mathrm{Im}(\Psi_{01\,\mathrm{vgs}})}{\mathrm{Re}(\Psi_{01\,\mathrm{vgs}})}\right)$$

  is the phase of $\Psi_{01\,\mathrm{vgs}}$. This procedure prevents vortex displacement.

At the end of the operations of rescaling and phase reconstruction we obtain the wavefunctions $\Psi_{1\,\mathrm{vgs}}$ and $\Psi_{2\,\mathrm{vgs}}$ for each value of N_2/L.

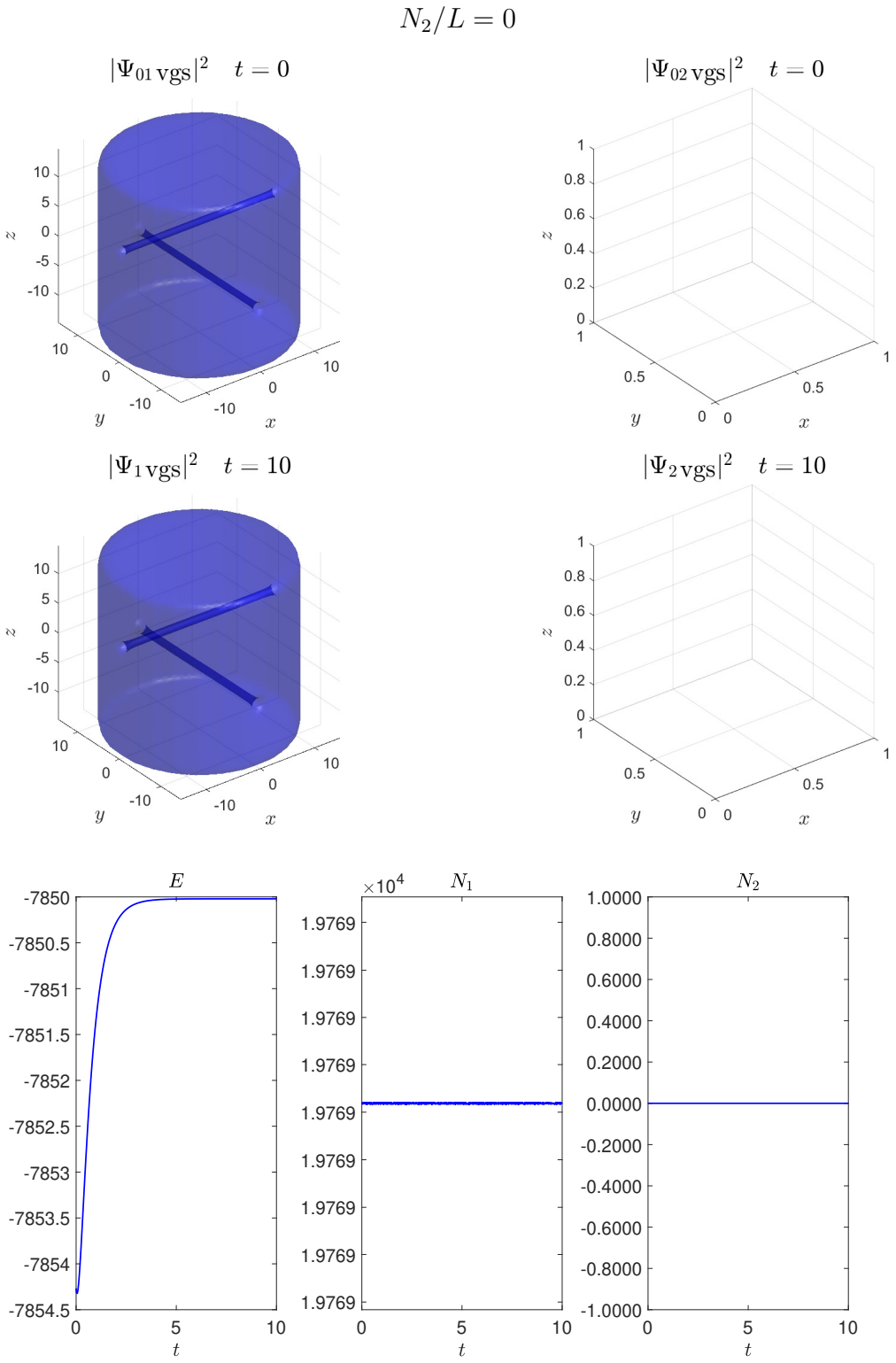

Figure 5.5: Case $N_2/L = 0$. First row: density of the condensate 1 with two perpendicular vortex lines (left) and density of the condensate 2 (here equal to 0 throughout the entire domain) (right), before imaginary time propagation. Second row: density of the condensate 1 with two perpendicular vortex lines (left) and density of the condensate 2 (equal to 0 throughout the entire domain) (right), after imaginary time propagation. Isosurfaces of $\rho = 0.3$ for condensate 1 and $\rho = 0.2$ for condensate 2. Third row: evolution during imaginary time propagation of total energy (5.9) (left), N_1 (middle) and N_2 (right), where N_1 and N_2 represent the number of atoms of the two components. We can see that the system relaxes toward the lowest-energy state while conserving the number of atoms.

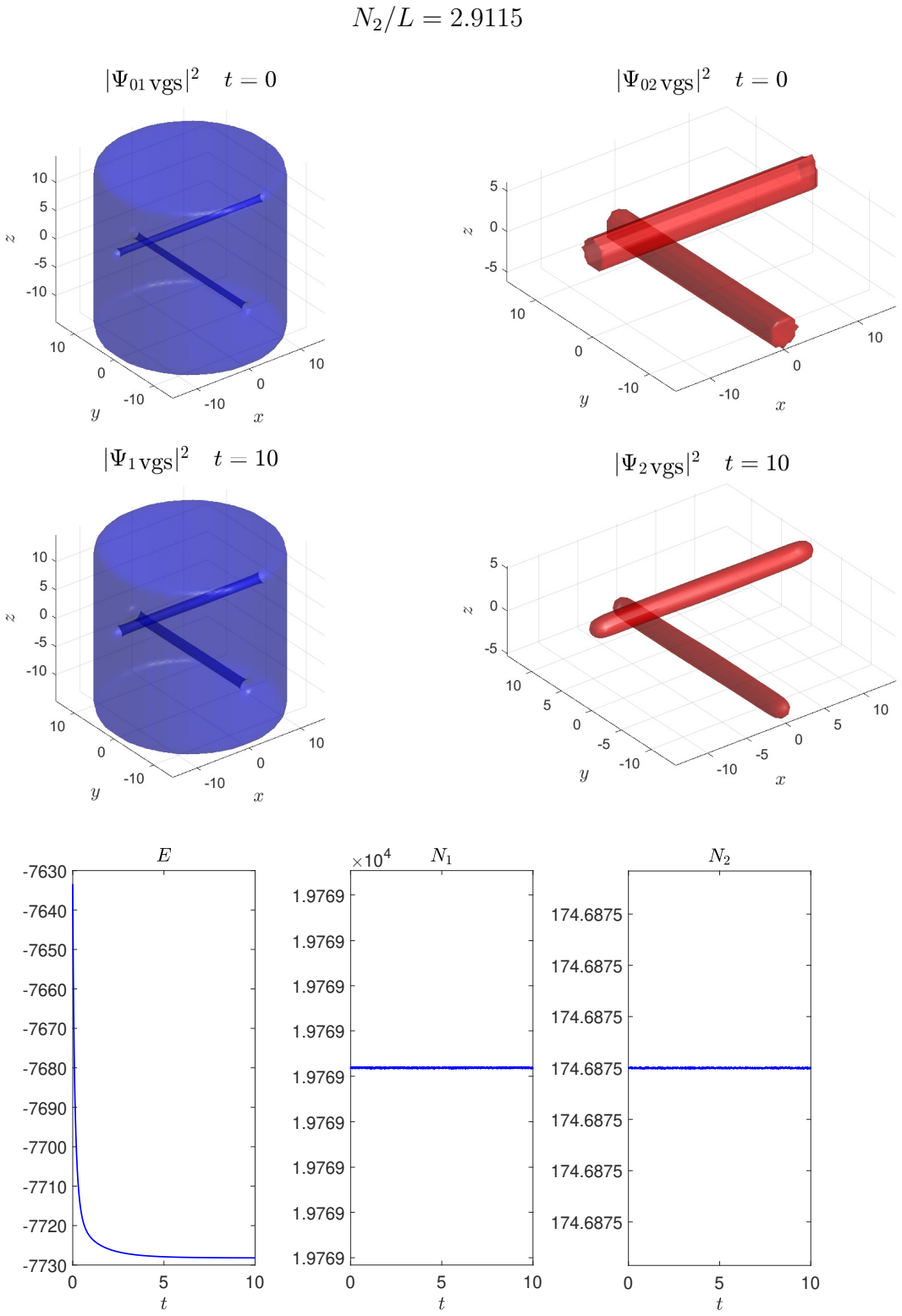

Figure 5.6: Case $N_2/L = 2.9115$. First row: density of the condensate 1 with two perpendicular vortex lines (left) and density of the condensate 2 (here equal to 0 throughout the entire domain) (right), before imaginary time propagation. Second row: density of the condensate 1 with two perpendicular vortex lines (left) and density of the condensate 2 (equal to 0 throughout the entire domain) (right), after imaginary time propagation. Isosurfaces of $\rho = 0.3$ for condensate 1 and $\rho = 0.2$ for condensate 2. Third row: evolution during imaginary time propagation of total energy (5.9) (left), N_1 (middle) and N_2 (right), where N_1 and N_2 represent the number of atoms of the two components. We can see that the system relaxes toward the lowest-energy state while conserving the number of atoms.

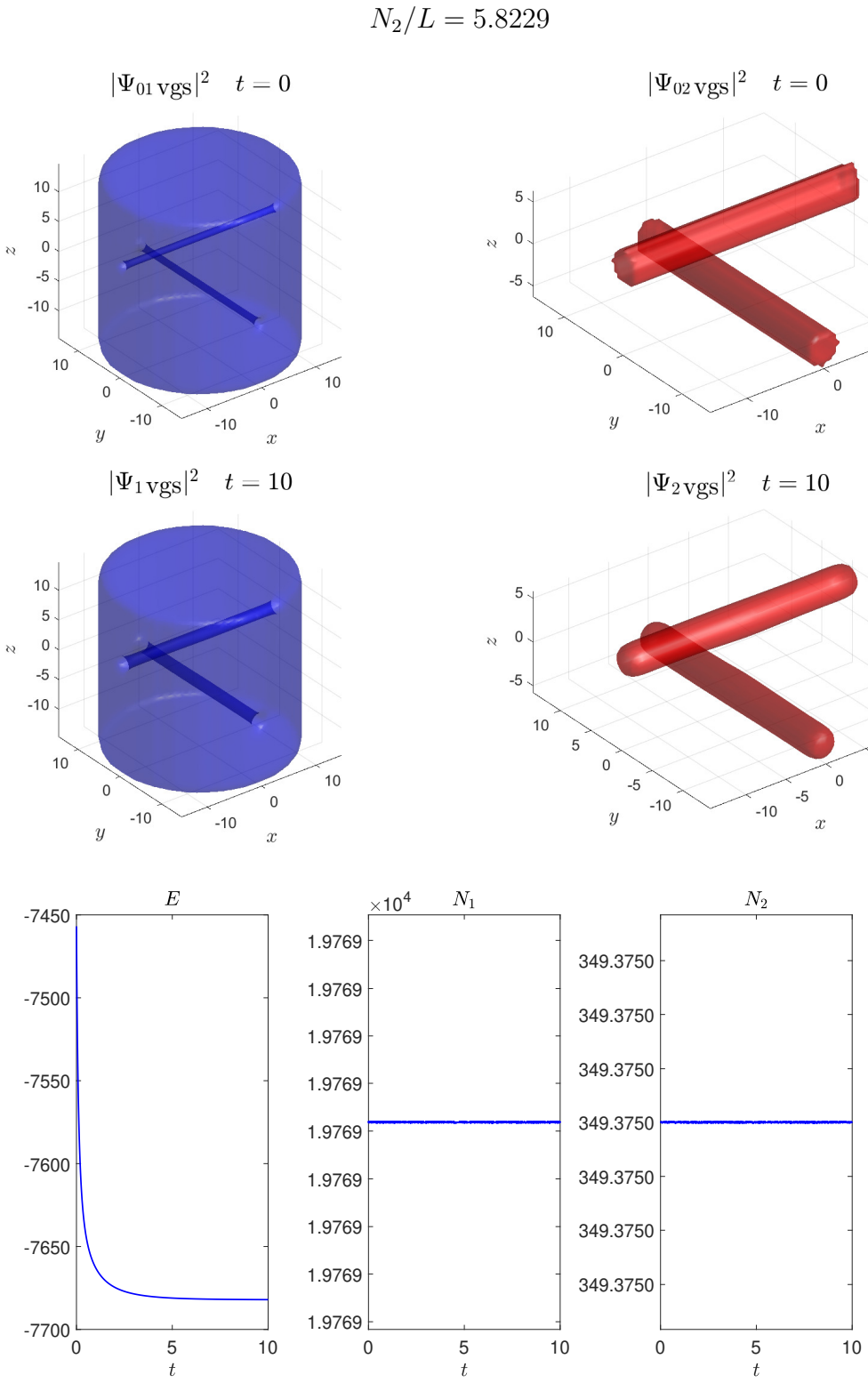

Figure 5.7: Case $N_2/L = 5.8229$. First row: density of the condensate 1 with two perpendicular vortex lines (left) and density of the condensate 2 (here equal to 0 throughout the entire domain) (right), before imaginary time propagation. Second row: density of the condensate 1 with two perpendicular vortex lines (left) and density of the condensate 2 (equal to 0 throughout the entire domain) (right), after imaginary time propagation. Isosurfaces of $\rho = 0.3$ for condensate 1 and $\rho = 0.2$ for condensate 2. Third row: evolution during imaginary time propagation of total energy (5.9) (left), N_1 (middle) and N_2 (right), where N_1 and N_2 represent the number of atoms of the two components. We can see that the system relaxes toward the lowest-energy state while conserving the number of atoms.

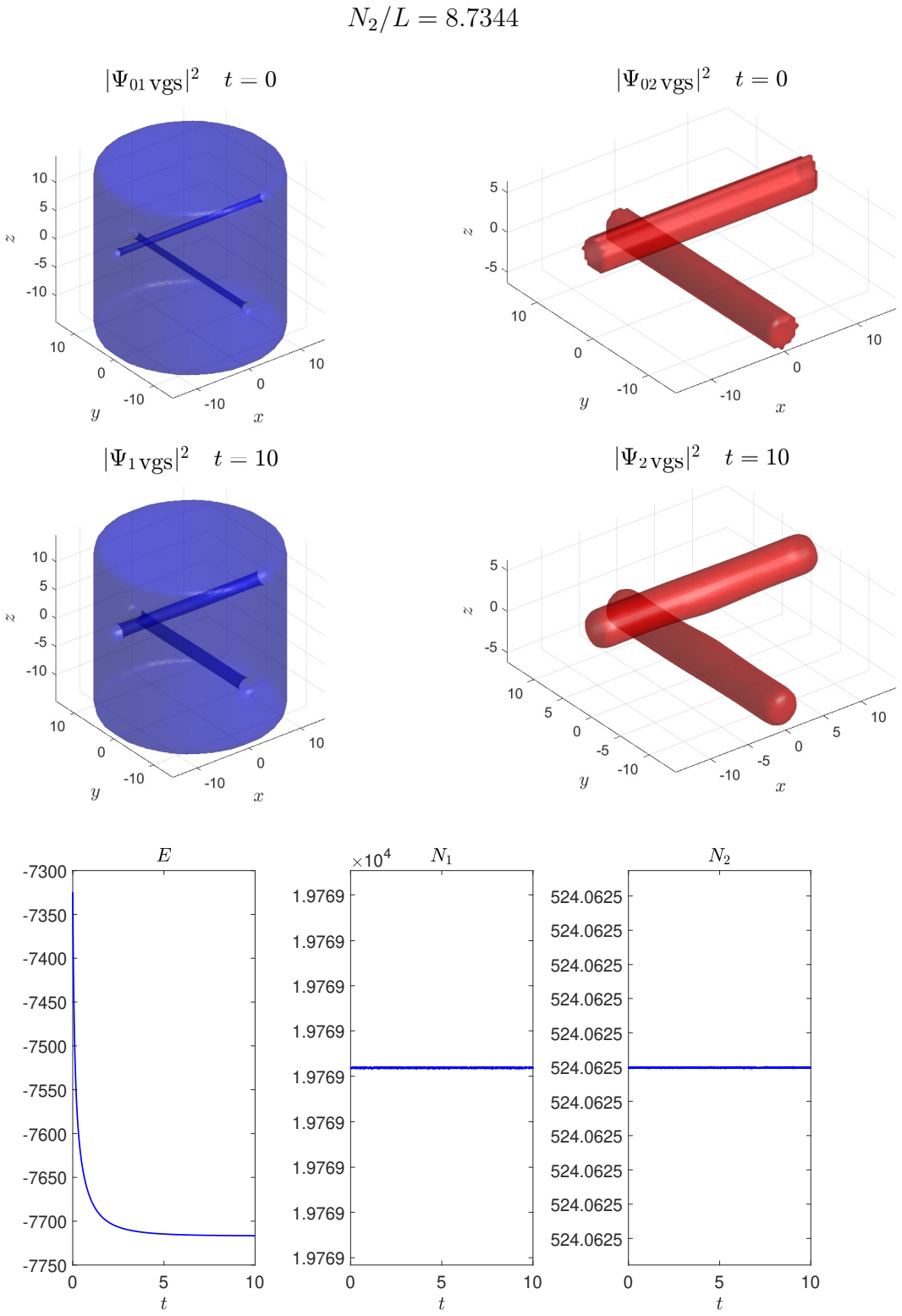

Figure 5.8: Case $N_2/L = 8.7344$. First row: density of the condensate 1 with two perpendicular vortex lines (left) and density of the condensate 2 (here equal to 0 throughout the entire domain) (right), before imaginary time propagation. Second row: density of the condensate 1 with two perpendicular vortex lines (left) and density of the condensate 2 (equal to 0 throughout the entire domain) (right), after imaginary time propagation. Isosurfaces of $\rho = 0.3$ for condensate 1 and $\rho = 0.2$ for condensate 2. Third row: evolution during imaginary time propagation of total energy (5.9) (left), N_1 (middle) and N_2 (right), where N_1 and N_2 represent the number of atoms of the two components. We can see that the system relaxes toward the lowest-energy state while conserving the number of atoms.

5.2.4 Vortex reconnections dynamics

For each value of N_2/L we impose the initial conditions $\Psi_{1\,\mathrm{vgs}}$ and $\Psi_{2\,\mathrm{vgs}}$ and numerically solve (5.2) in real time using the time step τ, and saving the solutions Ψ_1 and Ψ_2 every 50 time steps, corresponding to a time interval of $\Delta t = 0.25$. The final simulation time T varies with N_2/L (see Table 5.1) and is taken as the time preceding the onset of a second reconnection process, which is observed but not further analyzed.

This procedure allows us to simulate the time evolution of vortex reconnection between two perpendicular vortex lines in a two component BECs in the immiscible regime, while varying the number of atoms in the second component (see Figures 5.9- 5.12). For the complete simulations see the Supplemental Material [55].

For each value of N_2/L the numerical simulations suggest that the reconnection dynamics is qualitatively similar to that of the single-condensate case. Initially, the two vortex lines approach each other while maintaining an approximately perpendicular configuration. As they get closer their mutual interaction induces a local bending of the filaments leading to a highly curved configuration. Reconnection then occurs during which the vortex lines undergo a topology change, exchanging segments and form two newly connected filaments. Immediately after reconnection sharp cusps develop at the reconnection points, and the filaments move apart.

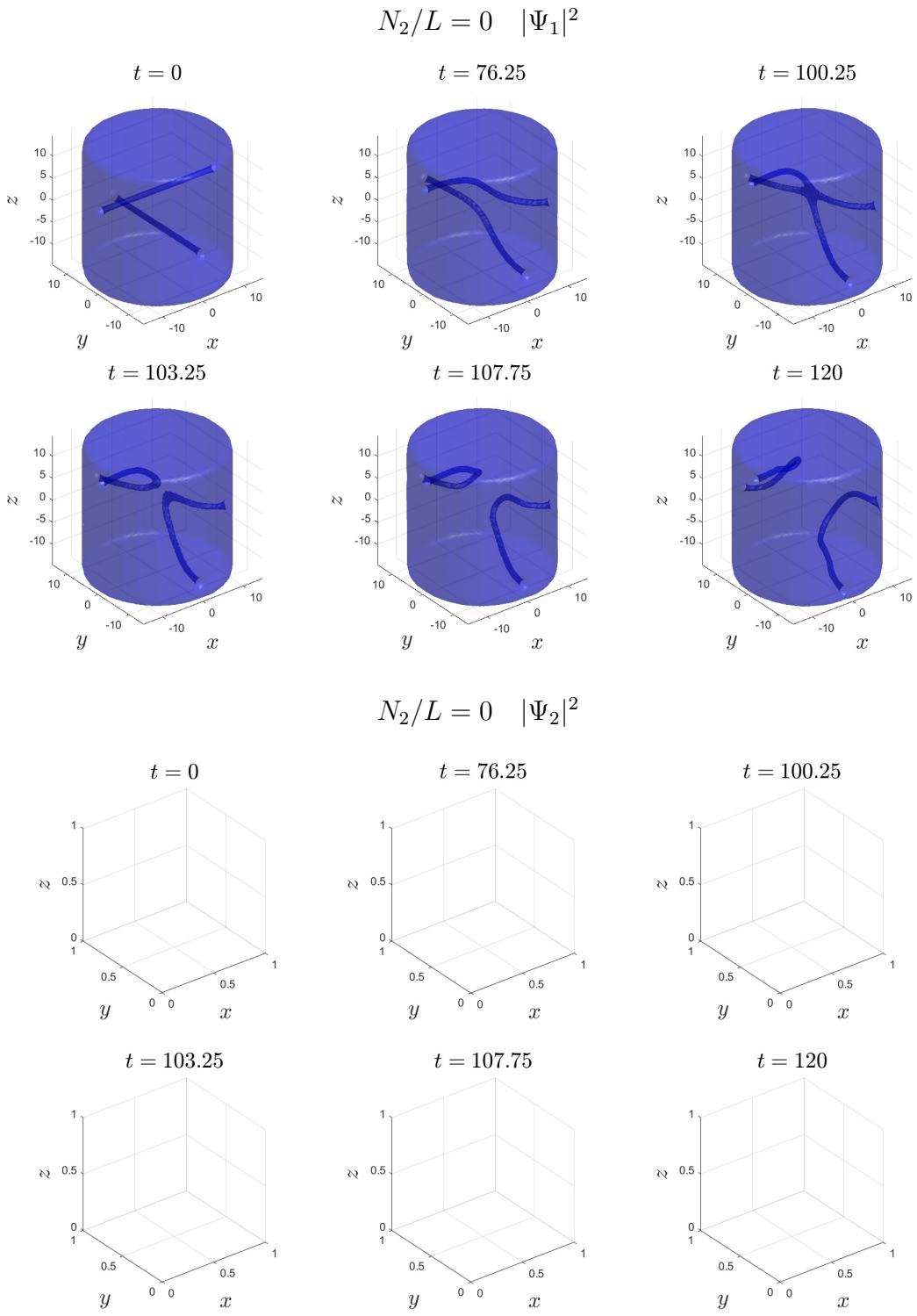

Figure 5.9: Time evolution of the reconnection between two perpendicular vortex lines in a two-component BEC in the immiscible regime, in the absence of condensate 2 (i.e., $N_2/L = 0$). Top panels: condensate 1 ($\rho = 0.3$ isosurfaces). Bottom panels: condensate 2, which is absent throughout the evolution (isosurfaces of $\rho = 0.2$).

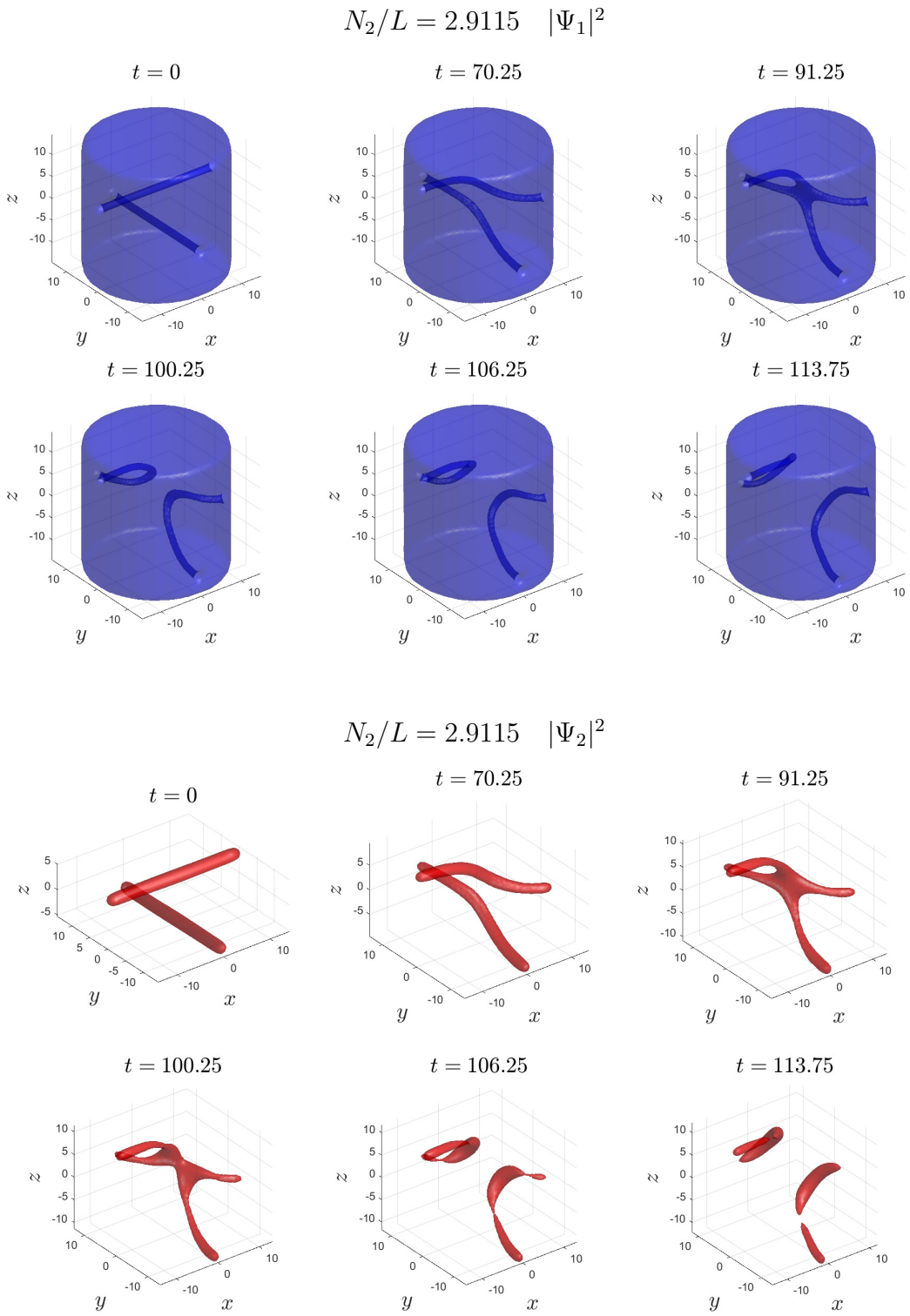

Figure 5.10: Time evolution of the reconnection between two perpendicular vortex lines in a two-component BEC in the immiscible regime, for $N_2/L = 2.9115$. Top panels: condensate 1 ($\rho = 0.3$ isosurfaces). Bottom panels: condensate 2 ($\rho = 0.2$ isosurfaces).

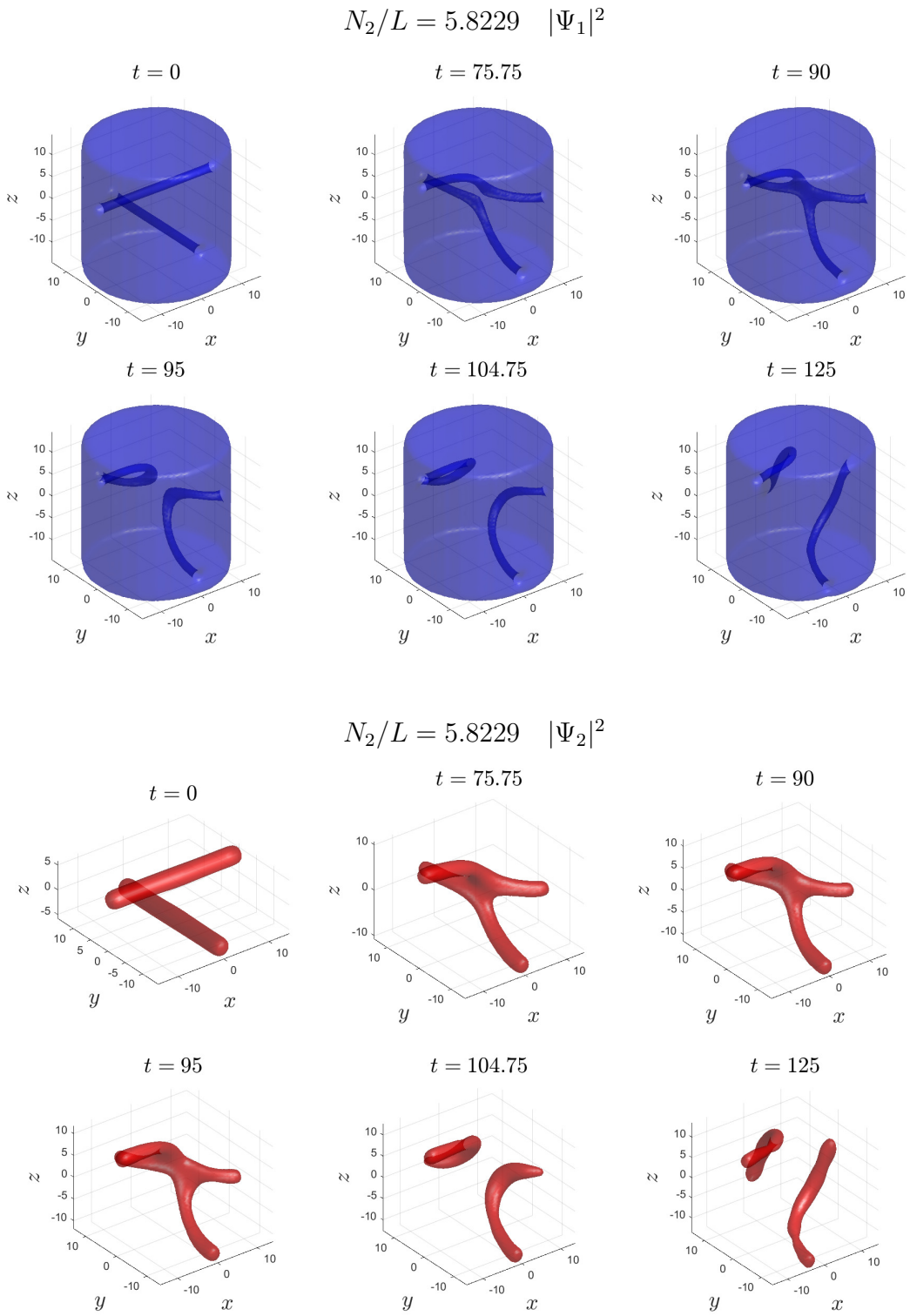

Figure 5.11: Time evolution of the reconnection between two perpendicular vortex lines in a two-component BEC in the immiscible regime, for $N_2/L = 5.8229$. Top panels: condensate 1 ($\rho = 0.3$ isosurfaces). Bottom panels: condensate 2 ($\rho = 0.2$ isosurfaces).

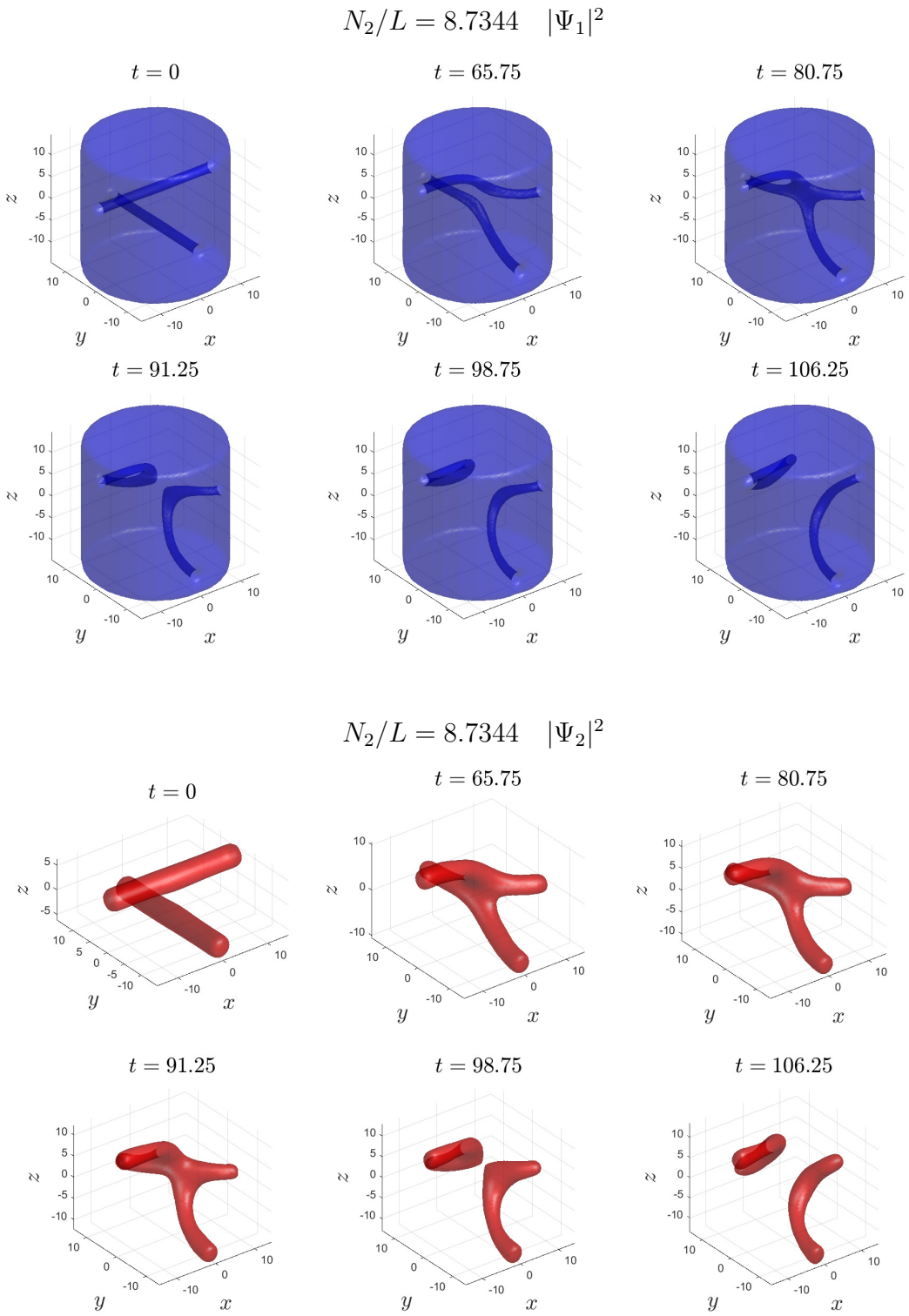

Figure 5.12: Time evolution of the reconnection between two perpendicular vortex lines in a two-component BEC in the immiscible regime, for $N_2/L = 8.7344$. Top panels: condensate 1 ($\rho = 0.3$ isosurfaces). Bottom panels: condensate 2 ($\rho = 0.2$ isosurfaces).

5.3 Scaling laws parameters

We consider the previously obtained numerical solutions Ψ_1 and Ψ_2, sampled every $\Delta t = 0.25$ for each value of N_2/L, and we extrapolate the vortex-core nodal lines of the reconnecting vortices using the numerical routine of [2, 51], in order to determine the minimum distance δ (see (3.1)). Hence let $P_1 = \{\mathbf{p}_i\}$ and $P_2 = \{\mathbf{q}_j\}$ be the extrapolated sets of points obtained for the two vortex nodal lines. We compute the Euclidean distance

$$D_{ij} = \|\mathbf{q}_i - \mathbf{p}_j\|$$

between all the two points $\mathbf{p}_i \in P_1$ and $\mathbf{q}_j \in P_2$. The minimum distance between the two vortex nodal lines at each Δt is then given by:

$$\delta = \min_{i,j} \; D_{ij} \, .$$

The plot of δ as a function of time t for each value of N_2/L is shown in Figure 5.13. We notice that the minimum of δ, i.e. $\delta \approx 0$, corresponds to the reconnection time t_0 reported in Table 5.1. These data allow us to observe that an increase in the number of atoms in the minority component leads to earlier reconnection.

Furthermore, we consider the scaling law (3.1) which in dimensionless units ($\hbar = m = 1$) reads

$$\delta(t)^{\pm} = A^{\pm}|t - t_0|^{\alpha} \, , \tag{5.17}$$

and by taking the logarithm of (5.17) we obtain

$$\log(\delta^{\pm}) = \log\left(A^{\pm}\right) + \alpha^{\pm} \log\left(|t - t_0|\right) \, .$$

Therefore, by plotting $\log(\delta)$ as a function of $\log(|t - t_0|)$ (see Figure 5.14), we expect a linear behavior.

Hence we perform a linear least-squares fit of $\log(\delta)$ versus $\log(|t - t_0|)$ using the MATLAB function `polyfit`, in order to extract the slope $\alpha^{\pm}$ and the intercept $\log(A^{\pm})$, and consequently determine $A^{\pm}$. The optimal fitting window is selected using a sliding-window method based on the emergence of a stable plateau in the local slope. This procedure allows us to isolate the universal dynamical regime, excluding initial transients, numerical noise in the vicinity of t_0, and deviations occurring towards the end of the simulation. Figure 5.15 shows the dashed red line corresponding to the best fit before and after the reconnection, respectively, while the extracted values of $\alpha^{\pm}$ and $A^{\pm}$ are reported in the legends and in Table 5.1. The corresponding optimal scaling regions are highlighted in Figure 5.16 by red intervals between the dot markers. From the results in Table 5.1 we can notice that $A^+ > A^-$ for all the values of N_2/L, confirming the irreversibility of the reconnection process. Additionally the values of $\alpha^{\pm}$ are far from the theoretical value of $1/2$ [13, 11, 4], but α^- is consistent with the numerical result reported in literature [2, 14]. To better investigate the possible influence of N_2 on reconnection process, we derive (5.17) with respect to time, obtaining the rate of approach and separation

$$v(t)^{\pm} = B^{\pm}(|t - t_0|^{\beta^{\pm}}) \, ,$$

with $B^- = -\alpha A^-$, $B^+ = \alpha A^+$, and $\beta^{\pm} = \alpha^{\pm} - 1$. The resulting values of the coefficients $B^{\pm}$ and $\beta^{\pm}$ are reported in Table 5.1. We observe that $B^+ > B^-$ for each value of N_2/L,

while $|B^-|$ increases with N_2/L and B^+ decreases with N_2/L, suggesting that increasing the number of atoms in the second condensate, the vortices approach more quickly and move apart more slowly.

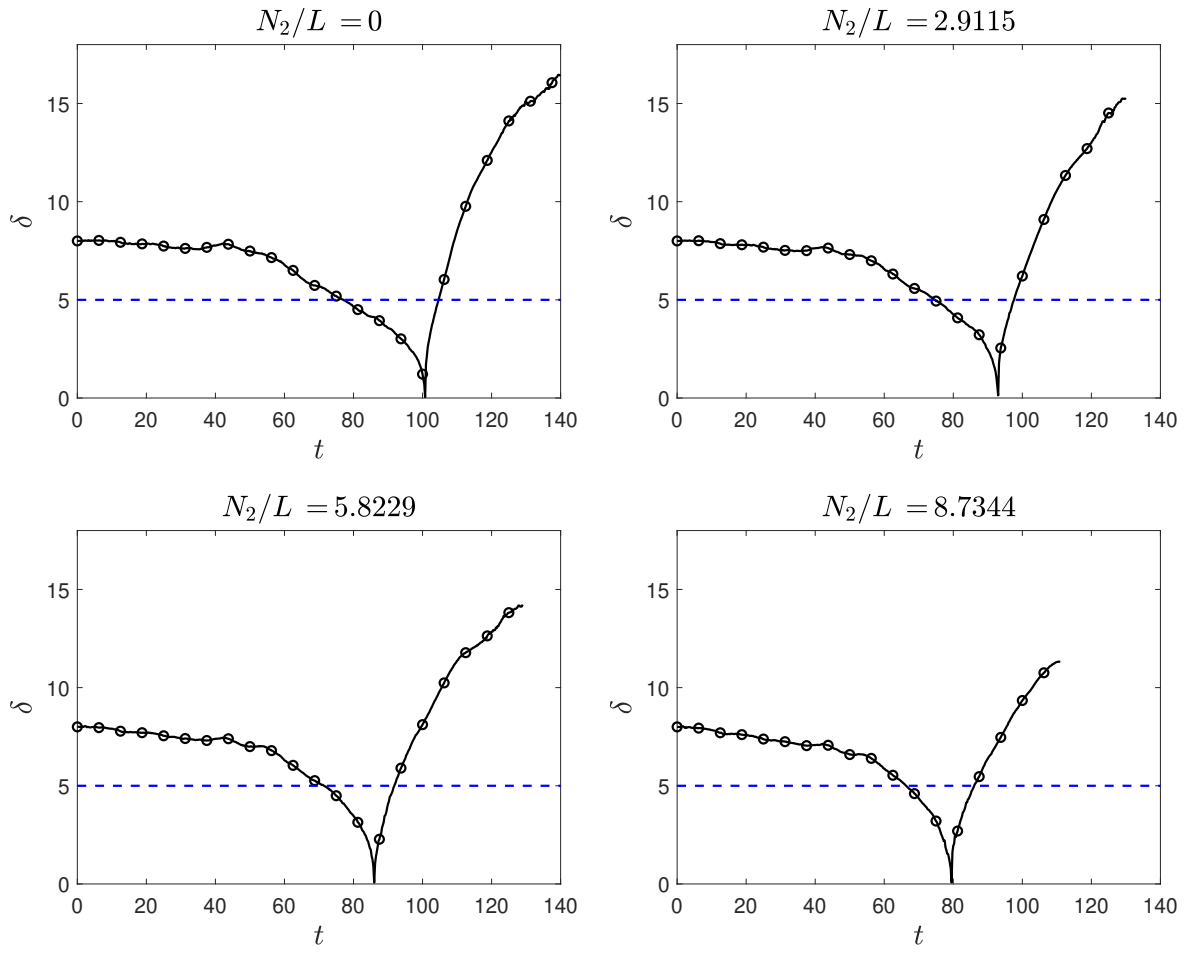

Figure 5.13: Minimum distance (δ) between reconnecting perpendicular vortices lines as a function of time t, for different values of N_2/L (n° of atoms of second condensate per total length of vortex lines). The unit of measure of δ is with respect to the healing length ξ_1. Dashed blue horizontal line indicates the width of the vortex core ($\approx 5\ \xi_1$).

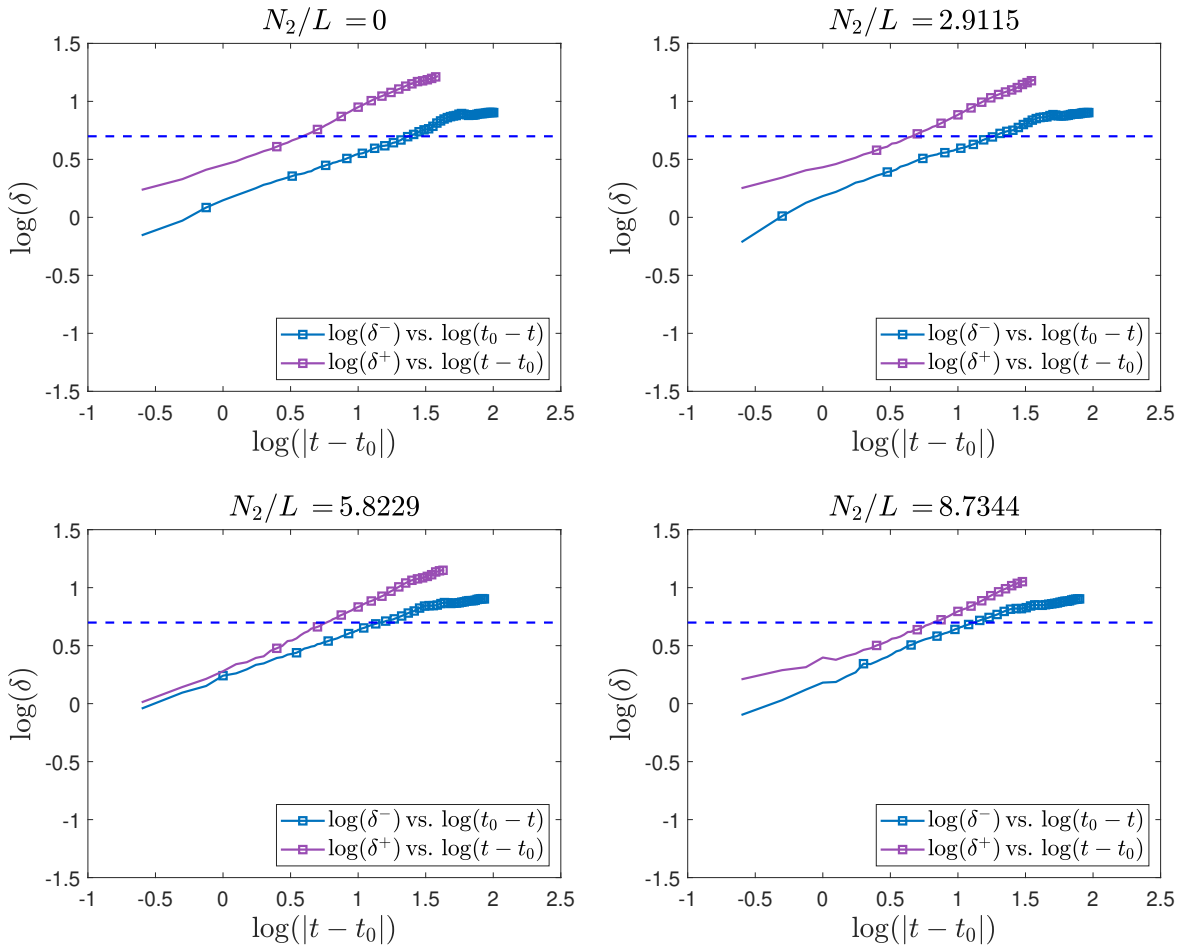

Figure 5.14: Log–log representation of the minimum distance δ as a function of $|t - t_0|$ before and after the reconnection, for different values of N_2/L (n° of atoms of second condensate per total length of vortex lines). Dashed blue horizontal line indicates the width of the vortex core ($\approx 5\ \xi_1$).

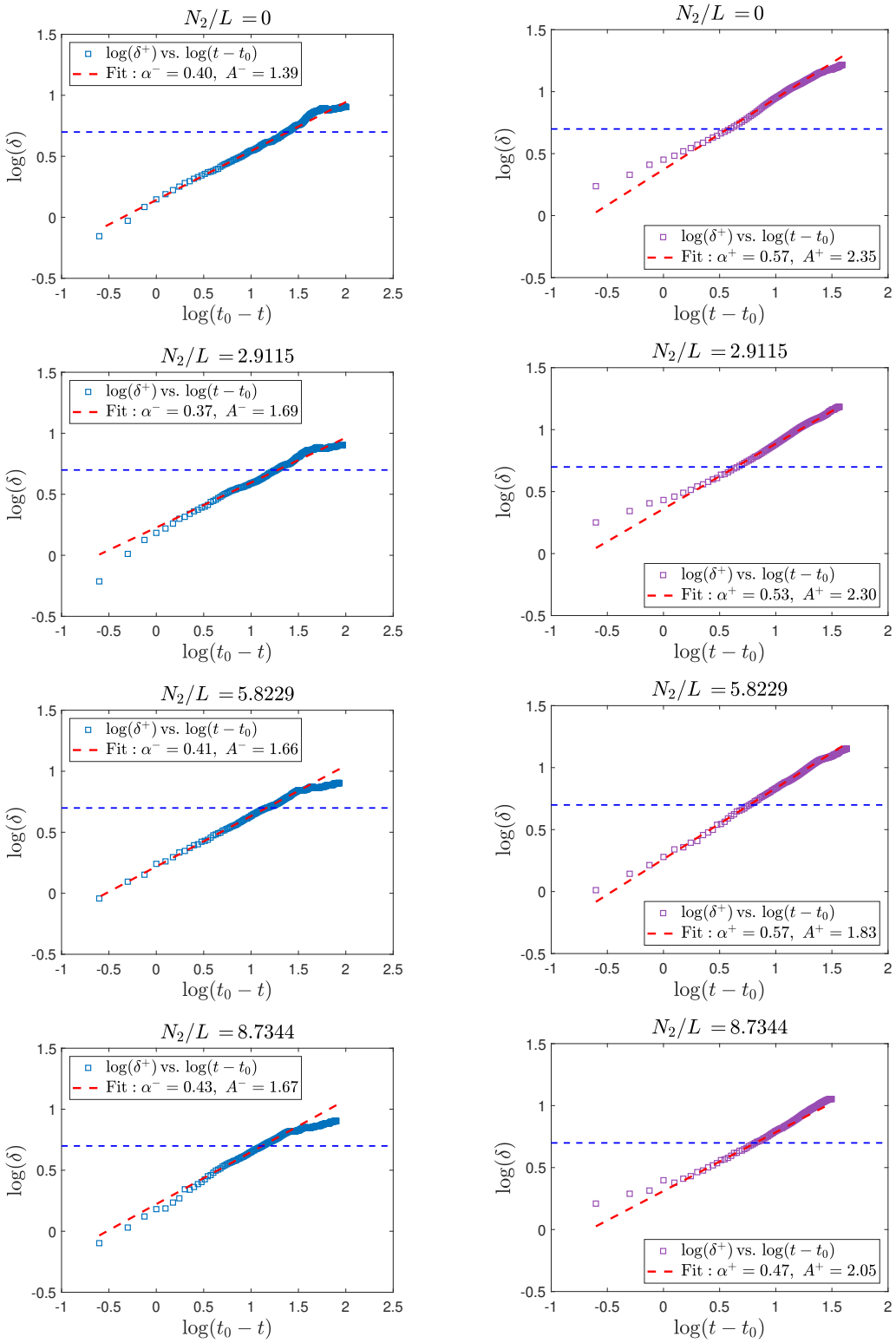

Figure 5.15: Best linear least-squares fit (dashed red line) of the log–log representation of the minimum distance δ as a function of $|t-t_0|$ before and after the reconnection, for different values of N_2/L (n° of atoms of second condensate per total length of vortex lines). Extracted values of $\alpha^{\pm}$ and $A^{\pm}$ are reported in the legends. Dashed blue horizontal line indicates the width of the vortex core ($\approx 5\ \xi_1$).

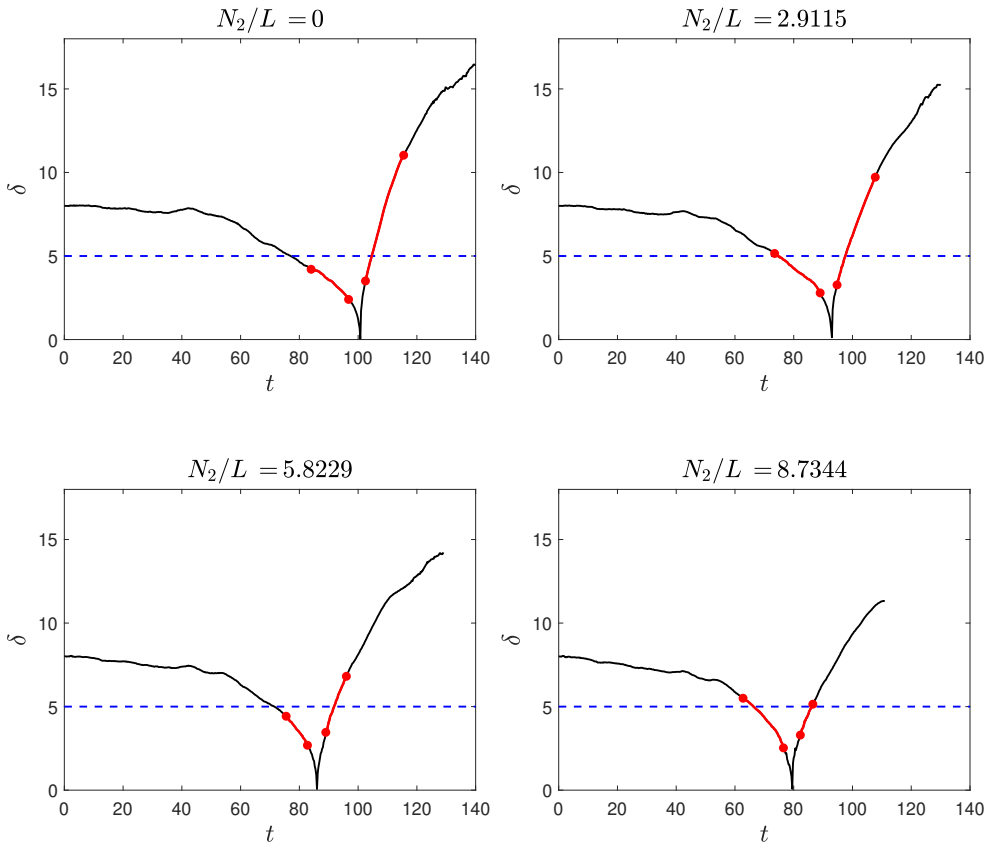

Figure 5.16: Optimal fitting regions for the scaling law $\delta = A^{\pm}|t - t_0|^{\alpha^{\pm}}$, determined via the sliding-window method for each value of N_2/L, are highlighted by red intervals between the markers. Dashed blue horizontal line indicates the width of the vortex core ($\approx 5\ \xi_1$).

Table 5.1: Coefficients $A^{\pm}$ and $\alpha^{\pm}$ obtained from the best fit of the scaling laws for the minimum distance $\delta^{\pm}(t) = A^{\pm}|t - t_0|^{\alpha^{\pm}}$, and coefficients $B^{\pm}$ and $\beta^{\pm}$ (with $B^{-} = -\alpha^{-}A^{-}$, $B^{+} = \alpha^{+}A^{+}$ and $\beta^{\pm} = \alpha^{\pm} - 1$) of the approach/separation rate $v^{\pm}(t) = B^{\pm}|t - t_0|^{\beta^{\pm}}$, for different values of N_2/L. Here t_0 denotes the reconnection time and T the final time of the reconnection processes.

N_2/L	0	2.9115	5.8229	8.7344
n_2/n_1	0	0.25	0.5	0.75
A^{-}	1.39	1.69	1.66	1.67
A^{+}	2.35	2.30	1.83	2.05
α^{-}	0.40	0.37	0.41	0.43
α^{+}	0.57	0.53	0.57	0.47
B^{-}	-0.56	-0.62	-0.68	-0.71
B^{+}	1.35	1.21	1.05	0.97
β^{-}	-0.60	-0.63	-0.59	-0.57
β^{+}	-0.43	-0.47	-0.43	-0.53
t_0	100.75	93	86	79.5
T	140	130	129	111

5.4 Concluding remarks

We performed numerical simulations of the reconnection between two perpendicular vortex lines in a two-component Bose–Einstein condensate. The vortices are located in the condensate with the larger number of atoms, while their cores are filled by a second condensate containing fewer atoms. To investigate the effect of the minority component on the reconnection process, we progressively increased the normalized number of atoms N_2/L in the second condensate.

By extrapolating the vortex core nodal lines we computed the minimum distance δ between the vortices. We found that reconnection occurs earlier as N_2/L increases, with the reconnection time t_0 decreasing accordingly. From a least-squares fit of the log–log scaling law

$$\log(\delta^{\pm}) = \log\left(A^{\pm}\right) + \alpha^{\pm} \log\left(|t - t_0|\right) ,$$

we extracted the parameters $A^{\pm}$ and $\alpha^{\pm}$. For all values of N_2/L we observe that $A^{+} > A^{-}$ confirming the irreversibility of the reconnection process.

The values of $\alpha^{\pm}$ deviate from the theoretical prediction of 0.5; however α^{-} is consistent with results reported in the literature, suggesting that the reconnection dynamics may be influenced by finite-domain effects. Hence in future work we will consider larger computational domains.

To further analyze the dynamics we differentiated the scaling law with respect to time, obtaining an expression for the approach/separation rate:

$$v(t) = B^{\pm}|t - t_0|^{\beta^{\pm}}, \tag{5.18}$$

where $B^{-} = -\alpha^{-}A^{-}$ and $B^{+} = \alpha^{+}A^{+}$. We find that $B^{+} > B^{-}$ for all values of N_2/L, with $|B^{-}|$ increasing and B^{+} decreasing as N_2/L increases. The results indicate that, as the number of atoms in the second component grows, the vortices approach more rapidly and separate more slowly.

To further validate these findings, we plan to repeat the analysis using different vortex configurations, for example, considering perpendicular vortices that are not aligned with the coordinate axes.

Appendix A

Helmholtz decomposition

To obtain the decomposition (3.5), we first introduce the following Theorem ([58],[28],[59]).

Theorem A.0.1 (Helhmoltz decomposition)**.** *Every vector field* $\mathbf{u} \in [L^2(\mathcal{D})]^3$ *on a Lipschitz domain* $\mathcal{D} \subseteq \mathbb{R}^3$*, has an* L_2*-orthogonal decomposition*

$$\mathbf{u} = \mathbf{u}_{\mathrm{v}} + \mathbf{u}_c + \mathbf{u}_{\mathrm{h}} = \nabla \times \mathbf{A}_{\mathrm{v}} + \nabla \Phi_c + \mathbf{u}_{\mathrm{h}}\,, \tag{A.1}$$

with the vector potential $\mathbf{A}_{\mathrm{v}} \in H(\mathrm{curl}, \mathcal{D})$*, the scalar potential* $\Phi_{\mathrm{c}} \in H^1(\mathcal{D})$ *and the harmonic component* $\mathbf{u}_{\mathrm{h}} \in [L^2(\mathcal{D})]^3$*. The vortical component* $\mathbf{u}_{\mathrm{v}}$ *satisfies* $\nabla \cdot \mathbf{u}_{\mathrm{v}} = 0$*, and a compressible component* $\mathbf{u}_{\mathrm{c}}$ *satisfies* $\nabla \times \mathbf{u}_{\mathrm{c}} = 0$*, and a harmonic component* $\mathbf{u}_{\mathrm{h}}$ *satisfies both* $\nabla \cdot \mathbf{u}_{\mathrm{h}} = 0$ *and* $\nabla \times \mathbf{u}_{\mathrm{h}} = 0$*.*

Then let us consider the domain

$$D = \{(x, y, z) \in \mathbb{R}^3 : |x| \leq L, |y| \leq L, |z| \leq L\}, \quad L \in \mathbb{R}^+\,.$$

We state the following proposition, which we will prove using the previous theorem.

Proposition A.0.2. *The vector field* $\sqrt{\rho}\mathbf{v}$ *defined on* D *can be decomposed, using the Helmholtz decomposition* (A.1)*, as*

$$\begin{cases} \sqrt{\rho}\mathbf{v} = (\sqrt{\rho}\mathbf{v})^{\mathrm{i}} + (\sqrt{\rho}\mathbf{v})^{\mathrm{c}}\,, \\ \nabla \cdot (\sqrt{\rho}\mathbf{v})^{\mathrm{i}} = 0\,, \\ \nabla \times (\sqrt{\rho}\mathbf{v})^{c} = 0\,, \end{cases} \tag{A.2}$$

which is equivalent to solve the Poisson equation

$$\nabla \cdot (\sqrt{\rho}\mathbf{v}) = \Delta \Phi\,, \tag{A.3}$$

where $(\sqrt{\rho}\mathbf{v})^c = \nabla \Phi$*, with* Φ *a scalar potential.*

Proof. To apply Theorem A.0.1 to the vector field

$$\mathbf{u} := \sqrt{\rho}\mathbf{v} = \sqrt{\rho}\frac{\hbar}{m}\nabla\theta\,,$$

we have to first verify that the assumptions of the theorem are satisfied.

- The domain D is Lipschitz by construction.
- Then, we have to prove that $\mathbf{u} = \sqrt{\rho}\mathbf{v} \in [L^2(D)]^3$. We introduce first the cylindrical coordinates

$$\begin{cases} x = r\cos\theta\,, \\ y = r\sin\theta\,, \\ z = z\,, \end{cases}$$

so the domain could be expressed as

$$D = \{(r,\theta,z) \in \mathbb{R}^3 \mid 0 \le r \le \hat{R}(\theta),\, 0 \le \theta \le 2\pi,\, |z| \le L\}\,,$$

where $\hat{R}(\theta) = \min\left(\frac{L}{|\cos\theta|}, \frac{L}{|\sin\theta|}\right)$. After that, we compute (see Figure A.1)

$$\begin{aligned}
\left\|\sqrt{\rho}\frac{\hbar}{m}\nabla\theta\right\|^2_{[L^2(D)]^3} &= \int_{-L}^{L}\int_0^{2\pi}\int_0^{\hat{R}(\theta)} \left|\sqrt{\rho}\frac{\hbar}{m}\nabla\theta\right|^2 r\,dr\,d\theta\,dz \\
&= \lim_{\varepsilon\to 0}\int_{-L}^{L}\int_0^{2\pi}\int_{\varepsilon}^{\hat{R}(\theta)} \left|\sqrt{\rho}\frac{\hbar}{m}\left(0,\frac{1}{r},0\right)\right|^2 r\,dr\,d\theta\,dz \\
&= \lim_{\varepsilon\to 0}\int_{-L}^{L}\int_0^{2\pi}\int_{\varepsilon}^{\hat{R}(\theta)} \rho\frac{\hbar^2}{m^2}\frac{1}{r^{\cancel{2}}}\,r\,dr\,d\theta\,dz \\
&= \lim_{\varepsilon\to 0}\int_{-L}^{L}\int_0^{2\pi}\int_{\varepsilon}^{a_0} \cancel{rn}\frac{\hbar^2}{m^{\cancel{2}}}\frac{1}{r}\,dr\,d\theta\,dz + \lim_{\varepsilon\to 0}\int_{-L}^{L}\int_0^{2\pi}\int_{a_0}^{\hat{R}(\theta)} \frac{\rho}{r}\,dr\,d\theta\,dz \\
&= \lim_{\varepsilon\to 0}\int_{-L}^{L}\int_0^{2\pi}\int_{\varepsilon}^{a_0} r^2\frac{\hbar^2}{m}\frac{1}{r}\,dr\,d\theta\,dz + \lim_{\varepsilon\to 0}\int_{-L}^{L}\int_0^{2\pi}\int_{a_0}^{\hat{R}(\theta)} \frac{\rho}{r}\,dr\,d\theta\,dz \\
&= \lim_{\varepsilon\to 0}\int_{-L}^{L}\int_0^{2\pi}\int_{\varepsilon}^{a_0} r\frac{\hbar^2}{m}\,dr\,d\theta\,dz + 2L\int_0^{2\pi}\int_{a_0}^{\hat{R}(\theta)} \frac{\rho}{r}\,dr d\theta \\
&= \frac{\hbar^2}{m}\frac{a_0^2}{2}2\pi 2L + 2L\int_0^{2\pi}\int_{a_0}^{\hat{R}(\theta)} \frac{\rho}{r}\,dr d\theta < \infty\,,
\end{aligned}$$

where we passed to the limit for an arbitrary small $\varepsilon > 0$ because $\nabla\theta$ diverges along the vortex core (and so along the axes z of the domain), then we computed $\nabla\theta$ in cylindrical coordinates[1] and finally we used the property that, for small r, the density n scales as r^2 (see Section 2.3.1).

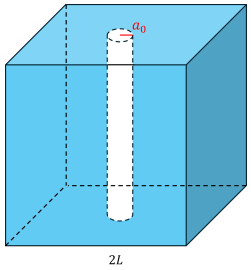

Figure A.1: Domain D with a vortex core.

[1] $\nabla = \frac{\partial}{\partial r}\mathbf{e}_r + \frac{1}{r}\frac{\partial}{\partial\theta}\mathbf{e}_\theta + \frac{\partial}{\partial z}\mathbf{e}_z$.

Hence the hypotheses of the Theorem A.0.1 are satisfied, therefore we can decompose $\sqrt{\rho}\mathbf{v}$ as in (A.1), and since $\mathbf{u}_\mathrm{h}$ satisfies both $\nabla \cdot \mathbf{u}_\mathrm{h} = 0$ and $\nabla \times \mathbf{u}_\mathrm{h} = 0$, the obtained components may include a harmonic component, so both potentials are denoted with a star superscript, according to [52] and [58]:

$$\begin{cases} \mathbf{u} = \mathbf{u}_\mathrm{v} + \mathbf{u}_c + \mathbf{u}_\mathrm{h} = \mathbf{u}_\mathrm{v}^* + \mathbf{u}_\mathrm{c}^* = \nabla \times \mathbf{A}_\mathrm{v}^* + \nabla \Phi_\mathrm{c}^* \,, \\ \mathbf{u}_\mathrm{v}^* = \mathbf{u}_\mathrm{v} + \beta \mathbf{u}_\mathrm{h} \,, \\ \mathbf{u}_\mathrm{c}^* = \mathbf{u}_\mathrm{c} + \gamma \mathbf{u}_\mathrm{h} \,, \\ \beta + \gamma = 1 \quad \text{with} \quad \beta, \gamma \in \mathbb{R} \,. \end{cases} \tag{A.4}$$

For any admissible decomposition, we aim to isolate the harmonic component within either the compressible or the vortical part by appropriately selecting the boundary conditions. The L_2-orthogonality of the decomposed components implies that

$$\begin{aligned} (\mathbf{u}_\mathrm{v}^*, \mathbf{u}_\mathrm{c}^*) &= \int_\Omega \mathbf{u}_\mathrm{v}^* \cdot \mathbf{u}_\mathrm{c}^* \, d\Omega = \int_\Omega (\mathbf{u}_\mathrm{v} + \beta \mathbf{u}_\mathrm{h}) \cdot (\mathbf{u}_\mathrm{c} + \gamma \mathbf{u}_\mathrm{h}) \, d\Omega \\ &= \int_\Omega \mathbf{u}_\mathrm{v} \cdot \mathbf{u}_\mathrm{c} + \gamma \mathbf{u}_\mathrm{v} \cdot \beta \mathbf{u}_\mathrm{h} + \beta\gamma \mathbf{u}_\mathrm{h} \cdot \mathbf{u}_\mathrm{c} + \beta\gamma \mathbf{u}_\mathrm{h} \cdot \mathbf{u}_\mathrm{h} \, d\Omega \\ &= \int_\Omega \beta\gamma \mathbf{u}_\mathrm{h} \cdot \mathbf{u}_\mathrm{h} \, d\Omega = 0 \,. \end{aligned}$$

Therefore, in order to ensure orthogonality, the harmonic component must be

- separated into the compressible component, i.e. $\gamma = 1$ and $\beta = 0$, obtaining $\mathbf{u}_\mathrm{c}^* = \mathbf{u}_\mathrm{c} + \gamma \mathbf{u}_\mathrm{h}$, $\mathbf{u}_\mathrm{v}^* = \mathbf{u}_\mathrm{v}$;
- or assigned to the vortical component, i.e. $\gamma = 0$ and $\beta = 1$, obtaining $\mathbf{u}_\mathrm{v}^* = \mathbf{u}_\mathrm{v} + \beta \mathbf{u}_\mathrm{h}$, $\mathbf{u}_\mathrm{c}^* = \mathbf{u}_\mathrm{c}$.

Selecting $\gamma = 0$ and $\beta = 1$ is preferable since, under low Mach number conditions, the resulting vortical component aligns with the incompressible flow behavior. Thus, the Helmholtz decomposition (A.1) becomes

$$\begin{cases} \mathbf{u} = \nabla \times \mathbf{A}_\mathrm{v}^* + \nabla \Phi_\mathrm{c}^* \,, \\ \nabla \Phi_\mathrm{c}^* = \mathbf{u}_\mathrm{c}^* = \mathbf{u}_\mathrm{c} \,. \end{cases} \tag{A.5}$$

We identify $\mathbf{u}_\mathrm{v}^* = \nabla \times \mathbf{A}_\mathrm{v}^*$ with the incompressible part of our field $(\sqrt{\rho}\mathbf{v})^\mathrm{i}$, and the compressible component $\mathbf{u}_\mathrm{c}^* = \mathbf{u}_\mathrm{c} = \nabla \Phi_\mathrm{c}^*$ with $(\sqrt{\rho}\mathbf{v})^\mathrm{c}$, hence the Helmholtz decomposition for $\sqrt{\rho}\mathbf{v}$ reads

$$\begin{cases} \sqrt{\rho}\mathbf{v} = (\sqrt{\rho}\mathbf{v})^\mathrm{i} + (\sqrt{\rho}\mathbf{v})^\mathrm{c} \,, \\ \nabla \cdot (\sqrt{\rho}\mathbf{v})^\mathrm{i} = 0 \,, \\ \nabla \times (\sqrt{\rho}\mathbf{v})^\mathrm{c} = 0 \,. \end{cases}$$

Now we take the divergence of (A.5) to obtain a scalar potential Poisson equation

$$\nabla \cdot \mathbf{u} = \Delta \Phi \quad \Rightarrow \quad \nabla \cdot (\sqrt{\rho}\mathbf{v}) = \Delta \Phi \,, \tag{A.6}$$

where we renamed Φ_c^* as Φ.

We now derive a unique boundary condition that ensures a distinct separation of the harmonic field into the vortical part with $\gamma = 0$ and $\beta = 1$. The orthogonality condition yields

$$\begin{aligned}(\mathbf{u}_v^*, \mathbf{u}_c^*) &= (\mathbf{u}_v^*, \nabla\Phi_c^*) \\ &= -\left(\underbrace{\nabla\cdot\mathbf{u}_v^*}_{=0}, \Phi_c^*\right) + \int_{\partial D} \Phi_c^* \mathbf{u}_v^* \cdot \mathbf{n}\, dS \\ &= \int_{\partial D} \Phi_c^* \left(\mathbf{u} - \mathbf{u}_c^*\right) \cdot \mathbf{n}\, dS \\ &= \int_{\partial D} \Phi_c^* \left(\mathbf{u} - \nabla\Phi_c^*\right) \cdot \mathbf{n}\, dS = 0\,, \end{aligned} \tag{A.7}$$

were in the second equality we integrated by parts. Thus, we have two choices: either the scalar potential has a homogeneous Dirichlet boundary (i.e. $\Phi_c^*|_{\partial D} = 0$), or the normal component of the velocity is entirely captured by the scalar potential (i.e. $\mathbf{u}_v^* \cdot \mathbf{n} = 0$). In the latter case, the scalar potential necessarily includes a harmonic contribution, implying that $\gamma = 0$. Consequently, the scalar potential Φ_c^* must satisfy (A.7) to ensure an orthogonal decomposition, and must be suitably adapted for the flow boundaries in order to have the condition $\gamma = 0$.
Finally we the following:

$$\begin{cases} \Delta\Phi = \nabla\cdot(\sqrt{\rho}\mathbf{v})\,, \\ \Phi\big|_{\partial D} = 0\,, \end{cases} \tag{A.8}$$

where $\Phi = \Phi_c^*$. □

Bibliography

[1] S. Nazarenko and R. West. "Analytical solution for nonlinear Schrödinger vortex reconnection". *J. Low Temp. Phys.* 132.1 (2003), pp. 1–10.

[2] S. Zuccher, M. Caliari, A. W. Baggaley, and C. F. Barenghi. "Quantum vortex reconnections". *Phys. Fluids* 24.12 (2012), p. 125108.

[3] S. Serafini, L. Galantucci, E. Iseni, T. Bienaimé, R. N. Bisset, C. F. Barenghi, F. Dalfovo, G. Lamporesi, and G. Ferrari. "Vortex reconnections and rebounds in trapped atomic Bose-Einstein condensates". *Phys. Rev. X* 7.2 (2017), p. 021031.

[4] P. Z. Stasiak, Y. Xing, Y. Alihosseini, C. F. Barenghi, A. Baggaley, W. Guo, L. Galantucci, and G. Krstulovic. "Experimental and theoretical evidence of universality in superfluid vortex reconnections". *PNAS* 122.21 (2025), e2426064122.

[5] C. F. Barenghi and N. G. Parker. *A primer on quantum fluids*. Springer, 2016.

[6] C. J. Pethick and H. Smith. *Bose–Einstein condensation in dilute gases*. Cambridge University Press, 2008.

[7] L. P. Pitaevskii and S. Stringari. *Bose-Einstein condensation and superfluidity*. Oxford University Press, 2016.

[8] E. P. Gross. "Structure of a quantized vortex in boson systems". *Nuovo Cimento* 20 (1961), pp. 454–477.

[9] L. P. Pitaevskii. "Vortex lines in an imperfect Bose gas". *Sov. Phys. JETP* 13 (1961), pp. 451–454.

[10] A. Villois, D. Proment, and G. Krstulovic. "Universal and nonuniversal aspects of vortex reconnections in superfluids". *Phys. Rev. Fluids* 2.4 (2017), p. 044701.

[11] L. Galantucci, A. W. Baggaley, N. G. Parker, and C. F. Barenghi. "Crossover from interaction to driven regimes in quantum vortex reconnections". *PNAS* 116.25 (2019), pp. 12204–12211.

[12] A. Villois, D. Proment, and G. Krstulovic. "Irreversible dynamics of vortex reconnections in quantum fluids". *Phys. Rev. Lett.* 125.16 (2020), p. 164501.

[13] G. P. Bewley, M. S. Paoletti, K. R. Sreenivasan, and D. P. Lathrop. "Characterization of reconnecting vortices in superfluid helium". *PNAS* 105.37 (2008), pp. 13707–13710.

[14] A. J. Allen, S. Zuccher, M. Caliari, N. P. Proukakis, N. G. Parker, and C. F. Barenghi. "Vortex reconnections in atomic condensates at finite temperature". *Phys. Rev. A* 90.1 (2014), p. 013601.

[15] H. Hasimoto. "A soliton on a vortex filament". *J. Fluid Mech.* 51.3 (1972), pp. 477–485.

[16] P. G. Saffman. *Vortex Dynamics*. Cambridge Monographs on Mechanics. Cambridge University Press, 1993.

[17] R. L. Ricca. "The contributions of Da Rios and Levi-Civita to asymptotic potential theory and vortex filament dynamics". *Fluid Dyn. Res.* 18.5 (1996), pp. 245–268.

[18] C. F. Barenghi, R. J. Donnelly, and W. F. Vinen. *Quantized vortex dynamics and superfluid turbulence*. Vol. 571. Springer Science & Business Media, 2001.

[19] D. Proment and G. Krstulovic. "Matching theory to characterize sound emission during vortex reconnection in quantum fluids". *Phys. Rev. Fluids* 5.10 (2020), p. 104701.

[20] M. Leadbeater, T. Winiecki, D. C. Samuels, C. F. Barenghi, and C. S. Adams. "Sound emission due to superfluid vortex reconnections". *Phys. Rev. Lett.* 86.8 (2001), pp. 1410–1413.

[21] R. J. Donnelly. *Quantized vortices in helium II*. Cambridge University Press, 1991.

[22] T. Araki and M. Tsubota. "Cascade process of vortex tangle dynamics in superfluid He-4 without mutual friction". *J. Low Temp. Phys.* 121.5 (2000), pp. 405–410.

[23] D. Kivotides, J. C. Vassilicos, D. C. Samuels, and C. F. Barenghi. "Kelvin waves cascade in superfluid turbulence". *Phys. Rev. Lett.* 86.14 (2001), p. 3080.

[24] W. F. Vinen. "Decay of superfluid turbulence at a very low temperature: The radiation of sound from a Kelvin wave on a quantized vortex". *Phys. Rev. B* 64.13 (2001), p. 134520.

[25] W. F. Vinen, M. Tsubota, and A. Mitani. "Kelvin-wave cascade on a vortex in superfluid He-4 at very low temperature". *Phys. Rev. Lett.* 91.13 (2003), p. 135301.

[26] C. F. Barenghi, R. Hänninen, and M. Tsubota. "Anomalous translational velocity of vortex ring with finite-amplitude Kelvin waves". *Phys. Rev. E* 74.4 (2006), p. 046303.

[27] C. Nore, M. Abid, and M. E. Brachet. "Decaying Kolmogorov turbulence in a model of superflow". *Phys. Fluids* 9.9 (1997), pp. 2644–2669.

[28] A. J. Chorin and J. E. Marsden. *A mathematical introduction to fluid mechanics*. Vol. 4. Springer-Verlag, New York, 1993.

[29] J. Koplik and H. Levine. "Vortex reconnection in superfluid helium". *Phys. Rev. Lett.* 71.9 (1993), p. 1375.

[30] R. Tebbs, A. J. Youd, and C. F. Barenghi. "The approach to vortex reconnection". *J. Low Temp. Phys.* 162.3-4 (2011), pp. 314–321.

[31] S. Zuccher and R. L. Ricca. "Helicity conservation under quantum reconnection of vortex rings". *Phys. Rev. E* 92.6 (2015), p. 061001.

[32] T. Zhu, M. L. Evans, R. A. Brown, P. M. Walmsley, and A. I. Golov. "Interactions between unidirectional quantized vortex rings". *Phys. Rev. Fluids* 1.4 (2016), p. 044502.

[33] S. Zuccher and R. L. Ricca. "Relaxation of twist helicity in the cascade process of linked quantum vortices". *Phys. Rev. E* 95.5 (2017), p. 053109.

[34] A. Villois, H. Salman, and D. Proment. "Scattering of line-ring vortices in a superfluid". *J. Low Temp. Phys.* 180.1 (2015), pp. 68–81.

[35] P. J. Green, M. J. Grant, J. W. Nevin, P. M. Walmsley, and A. I. Golov. "Quantized vortex rings and loop solitons". *J. Low Temp. Phys.* 201.1 (2020), pp. 11–17.

[36] R. Doran, A. W. Baggaley, and N. G. Parker. "Vortex solutions in a binary immiscible Bose-Einstein condensate". *Phys. Rev. A* 109.2 (2024), p. 023318.

[37] E. Madelung. "Quantentheorie in hydrodynamischer Form". *Z. Phys.* 40 (1926), pp. 322–326.

[38] L. Salasnich. *Modern physics*. Springer, 2022.

[39] L. Salasnich. *Derivation of the Gross-Pitaevskii equation and applications*. Conference presentation, Patna Conference on Quantum Fluids. 2019. URL: `https://materia.dfa.unipd.it/salasnich/talk-patna19b.pdf`.

[40] E. R. Priest. "Heating the solar corona by magnetic reconnection". *Astrophys. Space Sci.* 264.1 (1998), pp. 77–100.

[41] S. Kida and M. Takaoka. "Vortex reconnection". *Annu. Rev. Fluid Mech.* 26.1 (1994), pp. 169–177.

[42] E. Fonda, D. P. Meichle, N. T. Ouellette, S. Hormoz, and D. P. Lathrop. "Direct observation of Kelvin waves excited by quantized vortex reconnection". *PNAS* 111 (2014), pp. 4707–4710.

[43] F. Hussain and K. Duraisamy. "Mechanics of viscous vortex reconnection". *Phys. Fluids* 23.2 (2011), p. 021701.

[44] Z. Xue et al. "Observing the release of twist by magnetic reconnection in a solar filament eruption". *Nat. Commun.* 7 (2016), p. 11837.

[45] M. S. Paoletti, M. E. Fisher, and D. P. Lathrop. "Reconnection dynamics for quantized vortices". *Physica D* 239.14 (2010), pp. 1367–1377.

[46] A. Enciso and D. Peralta-Salas. "Vortex reconnections in classical and quantum fluids". *SeMA J.* 79.1 (2022), pp. 127–137.

[47] S. Ogawa, M. Tsubota, and Y. Hattori. "Study of reconnection and acoustic emission of quantized vortices in superfluid by the numerical analysis of the Gross-Pitaevskii equation". *J. Phys. Soc. Jpn* 71.3 (2002), pp. 813–821.

[48] M. Caliari and S. Zuccher. "A fast time splitting finite difference approach to Gross-Pitaevskii equations". *Commun. Comput. Phys.* 29.5 (2021), pp. 1336–1364.

[49] C. A. Jones and P. H. Roberts. "Motions in a Bose condensate. IV. Axisymmetric solitary waves". *J. Phys. A* 15.8 (1982), pp. 2599–2619.

[50] M. Leadbeater, D. C. Samuels, C. F. Barenghi, and C. S. Adams. "Decay of superfluid turbulence via Kelvin-wave radiation". *Phys. Rev. A* 67.1 (2003), p. 015601.

[51] S. Zuccher and R. L. Ricca. "Creation of quantum knots and links driven by minimal surfaces". *J. Fluid Mech.* 942 (2022), p. 22.

[52] S. Schoder, K. Roppert, and M. Kaltenbacher. "Postprocessing of direct aeroacoustic simulations using Helmholtz decomposition". *AIAA Journal* 58.7 (2020), pp. 3019–3027.

[53] M. Caliari and S. Zuccher. "Reliability of the time splitting Fourier method for singular solutions in quantum fluids". *Comput. Phys. Commun.* 222 (2018), pp. 46–58.

[54] M. Caliari, F. Cassini, L. Einkemmer, A. Ostermann, and F. Zivcovich. "A μ-mode integrator for solving evolution equations in Kronecker form". *J. Comput. Phys.* 455 (2022), p. 110989.

[55] *See Supplemental Material.* URL: `https://1drv.ms/f/c/a9007d17fc3c55c8/IgA2FmCLZ4RuTZMUCdDHZ4WyAW_yTNwAqgRmIm7rSxgfcks?e=yhWca0`.

[56] M. Caliari, F. Cassini, and F. Zivcovich. "A μ-mode BLAS approach for multidimensional tensor-structured problems". *Numer. Algorithms* 92.4 (2023), pp. 2483–2508.

[57] W. Bao and Y. Cai. "Mathematical theory and numerical methods for Bose–Einstein condensation". *Kinet. Relat. Models* 6.1 (2013), pp. 1–135.

[58] S. Schoder, K. Roppert, and M. Kaltenbacher. "Helmholtz's decomposition for compressible flows and its application to computational aeroacoustics". *Partial Differ. Equ. Appl.* 1.6 (2020), p. 46.

[59] G. K. Batchelor. *An introduction to fluid dynamics*. Cambridge University Press, 1999.